Measurements of Production and Decay Properties of Bs Mesons Decaying into J/Psi Phi with the CMS Detector at the LHC

A Thesis Presented for
The Doctor of Philosophy
Degree
The University of Tennessee, Knoxville

Giordano Cerizza

May 2012

A mia moglie Joey

Acknowledgements

I would like to thank many people, without whom this work would not have been possible. First, I would like to express my gratitude to Stefan Spanier for giving me the opportunity to do this Ph.D. study and for sharing his great knowledge and experience in particle physics. Throughout the past five years, his expert guidance, motivation, patience, and continuous support have been truly invaluable.

The CMS Pixel Online group helped me to understand the nuances of experimental detector design and operations. I would like to especially thank: Anders Ryd (Cornell); Danek Kotlinsky (PSI); Gino Bolla (Purdue); Karl Ecklund (Rice); Will Johns from (Vanderbilt); and all the graduate students and friends associated with CMS with whom I spent most of my time while stranded at CERN: Souvik Das, Ben Kreis, Vincenzo Lombardo, Simone Stracka, Marco Pappagallo, Antonio Petrella, Giacomo Fedi, and the UT colleagues Andrew York, Matt Hollingsworth, and Zongchang Yang.

The CMS B-Physics analysis working group helped me publishing the results presented in this dissertation with their careful scrutiny of the analysis. I want to thank: Paula Eerola (Helsinki); Vincenzo Chiochia (Zurich); Carlos Lourenço (CERN); Jim Olsen (Princeton); Gigi Rolandi (Pisa); Kevin Stenson (Colorado at Boulder); Nuno Leonardo (CERN); Hermine K. Wöhri (CERN); Alexander Schmidt (Hamburg); and all the other people who sent comments and suggestions during the approval stage of the analysis.

A special thank you to Laurent Gross from University of Strasbourg for all the time I spent in his office discussing and for his friendship outside the CERN. I really appreciate all the things you helped me with. Alfio Lazzaro, a great friend and colleague from CERN/openlab, who helped me greatly with discussions on the Maximum Likelihood fitting procedures; David Lopes Pegna from Princeton for giving me input on the analysis techniques and for an unforgettable overnight session of work during the conference organized by the University of Michigan; Keith Ulmer from University of Colorado at Boulder for the discussions and cross checks during the period of the analysis approval.

To Geri Ragghianti for his friendship and always prompt computing support with the Newton cluster. Your contribution to the final results was fundamental.

I would like to thank my fellow graduate student friends at UT for all the time we spent solving homework and having fun during the first two years: Merek Chertkow, Andrew York, Jason Lambert, Andrew Nicholson, Zach Barnett, Chris Smith, and Dwayne John. And, finally, the two Italians at UT: Norman Mannella and Paolo Vilmercati. Great times with great friends.

My mother and father, who always stood behind me during this overseas adventure, and my brother, who came to visit me in 2008 during a very hard year for me, deserve thanks as well. Above all, my greatest thanks to my wife Joey, who, for three long years, had to put up with incalculable schedules and indefinite plans. You encouraged me to accomplish this goal. Thank you.

"I don't know anything, but I do know that everything is interesting if you go into it deeply enough." Richard Feynman

Abstract

The production of hadrons containing b-quarks has been measured in proton anti-proton collisions up to center-of-mass energies of 1.96 TeV at the Tevatron. Information at lower energy is provided by electron-positron collision experiments. The underlying theory of hadronic interactions is tuned to those data but cannot reliably predict reaction rates from first principles for higher energies. Therefore, it is important to test the extrapolations and optimize model parameters for the new energy regime at the LHC. The b-hadrons from proton-proton collisions are a major source of background in searches for the Higgs boson and other heavy not-yet-discovered particles. Hence, it is important to quantify their presence in different reactions for the main research program at the LHC.

The measurement of the Bs-meson production cross section presented in this dissertation complements the measurements for the B+ and the Bd mesons. The outcome is compared to different models for quark production and hadronization. The three CMS measurement of B-meson production cross sections are used to calculate the Bs to J/psi phi branching fraction.

The measurement of the time-dependent decay rate of Bs mesons probes the weak interaction and includes the possibility to observe sizable particle anti-particle asymmetries caused by heavy particles and new forces between them that are not predicted by the Standard Model. In this dissertation the lifetime, lifetime difference, and CP-composition in the decay Bs to J/psi phi have been extracted with a

Maximum Likelihood fit. The J/psi meson decays into two muons, while the phi meson into two charged kaons.

The results are presented for the data recorded during the year 2010 with the Compact Muon Solenoid. It is a general-purpose particle detector centered at one of the interaction points of the Large Hadron Collider, a proton-proton collider located at the particle physics laboratory CERN in Geneva (Switzerland). It is designed to explore a wide range of physics in proton-proton collisions. The investigations presented here assess and benchmark the performance of a variety of detector components including track and muon reconstruction. For reconstruction of long-lived particles, such as the b-hadrons, the silicon pixel detector provides the most significant information.

Contents

List of Tables

List of Figures

Motivations

Elementary particle physicists study the smallest constituents of matter and the fundamental forces that act between them to arrive at a unified description of nature. Today, particle accelerators at the highest energies act as microscopes that resolve matter at a length scale smaller than 10^{-18} m. Measurements over the last 40 years have demonstrated that the interactions between particles can be successfully described by the Standard Model, which is a quantum field theory that involves the electromagnetic, weak, and strong force. This Standard Model of particle physics predicts to very high precision reaction rates and symmetry breaking phenomena in the energy regime accessible with present accelerator technologies but many questions remain unanswered, for example the link to models about the creation of the Universe. According to prediction, the Higgs boson is responsible for creating mass of all constituent particles and is so fundamental that a non-observation of this well-constraint particle will require a profound rethinking of the model. To challenge the Standard Model predictions at higher energies and answer the fundamental question of what produces the mass of particles, the Large Hadron Collider (LHC) at the European particle physics laboratory CERN in Geneva (Switzerland) has been built. Since 2009, it collides protons at center-of-mass energies of $\sqrt{s} = 7$ TeV with continuously increasing beam intensities.

There are six known quarks that are the constituents of hadrons, such as protons. Particles that contain the beauty (b)-quarks, the second heaviest quark, such as b-baryons and B mesons, are a unique laboratory to study strong and weak forces.

The production of heavy quarks in proton-proton collisions is predicted by the theory of strong interactions, the perturbative Quantum Chromodynamics (QCD) that is incorporated in the Standard Model. The theory can be tested by measuring yields of particles containing b-quarks as function of kinematic variables. The quantification of b-hadron production rates is crucial because they represent a major source of background for elusive processes, such as the production of the Higgs boson, top-quarks (the heaviest quark among the six quarks) and others that are known to decay via b-quarks, and because b-hadrons can emulate known signals as well as new signals from as-of-yet undiscovered particles. The measured production rates are used to improve simulated events produced via Monte Carlo generators of the proton-proton collisions at LHC at a given center-of-mass energy. Simulated events are reconstructed and selected by the same criteria that apply, for example, to the Higgs searches so that any event distribution originating from b-hadron production can be subtracted from event distributions in data and any residual event excess can be safely identified as signal.

The Compact Muon Solenoid (CMS) collaboration recently measured the cross sections for production of B^+ and B^0 in proton proton collisions at $\sqrt{s} = 7$ TeV. This dissertation presents the first measurement of the production of B^0_s mesons, which consist of a b- and s-quark, with B^0_s decaying into $\mathrm{J}/\psi\ \phi$, that adds complementary information to improve the understanding of b-quark production at this energy. Data are compared to higher-order corrections of QCD predictions for heavy-quark production. A consistency check amongst the three B meson (B^+,B^0, B^0_s) production cross sections is performed by measuring the branching fraction of B^0_s mesons decaying into $\mathrm{J}/\psi\ \phi$ with respect to the production of B^+ and B^0 particles and comparing it to the value measured by previous experiments. The measurement presented here is also performed in a kinematic regime complementary to the one accessible by the dedicated B-physics experiment LHC-b at the LHC.

The decays of the B^0_s meson and its anti-particle $\bar{\mathrm{B}}^0_\mathrm{s}$ are the least studied. While the B-factories BaBar and Belle were able to access the $\mathrm{B}_\mathrm{u,d}$ mesons (containing a b-quark and an u- or d-quark) via the $\Upsilon(4S)$ resonance production in electron-positron collisions at very high beam intensities, the $\mathrm{B_s^0}$ meson is only accessible with high enough rates for precision measurements at hadron colliders such as the Tevatron and the LHC. The decay $\mathrm{B_s^0} \rightarrow \mathrm{J}/\psi\ \phi$ proceeds at the quark-level via the $\mathrm{b}\rightarrow\mathrm{c\bar{c}s}$ transition (c stands for charm-quark, $\bar{\mathrm{c}}$ for charm anti-quark) due to weak interactions (or as modeled by quantum field theory due to the exchange of heavy W-bosons). As a direct consequence of quantum mechanics and the weak interaction, neutral $\mathrm{B_s^0}$ mesons can transform into their anti-particle $\mathrm{\bar{B}_s^0}$ ($\mathrm{B_s^0}$-$\mathrm{\bar{B}_s^0}$ mixing). The combination of mixing and decay transitions can exhibit a rate difference for particle versus anti-particle. Equal rates are expected if the fundamental symmetries parity (P) and charge conjugation (C) are conserved. The difference, or CP-violation, is predicted to be at the level of 10^{-3} in the Standard Model. New processes involving heavier exchange particles as predicted by theories beyond the Standard Model can contribute to the mixing and potentially enhance the CP violation effect. Hence, a precise measurement of the decay characteristics of the $\mathrm{B_s^0}$ meson in the $\mathrm{J}/\psi\ \phi$ final state is an indirect search for Physics beyond the Standard Model. This dissertation presents the first measurement of the $\mathrm{B_s^0}$-lifetime, lifetime-difference, and CP-content measurement with the first-year data from the LHC with the CMS detector.

The measurements of b-hadron production and decay properties require precision measurements of charged tracks near the proton-proton collision point. The average lifetime of b-hadrons is about 1.5×10^{-12} s. At high transverse momenta they propagate several hundred μm away from the collision point before they decay. Hence, a b-hadron can be identified and its lifetime measured by the displaced position of its decay, which is reconstructed from the charged decay products. In case of the $\mathrm{B_s^0} \rightarrow \mathrm{J}/\psi\ \phi$ decay there are two charged muons from the J/ψ decay and two charged kaons from the ϕ decay. The measurement closest to the beam is performed with the CMS silicon pixel detector. This dissertation describes the software that has been designed and implemented to guarantee maximum up-time and high data quality for this detector.

Chapter 1

Introduction on B Physics

1.1 Production and Decay of B_s^0 Mesons

The mechanism of production and decay of B_s^0 particles is described in the theoretical framework called the Standard Model (SM) of particle physics. The SM is a Quantum Field Theory (QFT) that treats forces between constituent particles as being mediated by force particles. The constituents particles of the SM are fermions (particles with half-integer spin) that are divided into quarks (like the anti-b and the s quarks that compose the so-called B_s^0 mesons) and leptons, like the electron. Three forces (electromagnetic, strong, and weak) describe interactions between leptons and quarks and occur via exchange of particles with integer spin, the bosons. The production of B_s^0 mesons is driven by the strong force and proceeds in two separate steps:

- b-quark pairs are produced from proton proton collisions through elementary quark (q) or gluon (mediator particle of the strong force) processes,
- b-quarks separate and turn into hadrons, which are more complex quark combinations, at the so-called hadronization stage.

The weak force is, instead, responsible for the B_s^0 mesons decaying into the J/ψ and ϕ particles. The study of this decay channel allows to measure the production rate of the $\mathrm{B_s^0}$ mesons, probe the structure of quark (flavor) mixing, and CP violating effects that may arise from the difference in rate between $\mathrm{B_s^0}$ and $\mathrm{\bar{B}_s^0}$ that decay into the same final state $\mathrm{J}/\psi\ \phi$.

Section 1.2 introduces the basic concept of the Standard Model. The description of the b-quark production mechanism and hadronization in $\mathrm{B_s^0}$ mesons is given in Section 1.3. Finally, the phenomenology of $\mathrm{B_s^0}$ decays, the mechanism of $\mathrm{B_s^0}$-$\mathrm{\bar{B}_s^0}$ mixing, and the CP violation in the $\mathrm{B_s^0} \rightarrow \mathrm{J}/\psi\ \phi$ decay is presented in Section 1.4.

1.2 The Standard Model of Particle Physics

The SM is a theoretical framework that describes particle reactions up to energies achieved by present-day accelerators to a very high precision Turner (1999). The building blocks of matter are classified in two categories: quarks and leptons. There are six types (flavors) of quarks divided into three families (generations) : up (u) and down (d), charm (c) and strange (s), top (t) and bottom (b). Their masses increase from the lightest u-quark to the heaviest one, the t-quark, which has approximately the mass equal to one gold atom. Quarks are characterized by a fractional electric charge (+2/3,−1/3) and for each quark there exists a charge-conjugated anti-quark. There are three different flavors of leptons, or electron-like particles: the electron, muon, and tau, each with a flavor-specific neutrino (electron neutrino, muon neutrino, and tau neutrino). Neutrinos have no electrical charge while electrons, muons, and tau particles have one unit of electrical charge. All leptons have corresponding anti-particles. The complete list of constituent particles with their properties can be found in Table 1.1.

Table 1.1: Properties of the fermions, spin-1/2 particles.

Family	Name	Symbol	Charge (in units of e)	Mass (GeV/c^2)
I	up	u	+2/3	$1.7 - 3.1 \times 10^{-3}$
	down	d	−1/3	$4.1 - 5.8 \times 10^{-3}$
	electron	e	−1	0.5×10^{-3}
	electron-neutrino	ν_e	0	0
II	charm	c	+2/3	1.3
	strange	s	−1/3	0.1
	muon	μ	−1	0.1
	muon-neutrino	ν_μ	0	0
III	top	t	+2/3	172.9
	bottom	b	−1/3	4.8
	tau	τ	−1	1.8
	tau-neutrino	ν_τ	0	0

The SM comprises four forces:

- Gravitation,
- Electromagnetic,
- Strong, and
- Weak.

The gravitation, force of attraction between masses, is not relevant at this energy scale ($E \lesssim 100$ GeV). All the forces, which are described by a QFT, involve the exchange of one or more particles (bosons), as listed in Table 1.2. The maximum range is dictated by the uncertainty principle since the mediator particles are created and exist only in the exchange process (as virtual particles).

Table 1.2: Properties of the bosons, mediator particles of the forces.

Force	Name	Symbol	Charge (in units of e)	Mass (GeV/c^2)
Electromagnetic	Photon	γ	0	0
Weak	Z boson	Z	0	91.2
	W boson	W	±1	80.4
Strong	gluon	g	0	0

The electromagnetism is described by the Quantum Electro Dynamics (QED), where the interaction between charged fermions is realized as an exchange force arising from the emission and absorption of virtual photons. The electromagnetic force is responsible for binding atoms and molecules together. The forces of electric attraction and repulsion of electric charges are so dominant over the other two fundamental forces that they can be considered negligible for the atomic and molecular structure.

The QFT describing the hadronic interaction between quarks is the Quantum Chromo Dynamics (QCD). It is mediated by exchanges of the massless gluons. It is the force responsible for holding the quarks together in particles. Only two types of quark combinations (hadrons) are established as existing in nature:

- meson = $q\bar{q}$ (quark anti-quark pair)

- baryon = qqq (three-quark state).

The quarks that determine the quantum numbers of the hadrons are called *valence* quarks. Any hadron may contain an indefinite number of virtual (or sea) quarks, anti-quarks, and gluons which do not influence its quantum numbers. The latter dominate the dynamics of hadrons in reactions at high energies, while at energies below 10 GeV the description of hadrons in terms of valence quarks is very successful. Parton is a generic term to describe any particle which may be present inside a hadron. It includes quarks, anti-quarks, and gluons. Of main interest in this dissertation are the $\mathrm{B_s^0}$ mesons, particles that are composed of the valence quarks anti-b and s (the corresponding anti-$\mathrm{B_s^0}$ meson consists of a b and an anti-s quarks). Proton and neutron, composed of uud and udd valence quark combinations, respectively, are examples of baryons. Figure 1.1 shows a representation of the components of a proton. The presence of multiple quarks with the same quantum numbers, as it is possible

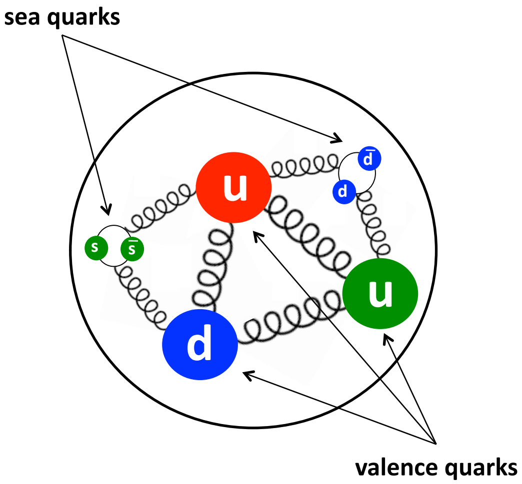

Figure 1.1: Representation of the constituents of a proton.

in baryons, violates the Pauli exclusion principle for identical fermions. To avoid this, a new degree of freedom called color charge was introduced Greenberg (1964). This charge is the source of the inter-quark force or also called color force. Three colors (with corresponding three anti-colors) exist: red, green, and blue. Quarks are assigned a color, while gluons mediate a color and an anti-color. In nature, no free quarks or gluons are found: the theory accounts for this fact by requiring that only color-less particles can be observed.

The Quantum Flavor Dynamics theory parameterizes the weak interaction. This is a very short range interaction because the mediator particles, W and Z^0, are very massive. All elementary particles participate in the weak interaction, either via charged W or the neutral Z^0. Neutrinos can only interact weakly with other particles. The quark states that undergo the weak interaction via exchange of $W^\pm$ are different from the strongly interacting mass eigenstates. Weakly interacting quarks can be expressed as an admixture of the latter ones. Historically, when only two generations of quarks were known, the strong quark states (d and s) were translated into weakly interacting states (d' and s') according to a 2×2 rotation or mixing matrix which depends on one angle, called Cabibbo angle Cabibbo (1963). This mixing matrix was extended by Kobayashi and Maskawa Kobayashi and Maskawa (1973) to three generations of quarks in what is commonly known as the Cabibbo-Kobayashi-Maskawa (CKM) quark-mixing matrix

$$\begin{pmatrix} d' \\ s' \\ b' \end{pmatrix} = V_{CKM} \begin{pmatrix} d \\ s \\ b \end{pmatrix} \tag{1.1}$$

with

$$V_{CKM} = \begin{pmatrix} V_{ud} & V_{us} & V_{ub} \\ V_{cd} & V_{cs} & V_{cb} \\ V_{td} & V_{ts} & V_{tb}. \end{pmatrix} \tag{1.2}$$

The CKM matrix contains the strengths of the nine possible transitions from one flavor to another that are mediated by the charged $W^\pm$ bosons. The corresponding diagram at quark level is shown in Figure 1.2. The definition given in Equation 1.2

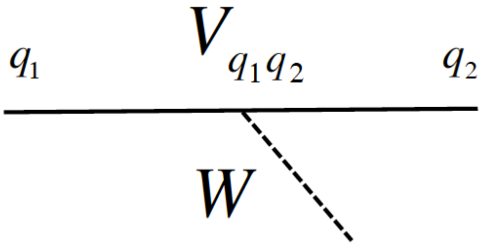

Figure 1.2: Transition between a quark q_1 to a quark q_2 by emitting a W boson. The strength of this transition (coupling strength) is the CKM matrix element $V_{q_1q_2}$.

in terms of down-type quarks is arbitrary and does not represent any sort of physical asymmetry between up-type and down-type quarks. Therefore, it is possible to define the matrix in the other way, describing the up-type quarks (u',c',t') in terms of (u,c,t). Since the CKM matrix is unitary, it results the same matrix. The electromagnetic and the weak forces are unified in the electroweak force as formulated by Glashow, Weinberg, and Salam Glashow (1961); Salam et al. (1964); Weimberg (1967).

Fundamental requirements in the parameterization of all the forces are *gauge invariance* and *renormalizability*. The principle of gauge invariance ensures that the description of the interaction of particles results in finite reaction rate calculations. The gauge invariance can be global, if the corresponding gauge transformation of the force field acts identically at all points in space-time. Invariance under global gauge transformation in electromagnetic interactions yields charge conservation. The gauge invariance is local if it varies according to the position. For example, the local gauge invariance of the QED requires the existence of the photon to mediate the field. Renormalization is the formal process of redefining infinities in the perturbative expansion of the theory to reproduce observed particle charges and masses. In consequence, predicted reaction rates become finite, i.e. have physical meanings. The invariance of a theory under global and local gauge invariance ensures that the theory is renormalizable t'Hooft, G. (1971a) t'Hooft, G. (1971b). The close agreement between theoretical predictions and experiment at energies below 100 GeV is a very successful outcome of this approach. The Standard Model depends on 19 parameters that can be measured: the masses of the constituent particles (9), the interaction coupling constants (3), the weak mixing angles (3) and a weak CP-phase (1) from the quark-mixing matrix, a QCD-related angle (1), and the parameters related to the Higgs mechanism (2). The Higgs mechanism Higgs (1964) is the most popular process to explain the origin of the particle masses: masses arise from the interaction of particles with a scalar quantum field called the Higgs field. The SM postulates a massive Higgs boson, which has not yet been observed. The search for the Higgs boson is one of the main mission conducted with the CMS experiment at the LHC. The theory of particle physics is also strongly correlated to some fundamental cosmological questions such as the absence of anti-matter in our universe Turner (1999) at a scale of 10^{20} light years. Starting with the generally accepted assumption that equal amounts of matter and anti-matter were first present in the universe, one is left with the conclusion that this symmetry was broken during its evolution. The hypothetical physical process that generated an asymmetry between baryons and anti-baryons in the very early universe is called baryogenesis. The explanation of this deficit may be found in the behavior of elementary building blocks of matter, the quarks. The SM of particle physics has ingredients to model the symmetry breaking between matter and anti-matter. One important element is the CP violation, where combined charge and parity symmetries are broken. It is observed as difference in the transition or decay rate of particle versus its anti-particle. CP violation was observed for the first time in 1964 Christenson (1964); Wolfenstein (1964) in the decay of neutral K mesons and, recently, with high precision by the B factories Aubert et al. (2002b); Abe et al. (2002). Those CP violation effects are in agreement with SM expectations but they are too small for any cosmological model to explain the observed asymmetry between matter and anti-matter indicating that the SM may be incomplete. In the SM, the parameterization of CP violation and the numbers of quark flavors are connected. For three quark generations the CKM matrix is parameterized with three Euler angles and one complex phase δ Nakamura et al. (2010)

$$V_{CKM} = \begin{pmatrix} c_{12}c_{13} & s_{12}c_{13} & s_{13}e^{-i\delta} \\ -s_{12}c_{23} - c_{12}s_{23}s_{13}e^{i\delta} & c_{12}c_{23} - s_{12}s_{23}s_{13}e^{i\delta} & s_{23}c_{13} \\ s_{12}s_{23} - c_{12}c_{23}s_{13}e^{i\delta} & -c_{12}s_{23} - s_{12}c_{23}s_{13}e^{i\delta} & c_{23}c_{13} \end{pmatrix} \tag{1.3}$$

where $c_{ij} = \cos\theta_{ij}$ and $s_{ij} = \sin\theta_{ij}$. The complex phase δ introduces the possibility of CP violation. This phase has been observed significantly different from zero $\delta = (73^{+22}_{-25})^\circ$ Nakamura et al. (2010). To observe the phase via measurement of particle decays requires that at least two different elementary processes contribute. The decay rate is proportional to the square of the sum of all possible transition amplitudes. If only one complex process amplitude contributes, the amplitude squared does not depend on the phase anymore. With at least two different amplitudes that interfere, the amplitude square results in terms that depend on the relative phase between the amplitudes, i.e. the transition rate becomes phase-dependent and CP-violating effects can be observed, if the relative phase also contains the CP phase. Based on the fact that $s_{13} \ll s_{23} \ll s_{12} \ll 1$, the CKM matrix can be expanded in a series of the parameter $\lambda = s_{12} \approx 0.23$. In the Wolfenstein parametrization Wolfenstein (1983) the matrix is written as

$$V_{CKM} = \begin{pmatrix} 1-\lambda^2/2 & \lambda & A\lambda^3(\rho - i\eta) \\ -\lambda & 1-\lambda^2/2 & A\lambda^2 \\ A\lambda^3(1-\rho-i\eta) & -A\lambda^2 & 1 \end{pmatrix} + \mathcal{O}(\lambda^4), \tag{1.4}$$

with $A = s_{23}/s_{12}$, $\rho = s_{13}s_{12}/s_{23}\cos\delta$, and $\eta = s_{13}s_{12}/s_{23}\sin\delta$. The CP-violating parameter η is assigned to the elements V_{td} and V_{ub}. The multiplicative term $A\lambda^3 \approx 10^{-3}$ is responsible for the suppression of CP violation in the Standard Model in the quark sector. The unitarity of the CKM matrix defines a set of equations that the matrix elements must satisfy:

$$\sum_i V_{ij}V^*_{ik} = \delta_{jk}, \tag{1.5}$$

$$\sum_j V_{ij}V^*_{kj} = \delta_{ik}, \tag{1.6}$$

where the six vanishing combinations represent triangles in a complex plane. Triangles of adjacent rows or columns are almost degenerate, meaning that two angles are almost 90° whereas the third angle is close to 0°. The most commonly used unitarity relation is given by

$$V_{ud}V^*_{ub} + V_{cd}V^*_{cb} + V_{td}V^*_{tb} = 0. \tag{1.7}$$

Dividing by the best known value $V_{cd}V^*_{cb}$, the equation defines a triangle (see Figure 1.3) with vertices exactly at $(0,0)$, $(0,1)$, and $(\bar{\rho},\bar{\eta})$, where $\bar{\rho} = \rho(1-\lambda^2+\ldots)$ and $\bar{\eta} = \eta(1-\lambda^2+\ldots)$. The different mixing parameters have been measured in a huge variety of experiments Nakamura et al. (2010). Direct measurements of the angle of the unitarity triangle result in $(\alpha+\beta+\gamma) = (180^{+27}_{-30})^\circ$, which is consistent with the Standard Model prediction. The CKM matrix elements can also be obtained by combining all available measurements with the SM constraints (i.e. three generation

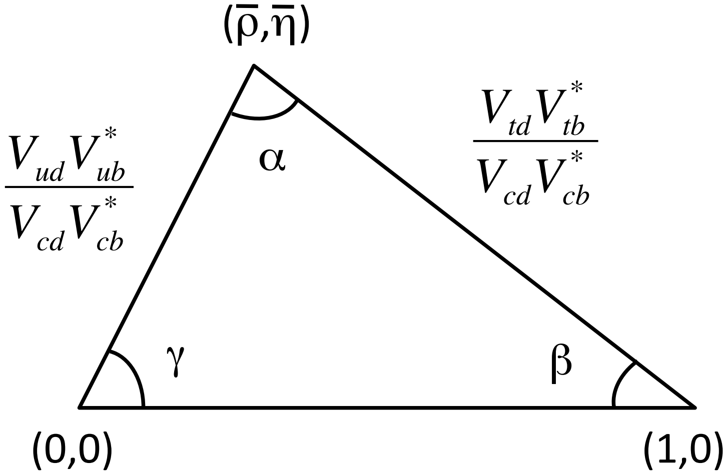

Figure 1.3: Representation of the unitarity triangle.

unitarity) in one global fit. This must also take into account theoretical predictions for hadronic matrix elements which can have significant uncertainties. The two best known fits are CKMfitter, which uses a frequentist statistical approach Charles et al. (2005), and UTfit, which, instead, uses a Bayesian approach Bona et al. (2005). Both provide similar results; the results from CKMfitter Nakamura et al. (2010) are:

$$\begin{aligned}
\lambda &= 0.22521 \pm 0.00082 \\
A &= 0.8116^{+0.0097}_{-0.0241} \\
\rho &= 0.139^{+0.025}_{-0.027} \\
\eta &= 0.341^{+0.016}_{-0.015}.
\end{aligned}$$

The B meson decays provide access to five elements of the CKM matrix. These elements are measured as

- V_{ub}: from inclusive decays B $\rightarrow X_u l\bar{\nu}$ decays, where X_u is any particle with a valence u-quark, i.e. π, and $l\bar{\nu}$ is a lepton with the corresponding neutrino;
- V_{cb}: from exclusive and inclusive semi-leptonic decays of B mesons to charm, i.e. B $\rightarrow X_c l\bar{\nu}$, where X_c is any particle with a valence c-quark, i.e. D mesons;
- V_{td} and V_{ts}: they cannot be measured directly from decays of the t-quark. Therefore, the determination of these elements rely on the virtual coupling of the d- and s-quark with the t-quark, as it occurs in the $\mathrm{B}_q\bar{\mathrm{B}}_\mathrm{q}$ oscillations (for more details see Section 1.4.2) or in the rare $\mathrm{B}_q \rightarrow X_q \nu\nu$ decays (with $q = d, s$);
- V_{tb}: from the ratio measurements of the $t \rightarrow Wb$ decay over the three $t \rightarrow Wq$ (with $q = d, s, b$) decay channels.

The remaining four CKM elements (V_{qd} and V_{qs} with $q = u, c$) are, instead, measured through direct decays of hadrons into leptons and neutrinos.

The dominant types of amplitudes for B meson decays are represented by: tree, hadronic color-suppressed, penguin, and box diagrams, as shown in Figure 1.4. Tree

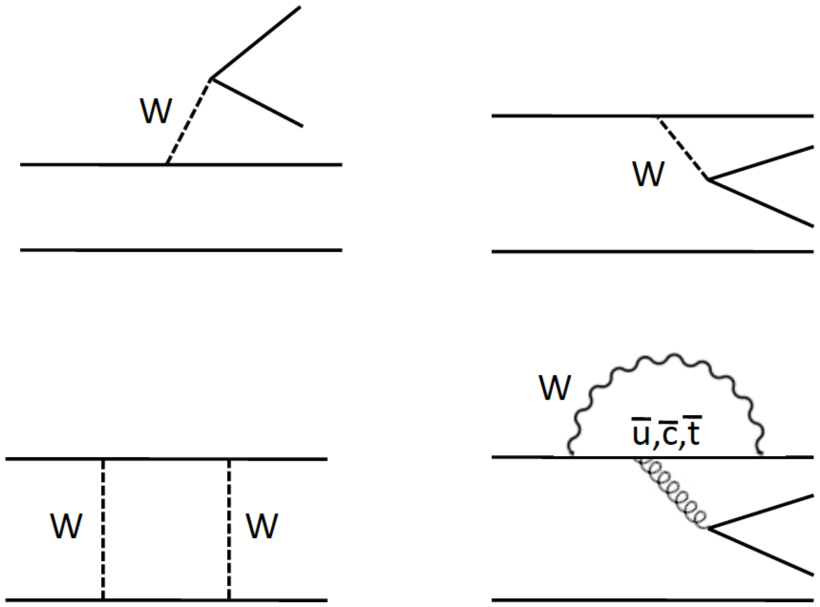

Figure 1.4: Representation of the diagram corresponding to the tree (top left), color-suppressed (top right), box (bottom left), and gluonic penguin (bottom right) amplitudes of the B-meson decays.

level diagrams describe a process in which a quark decays into a lighter quark via emission of a W boson. The W further decays into a quark anti-quark or a lepton-neutrino pair. The other valence quark does not participate in the interaction (spectator quark). These processes are favored most of the time.

Another type of tree-level process is the color-suppressed; in this diagram, the quark anti-quark pair from the decay of the charged W boson has to match the color of the initial valence quarks. Naively, one expects that this process is suppressed with respect of the external spectator decay by a factor of 1/3 since the color charge of the two quark systems have to match. However, strong interaction effects can change the color charges and the suppression might be reduced or even disappear.

Box diagrams occurs via the exchange of two W bosons. These diagrams describe the mechanism of transformation of a neutral B-meson into its anti-particle and vice versa. In these processes, there is also the possibility that new particle and forces between them not included in the SM can contribute to the transition and alter the predicted decay pattern. As today, neither the B^0 or the B_s^0 systems have shown hints of physics beyond the SM Raven, G. (2011).

Penguin diagrams refer to one-loop processes in which a quark temporarily changes flavor (via a W or Z loop), and the flavor-changed quark engages in some tree interaction, typically a strong one. Processes dominated by loops introduce the possibility of new heavy particles that do not explicitly decay but gets reabsorbed and that may virtually contribute. In the B^0 system, no significant deviations from the SM have been observed in emission and reabsorption transitions in decays such as $\mathrm{B}^0 \to \phi K$ Aubert et al. (2005a) or $\mathrm{B}^0 \to \eta' K$ Aubert et al. (2005b).

1.3 Production Mechanism of B Mesons at the LHC

At the LHC the collisions between protons produce b-quark anti-b ($\bar{\mathrm{b}}$) quark pairs that combine with other quarks to form B mesons (hadronization). The first stage at elementary parton level is presented here.

1.3.1 Production of $\mathrm{b\bar{b}}$ Quark Pairs

The primary collision between hadron constituents is described by the QCD theory and categorized according to variables that describe the momentum and angular ranges of the reaction products:

- the transverse momentum p_{T}: the component of the momentum in the plane perpendicular to the direction of the collisions,
- the pseudorapidity η: spatial coordinate that describes the angle of a particle relative to the beam direction. It is defined by the equation

  $$\eta = -\ln\left[\tan\left(\frac{\theta}{2}\right)\right], \tag{1.8}$$

  where θ is the angle between the particle momentum $\vec{p}$ and the beam direction.
- the rapidity y: it is defined as

  $$y = \frac{1}{2}\ln\left(\frac{E + p_{\mathrm{L}}}{E - p_{\mathrm{L}}}\right) \tag{1.9}$$

  where E is the energy of the particle and p_{L} is the momentum along the proton beam direction. In the limit where the particle is traveling close to the speed of light, or in the approximation that the mass of the particle is negligible if compared to the energies involved in the process, pseudorapidity is numerically close to the definition of rapidity. In hadron colliders, the rapidity is preferred over the pseudorapidity, because the latter depends only on the polar angle of the particles' trajectories, and not on their energies.

The three categories are: hard, semi-hard, and soft scattering. Hard processes occur at high-energy momentum transfer or mass scales of the order of several tens of GeV, resulting in outgoing particles that can have high p_{T} (low η). Since CMS measures particle production at high p_{T}, this is the main regime of interest. Semi-hard processes are QCD processes where partons with transverse momenta of a few GeV are produced. Soft processes are those that occur at low-energy momentum transfer of the order of tens of MeV with production of particles with low p_{T} (high η). At the collision point, hard scattering processes occur between the partons, that are treated as unbound particles. The primary partons may undergo initial state radiation (or splitting), and, as consequence, two partons (each connected to one of the incoming hadrons) participate in the hard scattered interaction (see Figure 1.5). In the case of QCD, the remnant partons of the incoming hadrons are not completely disconnected from the rest of the event. They interact softly and contribute to the so-called *underlying events* (UE). The hard scattering process is described by a peculiar property of the QCD theory, the asymptotic freedom. This term is used to describe the observed decrease in the intrinsic strength (defined in terms of the strong coupling constant α_s) of the color force between partons as they are brought closer together (or the transferred momentum is very high), letting the quarks behave as if they were virtually free inside the hadron. Because QCD is a nonlinear theory, i.e. it is not analytically solvable, perturbative expansions in the interaction strength α_s produce few precise predictions over the full energy spectrum. At high-energy momentum transfer, though, it is possible to use perturbative approximations that provide very accurate results. The threshold energy, defined as the energy scale at which the constant α_s is of the order of the unit, is set by the parameter Λ_{QCD}, that has been experimentally measured to be $\Lambda_{QCD} = 217^{+25}_{-23}$ MeV Nakamura et al. (2010).

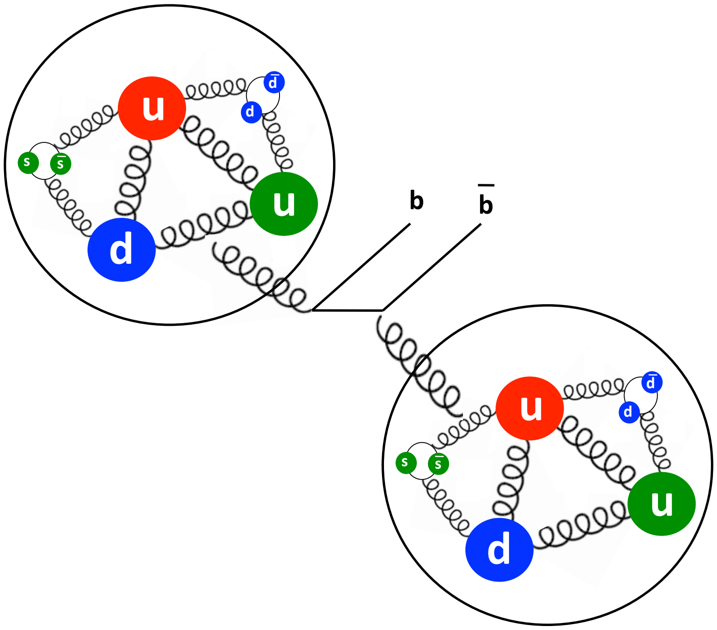

Figure 1.5: Representation of the composition of a proton: shown are the constituent quarks in three different colors (uud) and the sea quarks and gluons that are present. Hadron production at LHC in transverse direction is accessed mostly via the interaction between gluons, as shown here.

The b-quarks are of special interest because:

- the production processes occur at an energy scale significantly above Λ_{QCD} where perturbative calculations (the b-quark mass at rest is already $\sim$ 5 GeV/c^2) can be applied with a precision comparable to measurements, and
- they are produced abundantly at the LHC.

The total predicted cross section for the production of b$\bar{\text{b}}$-quark pairs from the collision of two protons at 7 TeV center of mass energy can be calculated perturbatively as an expansion in series of α_s Nason et al. (1988). Three elementary production processes contribute to the total cross section:

- Flavor creation: it is the Leading Order (LO) process in α_s. Its cross section is proportional to α_s^2, where each α_s correspond to an interaction vertex in the Feynman diagram, as shown in Figure 1.6. It comprises quark annihilation of light quarks $q\bar{q} \to$ b$\bar{\text{b}}$ (Figure 1.6 on the left) and gluon-gluon fusion $gg \to$ b$\bar{\text{b}}$ (Figure 1.6 on the right).

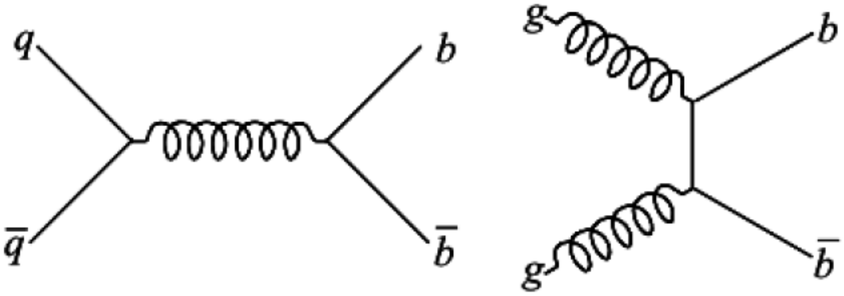

Figure 1.6: Leading order $\mathcal{O}(\alpha_s^2)$ diagrams for b$\bar{\text{b}}$-pair production: gluon-gluon fusion quark annihilation. These diagrams represent reaction amplitudes that add coherently. The total amplitude squared is proportional to the cross section.

- Flavor excitation: it is a Next-to-Leading Order (NLO) process (cross section proportional to α_s^3) in which a heavy quark is assumed to be already present as sea quark of the proton (Figure 1.7 on the left).

- Gluon splitting: it is another NLO process at somewhat lower strength where a gluon converts into a heavy-quark pair ($g \rightarrow \mathrm{b\bar{b}}$) in either the initial state or the final state radiative processes (Figure 1.7 on the right).

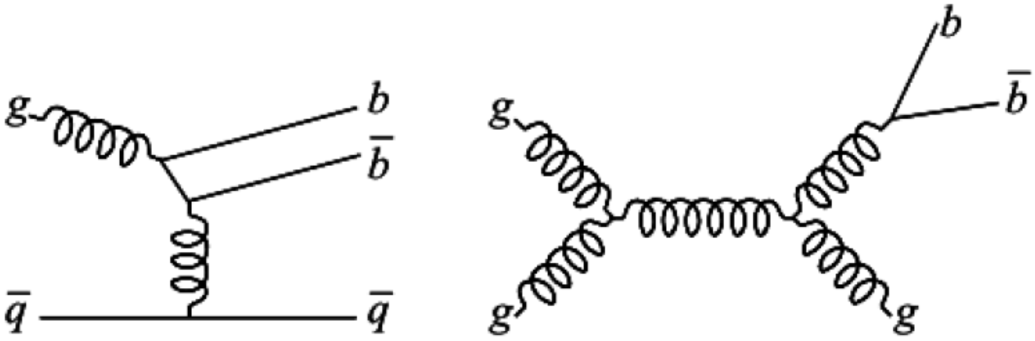

Figure 1.7: Next-to-Leading order $\mathcal{O}(\alpha_s^3)$ diagrams for $\mathrm{b\bar{b}}$-pair production: flavor excitation (on the left) and gluon splitting (on the right).

Additional next-to-leading order processes arise from $\mathcal{O}(\alpha_s^3)$ corrections to the parton fusion process, that include real and virtual gluon emission. The $\mathrm{b\bar{b}}$ cross section has been precisely calculated up to the NLO terms Nason et al. (1988). At the LHC, the dominant contribution to the $\mathrm{b\bar{b}}$ cross-section ($\sim 90\%$) is given by the NLO processes which happen in the semi-hard and soft regimes because the partons involved in the interaction carry a small momentum fraction Andreev (2007). This means that the b-quark production occurs mostly in the forward and backward directions, at small angles with respect to the proton beams.

The first measurements of b-hadron production were made more than two decades ago by the UA1 Collaboration at the CERN $\mathrm{p\bar{p}}$ collider Albajar et al. (1988) operating at $\sqrt{s} = 0.63$ TeV, while more recent measurements have been made by the CDF and D0 Collaborations at the Fermilab Tevatron for center-of-mass energies of 1.8 and 1.96 TeV Abe et al. (1993, 1995); Acosta et al. (2002); Abachi et al. (1995); Abbott et al. (2000b,a); Acosta et al. (2005); Abulencia et al. (2007). Over the years, the various discrepancies between the predictions and the measurements have been reduced, however not completely resolved Collins and Ellis (1991); Catani et al.

(1991); Cacciari and Greco (1994); Cacciari et al. (2004). Studies at the LHC collider with higher center-of-mass energies expand the reach and provide tests at precisions comparable to the present theoretical uncertainties Cacciari et al. (1998); Kniehl et al. (2008). Figure 1.8 shows the total predicted cross-section $\sigma_{b\bar{b}}$ as a function of the center-of-mass energy.

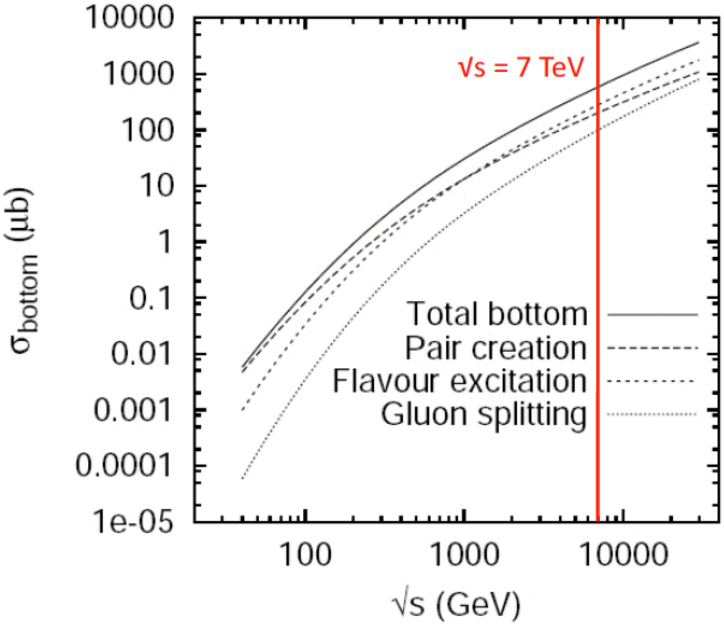

Figure 1.8: The total $b\bar{b}$ production cross-section in pp collisions as a function of the center-of-mass energy $E_{CM} = \sqrt{s}$, and the different contribution from pair creation, flavor excitation and gluon splitting at parton level Norrbin et al. (2000).

1.3.2 Hadronization

Once a $b\bar{b}$-quark pair is produced, the hadronization process starts. The fact that a single quark or gluon is not observed leads to the conjecture that quarks may be permanently confined within hadrons. This is the QCD property known as quark confinement. As two quarks separate, the potential energy due to the color force attraction between the quarks increases until it is more energetically favorable to generate a virtual quark anti-quark pair from the vacuum sea into physical reality.

This process, finally, creates hadrons with constituent b-quarks (b-hadrons). A shower of hadrons is produced along the direction of the primary quarks. As they separate, the new hadrons emerge with small transverse momenta with respect to the initial parton momentum in the center of mass frame. The result is mostly two, less likely more, particle jets in a collision event. The dynamics of the hadronization process is modeled and parameterized in a number of phenomenological ways. One general approach to hadronization is the hypothesis of *local parton-hadron duality.* In this case one assumes that both, the flow of momentum and quantum numbers at the hadron level, tend to follow solely the flow established at the parton level, i.e. the flavor of a quark initiating a jet should be found in a hadron near the jet axis. The most known models are Webber (1994):

- Longitudinal phase space or tube: it is a simple model that describes many of the gross features of hadronization. A parton (or, more realistically, a color-connected pair of partons) produces a jet of light hadrons which occupy a tube in (y,p_T)-space, where the rapidity y and the transverse momentum p_T are both measured with respect to the direction of the initial parton.

- Field and Feynman approach: it is a scheme for generating hadron distributions as function of the transverse momentum. It assumes that each parton fragments independently. The process starts with a quark that is combined with an antiquark from a $q\bar{q}$ pair, that was created from the vacuum. They form a first-generation meson with energy fraction z. The leftover quark, with energy fraction $(1 - z)$, is fragmented in the same way until the leftover energy falls below a phenomenological cutoff value that depends on the quark flavor. For gluon fragmentation, the gluon is first split into a quark anti-quark pair, either assigning all the gluon's momentum to one or the other ($z = 0$ or 1) with equal probability, so that the gluon behaves like a quark of random flavor, or using more advanced splitting functions. A weakness of treating the partons separately is that the fragmentation depends on the parton energy rather than its virtuality, constraining and limiting the different species of hadrons produced. Also, it is not a model that describes quark confinement.

- Lund string model: the assumption of linear confinement provides the starting point for this model. As the q and $\bar{q}$ partons move apart from their common production vertex, the color flux tube that connects q and $\bar{q}$ is stretched. As the q and $\bar{q}$ move apart, the potential energy stored in the string increases, and the string may break by the production of a new $q'\bar{q}'$ pair, so that the system splits into two color-singlet systems $q\bar{q}'$ and $q'\bar{q}$. If the invariant mass of either of these string pieces is large enough, further breaks-up may occur. In the Lund string model, the string break-up process is assumed to proceed until only massive hadrons remain, each hadron corresponding to a small piece of string with a quark attached on one end and an antiquark on the other end. In order to generate the quark anti-quark pairs $q'\bar{q}'$, which lead to string break-ups, the Lund model invokes quantum mechanical tunneling. When the quarks and antiquarks from two adjacent string separate they are combined such that they most likely form pseudoscalar and vector mesons.

- Cluster model: this model assumes that the hadronization starts with concatenated radiative processes of the partons that carry a fraction of the momentum to the next stage (parton shower). During the shower, gluons are emitted and they convert into $q\bar{q}$ pairs in a non-perturbative way. The $q\bar{q}$ combinations are assumed to form clusters, which mostly undergo isotropic decay into pairs of hadrons, that are chosen according to the density of states with appropriate quantum numbers. This model has few parameters and a natural mechanism for generating transverse momenta and suppressing heavy particle production in hadronization.

All these models are based on parton distribution functions, which parametrize the probability to find partons in a hadron as function of the fraction of the proton's momentum carried by the parton. Several sets of parton distribution functions are available for the different hadronization models. They are determined from data in collision experiments. The two most common set is called CTEQ Pumplin et al. (2002) and it is available in two different versions CTEQ6L1 and CTEQ6M. Other QCD parameters, such as renormalization and factorizations factors, and the quark masses enter in the modeling of the hadronization processes with not-negligible effects. The typical relative uncertainties for heavy-quark production cross section are as large as 40%. Estimates for the $\mathrm{B_s^0}$ meson species are presented in Section 5.9.

1.3.3 Monte Carlo Generator Implementation

Current Monte Carlo (MC) collision event simulations at parton level generate NLO by treating the hard scattering and the b-quark production subsequently, rather than evaluating all the contributions. To generate b-quark pairs from gluon splitting, for example, first the LO hard scattering process $gg \to gg$ is used and then each gluon is split into a b-quark pair. Two common MC generators, PYTHIA Sjöstrand et al. (2006) and HERWIG+MC@NLO Corcella et al. (2001); Frixione et al. (2003), are based on Lund string and the cluster hadronization models, respectively. For pp collision at the LHC at the center-of-mass energy of $\sqrt{s} = 7$ TeV, the total cross section $\sigma(\mathrm{pp} \to \mathrm{b\bar{b}})$ is predicted to be 238^{+95}_{-60} μb by MC@NLO Frixione et al. (2003); S. et al. (2003) and 429 μb by PYTHIA Norrbin et al. (2000).

Measurements of b-quark (b-hadron) production cross sections have been performed in e^+e^- collisions at energies near the Υ(4S) resonance (ARGUS, CLEO, Belle, BaBar) Albrecht et al. (1991); Fulton et al. (1990); Abe et al. (2002); Aubert et al. (2002b) and Υ(5S) resonance (CLEO, Belle) CLEO Collaboration (2006); Drutskoy et al. (2007), as well as at higher energies, at the Z resonance (LEP) Lesiak (2001) and in $\mathrm{p\bar{p}}$ collisions at $\sqrt{s} = 1.96$ TeV at the Tevatron Abe et al. (1992a,b, 1993). The $e^+e^- \to \mathrm{b\bar{b}}$ production cross-section at the Z, Υ(4S), and Υ(5S), are about 6.6 nb, 1.1 nb, and 0.3 nb, respectively Nakamura et al. (2010). High-energy hadron collisions produce b-flavored hadrons of all species with much larger cross-sections:

$\sigma(\mathrm{p\bar{p}} \to \mathrm{b}X) \sim 30\ \mu$b at the Tevatron ($\sqrt{s} = 1.96$ TeV) Nakamura et al. (2010) and are predicted to be even higher at the energies of the LHC pp collider (see Figure 1.9).

The production of b-quarks at the Z and Υ resonance masses and in hadronic collisions are described by different processes. Therefore, the momentum distributions of the b-quarks result different, for example, close to mean value of the b-quark mass ($m \sim 5$ GeV/c^2) at the Tevatron and LHC and close to $m_Z/2$ at the LEP, where m_Z is the mass of the Z resonance.

Once produced, the b- and $\bar{\mathrm{b}}$-quarks can hadronize with different probabilities into the full spectrum of b-hadrons, either in their ground or excited states, and then decay further into lighter hadrons and leptons. Hadronization fractions have been measured in $Z \to \mathrm{b\bar{b}}$ and pp (or $\mathrm{p\bar{p}}$) collisions. Assuming that the hadronization process and the primary b-quark production factorize, those fractions should be equal. The current measurements from the LEP and the Tevatron differ by 1.8σ Nakamura et al. (2010). Table 1.3 shows the measured hadronization fractions f_u, f_d, f_s, and f_{baryon} for B^+, B^0, B^0_s, and b-baryons, respectively, produced at the Z resonance and $\mathrm{p\bar{p}}$ collisions Nakamura et al. (2010). The table also shows their combination, which is implemented in the MC generators that were used for the analysis presented here.

Table 1.3: Fractions of b-hadron species measured in $Z \to \mathrm{b\bar{b}}$ decay and in $\mathrm{p\bar{p}}$ collisions at $\sqrt{s} = 1.8$ TeV.

b hadron	Fraction at Z (%)	Fraction at $\bar{p}p$ (%)	Combined (%)
B^+,B^0	40.2 ± 0.9	33.2 ± 3.0	40.0 ± 1.2
B^0_s	10.5 ± 0.9	12.2 ± 1.4	11.5 ± 1.3
b-baryons	9.1 ± 1.5	21.4 ± 6.8	8.5 ± 2.1

The combined results are obtained from a fit where the fractions are constrained to add up to 1, neglecting the production of $\mathrm{B_c}$ mesons ($\bar{b}c$). From the observed yields of $\mathrm{B_c}$ mesons at the Tevatron Abe et al. (1998), one can estimate $f_c = 0.2$ % which is below the current experimental uncertainties for the other fractions. The

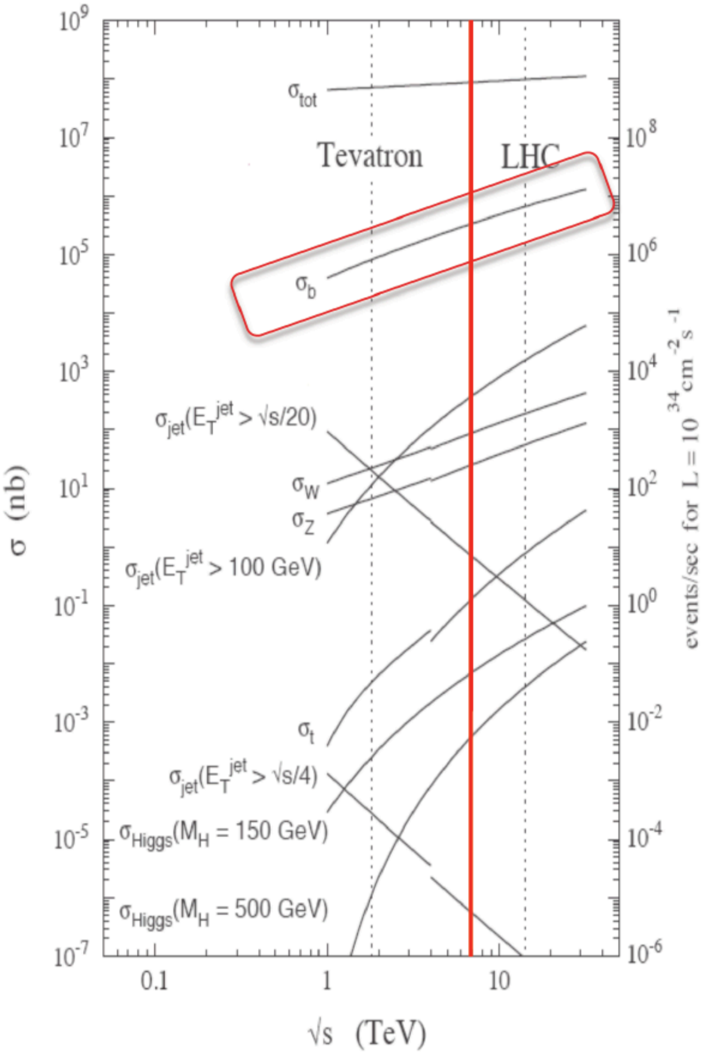

Figure 1.9: The total cross section and cross sections for exclusive production processes versus collision energy in the center of mass frame Flügge, G (1994). The red box encapsulates the production of b-quarks. The dashed lines indicate the center of mass energies of the Tevatron and the highest design energy at the LHC. The red line indicates the measurement point corresponding to this analysis.

measurement of different b-hadron production cross sections will contribute to the evaluation of the hadronization fractions.

1.4 B Decays

Particles containing anti-b quarks can be B^0, B^+, B^0_s, or B^+_c mesons, depending on whether the light quark that it pairs with has d-, u-, s-, or c-flavor. They also can be baryons containing two other quarks, such as $\Lambda_b = (udb)$. In the SM, the decay rate of quarks via W-emission is parametrized by the CKM matrix (see Section 1.2). This dissertation focuses on the B^0_s-$\bar{\mathrm{B}}^0_\mathrm{s}$ meson mixing and B^0_s decay into the J/ψ and ϕ particles.

1.4.1 The $\mathrm{B}^0_\mathrm{s} \to$ J/ψ ϕ Decay

The diagrams of B^0_s-$\bar{\mathrm{B}}^0_\mathrm{s}$ mixing and decay into the J/ψ and ϕ particles are shown in Figure 1.10 top and bottom, respectively. In the mixing process, the coupling between the virtual (u, c, t) and the real (s, b) quarks are proportional to $V^*_{qs}V_{qb}$, where $q = t, c, u$. The decay occurs via b→c$\bar{\mathrm{c}}$s transitions. The pair c$\bar{\mathrm{c}}$ and s$\bar{\mathrm{s}}$ form the particles J/ψ and ϕ, respectively. The corresponding amplitude is proportional to $V^*_{cs}V_{cb}$. The

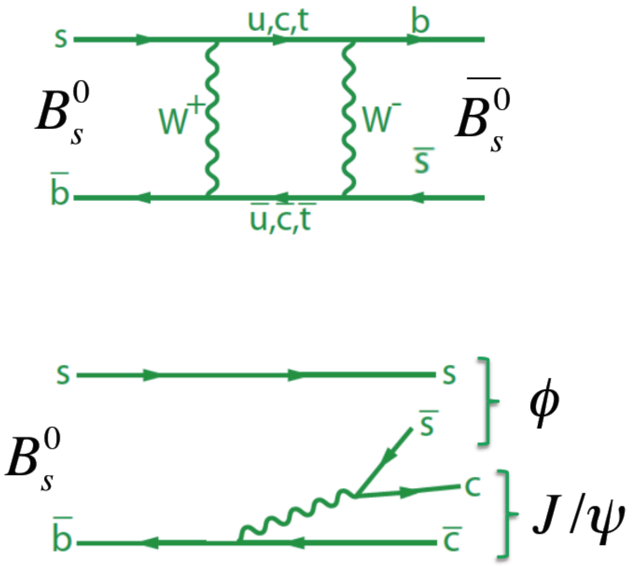

Figure 1.10: Feynman diagrams for B^0_s-$\bar{\mathrm{B}}^0_\mathrm{s}$ mixing (top) and decay (bottom) into the J/ψ and ϕ particles.

$B_s^0 \rightarrow J/\psi\ \phi$ decay channel allows to study CP violation in weak interaction, as described by the Standard Model. There is also the possibility that processes with particles and forces between them not included in the SM, can contribute to the transitions and alter the decay pattern predicted by the SM. A description of the main features of the $B_s^0 \rightarrow J/\psi\ \phi$ decay is presented in the following paragraphs.

1.4.2 $B_s^0 - \bar{B}_s^0$ Mixing

Neither electric-charge conservation nor any other conservation law respected by the weak interactions prevent B_s^0 ($\bar{b}s$) and $\bar{B}_s^0$ ($b\bar{s}$) from having both real and virtual transitions to common states. As a consequence, B_s^0 and $\bar{B}_s^0$ mix, i.e., they translate into each other over time (oscillate). The oscillation occurs via the exchange of two W bosons as shown in Figure 1.11. By definition the $| B_s^0\rangle$ and $| \bar{B}_s^0\rangle$ are eigenstates of the strong and electromagnetic interactions and have common mass m_0 and opposite flavor content. Therefore, the weakly decaying (transitioning) states can be written as a composition of the two flavor eigenstates at proper decay time $t = 0$

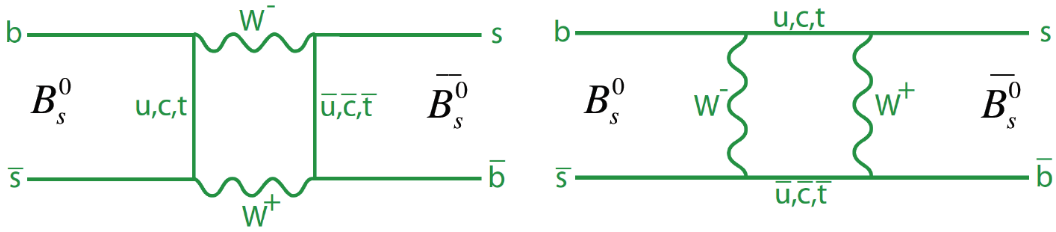

Figure 1.11: Dominant box diagrams for $B_s^0 \leftrightarrow \bar{B}_s^0$ oscillations.

$$| \psi(0)\rangle = a(0)\cdot | B_s^0\rangle + b(0)\cdot | \bar{B}_s^0\rangle \tag{1.10}$$

where the proper decay time t is measured in the B_s^0-$\bar{B}_s^0$ rest frame. This state will evolve in time by oscillating or decaying into the common final states f_1,f_2,...

$$| \psi(t)\rangle = a(t)\cdot | B_s^0\rangle + b(t)\cdot | \bar{B}_s^0\rangle + c_1(t)\cdot | f_1\rangle + c_2(t)\cdot | f_2\rangle + \ldots \tag{1.11}$$

In general, the evolution of such a state is very complicated. For the calculation of the values of $a(t)$ and $b(t)$ on a time scale much larger than that for the strong-interactions ($t \gg 10^{-20}$ s), the evolution can be simplified (Wigner-Weisskopf approximation) Branco et al. (1999) and the state is described by a two-component wave function:

$$| \psi(t)\rangle = \psi_1(t)\cdot \mid \mathrm{B_s^0}\rangle + \psi_2(t)\cdot \mid \mathrm{\bar{B}_s^0}\rangle. \tag{1.12}$$

The wave function evolves according to the time-dependent Schroedinger-like equation:

$$i\frac{d}{dt}\begin{pmatrix} \psi_1 \\ \psi_2 \end{pmatrix} = R \begin{pmatrix} \psi_1 \\ \psi_2 \end{pmatrix} \tag{1.13}$$

The matrix R is not Hermitian since otherwise the meson would just oscillate and not decay. It can be written as

$$R = M - \frac{i}{2}\Gamma \tag{1.14}$$

with $M = M^\dagger$ and $\Gamma = \Gamma^\dagger$. The diagonal elements of M and Γ are associated with the flavor conserving transitions $\mathrm{B_s^0} \to \mathrm{B_s^0}$ and $\mathrm{\bar{B}_s^0} \to \mathrm{\bar{B}_s^0}$, while the off-diagonal elements correspond to the flavor changing transitions $\mathrm{B_s^0}{\to}\mathrm{\bar{B}_s^0}$ and $\mathrm{\bar{B}_s^0}{\to}\mathrm{B_s^0}$. From Equations 1.13-1.14 it follows:

$$\frac{d}{dt}\left(|\psi_1|^2 + |\psi_2|^2\right) = -(\psi_1^*\psi_2^*)\Gamma \begin{pmatrix} \psi_1 \\ \psi_2 \end{pmatrix}. \tag{1.15}$$

Because the $\mathrm{B_s^0}$- and $\mathrm{\bar{B}_s^0}$-mesons decay, the left-side of the above equation must be negative for any value of ψ_1 and ψ_2, and therefore Γ is positive definite. The two eigenstates of R can be distinguished by labels H and L, for heavy and light respectively. Since R is not Hermitian, its eigenvalues are complex and can be written as $\mu_\mathrm{H} = m_\mathrm{H} - (i/2)\Gamma_\mathrm{H}$ and $\mu_\mathrm{L} = m_\mathrm{L} - (i/2)\Gamma_\mathrm{L}$, where m_H and m_L are the masses of $\mathrm{B_s^H}$ and $\mathrm{B_s^L}$, respectively, while Γ_H and Γ_L are their respective decay widths. The following definitions are commonly used:

$$\begin{aligned} m &\equiv \frac{m_{\mathrm{H}} + m_{\mathrm{L}}}{2}, \\ \Gamma &\equiv \frac{\Gamma_{\mathrm{H}} + \Gamma_{\mathrm{L}}}{2} \equiv \frac{1}{\tau} \end{aligned}$$

where m is the average mass and τ is the average lifetime of the $\mathrm{B}_{\mathrm{s}}^{0}$ mesons as measured in the center of mass frame. Furthermore, it is common to define

$$\begin{aligned} \Delta\mu &\equiv \mu_{\mathrm{H}} - \mu_{\mathrm{L}} && (1.16) \\ &= \Delta m - \frac{i}{2}\Delta\Gamma, && (1.17) \end{aligned}$$

$$\Delta m \equiv m_{\mathrm{H}} - m_{\mathrm{L}} = 2|M_{12}|, \tag{1.18}$$

$$\Delta\Gamma \equiv \Gamma_{\mathrm{H}} - \Gamma_{\mathrm{L}} = 2|\Gamma_{12}| \cos\phi_s \tag{1.19}$$

where

$$\phi_s = \arg\left[-\frac{M_{12}}{\Gamma_{12}}\right]. \tag{1.20}$$

The mass difference Δm is positive by definition. The sign of $\Delta\Gamma$ is physically meaningful, and in the SM, $\Delta\Gamma/\Gamma$ is expected to be 0.12 ± 0.06 Dunietz et al. (2001). The two eigenvectors of R are constructed as follows:

$$|\,\mathrm{B}_{\mathrm{s}}^{\mathrm{L}}\rangle = p\,|\,\mathrm{B}_{\mathrm{s}}^{0}\rangle + q\,|\,\bar{\mathrm{B}}_{\mathrm{s}}^{0}\rangle \tag{1.21}$$

$$|\,\mathrm{B}_{\mathrm{s}}^{\mathrm{H}}\rangle = p\,|\,\mathrm{B}_{\mathrm{s}}^{0}\rangle - q\,|\,\bar{\mathrm{B}}_{\mathrm{s}}^{0}\rangle \tag{1.22}$$

where p and q are complex, and $|p|^2+|q|^2 = 1$ for normalization. The time-dependence of the mass eigenstates is given as

$$\begin{aligned}
| \mathrm{B_s^L}(t)\rangle &= e^{-\Gamma_L t/2} e^{-im_L t/2} \mid \mathrm{B_s^L}(0)\rangle \qquad (1.23)\\
| \mathrm{B_s^H}(t)\rangle &= e^{-\Gamma_H t/2} e^{-im_H t/2} \mid \mathrm{B_s^H}(0)\rangle. \qquad (1.24)
\end{aligned}$$

With Equation 1.21-1.22, this yields the following time evolution of the flavor eigenstates:

$$\begin{aligned}
| \mathrm{B_s^0}(t)\rangle &= e^{-\left(im+\frac{\Gamma}{2}\right)t} \left(\cos\frac{\Delta m t}{2} \mid \mathrm{B_s^0}(0)\rangle + i\frac{q}{p}\sin\frac{\Delta m t}{2} \mid \mathrm{\bar{B}_s^0}(0)\rangle \right) \qquad (1.25)\\
| \mathrm{\bar{B}_s^0}(t)\rangle &= e^{-\left(im+\frac{\Gamma}{2}\right)t} \left(i\frac{p}{q}\sin\frac{\Delta m t}{2} \mid \mathrm{B_s^0}(0)\rangle + \cos\frac{\Delta m t}{2} \mid \mathrm{\bar{B}_s^0}(0)\rangle \right). \qquad (1.26)
\end{aligned}$$

The probability $\mathcal{P}(t)$ for a $\mathrm{B_s^0}$ to oscillate into a $\mathrm{\bar{B}_s^0}$ after the proper time t is then:

$$\mathcal{P}(t)(\mathrm{B_s^0} \to \mathrm{\bar{B}_s^0}) = \frac{1}{2}\Gamma e^{-\Gamma t}[1+\cos(\Delta m t)]. \qquad (1.27)$$

The Equation 1.18 defines the mixing frequency Δm in terms of the matrix element M_{12}. The mixing amplitude can be estimated in the SM by calculation of the dispersive and absorptive parts of the box diagrams Nakamura et al. (2010) that yield the following prediction:

$$\Delta m_s \propto m_{B_s} \xi_s m_t^2 |V_{ts}^* V_{tb}|^2. \qquad (1.28)$$

It is proportional to the masses of the virtual intermediate quarks. Therefore, the contributions of the diagrams with virtual up and charm quarks are negligible compared to the ones with virtual top quarks. For both $\mathrm{B_d^0}$ and $\mathrm{B_s^0}$ mesons it is possible to define the mixing frequencies in terms of SM parameters as follows

$$\frac{\Delta m_s}{\Delta m_d} \propto \frac{m_{B_s}}{m_{B_d}} \xi^2 \left| \frac{V_{ts}}{V_{td}} \right|^2 \qquad (1.29)$$

where $m_{B_{d,s}}$ are the masses of the B^0_s and B^0_d mesons, $\xi = 1.210^{+0.047}_{-0.035}$ is a theoretical factor that takes into account decay differences for the two B-meson species, and V_{ij} are the matrix elements with $V_{tb} \approx 1$. The B^0_d mixing frequency has been measured by many experiments at LEP ALEPH Collaboration (1997) DELPHI Collaboration (1997) L3 Collaboration (1998) OPAL Collaboration (1996) and at the Tevatron CDF Collaboration (1998) D0 Collaboration (2006), but very precisely by the BaBar Aubert et al. (2002a) and Belle Hastings et al. (2003) collaborations. The combined results yield to an average of $\Delta m_d = \ (0.507 \pm\ 0.005)$ ps^{-1}.

The measurement of Δm_d can constrain the length of one side of the unitary triangle shown in Figure 1.3, from $(0, 1)$ to (ρ, η), i.e., $|V_{td}V^*_{tb}/V_{cd}V^*_{cb}|$. This result be used to extract the magnitude of the CKM matrix element V_{td} within the SM. The oscillation proceeds by a factor of ~ 30 faster in the B^0_s system as compared to the B^0_d system, which experimentally cannot be resolved as rate asymmetry measurements. In particular, it requires to identify the b-quark flavor of the decaying B^0_s-meson via its decay products. The CMS detector does not provide hadron-identification at high momenta which would provide this information. The time-dependent decay rate of B^0_s mesons becomes independent of the mixing frequency Δm_s if the weak phase is assumed as predicted by the SM ($\phi_s \sim 0$), as described in Section 1.4.3.

The latest value for Δm_s as reported by PDG Nakamura et al. (2010) is dominated by CDF's measurement:

$$\Delta m_s = (17.77 \pm 0.10 \pm 0.07)\ \mathrm{ps}^{-1} \tag{1.30}$$

where the first uncertainty is statistical and the second systematic. The LHCb experiment at the LHC measured the B^0_s mixing frequency during the first year of data taking Krocker (2011). The result confirms and improves the previous CDF measurement:

$$\Delta m = (17.725 \pm 0.041 \pm 0.026)\ \mathrm{ps}^{-1} \tag{1.31}$$

where the first error is statistical and the second systematic.

1.4.3 CP Violation in the B_s^0 System

In general, a symmetry of a physical system is characterized by a transformation that does not change the system or its appearance. Invariance under a certain symmetry transformation implies a conservation law Noether (1918). There are three discrete symmetries in nature:

- Charge conjugation (C): $\mathcal{C}$ transforms the particle into its anti-particle, leaving particle mass, momentum, and the particles' internal angular momentum (spin) unchanged.

- Parity (P): $\mathcal{P}$ creates a mirror image of the physical system, reversing the signs of the three spatial coordinates. This operation also reverses the sign of the particle momentum while leaving its angular momentum and spin unchanged.

- Time reversal (T): $\mathcal{T}$ reverses time. As consequences, it reverses the momentum and spin of a particle.

The CPT theorem states that all interactions are invariant under the combined operation of $\mathcal{C}$, $\mathcal{P}$, and $\mathcal{T}$. It was explicitly proven in 1954 by Gerhard Luders Luders (1954), Wolfgang Pauli Pauli et al. (1955), and John Stewart Bell Bell (1954), and later by Res Jost Jost (1957) in a more general way. Before 1956, those symmetries were thought to be conserved individually by all forces that act between elementary particles. The violation of the parity P was first observed in weak decays of ^{60}Co by C.S. Wu et al. Wu (1957) in 1957 by measuring the anisotropy in the β^- ray emission in a strong magnetic field. Soon after, it was also discovered that the weak force did neither preserve the charge conjugation symmetry C. This was demonstrated by examining the spins of electrons and positrons emitted in the decays of positively and negatively charged muons, respectively. The hypothesis that the combined CP-symmetry is preserved was falsified in 1964, when CP violation was discovered in the decays of neutral kaons decay Christenson (1964) Wolfenstein (1964). After 2000, CP violation was measured by the BaBar and Belle collaborations in the neutral B_d^0

meson system with very high precision Aubert et al. (2002b) Abe et al. (2002) and in the B_s^0 meson system by CDF CDF Collaboration (2008) and D0 D0 Collaboration (2008).

To observe the CP-violating phase via measurement of particle decays requires that at least two different weak transition contribute. The decay rate is proportional to the square of the coherent sum of the corresponding transition amplitudes. If only one complex process amplitude is present, the amplitude squared does not depend on the phase anymore. Instead, with at least two different amplitudes that interfere, the amplitude square depends explicitly on the relative phase between the amplitudes. Therefore, the transition rate becomes phase-dependent and, if the relative phase contains the CP phase, CP-violating effects are observed. Three types of CP violation can be observed in the B meson systems:

- CP violation in decays (direct): it is present if the decay amplitude $\mathcal{A}_f$ of a neutral or charged B meson into a final state f is different from the one of the CP conjugate decay $\bar{\mathcal{A}}_{\bar{f}}$ of the antiparticle $\bar{\mathrm{B}}$ into the final state $\bar{f}$,

$$\left|\frac{\bar{\mathcal{A}}_{\bar{f}}}{\mathcal{A}_f}\right| \neq 1.$$

- CP violation in mixing (indirect): as shown in Equation 1.21-1.22, two neutral B meson mass eigenstates are linear combinations of the flavor eigenstates that depend on the two complex parameters p and q. CP symmetry is violated if the mass eigenstates are not equal to the CP eigenstates, i.e.

$$\left|\frac{q}{p}\right| \neq 1,$$

- CP violation in interference between mixing and decay: when both neutral B and $\bar{\mathrm{B}}$ mesons are able decay to the same final state (f) the time-dependent CP

> asymmetry can be studied. CP is violated if
>
> $$\lambda = \frac{q}{p} \cdot \frac{\bar{\mathcal{A}}}{\mathcal{A}} = \eta_{\mathcal{CP}} e^{i\phi_s} \neq 1 \tag{1.32}$$
>
> which requires only that λ acquires a non-zero phase ϕ_s, as defined in Equation 1.20, with q and p being complex. This case is typically least dependent on models for the hadronic interaction of the final state particles and, hence, allows high precision comparison between theory and experiment.

In the decay $\mathrm{B}_\mathrm{s}^0 \rightarrow$ J/ψ ϕ, the final state is accessible to both, B_s^0 and $\bar{\mathrm{B}}_\mathrm{s}^0$ and CP violation manifests itself as interference between mixing and decay. The B_s^0 decay probes the CP violating phase ϕ_s, which is introduced by the mixing amplitude that is proportional to the CKM matrix element V_{ub}. The phase ϕ_s can be expressed as function of the angle β_s of the unitarity triangle (see Figure 1.3) by the relation:

$$\phi_s \approx -2\beta_s \equiv -2\mathrm{arg}\left[-\frac{V_{ts}V_{tb}^*}{V_{cs}V_{cb}^*}\right] \tag{1.33}$$

where the approximation holds in the SM because the M_{12} and Γ_{12} terms of the ϕ_s definition, as given in Equation 1.20, are much smaller than the current experimental resolution Nakamura et al. (2010). The CP-violating phase is predicted by the SM to be close to zero with small theoretical uncertainty ($\phi_s = -0.037 \pm 0.002$ rad). If new virtual processes contribute to the B_s^0-$\bar{\mathrm{B}}_\mathrm{s}^0$ box diagrams (see Figure 1.12), new amplitudes could be added enhancing observable CP-violation effects (New Physics) Dunietz et al. (2001) J. et al. (2007). In this way the measurement of CP violation indirectly probes New Physics, complementary to direct searches of new particles.

1.4.4 Angular Analysis

In the SM, CP violation in mixing is a negligible effect at the present level of experimental precision. The mixing ratio is expected $|p/q| \approx 1$, meaning that the

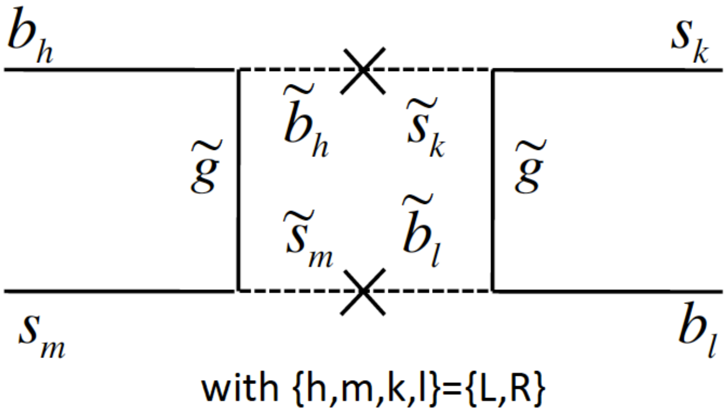

Figure 1.12: Example of Feynman diagrams for mixing processes with contributions from New Physics.

light $\mathrm{B_s^0}$ mass eigenstate $\mathrm{B_s^L}$ is nearly a pure CP-even state, and the heavy eigenstate $\mathrm{B_s^H}$ nearly a pure CP-odd state. If new particles and forces between them enter the box diagram and introduce amplitudes with new phases, the mixing ratio may change resulting in effects not foreseen by the SM. In case of the decay $\mathrm{B_s^0} \to \ \mathrm{J}/\psi\ \phi$ the final state is a composition of CP-odd and CP-even states Dighe et al. (1996, 1999); Dunietz et al. (2001). Because the $\mathrm{B_s^0}$ is a pseudoscalar meson ($J^P = 0^-$), it decays into the J/ψ and ϕ, which are both vector mesons ($J^{PC} = 1^{--}$) with relative orbital angular momentum between the two decay products of $L = 0, 1, 2$. For a two-meson state with relative orbital angular momentum L the parity is $P = (-1)^L$. As immediate consequence, there exist two possible CP states with eigenvalues ±1. Therefore, to identify the CP-even and CP-odd content of the $\mathrm{B_s^0} \to \ \mathrm{J}/\psi\ \phi$ decays an angular analysis that resolves the contributions of the different angular momentum states is required. It is advantageous to define three amplitudes for the different angular dependencies in the transversity frame Dighe et al. (1999) because the time-dependent decay rate naturally can divide into CP-even and CP-odd terms. The three amplitudes are: $A_0(t)$ which is CP-even and longitudinally polarized, and the two transversely polarized amplitudes $A_{||}$ (CP-even) and $A_{\perp}$ (CP-odd). In this context, longitudinal polarization means that both vector mesons are longitudinally polarized with respect to the decay axis, while, transversal means that both are transversally polarized with respect to the decay axis, in one case with the linear polarization vector parallel (||) while in the other case perpendicular ($\perp$) to each other. Figure 1.13 illustrates the definition of the coordinate system and the angles. The angle ψ is defined as the angle between one product of the ϕ decay (K^+) in its rest frame and the direction of flight of the ϕ in the $\mathrm{B_s^0}$ rest frame. In the J/ψ rest frame, the axes (x,y,z) are defined such that x has the same direction as the ϕ momentum. The z-axis is the normal direction to the plane defined by the ϕ decay kaons in the rest frame of the J/ψ. The y-axis completes the orthogonal reference frame. The angles θ and φ are the polar and azimuthal angles of the positive muon of the J/ψ. The

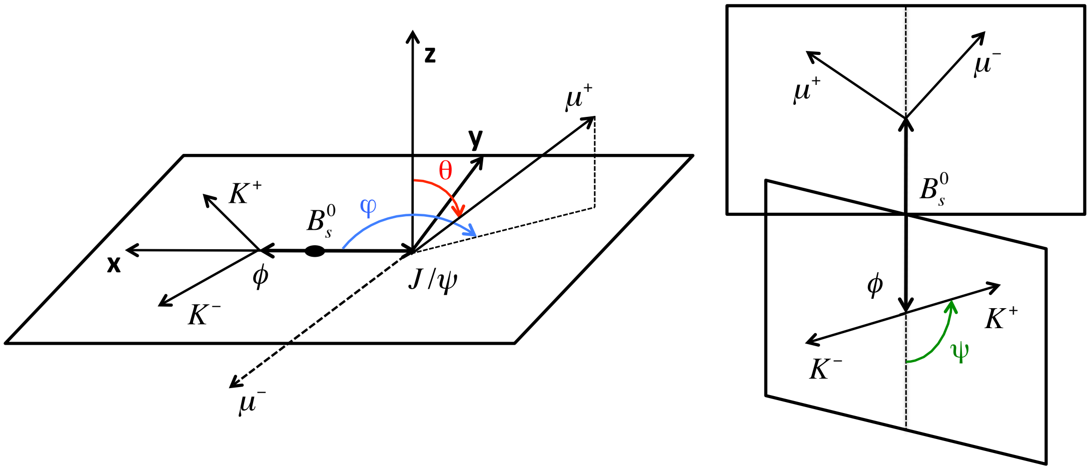

Figure 1.13: The three angles in the transversity frame: θ, ψ, and φ shown in the example of $\mathrm{B_s^0} \rightarrow$ J/ψ ϕ decay.

trigonometric functions of the angles, that are used to describe the kinematics of the products $\Theta = (\cos\theta, \varphi, \cos\psi)$, are defined in the transversity basis. The unit vectors and the aforementioned angles can be written in terms of the unit momentum vectors

$\mathbf{p}$ of the final state particles as follows:

$$\begin{aligned}
\mathbf{x} &= \mathbf{p}_{\phi}, && (1.34)\\
\mathbf{y} &= \frac{\mathbf{p}_{\mathrm{K}^+} - \mathbf{p}_{\phi}(\mathbf{p}_{\phi} \cdot \mathbf{p}_{\mathrm{K}^+})}{|\mathbf{p}_{\mathrm{K}^+} - \mathbf{p}_{\phi}(\mathbf{p}_{\phi} \cdot \mathbf{p}_{\mathrm{K}^+})|}, && (1.35)\\
\mathbf{z} &= \mathbf{x} \times \mathbf{y}, && (1.36)\\
\sin\theta\cos\varphi &= \mathbf{p}_{\mu^+} \cdot \mathbf{x}, && (1.37)\\
\sin\theta\sin\varphi &= \mathbf{p}_{\mu^+} \cdot \mathbf{y}, && (1.38)\\
\cos\theta &= \mathbf{p}_{\mu^+} \cdot \mathbf{z}, && (1.39)\\
\cos\psi &= -\mathbf{p}_{\mathrm{K}^+} \cdot \mathbf{p}_{\mathrm{J}/\psi}. && (1.40)
\end{aligned}$$

With the decomposition in CP-even and CP-odd components, the decay rate for the $\mathrm{B}^0_\mathrm{s} \rightarrow\ \mathrm{J}/\psi\ \phi$ decay can be factorized in two time- and angular-dependent parts. The differential decay rate analytically is written as

$$\frac{d^4\Gamma(\mathrm{B}^0_\mathrm{s} \rightarrow\ \mathrm{J}/\psi\ \phi)}{d\Theta dt} = f(\Theta, \overrightarrow{\alpha}, t) = \sum_{i=1}^{6} \mathcal{O}_i(\overrightarrow{\alpha}, t) \cdot g_i(\Theta) \tag{1.41}$$

where $\mathcal{O}_i(\overrightarrow{\alpha}, t)$ describe the time evolution of the angular distribution $g_i(\Theta)$ and it can be expressed in terms of real or imaginary parts of bilinear combinations of decay amplitudes. The set of physical parameters is represented by $\overrightarrow{\alpha}$, while the angles which define the kinematics of the decay are denoted by Θ. The observables $\mathcal{O}_i(\overrightarrow{\alpha}, t)$ are given by

$$|A_f(t)|^2 \text{ with } f \in (0, ||, \perp) \tag{1.42}$$

as well as by the interference terms

$$\mathcal{R}e\left(A_0^*(t)A_{||}(t)\right) \text{ and } \mathcal{I}m\left(A_f^*(t)A_{\perp}(t)\right) \text{ with } f \in (0, ||)\,. \tag{1.43}$$

Writing explicitly the analytic form for the observables defined in Equation 1.42, which correspond to the "ordinary" decay rates, it results

$$\begin{aligned}
\mathcal{O}_1 = |A_0(t)|^2 &= |A_0(0)|^2 e^{-\bar{\Gamma}t}\left[\cosh\frac{\Delta\Gamma t}{2} - |\cos\phi_s|\sinh\frac{|\Delta\Gamma|t}{2} + \sin\phi_s\sin(\Delta m t)\right] \\
\mathcal{O}_2 = |A_{||}(t)|^2 &= |A_{||}(0)|^2 e^{-\bar{\Gamma}t}\left[\cosh\frac{\Delta\Gamma t}{2} - |\cos\phi_s|\sinh\frac{|\Delta\Gamma|t}{2} + \sin\phi_s\sin(\Delta m t)\right] \\
\mathcal{O}_3 = |A_{\perp}(t)|^2 &= |A_{\perp}(0)|^2 e^{-\bar{\Gamma}t}\left[\cosh\frac{\Delta\Gamma t}{2} + |\cos\phi_s|\sinh\frac{|\Delta\Gamma|t}{2} - \sin\phi_s\sin(\Delta m t)\right]
\end{aligned}$$

while for the interference terms

$$\begin{aligned}
&\mathcal{O}_4 = \mathcal{R}e\left(A_0^*(t)A_{||}(t)\right) = |A_0(0)||A_{||}(0)|\cos(\delta_2-\delta_1)e^{-\bar{\Gamma}t} \\
&\quad\times\left[\cosh\frac{\Delta\Gamma t}{2} - |\cos\phi_s|\sinh\frac{|\Delta\Gamma|t}{2} + \sin\phi_s\sin(\Delta m t)\right] \\
&\mathcal{O}_5 = \mathcal{I}m\left(A_{||}^*(t)A_{\perp}(t)\right) = |A_{||}(0)||A_{\perp}(0)|e^{-\bar{\Gamma}t} \\
&\quad\times\left[\sin\delta_1\cos(\Delta m t) - \cos\delta_1\cos\phi_s\sin(\Delta m t) - \cos\delta_1\sin\phi_s\sinh\frac{|\Delta\Gamma|t}{2}\right] \\
&\mathcal{O}_6 = \mathcal{I}m\left(A_0^*(t)A_{\perp}(t)\right) = |A_0(0)||A_{\perp}(0)|e^{-\bar{\Gamma}t} \\
&\quad\times\left[\sin\delta_2\cos(\Delta m t) - \cos\delta_2\cos\phi_s\sin(\Delta m t) - \cos\delta_2\sin\phi_s\sinh\frac{|\Delta\Gamma|t}{2}\right].
\end{aligned}$$

For the SM predicted value of the weak phase $\phi_s \sim 0$, the decay rates become independent of the mixing frequency Δm. The physical parameters in the time-dependent observables are: $|A_0(0)|$, $|A_{||}(0)|$, and $|A_{\perp}(0)|$ the magnitudes of the amplitudes at $t = 0$, with the constraint $|A_0(0)|^2 + |A_{||}(0)|^2 + |A_{\perp}|^2 = 1$, $\bar{\Gamma} = (\Gamma_{\rm H} + \Gamma_{\rm L})/2$ the average width (inverse of the lifetime, $\bar{\Gamma} = 1/\tau$ ps^{-1}), $\Delta\Gamma = \Gamma_{\rm H} - \Gamma_{\rm L}$ the width difference, ϕ_s the CP-violating weak phase, and δ_i (with $i = 1, 2$) the CP-conserving strong phases defined as $\delta_1 \equiv arg(A_{||}^*(0)A_{\perp}(0))$ and $\delta_2 \equiv arg(A_0^*(0)A_{\perp}(0))$. The angular distribution are given by the following analytical forms:

$$
\begin{aligned}
g_1 &= 2\cos^2\psi(1-\sin^2\theta\cos^2\varphi), && (1.44)\\
g_2 &= \sin^2\psi(1-\sin^2\theta\sin^2\varphi), && (1.45)\\
g_3 &= \sin^2\psi\sin^2\theta && (1.46)\\
g_4 &= \sin^2\psi\sin 2\theta\sin\phi, && (1.47)\\
g_5 &= 1/\sqrt{2}\sin 2\psi\sin^2\theta\sin 2\phi, && (1.48)\\
g_6 &= 1/\sqrt{2}\sin 2\psi\sin 2\theta\cos\phi. && (1.49)
\end{aligned}
$$

The differential decay rate, as function of only one angle at the time, is presented in Figure 1.14 with the CP-even and CP odd contributions displayed separately. The input values are listed in Table 1.4.

Table 1.4: Input values for the $\mathrm{B_s^0}$ mixing parameters, decay amplitudes, strong and weak phases in the simulation of the $\mathrm{B_s^0} \to \mathrm{J}/\psi\ \phi$ Monte Carlo sample.

Parameter	Embedded Value
$\tau = 1/\bar{\Gamma}$	1.472 ps
$\Delta\Gamma/\Gamma$	0.1
Δm	20 ps
$\lvert A_0(0)\rvert^2$	0.57
$\lvert A_{\lvert\lvert}(0)\rvert^2$	0.25
$\lvert A_\perp(0)\rvert^2$	0.18
δ_1	2.50
δ_2	-0.17
ϕ_s	-0.04

Minimal Model

Equation 1.41 describes the decay rate model for $\mathrm{B_s^0} \to \mathrm{J}/\psi\ \phi$ decays as function of the proper decay time (t) and the set of the transversity basis angles (Θ). It is possible to reduce the model by integrating over the angular variables φ and $\cos\psi$ (so called

Minimal model). This now depends only on the observables corresponding to the decay rates, while all the interference terms vanish. In terms of physical parameters, the amplitude strength $A_f(0)$ (where $f = 0, ||, \perp$) and the weak phase ϕ_s are still present and measurable Dunietz et al. (2001). The new formulation of the decay rate can be explicitly written as:

$$
\begin{aligned}
\frac{d^2\Gamma(\mathrm{B_s^0} \rightarrow\ \mathrm{J}/\psi\ \phi)}{d\cos\theta dt} &= f(\cos\theta, \overrightarrow{\alpha}, t) = \sum_{i=1}^{3} \mathcal{O}_i(\overrightarrow{\alpha}, t) \cdot g_i(\cos\theta) \\
&= f_{even} \cdot (1 + \cos^2\theta) \\
&\quad \times e^{-\bar{\Gamma}t}\left[\cosh\frac{\Delta\Gamma t}{2} - |\cos\phi_s| \sinh\frac{|\Delta\Gamma| t}{2}\right] \\
&\quad + f_{odd} \cdot (1 - \cos^2\theta) \\
&\quad \times e^{-\bar{\Gamma}t}\left[\cosh\frac{\Delta\Gamma t}{2} + |\cos\phi_s| \sinh\frac{|\Delta\Gamma| t}{2}\right] \qquad (1.50)
\end{aligned}
$$

where $f_{even} = |A_0(0)|^2 + |A_{||}(0)|^2$ and $f_{odd} = 1 - f_{even} = |A_\perp(0)|^2$. This model has been used to extract the average lifetime, lifetime difference, and CP fraction in the $\mathrm{B_s^0} \rightarrow\ \mathrm{J}/\psi\ \phi$ decays from the CMS data recorded during the year 2010 (more details can be found in Section 7).

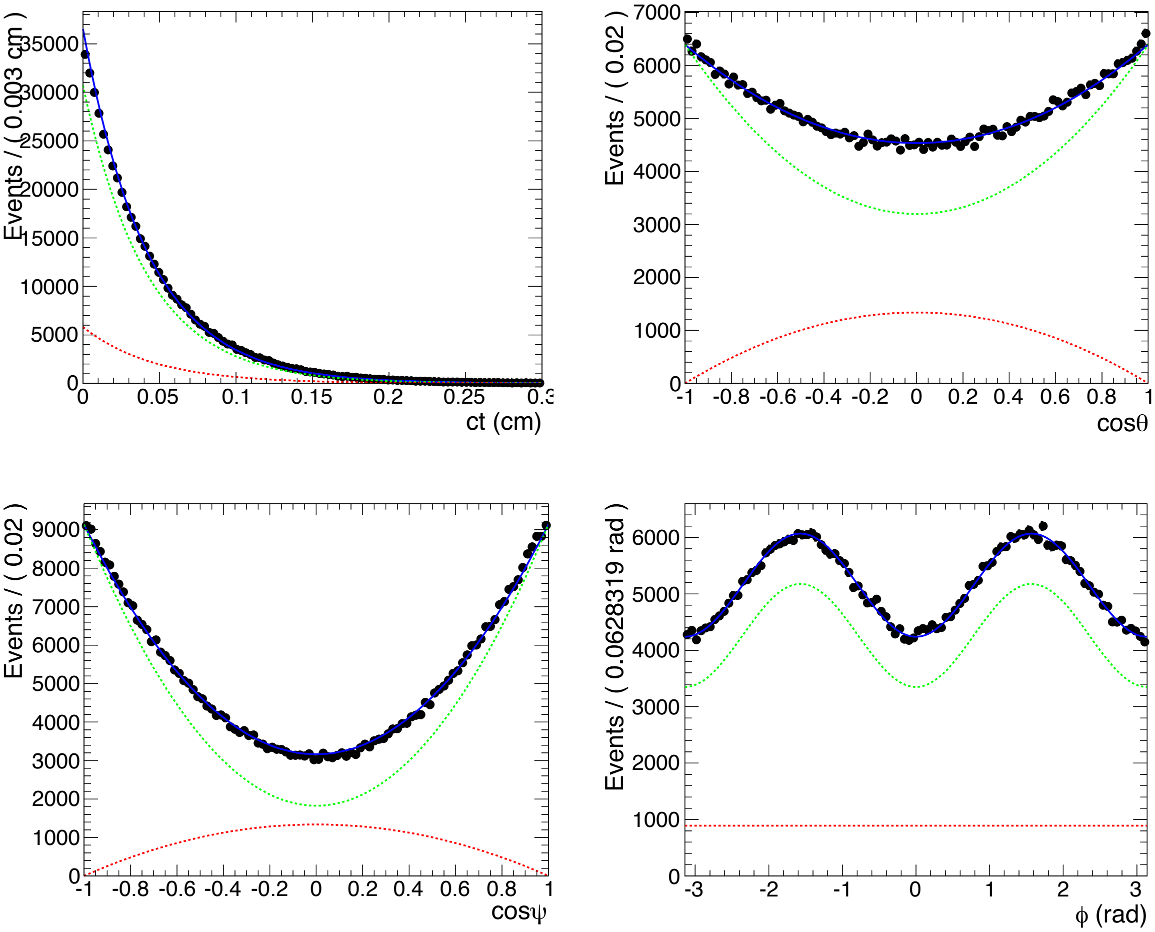

Figure 1.14: Analytic form of the differential decay rate $d^4\Gamma/d\Theta dt$ projected onto the proper decay time (top left) and three angular axes $\cos\theta$ (top right), $\cos\psi$ (bottom left), and ϕ (bottom right). The projections are obtained by integrating over the other three variable of the model. The CP-even and CP-odd contributions are indicated by the green and red dashed line, respectively. Input values used are given in Table 1.4.

Chapter 2

Experimental Setup

2.1 The Large Hadron Collider

The physics program outlined in the previous chapter requires center-of-mass energies between the proton constituents exceeding significantly 100 GeV and, due to the expected small cross sections, very high beam intensities and collision rates. The Large Hadron Collider (LHC) Bruning et al. (2004) L. and Bryant (2008) is a proton-proton collider located at the European Organization for Nuclear Research (known by its acronym CERN [*]), near Geneve. The requirements on the LHC are:

- accelerate protons to final beam energy of maximal 7 TeV. The available center-of-mass energy for the production of resonances is about 1/3 of the kinetic energy of the proton, therefore, to reach the TeV energy, multiple TeVs for the individual beams are required,
- accumulate as many protons as possible,
- bring protons to collision as often as possible for a very long time without interruption.

---

[*] Originally, Conseil Européen pour la Recherche Nucléaire, now, Organisation Européen pour la Recherche Nucléaire

To fulfill these requirements, LHC is a proton storage ring that recycles the proton beam. This is possible since the intensity of the proton beam is not much affected by collisions. The LHC is housed in the pre-existing LEP tunnel. To keep the beam on the circular orbit and focus it, several thousands of magnets of different multipole order are placed around the ring. LHC makes use of the accelerator infrastructure at CERN to reach the final energies and intensities in stages: protons are accelerated from kinetic energies of 50 MeV to 450 GeV before they are injected into the LHC ring in two opposite directions, where they are further accelerated to the final energy of 3.5 TeV and brought to collision. Table 2.1 summarizes the LHC parameters. The opposite proton beams intersect at four locations in the tunnel (see Figure 2.1). At the so-called Point 5 (P5), the Compact Muon Solenoid CMS Collaboration (2006a, 2008) (CMS) experiment is located. The CMS is a general purpose experiment whose main goals are to explore a wide range of physics at the TeV scale. The description of LHC is presented in three main categories: proton acceleration (see Section 2.1.1), magnet system for beam steering and focusing (see Section 2.1.2), and machine luminosity (see Section 2.1.3). The CMS experiment is introduced in Section 2.2.

Table 2.1: Summary table of the LHC parameters achieved during the startup period covered by this thesis. The design parameters expected to be achieved over the next years are reported in parenthesis.

Parameter	Current (Design) Value
Beam energy E_{beam}	3.5 (7) TeV
Circulating current per beam I_p	0.25 (0.54) A
Number of bunches per beam n_b	368 (2808)
Number of protons per bunch N_p	$10^9 - 10^{11}$ (1.15×10^{11})
Collision frequency f	50 (25) ns
Cross section of the bunch σ_{xy}	2.56×10^{-8} cm^2
Peak luminosity $\mathcal{L}$	2×10^{32} (1×10^{34}) cm^{-2}s^{-1}

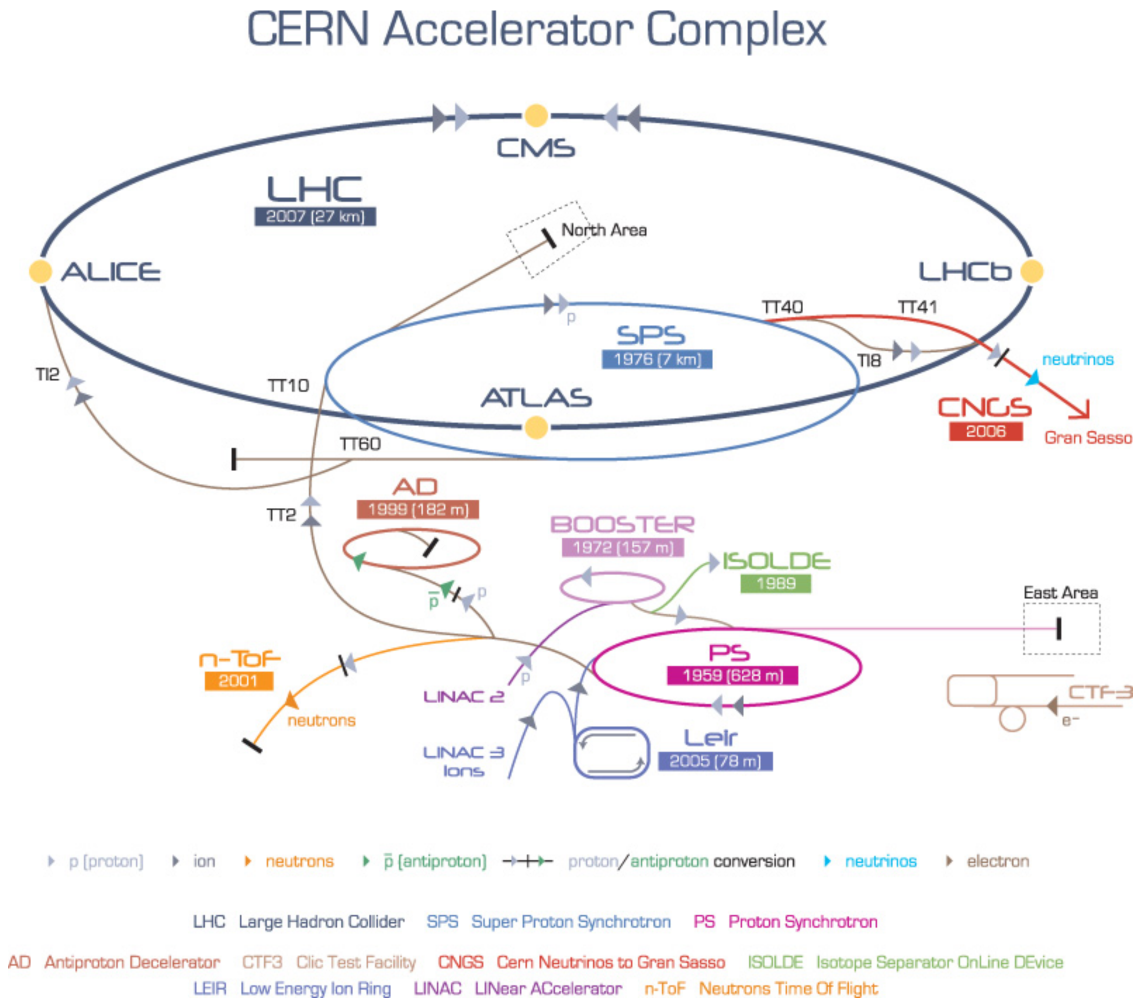

Figure 2.1: The accelerator chain at the CERN complex. The arrows show the direction of proton beams in the accelerators and the energy of the beam at these points. Filled circles show the locations of the four major detectors on the LHC (utility insertions are not shown).

2.1.1 Acceleration

To reach the highest energy, the LHC program makes use of existing accelerators at CERN. The proton beam starts from a bottle of compressed hydrogen gas (see Figure 2.2). Hydrogen atoms from this gas cylinder are injected into the (plasma) source chamber of the linear accelerator (LINAC2), as shown in Figure 2.1, where electrons are either attached to hydrogen or stripped off to turn them into ions suitable for acceleration. The acceleration at any stage is achieved with a time-dependent electric field applied to Radio-Frequencies (RF) cavities. A RF cavity is a combination of gaps between two field-free sections. The field-free section is a metal enclosure that acts as Faraday cage. Voltage is supplied to the metal structure creating an electric field in the gap between the two adjacent cavities. Particles that pass the gap in time, when the field has the correct orientation and nearly maximum strength, are accelerated. The particles drift within the field-free region, while at the subsequent gap, the voltage has time to reverse polarity to be ready when the particles enter the

Figure 2.2: The source of protons for the LHC.

gap. The RF cavities in the LHC ring are able to provide an amount of energy per second of 55 GeV/s. As the protons in the first stages are non-relativistic ($\beta < 1$), for a constant RF frequency, the lengths of the field-free regions in the linear accelerator vary along the beam pipe while for relativistic protons ($\beta \approx 1$) they are constant. This is the case in the ring accelerators and the frequency in the cavity is an integer multiple of the revolution frequency (harmonic number). To be able to use this method of acceleration the protons have to be accumulated and clumped together in bunches around the accelerating ring that are synchronized with the RF frequency and fit in between the gaps. The virtual positions occupied along the LHC circumference by the bunches of protons are called buckets. Each bunch can contain up to $\sim 10^{10}$ protons. For the LHC, 2808 bunches are positioned in the buckets to provide a spacing of 25 ns. First, the protons are accelerated in the LINAC2 and then injected into the Proton Synchrotron Booster (PSB), which is the smallest circular proton accelerator in the accelerator chain at the LHC injection complex. It increases the kinetic energy of the protons to 1.4 GeV. The PSB separates the beam into well-defined bunches of $\sim 10^{10}$ protons each, spaced a minimum of 300 ns apart. These bunches are then transferred to the Proton Synchrotron (PS). Two batches, containing a total of seven bunches, are accelerated for several revolutions to reduce space charge and increase the proton density by halving the occupied circumference. This is achieved by increasing the number of harmonics in the ring. The protons are accelerated further to an energy of 25 GeV, while the beam is split up steps using the RF on higher harmonics until 72 bunches of $\sim 10^{11}$ protons each are spaced by 25 ns. Those are transferred into the Super Proton Synchrotron (SPS) that accelerates them to an energy of 450 GeV and, finally, injects them into the LHC, both in a clockwise and anti-clockwise direction. The total filling time is about five minutes per LHC ring. The bunches of protons are accumulated for up to 20 minutes in the LHC at the 450 GeV injection energy before LHC ramps to the final energy within 25 minutes. During the first year of data taking in 2010 (the period covered by this dissertation) up to 368 bunches of $10^9 - 10^{11}$ protons were collided every 50 ns.

2.1.2 Beam Steering and Focus

A charged particle that moves in a plane perpendicular to a homogenous magnetic field is forced on a circular path. The radius of curvature of the particle trajectory (r) follows from the equality of centripetal and Lorentz force:

$$r[\mathrm{m}] = 0.3\frac{p[\mathrm{GeV}/c]}{qB[\mathrm{T}]}, \tag{2.1}$$

where p is the particle momentum measured in GeV/c, q is the particle charge in electrical units, and B the magnetic field measured in Tesla. Dipole magnets bend and focus the beams towards the optimum trajectory around the ring and recapture them after collision. The magnetic field strength of 8 T deflects both proton beams toward the average curvature of the pre-existing LEP tunnel so that it can be reused for LHC. To achieve head-on collisions, the second beam of protons has to be steered in opposite direction. A proton that moves in opposite direction has a reversed sign in momentum (see Equation 2.1). Therefore, to guide it along the same trajectory, the magnetic field direction has to be inverted. The dipole magnets at the LHC generate a magnetic field perpendicular to the direction of motion. The winding in every dipole is chosen such that it reverses the field direction between the two encapsulated beam pipes. This configuration, called 2-in-1, is achieved by reversing the winding of the cables in each dipole magnet so that the same current circulates in opposite directions, as shown in Figure 2.3. The magnets are superconducting and are generally operated at a temperature of 1.9 K in a bath of superfluid helium. To prevent the beam from diverging and to achieve a minimum beam cross-sectional area at the interaction points particles have to be redirected back to the optimum orbit. Higher order multipole magnets provide such functions for a charged particle beam analogous to optical lenses for a light beam. A single quadrupole magnet focuses the beam in one direction perpendicular to the beam, say x, while at the same time it defocuses in the other direction, y. A combination of two quadrupole magnets, rotated relative to each other by precisely 90°, therefore, results in an overall focusing of the

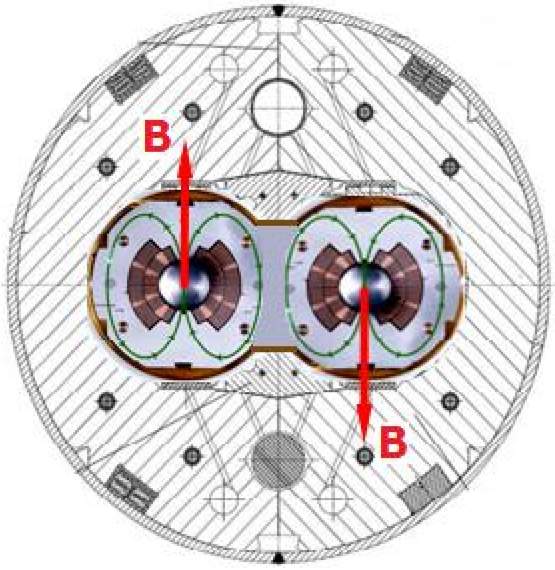

Figure 2.3: Magnetic field in the LHC dipole magnets. The two vacuum pipes for the proton beam are spaced 20 cm horizontally.

beam. Higher order multipole magnets (sextupole and octupoles) provide higher order corrections that can be associated with chromatic corrections with lenses in light beams. Table 2.2 summarized the number of dipoles, quadrupoles and higher-order multipoles installed in the LHC ring.

Table 2.2: Summary table of the LHC multiples magnets.

Order of the multipoles	Number of magnets
Dipoles	1232
Quadrupoles	858
Higher-order multipoles	~ 7200

2.1.3 Luminosity

The luminosity ($\mathcal{L}$) is a measure of the capability of an accelerator to probe a particular particle reaction with a cross section σ. The cross section is an effective area assigned to two colliding particles. The size of the area represents the probability that they interact elastically or inelastically. The rate R at which this reaction is observed is given as:

$$R = \mathcal{L}\,\sigma. \tag{2.2}$$

The luminosity can be derived from accelerator parameters as

$$\mathcal{L} = \frac{f N_1 N_2 n_b}{4\pi\sigma_x\sigma_y}, \tag{2.3}$$

where N_1 and N_2 are the number of protons in each bunch for beam 1 and beam 2, n_b is the number of colliding bunches in the beams, and f is the bunch crossing frequency. The $\sigma_{x,y}$ is the transverse size of the beam in x and y, assuming a Gaussian-like profile along those directions. The final 2010 running conditions were such that $f = 1/(50\text{ ns})$, $\sigma_{x,y} \approx 16 \times 10^{-4}\text{ cm}^2$, $N_1 = N_2 = 1 \times 10^9$ protons per bunch, and $n_b \sim 350$, yielding an average instantaneous luminosity of $\mathcal{L} \sim 2 \times 10^{32}\text{ cm}^{-2}\text{s}^{-1}$. Assuming a production cross section for b-quarks of $\sigma_{\mathrm{b\bar{b}}} = \sigma(\mathrm{pp} \to \mathrm{b\bar{b}}) = 429\ \mu\text{b}$ Sjöstrand et al. (2006); Nakamura et al. (2010) and a luminosity of $\mathcal{L} = 2 \times 10^{32}\text{ cm}^{-2}\text{s}^{-1}$, the production rate for b-hadrons (including $\mathrm{B_s^0}$ mesons) is

$$R = \mathcal{L}\,\sigma_{\mathrm{b\bar{b}}} \approx 172,000\text{ b hadrons/s} \tag{2.4}$$

(two hadrons per event). According to Table 1.3, the production of $\mathrm{B_s^0}$ mesons from b-quarks occurs in 11.5% of all cases. Assuming that only one of the b-quark of the pair produced turns into a $\mathrm{B_s^0}$ meson, the production rate is $R_{\mathrm{B_s^0}} \approx 10,000$ $\mathrm{B_s^0}$ mesons/s. This rate is too large for data acquisition and fast evaluation of partially reconstructed collision events is needed to be able to pick interesting events only (event trigger). To describe the total amount of data collected in an experiment, the integral of the instantaneous luminosity with respect to the time (integrated luminosity) is used. The total number of events observed in a particular reaction is then

$$N = \sigma \int \mathcal{L} dt. \tag{2.5}$$

During the year 2010, the instantaneous luminosities increased from 1×10^{29} cm^{-2} s^{-1} to 2×10^{32} cm^{-2} s^{-1} over a period of six months: the corresponding instantaneous and integrated luminosities are shown in Figure 2.4. The instantaneous luminosity is also measured by the CMS detector, independently from the LHC, from signals in the forward hadronic (HF) calorimeter (for more details see Section 4.1.4). The trend shown in Figure 2.4 (top) reflects the continued optimization of the running conditions during the year 2010. The priority during the year 2010 was to test the LHC capabilities in order to deliver 1 fb^{-1} in 2011. The data taking in 2010 can be divided into three main periods: the initial luminosity run with low bunch currents and single bunch collisions ($\mathcal{L} \sim 10^{29}$ cm^{-2} s^{-1}), nominal bunch operation with up to 48 bunches ($\mathcal{L} \sim 10^{30} - 10^{31}$ cm^{-2} s^{-1}), and the performance ramp up period after the commissioning of bunch trains with the peak luminosity target of 2×10^{32} cm^{-2}s^{-1} via collisions of 368 bunches. The last two periods have been used in this analysis. The luminosity of LHC increased over three orders of magnitude influencing the physics program. Because of the scheduled start with low luminosities, and therefore lower production rates, data could be accumulated with loose selection criteria for the trigger. Furthermore, due to low beam intensities the probability for multiple collisions during a bunch crossing (pile up) was negligible. The CMS B-physics program took advantage of this situation by utilizing triggers that identify the presence of two muons in a collision event (di-muon trigger) with the least possible restrictions on their transverse momenta. Due to the high b-hadron production cross sections, significant studies of the b-hadron decays were already possible with the first available data. A data amount corresponding to an integrated luminosity of 39.6 ± 1.6 pb^{-1} (91.8% efficiency) was accumulated during the 2010 commissioning period. The goal of delivering at least 1 fb^{-1} of data in 2011, under more challenging conditions for B-physics though, has been surpassed.

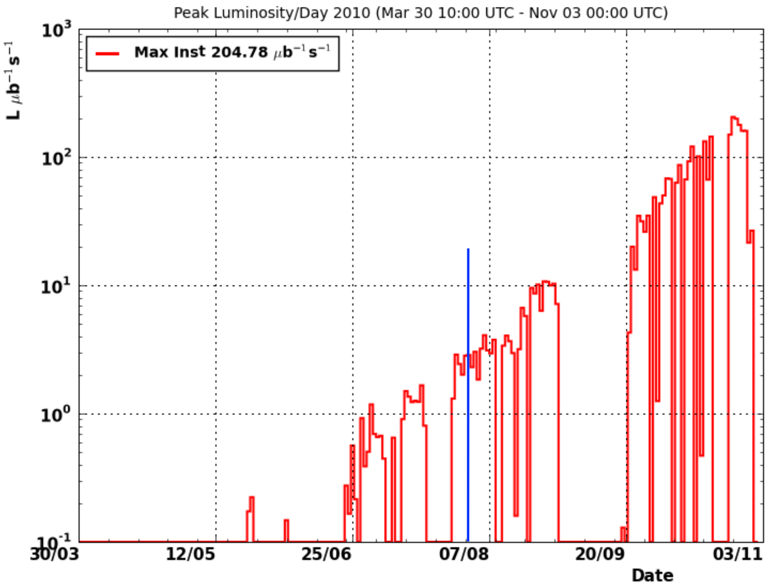

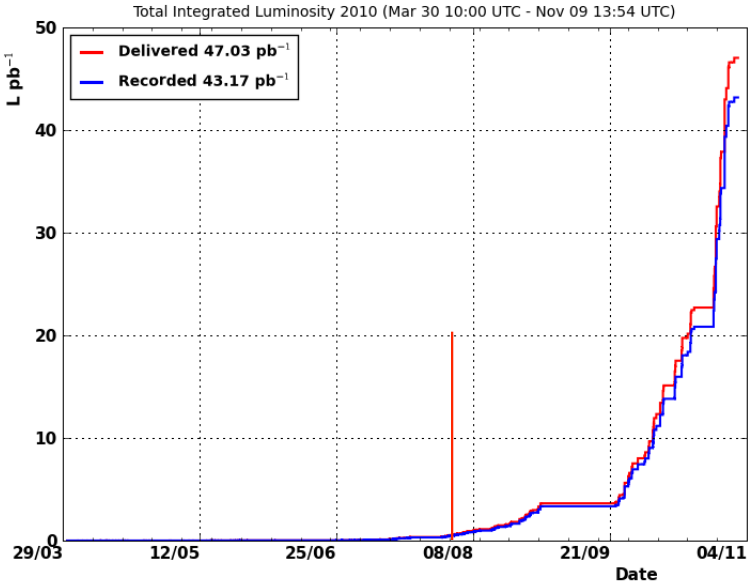

Figure 2.4: Instantaneous (top) and integrated luminosity (bottom) as recorded by the CMS experiment until November 2010. This analysis covers the data taking period from August-November, as indicated by the two vertical lines.

2.2 The Compact Muon Solenoid

The Compact Muon Solenoid (CMS) CMS Collaboration (2006a, 2008) is one of the two general-purpose particle detectors centered at one of four interaction points of the LHC. It is designed to explore a wide range of physics in proton-proton collisions at center-of-mass energies up to 14 TeV and interaction rates of more than 800 MHz, as bunches collide every 25 ns (40 MHz) and up to 20 proton-proton collisions can occur simultaneously. The CMS detector is built to search for the Higgs boson in a wide range of long-lived final state particles, which makes it suitable for the search and study of a large variety of heavy particles included in the SM or to be discovered. These final state particles are photons (reconstructed as energy towers in the electromagnetic calorimeter), muons (identified and reconstructed in the muon stations, the outermost layers of the CMS detector), and jets of hadrons (detected in the hadronic calorimeter). The design of the CMS detector is based on sub-detectors that are arranged cylindrically around the beam-pipe, as illustrated in Figure 2.5. From inside out these are the pixel detector and the silicon tracker, followed by the electromagnetic and hadronic calorimeters, and the muon detectors. The CMS solenoid magnet produces a solenoidal field along the beam of 3.8 T for charged particle tracking whereas the yoke is responsible for the return of the magnetic flux with a corresponding magnetic field of 2 T. It is equipped with detectors to identify and track muons. The following sections describe the different detector parts and sub-detector systems of CMS: the silicon tracker (Section 2.2.2), the electromagnetic calorimeter (Section 2.2.3), the hadronic calorimeter (Section 2.2.4), and the muon system (Section 2.2.5). Finally, the CMS trigger system (Section 2.3) and the analysis software for charged particle trajectory reconstruction and muon identification is presented in Section 2.4.

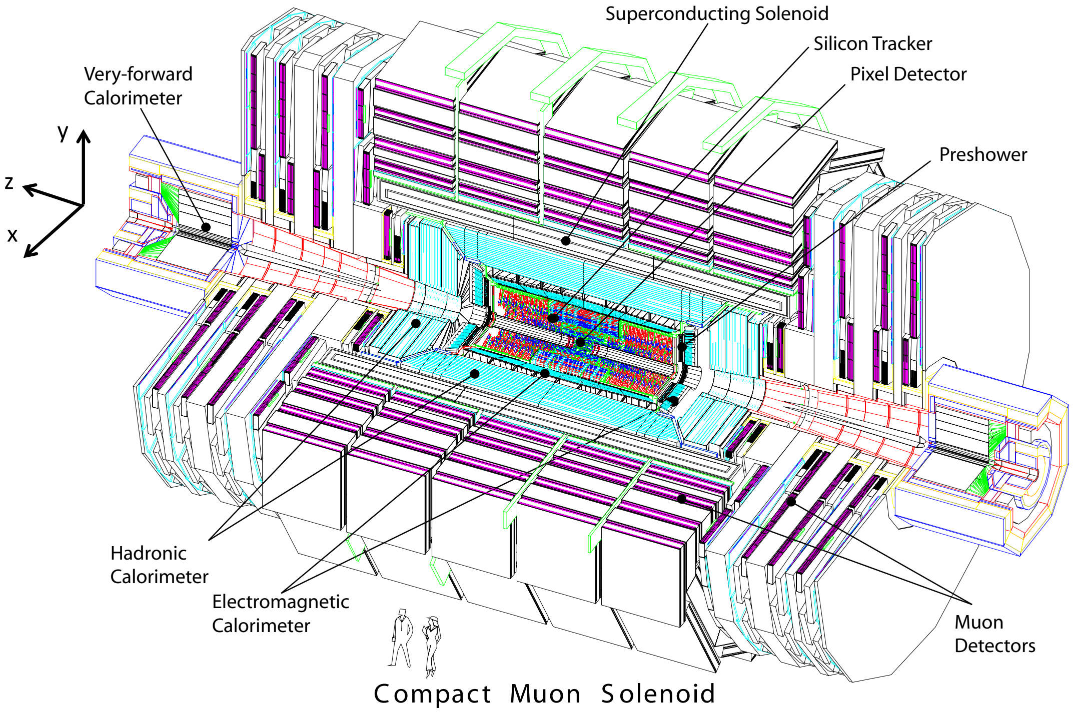

Figure 2.5: A cut-away view of the CMS detector showing the sub-detector systems. A cartesian coordinate system has been chosen as reference frame. In this frame, the z-axis is taken to be the LHC beam-pipe. When the LHC is viewed from above, the proton beam traveling with an anti-clockwise rotation around the ring is defined to be moving in the positive-z direction through CMS. The positive-y axis points upward on the surface of the Earth. To complete a proper right-handed coordinate system, the positive-x axis points toward the center of the LHC ring.

The CMS detector is well suited for the reconstruction of the $\mathrm{B_s^0}$ meson and its decay into J/ψ and ϕ particles, where J/ψ subsequently decays into two oppositely charged muons, and ϕ into two oppositely charged kaons, as shown in Figure 2.6. The lifetime of charged kaons is $\tau \approx 1.2 \times 10^{-8}$ s and for muons is $\tau \approx 2.1 \times 10^{-6}$ s so that for typical momenta of several GeV/c the probability that they decay within the CMS detector is negligible.

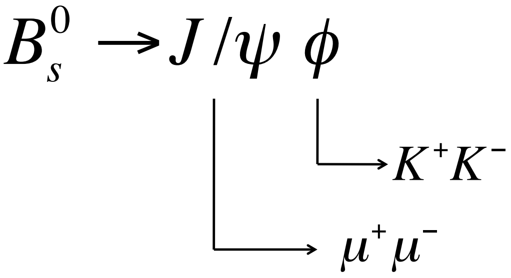

Figure 2.6: Decay of the $\mathrm{B_s^0}$ meson in J/ψ and ϕ.

Having good relative momentum resolution is fundamental for measuring the invariant mass of two charged particles. Their invariant mass is given as

$$M^2 = m_1^2 + m_2^2 + 2(E_1 E_2 - \vec{p_1} \cdot \vec{p_2}) \tag{2.6}$$

where $E_i = \sqrt{p_i^2 + m_i^2}$, with m_i mass and $\vec{p_i}$ momenta of the two $(i = 1, 2)$ muons and kaons, and θ is the angle between the momenta of the two particles. The maximum transverse momentum for the charged decay products is about 15 GeV/c.

Hence, the study of this decay channel requires:

- an efficient trigger to enhance any rare high-p_T resonance production,
- the identification of the decay particles to assign the masses m_i,
- the ability to measure precisely magnitude and direction of the momentum for the four charged particles to calculate the $\mu^+\mu^-$, $\mathrm{K^+K^-}$, and J/ψ ϕ invariant masses. These particles show up as resonance line-shapes in the distribution of

M convoluted with the detector resolution. Higher precision in the momentum measurement, therefore, results in more distinct signals allowing to define tighter ranges in M for selection. This improves the ratio of signal to background events that are reconstructed in the signal rage.

- high precision in the spatial resolution of charged particle tracks for the determination of the B_s^0 decay vertex (secondary vertex): the B_s^0 meson has a mean lifetime of 1.5 ps, and hence, for an average transverse momentum of 7 GeV/c, the corresponding mean decay length in the laboratory is 600 μm.

The CMS detector provides 40 layers of silicon strip detectors and 3 (or 2, if in the forward/backward regions) silicon pixel detectors for high precision charged particle tracking close to the interaction point. The pixel detector, the innermost part, is designed to have a high granularity to obtain a low single-pixel hit rate at high particle flux rates. For the momentum reconstruction, its measurements of particle trajectories close to the interaction point are the most constraining. Furthermore, the high-precision measurement of particle tracks leads to a high accuracy of the determination of their origin from the intersection with other particle tracks. The muons on the other hand are identified by the CMS muon system using the fact that they have a significantly larger interaction length in iron compared to hadrons. The muon system can select online events that contain single and multiple muons. It also provides additional position measurements and, by taking advantage of the 2 T magnetic return field, it measures the signed momenta of muons. The additional track measurements from the muon stations improve the resolution of momentum measurements with the tracker. Because the CMS experiment cannot distinguish hadrons from each other, all measured tracks not identified as muons are considered to be kaons.

2.2.1 Momentum Measurement of Charged Particles

A particle of charge q and velocity $\vec{v}$, that is subjected to a uniform magnetic field $\vec{B}$ experiences a force $\vec{F}$ given by the Lorentz law. The Lorentz force is always perpendicular to both the velocity of the particle and the magnetic field that created it. In general, when a charged particle moves in a static magnetic field, it will trace out a helical path in which the helix axis is parallel to the magnetic field and in which the speed of the particle will remain constant. The geometry of the CMS detector is best described in a cylindrical coordinate system. In such a system, the z-axis points along the LHC beam-pipe, the x-axis points towards the center of the LHC ring, and the y-axis is perpendicular to the plane of the LHC ring. The azimuthal angle φ is defined such that $\varphi = 0$ corresponds to the x-axis, and ρ is the radial distance from the beam. Then, the helix trajectory can be reconstructed from measured positions along the particle path of length s:

$$\begin{aligned} x(s) &= x_0 + \frac{1}{r_0}\left[\cos\left(\phi_0 + \frac{Hs}{r_0}\cos\lambda\right) - \cos\phi_0\right] \\ y(s) &= y_0 + \frac{1}{r_0}\left[\sin\left(\phi_0 + \frac{Hs}{r_0}\cos\lambda\right) - \sin\phi_0\right] \\ z(s) &= z_0 + s\sin\lambda \end{aligned} \tag{2.7}$$

where (x_0, y_0, z_0) is the starting point at length $s = 0$, r_0 is the radius, and λ is the polar (dip) angle. The $H = \pm 1$ is the sense of rotation of the projected helix in the transverse plane. It is the product of the sign of the charge of the particle and the direction of the magnetic field along z. The ϕ_0 is the azimuth angle of the starting point with respect to the helix axis.

In the transverse plane (x,y), the particle follows a circular path with radius r_0 given by Equation 2.1. For high momentum particles, only a small arc of the circle is observed. For a particle of transverse momentum p_{T} passing through a region of length L, within a magnetic field B, the deviation from a straight line s is known as the sagitta of the track (see Figure 2.7 for the definition). The sagitta s determines

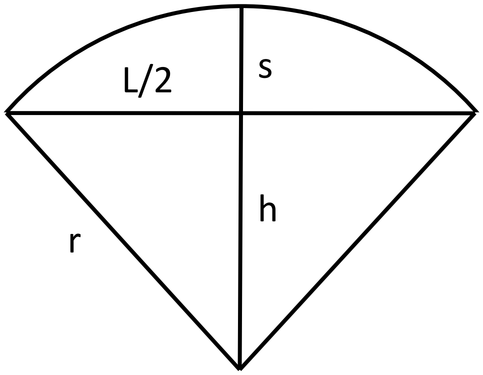

Figure 2.7: Definition of the sagitta s for a particle of transverse momentum p_{T} passing through a region, of length L, with a magnetic field B.

the momentum of the track, p_{T},

$$s = r - h = \frac{L^2}{8r} \tag{2.8}$$

since replacing r with Equation 2.1 yields:

$$p_{\mathrm{T}} = \frac{qL^2B}{8s}. \tag{2.9}$$

The magnitude of the total momentum is given as

$$p_{\mathrm{tot}} = p_{\mathrm{T}}\sqrt{1 + \tan^2\lambda}. \tag{2.10}$$

The direction of the momentum is evaluated along the track (see Equation 2.8). The uncertainty of the momentum measurement is related to the error of the measured sagitta $\sigma(s)$ as follows

$$\frac{\sigma(p_{\mathrm{T}})}{p_{\mathrm{T}}} = \frac{8}{qBL^2}p_{\mathrm{T}} \cdot \sigma(s). \tag{2.11}$$

It is directly proportional to the error of the sagitta and to the transverse momentum p_{T} itself, but, inversely proportional to the strength of the magnetic field and to the distance L^2. Hence, along the track, the measurement closest to the interaction point is dominant, as provided by the silicon pixel detector. According to Gluckstern (1963), the uncertainty also depends on the number of hits in the silicon layers (N) and their spatial resolution ($\sigma_{r\varphi}$):

$$\sigma(s) = \sqrt{\frac{720}{N+4}} \frac{\sigma_{r\varphi}}{8}, \tag{2.12}$$

The point error $\sigma_{r\varphi}$ has a constant contribution from the detector intrinsic hit resolution and from multiple scattering. The intrinsic resolution depends on the production and collection of secondary charges and details of the readout electronics are explained later. The multiple scattering is caused by Coulomb scattering of the particle inside the detector material. This leads to many relatively small random changes of the direction of flight, that worsen the position resolution toward lower particle momenta. Multiple scattering depends on the distance in the material (l) and on the radiation length of silicon ($X_0 = 9.4$ cm). The uncertainty of the momentum measurement due to both effects can be parameterized as

$$\frac{\sigma(p_\mathrm{T})}{p_\mathrm{T}} \propto a \cdot p_\mathrm{T} \oplus b \cdot \sqrt{\frac{l}{X_0}} \tag{2.13}$$

where a and b are constant terms. Figure 2.8 shows the resolution for muons with transverse momenta of 1, 10, and 100 GeV/c as function of the pseudorapidity (η). In this analysis the average relative transverse momentum resolutions for kaons and muons is found to be $\sigma_{p_\mathrm{T}}/p_\mathrm{T} \sim 1\%$. This translates into invariant mass resolutions of 30 MeV/c^2 and 10 MeV/c^2 for the J/ψ and ϕ signals, respectively. For the B^0_s mesons, the average invariant mass resolution is expected to be about 50 MeV/c^2.

The Figure 2.9 displays for reconstructed particle trajectories in the $r - \varphi$ projection the first $\mathrm{B}^0_\mathrm{s} \to \mathrm{J}/\psi(\to \mu^+\mu^-)\phi(\mathrm{K}^+\mathrm{K}^-)$ candidate that was recorded at the beginning of July 2010. In this event display of CMS Kovalskyi et al. (2010) CMS Collaboration (2010a) the lines correspond to reconstructed trajectories of the charged particles with a minimum threshold of $p_\mathrm{T} > 0.3$ GeV/c. The circle represents the

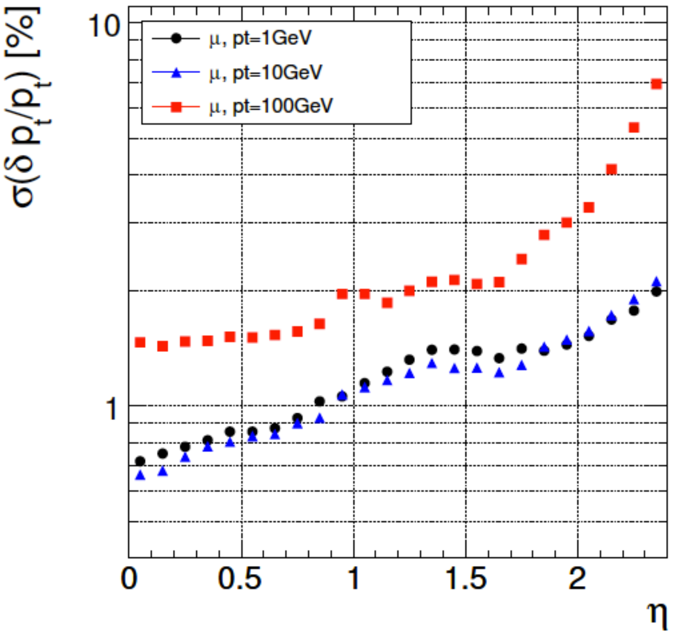

Figure 2.8: Relative transverse momentum resolution for muons with transverse momenta of 1, 10, and 100 GeV/c as function of the pseudorapidity.

outermost layer of the silicon tracking system at a radius of 1.2 m. The lines in red represent reconstructed tracks that have been identified as muons. When the four momenta of the muons are combined, the $\mu^+\mu^-$ invariant mass is close to the world average value for the J/ψ meson Nakamura et al. (2010). The two blue trajectories are two oppositely charged particles originating from a common point. They are assumed to be the kaons. Their invariant mass is close to the mass of the ϕ meson Nakamura et al. (2010). The combination of the four momenta of the J/ψ and ϕ candidates results in a B_s^0 candidate with J/ψ ϕ invariant mass close to the expected value for the B_s^0 meson Nakamura et al. (2010). Table 2.3 summarizes the measured kinematic variables of the $B_s^0 \rightarrow$ J/ψ ϕ candidate. Figure 2.10 shows a close up view of the event in an arbitrary orientation. The intersection between the B_s^0 decay particles, called secondary vertex, is indicated with a circle. The other tracks in the event originate from the collision point (primary vertex). The distance between these two points, relativistically transformed (boosted) into the rest frame of the B_s^0 meson,

Table 2.3: Summary table of the event parameters for the $\mathrm{B_s^0} \rightarrow \mathrm{J}/\psi\ \phi$ candidate. The p_T is the transverse, p_z the longitudinal momentum. The world-average central mass values are $3,096.9 \pm 0.1$ MeV/c^2 for J/ψ, $1,019.4 \pm 0.1$ MeV/c^2 for ϕ and $5,366.3 \pm 0.6$ MeV/c^2 for $\mathrm{B_s^0}$ Nakamura et al. (2010).

	Measured Value
$\mu_1\ p_\mathrm{T}$	2.9 GeV/c
$\mu_1\ p_\mathrm{Z}$	15.2 GeV/c
$\mu_2\ p_\mathrm{T}$	2.1 GeV/c
$\mu_2\ p_\mathrm{Z}$	7.3 GeV/c
$\mu\mu$ inv. mass	3.104 GeV/c^2
$\mu\mu\ p_\mathrm{T}$	4.1 GeV/c
$\mu\mu\ p_\mathrm{Z}$	22.5 GeV/c
$K_1\ p_\mathrm{T}$	1.4 GeV/c
$K_1\ p_\mathrm{Z}$	3.1 GeV/c
$K_2\ p_\mathrm{T}$	2.2 GeV/c
$K_2\ p_\mathrm{Z}$	5.1 GeV/c
KK inv. mass	1.019 GeV/c^2
$KK\ p_\mathrm{T}$	3.6 GeV/c
$KK\ p_\mathrm{Z}$	8.2 GeV/c
J/$\psi\ \phi$ inv. mass	5.346 GeV/c^2
J/$\psi\ \phi\ p_\mathrm{T}$	7.7 GeV/c
J/$\psi\ \phi\ p_\mathrm{Z}$	30.6 GeV/c

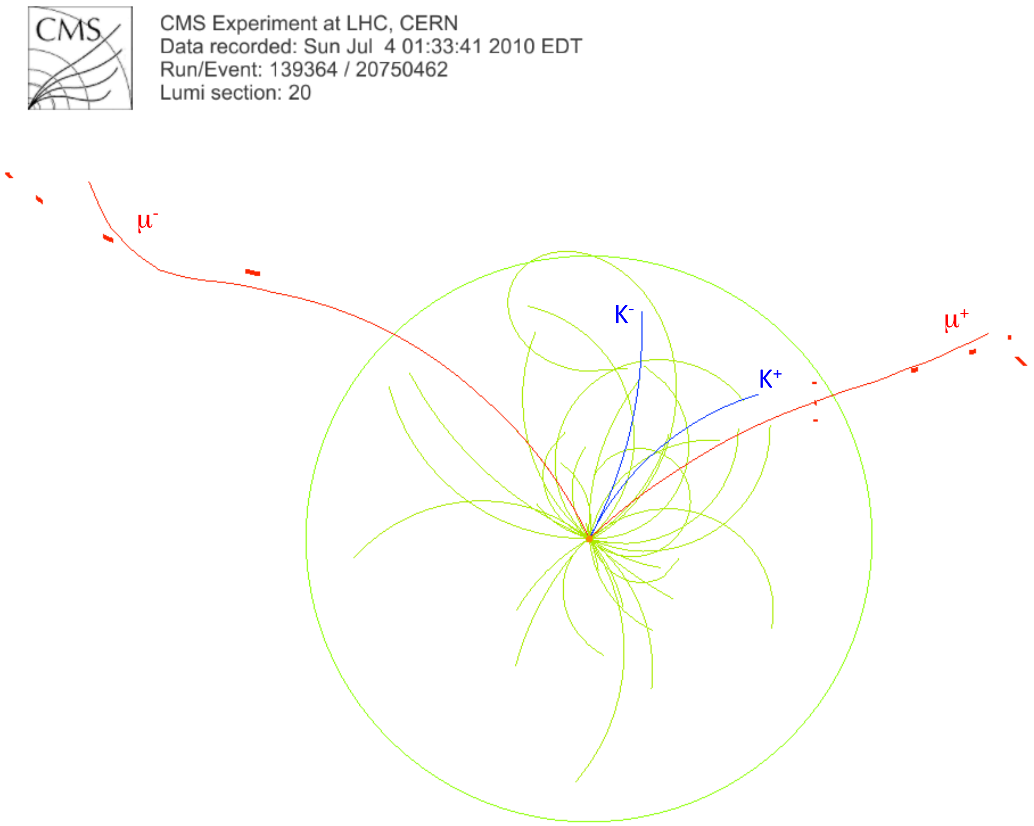

Figure 2.9: Event display of a golden $B_s^0 \rightarrow J/\psi\ \phi$ candidate in the plane transversed to the proton beam (shown as dot in the center). The hit information in silicon tracker and muon detector system are shown. The radial distance of the muon system is reduced to fit in the same range. The reconstructed tracks, that are identified as muons originating from a J/ψ meson decay, are indicated in red. The kaon tracks from the ϕ decay are shown in blue. All displayed tracks have a minimum reconstructed transverse momentum of $p_{\mathrm{T}} > 0.3$ GeV/c in the vicinity of the collision point.

is called proper decay length. It is derived from the measured decay distance (D) between the primary and secondary vertices in the laboratory and the $\mathrm{B_s^0}$ transverse momentum in the laboratory p_{T}

$$ct = \frac{M}{p_{\mathrm{T}}} D. \tag{2.14}$$

The c is the speed of light and M is the assumed central mass value of the $\mathrm{B_s^0}$ meson. From Figure 2.10, the $\mathrm{B_s^0}$ flight length D is estimated to be about 5 mm with the measured momentum of the $\mathrm{B_s^0}$ of $p_{\mathrm{T}} = 32$ GeV/c. This corresponds to a proper decay length of $c\tau = 895$ μm or a proper decay time of $t \approx 3$ ps.

This is the first unambiguously identified $\mathrm{B_s^0}$ candidate with the CMS experiment Leonardo (2010) CMS Collaboration (2010a).

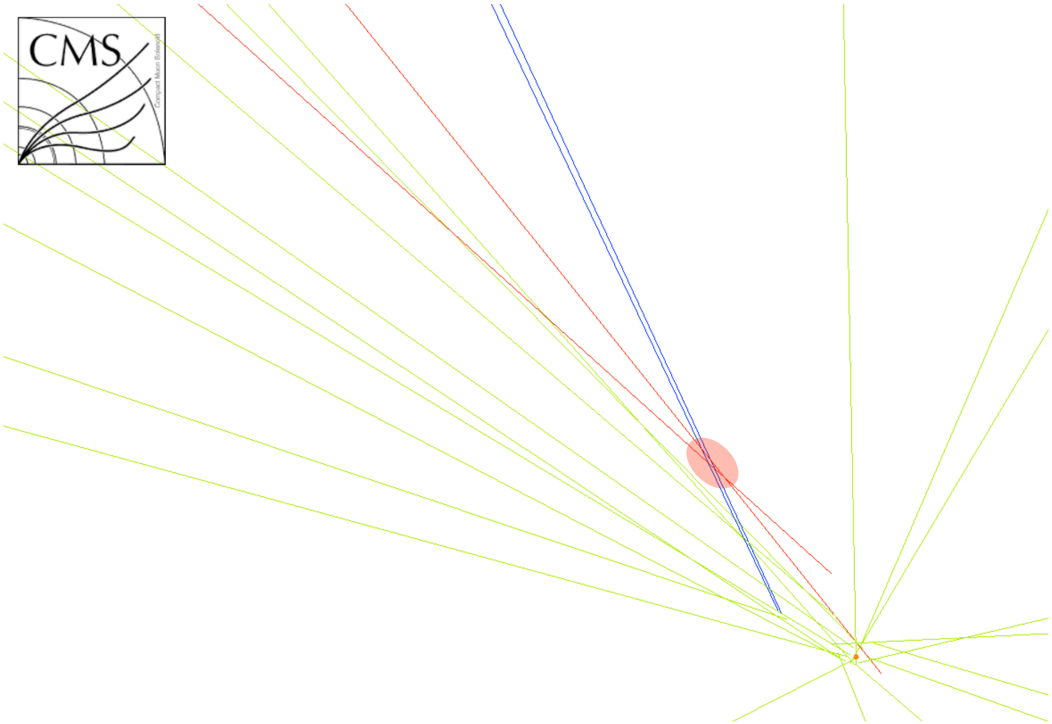

Figure 2.10: Event display of a golden $B_s^0 \to J/\psi\ \phi$ candidate in an arbitrary view. The reconstructed tracks, that are identified as muons originating from a J/ψ meson decay, are indicated in red. The kaon tracks from the ϕ decay are shown in blue. The B_s^0 candidate, is a combination of the J/ψ and ϕ candidates. Its flight length of $ct \approx 500\ \mu$m is the distance between primary and secondary vertex (circle) to be ≈ 5 mm. All displayed tracks have a minimum reconstructed transverse momentum of $p_T > 0.3$ GeV/c in the vicinity of the collision point.

2.2.2 The Silicon Tracker

At the design luminosity of 10^{34} cm^{-2}s^{-1}, during each LHC bunch crossing an average of $1,000$ particles hit the innermost layers of the tracker. In addition, with the strong magnetic field, low-p_{T} tracks curl around the beam pipe leading to high charged particle densities. At the innermost pixel layer the flux is dominated by pions that are created in collisions of protons with each other or by stray protons in material. The detector is exposed to fluences of up to 10^{14} n_{eq}/cm^2 per year (where 1 n_{eq} is a MeV neutron equivalent particle) making the region around the collision point a hostile radiation environment and potentially damaging any detection device over a short time period. To provide high precision charged particle tracking under those conditions, the detector has to:

- survive in the hostile environment near the beam of the LHC,
- reconstruct charged particle trajectories close to the interaction point for the determination of momentum and secondary vertices of long-lived objects,
- provide the highest possible number of hits per track, with a single-hit precision to better than ~ 20 μm (for tracks that cross the detector at 90°).

The material for such a detection device was chosen to be silicon that is doped with donor impurity atoms. Such silicon is a semi-conducting material with good intrinsic energy resolution. An energy deposit of 3.6 eV is needed to create an electron-hole pair in the detector material. All liberated charges are collected in a strong electric field that is generated by reverse biasing a $p - n$ junction of the silicon materials. The low ionization threshold leads to a large number of charges. Unlike the situation for gas detectors, there is no multiplication of primary charge and the collected signal is only a function of the detector thickness. To minimize the multiple Coulomb scattering, the detector thickness, on the other hand, should be as small as possible (see Section 2.2.1). A practical limit is set by the signal-to-noise ratio. For a typical thickness of 300 μm, one obtains an average of 3×10^4 electron-hole pairs, a signal very detectable with low noise electronics, and it represents only 0.3% of the radiation length. Silicon-based sensors have excellent position resolution of a few tens of micrometers, their signal collection time is short, and they can be operated in strong magnetic fields. The smallest radius at which a traditional silicon micro-strip detector can function in such an environment is limited by occupancy and radiation damage. By reducing the size of the sensor elements, the hit rate per sensor area is smaller leading to a higher spatial resolution. Therefore, silicon pixels constitute the innermost part of the CMS tracking detector. At larger radii the amount of pixel channels and, hence, the cost for the readout electronics increases with the area proportional to r^2. Simultaneously, the particle flux reduces proportional to $1/r^2$ and the requirement for single-hit resolution is relaxed. Hence, for radii greater than 15 cm silicon strip detectors were chosen.

The pixel detector consists of three cylindrical (barrel) layers (BPix) and two layers of forward and backward disks (FPix). The pixel detector is essential for forming seed tracks for the outer track reconstruction and for the reconstruction of secondary vertices from b-hadrons and τ decays. The 53 cm long BPix layers are located at mean radii of 4.4, 7.3, and 10.2 cm. The FPix disks, radially extending from 6 to 15 cm, are placed on each side at $z = \pm 34.5$ and $z = \pm 46.5$ cm. The BPix (FPix) contains 48 million (18 million) pixels resulting in an occupancy of 10^{-4} hits per pixel per bunch crossing at full luminosity. The Figure 2.11 shows the geometric arrangement and the coverage as a function of pseudorapidity. The pixel detector covers a pseudo rapidity range $-2.5 < \eta < 2.5$, matching the acceptance of the central tracker. In the high-η region reconstructed hits from the two disks are combined with the lowest possible radius point from the 4.4 cm barrel layer.

The pixel size in the innermost three cylindrical layers of the barrel is 150×100 μm^2. Here, the 150 μm is along the direction where ionization charges are directed sideways by the Lorentz force while they drift toward the collection electrode, spreading over more than one pixel. The 100 μm direction is, instead, parallel to the magnetic field. The pixel system has an analog pulse height readout. For each pixel the

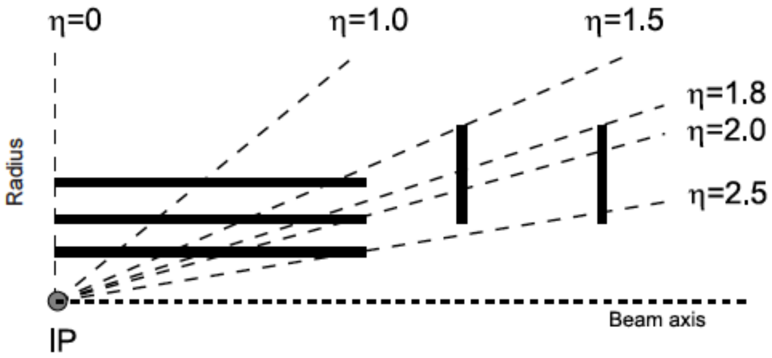

Figure 2.11: Geometrical layout of the pixel detector and hit coverage as function of the pseudorapidity. IP refers to interaction point.

position resolution due to charge sharing in neighboring pixels helps to separate signal and noise hits as well as to identify large hit clusters from overlapping tracks. Charge interpolation based on analog pulse yields a spatial resolution in the range of $10 - 12$ μm for perpendicular tracks. The forward/backward detectors are tilted at 20° in a turbine-like geometry to enforce charge sharing since otherwise the drift direction of electrons is parallel to the magnetic field.

Radiation damage induces charge trapping in the silicon material, reduces the depletion depth due to random released charges, and decreases the charge sharing. This is partially compensated by increasing the bias voltage until the radiation damage cannot be overcome. The gradual decrease of the depletion depths leads to fewer collected charges diminishing charge sharing and, consequently, spatial resolution. Therefore careful monitoring of the detector performance and the radiation environment is crucial. Ultimately, within a few years the innermost layers need to be replaced. A more detailed description of the pixel detector can be found in Chapter 3 together with the Pixel Online Software that monitors and reports messages for a real-time diagnosis of the apparatus during data taking. The development and implementation of this software was subject of this dissertation work.

The CMS silicon strip detector is the outermost part of the CMS tracking system, radially surrounding the pixel detector. This system is 5.8 m long and has a diameter of 2.5 m. The total active silicon area, embodying 75 million readout channels, covers an area of 200 m^2, which makes the CMS tracker the largest silicon detector device ever built. The silicon strip tracker is divided into inner barrel part (TIB), the inner disks (TID), covering a radial region $20 < r < 55$ cm, and the outer barrel (TOB) and outer end-caps (TEC) at radii $r > 55$ cm. For a schematic layout of the CMS silicon strip tracker see Figure 2.12. As shown in Figure 2.12, in the range $|\eta| < 2.4$ a track crosses at least nine strip detector layers. The tracker acceptance ends at $|\eta| < 2.5$. The silicon strip detector complements hit measurements along charged particle trajectories up to radial distances from the collision point of 1.2 m. At a distance of 15 cm the particle flux is low enough so that silicon strips can be used. The strip readout pitch, which is the inter-strip distance, increases with the radius. The strips width, pitch, and length are chosen in order to optimize the resolution and occupancy. For the region closer to the pixel detector, the barrel is instrumented with a four layer micro-strip silicon detector complemented by three disks at each side.

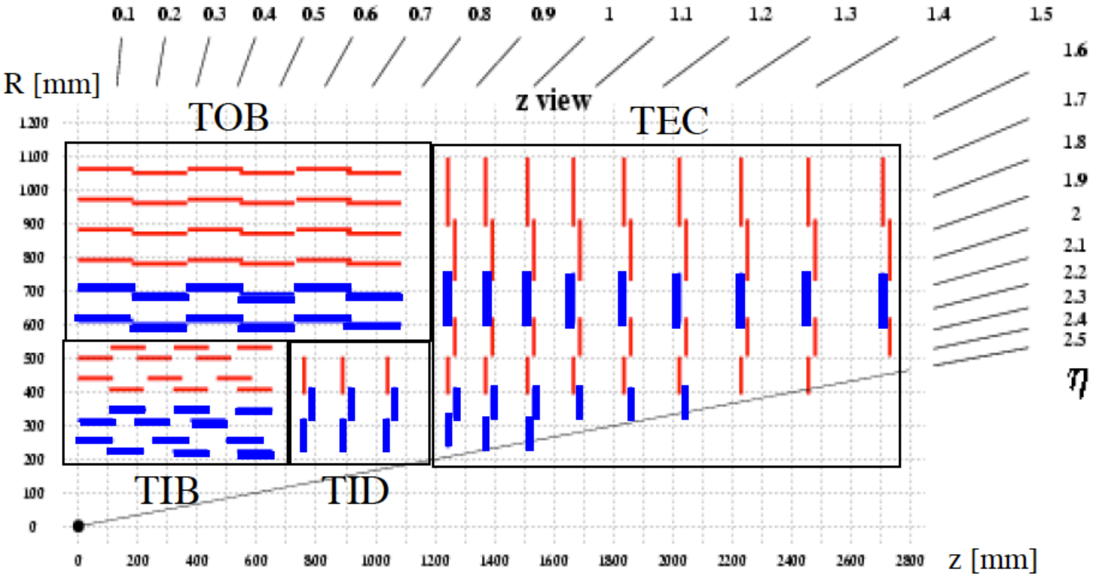

Figure 2.12: Layout of one quarter of the CMS silicon strip tracker components.

The strips are 10 cm in length with a minimum pitch of 80 μm in the barrel region and 100 μm in the endcaps giving an occupancy of up to $2-3\%$ per bunch crossing for single strip. Depending on the $r-\varphi$ pitch, the single point resolution in $r-\varphi$ ranges from 23 μm to 35 μm. In the outermost region ($r > 55$ cm) the magnetic field enhances the rapid decrease of charged particle rates. The particle flux is sufficiently low enough so that the strip length can be increased to 25 cm and a maximum pitch of 180 μm and 184 μm in the barrel and endcap region, respectively, are possible. The increase in strip size, conveniently, limits the number of readout channels covering the large area. However, electronic noise grows linearly with the strip length and in order to keep the signal to noise ratio above ten, the thickness of the sensors was increased to 500 μm in the outer region of the tracker. The resulting higher depletion voltage can be reduced by choosing a higher initial resistivity, keeping the initial depletion voltages of the thick and thin sensors within the same range. The outer tracker consists of six barrel layers of silicon micro-strip detector that surround the inner tracker, supplemented by nine disks on both sides. The occupancy of the whole outer tracker amounts to approximately 1% per bunch crossing. The single point resolution in the outer barrel is between 35 μm and 53 μm in $r-\varphi$, dependent on the pitch. Some layers are equipped with stereo-modules, shown in blue in Figure 2.12. In that case, two modules are mounted back-to-back at a stereo angle of 100 mrad, hence providing a measurement in (r, z) as well as in (r, φ). They provide single point resolutions of 230 μm and 530 μm in z in the inner and outer barrel, respectively. The silicon strip detector material budget, in units of radiation length, increases as function of the pseudorapidity from 0.4 X_0 at $\eta \approx 0$ to about 1.8 at at $\eta \approx 1.4$; beyond that it reduces to about 1 X_0 as it approaches $\eta \approx 2.5$. The relative transverse momentum resolution for the full silicon tracker, pixel and strip technologies, is show in Figure 2.8.

2.2.3 The Electromagnetic Calorimeter

This analysis does not make direct use of information from this sub-detector. For completeness, a brief discussion is given here. For neutral Higgs bosons, with masses below ~ 140 GeV, the decay into two photons offers one of the cleanest channels for discovery. The identification of the Higgs via the two-photon invariant mass requires a measurement of the total energy and direction of the decay photons with energies above 100 GeV. The CMS electromagnetic calorimeter uses an array of lead tungstate crystals ($PbWO_4$) to measure the energy deposition of electrons and photons in that regime. Lead tungstate is an ideal material for this purpose because of its stability in high-radiation environments, its relatively fast scintillation response time (80% of the light released within 25 ns), and its small radiation length (0.89 cm). The small Moliere radius of transverse particle showers in the material (2.2 cm) allows to build a compact calorimeter. The total amount of secondary light collected from the crystals is proportional to the amount of energy lost by the incident particle. If the particle stops completely, then the total energy of the particle is deposited and converted into light. The $61,200$ crystal in the barrel region (EB) and the $7,324$ crystals in each of the two endcaps (EE) provide a hermetic, homogeneous coverage up to $|\eta| < 3$. Groups of 25 crystals are arranged in a geometric structure called tower. In front of each ECAL Endcap is a preshower detector (ES), from $1.65 < |\eta| < 2.6$ made from silicon strip detectors in order to reject the $\pi^0 \to \gamma\gamma$ decays. The geometrical configuration of one quarter of the crystals is illustrated in Figure 2.13 by a transverse section of the ECAL. The measurement of charged track trajectories and momenta (for both muons and kaons) is not degraded by the calorimeter material budget. The energy loss by muons that traverse the crystal is negligible because of the small radiation length. For hadron, instead, the problem does not exist because the reconstruction measurement are performed in the silicon tracker, which is positioned inside the calorimeter gap.

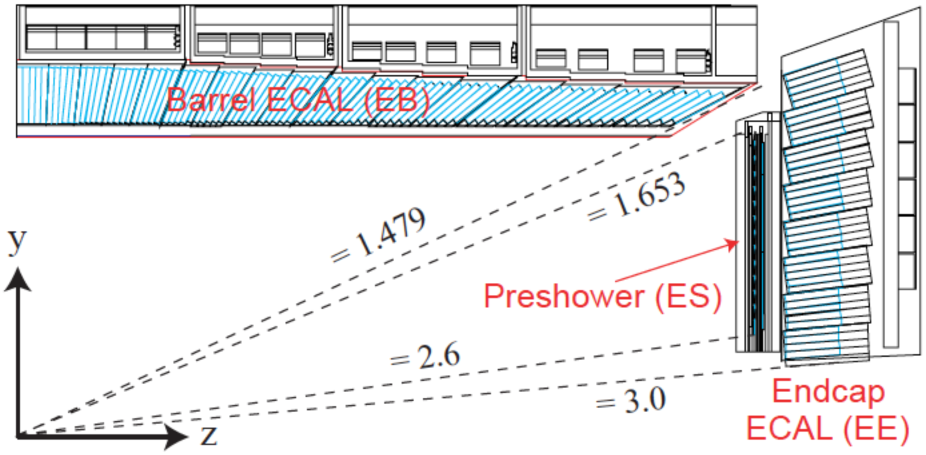

Figure 2.13: Partial transverse section through the ECAL, showing the geometrical configuration.

2.2.4 The Hadronic Calorimeter

Between the electromagnetic calorimeter and the CMS solenoid magnet in the barrel, and outside the ECAL end-cap, there is a second calorimeter system called the Hadronic Calorimeter (HCAL) CMS Collaboration (1997a). It is used for

- the measurement of the energy of hadrons from collisions products in CMS, typically several traveling in the same direction as jets or single hadrons and muons,
- the generation of energy segments for High Level Trigger (HLT) decisions, and
- the measurement of the instantaneous luminosity of the LHC.

The design of the HCAL shows a significantly greater depth with respect to the ECAL. Due to the fact that hadronic showers, in general, have a much longer nuclear radiation absorption length than the interaction length governing electromagnetic showers, the HCAL is required to have as much interaction lengths of material as possible inside the magnetic coil. Each HCAL tower is placed behind a corresponding ECAL tower (except in the forward region) to produce a long structure capable of measuring the total energy of the hadrons in a well defined (η,φ) region with minimal leakage.

Figure 2.14 illustrates a section of the CMS with the HCAL components labelled. The HCAL is composed of four sub detectors, the Hadron Barrel (HB), covering a pseudorapidity range of $|\eta| < 1.4$, the Hadron Endcaps (HE) for the range $1.3 < |\eta| < 3$, the Hadron Outer (HO) for $|\eta| < 1.3$, and the Hadron Forward (HF) calorimeters, symmetrically positioned at each side and covering the forward pseudorapidity regions $2.8 < |\eta| < 5.2$. The HB, and HE are located in between the ECAL and the magnet, while, the HO sits between the magnet and the muon system, due to the constraint of the space, with the function of tail catcher of the hadronic shower.

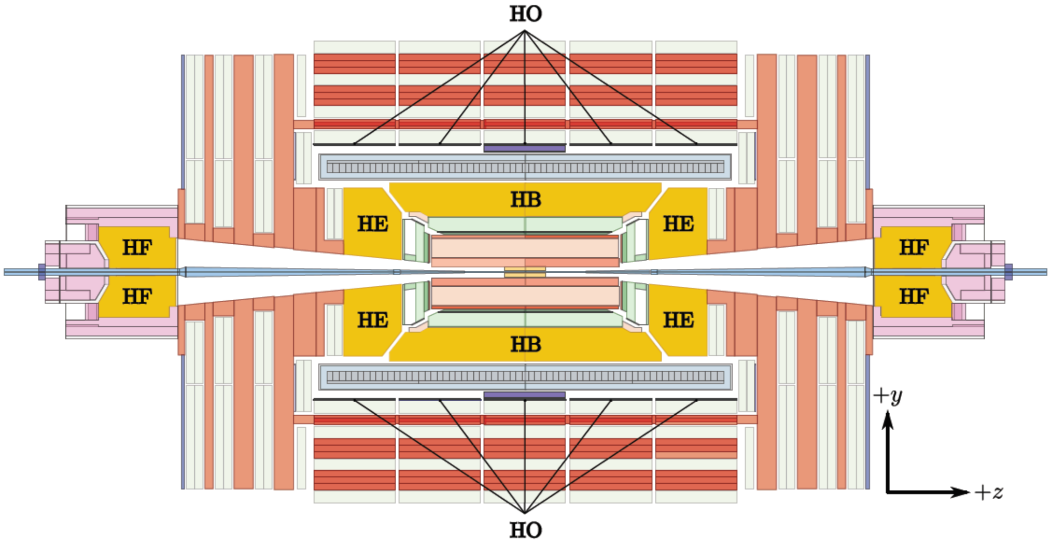

Figure 2.14: A view of the CMS detector in y-z projection with the components of the hadronic calorimeter labeled.

The barrel, the end-cap, and the outer hadronic calorimeters are all sampling calorimeters. They consists of plastic scintillators sandwiched between brass absorbers. Thus, the scintillators sample the showers of the charged particles produced by the nuclear interactions of the hadrons with the nuclei of the absorber. At 90°, the absorber of the barrel calorimeter is 5.82 interaction lengths deep: the effective thickness increases with the polar angle as $1/\sin\theta$, resulting in 10.6 interaction lengths at edge of the barrel. The total depth of the end-cap of the hadronic calorimeter is 10 interaction lengths, which takes into account the electromagnetic calorimeter in front of it. The outer calorimeter is positioned outside of the magnet and uses it as an additional absorber in front of another 19.5 cm thick iron. Thus the total depth of the calorimeter system is at least of 11.8 interaction lengths. Being very close to the beam-pipe, each HF detector is exposed to roughly 380 GeV of energy per pp collision due to low-angle scattering, compared to only 100 GeV of energy deposited in the rest of the detector. In this high particle flux environment, a different type of detection system is chosen. The forward calorimeter is also a sampling calorimeter. However, it uses scintillating quartz fibers, which run along the developing electromagnetic and hadronic showers, instead of scintillating plates in the perpendicular direction as in the central hadronic calorimeter. Quartz fibers act as the active medium and the signal is generated when charged particles generate Cherenkov light making the HF mostly sensitive to the EM component of showers. The HF is essentially an iron cylinder, that acts as an absorber with total depth 165 cm or $\approx$ 10 interaction lengths.

The energy resolution of the combined barrel calorimeters for hadrons, electron and muons in the energy range $2-350$ GeV can be parametrized as

$$\left(\frac{\sigma}{E}\right)^2 = \left(\frac{84\%}{\sqrt{E}}\right)^2_S \oplus (7\%)_C \tag{2.15}$$

where the first and second terms in the equation represent the stochastic and constant term respectively. Corrections to compensate for the different intrinsic electron to hadron response (e/h) in the ECAL and HCAL have been applied. The role of the HCAL within the HLT decision scheme is described in Section 2.3. The HF calorimeter also provides luminosity information during data taking (see Section 4.1.4).

2.2.5 The Muon System

The muon system has three purposes: distinguish muons from hadrons, perform a fast muon multiplicity count, and measure the muon (signed) momenta. The identification and momentum measurement of muons is of central importance to CMS. The CMS muon system provides important information for the:

- search for the "gold plated" signal of the Higgs Boson in its decay into ZZ or ZZ^* which in turn decay into four charged muons,
- search for new gauge bosons, such as $Z' \rightarrow \mu^+\mu^-$ with $p_{\mathrm{T}}^{\mu} > 1$ TeV,
- lepton and photon isolation criteria,
- b-jet tagging, exploiting the $\mathrm{b} \rightarrow \mu$ decay, which is essential for detailed Higgs studies, top studies, and SUSY searches,
- lighter particle spectroscopy and the measurement of b-hadron decays into J/ψ mesons, as in case of $\mathrm{B}_{\mathrm{s}}^0 \rightarrow \mathrm{J}/\psi\ \phi$.

Muons are unique among the products of high-energy collisions because they have a long lifetime (2.2 μs in their rest frame), a large rest-mass (105.7 MeV/c^2) and are not strongly interacting. The long lifetime enables the muons to survive to the outer layers of the detector and beyond. Due to their greater mass, muons are not as accelerated as electrons when they encounter electromagnetic fields, and do not emit as much bremsstrahlung radiation, which is the primary mechanism of energy loss for decelerating charged particles. This allows muons of a given energy to penetrate more deeply into the detector material than electrons. Relativistic muons are also called Minimum-Ionizing Particles (MIPs) because the amount of energy lost by the muon per unit distance traveled in a medium is close to the minimum. The energy loss rate of a muon increases only logarithmically between momenta of $p = 1$ GeV/c and $p = 100$ GeV/c, so that all muons in this momentum range are effectively minimum-ionizing. Finally, because the muons do not experience the strong nuclear force, they do not lose energy due to inelastic nuclear collisions in the dense calorimeter material as hadrons do. Thus muons reach the outside of the solenoid magnet with relatively little energy lost. The physics goals are achieved as follows:

- muon identification: at least 16 radiation lengths of material are needed to ensure absorption of other charged particles before (in the HCAL and ECAL) and inside the muon system (in the iron yoke),
- muon trigger: the combination of muon chambers and fast muon counters provide unambiguous beam crossing identification and trigger on single and multi-muon events with well defined p_{T} thresholds from a few GeV/c to 100 GeV/c for $\eta \leq 2.1$,
- relative transverse momentum resolution: from $8-15\%$ $\delta p_{\mathrm{T}}/p_{\mathrm{T}}$ (at 10 GeV/c) to $20-40\%$ (at 1 TeV) for muons reconstructed with the muon system, and from $1-2\%$ (at 10 GeV/c) to $6-17\%$ (at 1 TeV) after combining the reconstructed muon in the muons system with a track from the CMS tracker,
- charge assignment: evaluated from the helix trajectories reconstructed from the measured positions and correct to 99% confidence up to the kinematic limit of 7 TeV,
- capability of withstanding the high radiation and interaction background expected at the LHC.

Due to the shape of the solenoid magnet, the muon system has a cylindrical barrel section and two planar endcap regions. The muon system uses three types of gaseous particle detectors:

- Drift Tubes (DT): used in the barrel region ($|\eta| < 1.2$) were the magnetic field is confined to the iron yoke, the muon rate is low, and the background rates are small,

- Cathode Strip Chambers (CSC): instrumented in the the endcap discs ($0.9 < |\eta| < 2.4$) in order to deal with the strong, non-uniform magnetic field and the high charged particle rates in the forward region,

- Resistive Plate Chambers (RPC): extended over the barrel as well as the endcap; they are used to supplement the other two technologies.

Figure 2.15 shows the muon spectrometer CMS Collaboration (1997b, 2008) which is located in the magnet return yoke and provides a full geometric coverage up to $|\eta| < 2.4$.

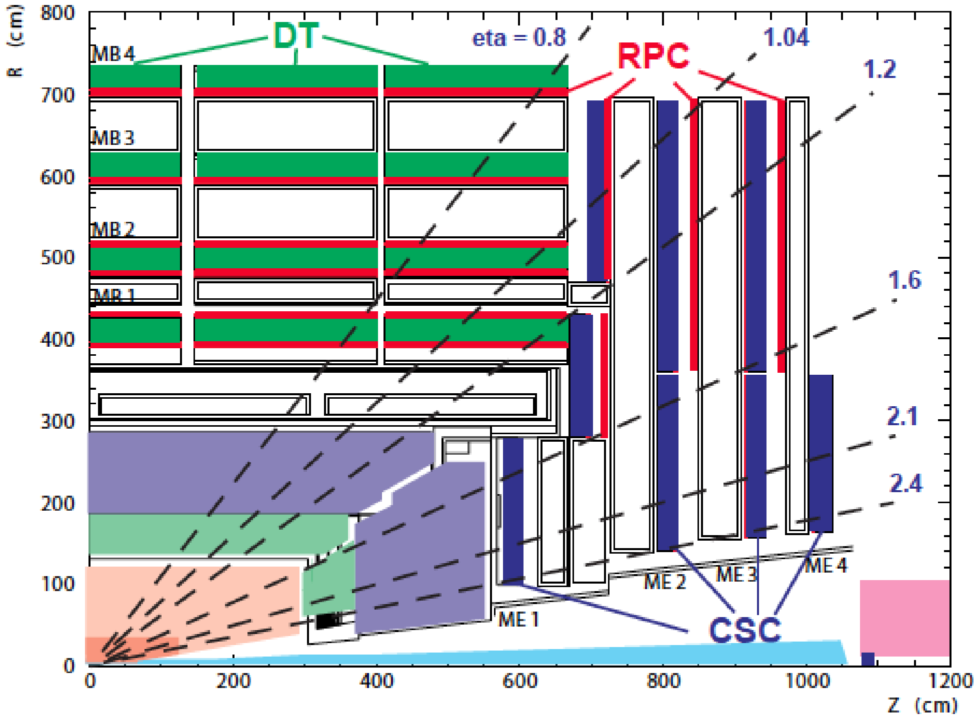

Figure 2.15: Layout of one quarter of the muon system.

A Drift Tube (DT) consists of a cylindrical cathode tubes with a tensioned anode wire in the center. The tube is filled with a gas mixture slightly above atmospheric pressure. An ionizing particle that passes through the tube will ionize surrounding gaseous atoms. As the liberated electrons move toward the anode wire they are accelerated to cause secondary ionizations that produce an electric current signal.

Together with precise timing of the current pulses with respect to the particle passage electrons for the known drift time of the charges in the tube, the distance at which the particle passed the wire can be measured. This requires well controlled pressure, temperature, flow, and purity (crucial for having a stable time-to-distance relationship). The DT system chambers are made of 3 Super-Layers (SL), with each SL consisting of four layers of drift tubes; the two outer SLs ($r-\varphi$ type) measure the track coordinates in the bending plane while the inner SL (z type) measures the track coordinate in the beam direction. Multiple chamber are clustered in stations, for a total of four embedded in the gaps within the flux return yoke. Each of the first three stations (MB1, MB2, MB3) contain eight chambers, in two groups of four, which measure the muon coordinate in the $r-\varphi$ bending plane, and four chambers, which provide a measurement in the z direction. The fourth station (MB4) does not contain any z planes. The two projections are combined to build a three-dimensional segment in the chamber. Figure 2.15 shows the configuration of the four stations in the barrel region. DT chambers in the four different MB stations are staggered so that a high-p_{T} muon produced near a sector boundary crosses at least 3 out of the 4 stations. Additionally, DT chambers are installed alternately to RPCs (one or two, depending on station), hence, a high-p_{T} muon crosses up to six RPCs and four DT chambers, producing up to 44 measured points in the DT system from which a muon-track candidate can be built. The resolution on the segment position varies between 100 μm (for an eight points reconstructed track) to 250 μm (for a single point), while the resolution on the direction is about 0.5 mrad, in the $r-\varphi$ projection.

The Cathode Strip Chamber (CSC) is trapezoidal multi-wire proportional chamber and consists of six gas gaps. Each gap has a plane of radial cathode strips and a plane of anode wires that run almost perpendicularly to the strips. The gas ionization and subsequent electron avalanche caused by a charged particle traversing each plane of a chamber produce charges on the anode wire and image charges on a group of cathode strips; thus, each CSC measures the space coordinates (r, φ, z) in each of the six layers. Closely spaced wires make the CSC a fast detector (response time of

~ 4.5 ns), but the position resolution is rather coarse; a precise position measurement is made by determining the centre-of-gravity of the charge distribution induced on the cathode strips (spatial resolution ~ 200 μm, angular resolution ~ 10 mrad). CSCs can operate in large and non-uniform magnetic fields without significant deterioration in their performance; gas mixture composition, temperature, and pressure do not directly affect the CSC precision. Hence, a stringent control of these variables is not required.

The Resistive Plate Cathodes (RPC) are gaseous parallel-plate detectors that do not use wires: two resistive plates, made of bakelite, are kept parallel to one another by insulating spacers, which define the size of the gas gap. A uniform electric field of a few kV/mm causes an avalanche multiplication of the ionization electrons across the gap. The readout is performed by one set of copper strips placed in the middle of the gaps; the avalanche-mode operation requires a high signal amplification in the front-end electronics to compensate for the low gas amplification. The electrode resistivity mainly determines the rate capability, while the gap width determines the time performance. RPCs guarantee a precise bunch crossing assignment thanks to their fast response and good time resolution. Time resolutions of 3 ns are typical with unambiguous assignment of a muon track to the correct bunch crossing but the space resolution is of the order of 1 cm.

These three detectors operate within the Level-1 (hardware based) trigger system that is described in Section 2.3. The muon detection system is capable of identifying single and multi-muon events with well determined p_{T} in the range of a few GeV/c to TeV/c.

The relative muon momentum resolutions as a function of transverse momentum are illustrated in Figure 2.16. For p_{T} values below 200 GeV/c, where the resolution in the muon chambers is dominated by multiple scattering, the silicon tracker provides the best momentum. At high momenta, where the multiple scattering and energy losses are negligible, the muon trajectory, reconstructed from muon-detectors only, can be extrapolated back to the collision region, thus improving the muon transverse momentum resolution.

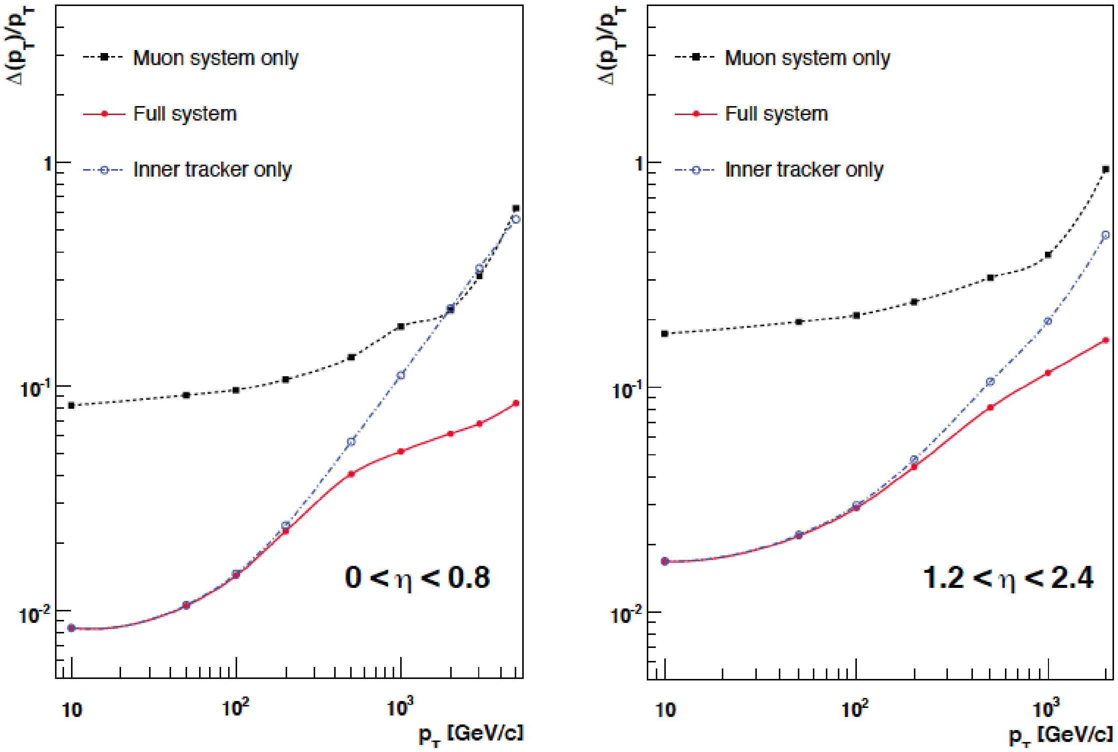

Figure 2.16: Relative muon transverse-momentum resolution as a function of transverse-momentum for measurements with the muon system only, with the inner tracking only, and with both systems in different regions of η: left plot for $|\eta| < 0.8$, while right plot for $1.2 < |\eta| < 2.4$ CMS Collaboration (2006b).

2.3 The CMS Trigger

At full intensity, the LHC will collide proton bunches at a rate of 40 MHz. Even with efficient zero-suppression of uninteresting data channels, it is still unfeasible with present computing technologies to store every single event. The data coming from the CMS detector must therefore be sorted very rapidly into interesting events, to be stored for off-line analysis, and uninteresting events, to be immediately discarded. CMS employs a two-tiered trigger system to make these decisions: a hardware-based Level-1 (L1) trigger CMS Collaboration (2006c) and a software-based High-Level Trigger (HLT) CMS Collaboration (2002b). The L1 trigger is designed to make decisions within 3.2 μs after a collision occurs. It reduces the event rate by a factor of 10^{-3}. Together with the HLT, that reduces the rate by another factor of 10^{-2}, the rate at which events are selected for further storage is 100 Hz.

2.3.1 Level-1 Trigger

The CMS L1 trigger CMS Collaboration (2006c) is entirely hardware-based and it uses only the calorimeters and muon systems in the decisions because information from the central tracking subsystems is too complex to be analyzed on the short time-scales required for L1 decisions. The architecture of the L1 system is shown in Figure 2.17. The L1 trigger is divided into local, regional, and global components. At the local level, the individual sub-detectors use pattern-matching logic to find high-energy deposits in the calorimeter system, or high-momentum charged tracks in the muon system. The highest-quality primitives (defined as muon track segments or electron/photon energy towers) are assigned on the basis of parameters such as energy deposited and reconstructed momentum from the local levels and sent from each subsystem to one of two regional-level triggers: the Regional Calorimeter Trigger (RCT) and the DT and CSC Muon system Track Finders. The first one is an algorithm that combines information from HCAL and ECAL to find electron/photon candidates. For each region where energy deposits are found, the algorithm processes the input

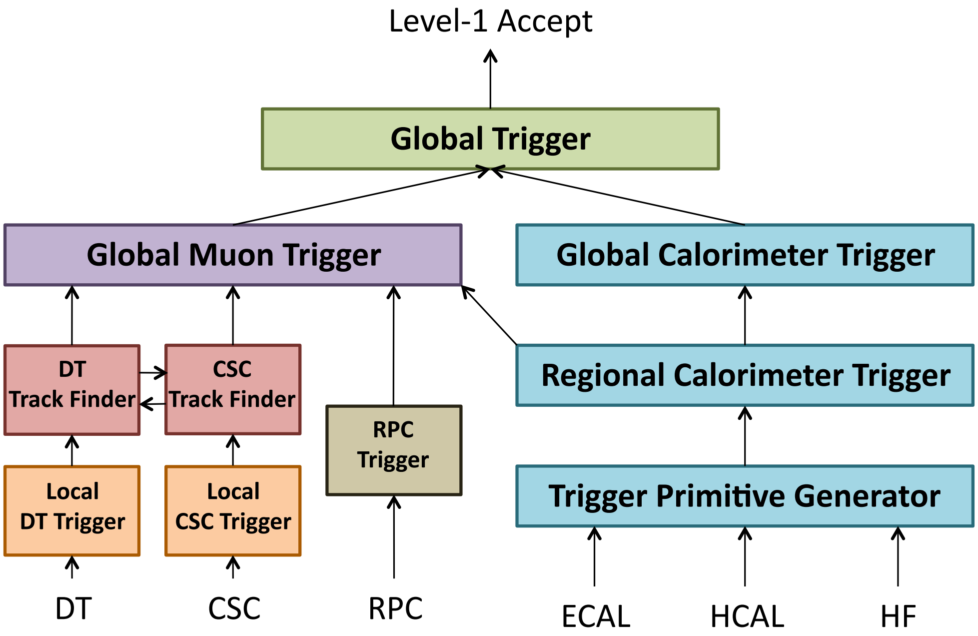

Figure 2.17: Input to the global muon trigger.

and creates two sets of information: the total energy sum for each region, and a pair of the highest-energy electron candidates, where a candidate consists of a local energy deposit with an energy higher than that of its neighboring crystals. The best eight candidates, position, and energy region sums are collected in an intermediate buffer area and then forwarded to the Global Calorimeter Trigger (GCT). The second regional trigger, instead, uses two of the muon sub-systems, the DTs and the CSCs to convert detection information, such as chamber ID, strip patterns etc., into coordinates (r,φ). The reconstruction of a muon track starts with each separate DT chamber generating a φ-projection of a traversing muon and each CSC chamber generating a three-dimensional track segment. The dedicated muon trigger hardware forwards those track segments that match the pattern of a high-momentum muon coming from the interaction point to the muon Track Finders (TF). The DT and CSC Track Finder algorithm combines the segments from the individual chambers and makes an approximate measurement of the transverse momenta of the muons. The best four muons (sorted by transverse momentum) from both, the CSC and

DT Track Finders, are forwarded to the Global Muon Trigger (GMT). The RPCs do not generate primitives, but forward all of their data to a specialized regional trigger system that detects muons based on hits in adjacent RPC chambers. The RPC Pattern Comparator Trigger (PaCT) also uses data from the Hadron Outer (HO) detector to identify muons and measure their transverse momenta in the barrel portion of the CMS detector. The PaCT forwards the four best muon candidates that it identifies to the GMT (sorted by transverse momentum) from the barrel and end-cap regions of the muon system. The GMT receives transverse momentum, charge, r- and φ-coordinates, and quality of the pattern-matching information for every muon candidate from the CSC TF, DT TF, and RPC PaCT systems. The CMS Global Trigger (GT) compiles all the information from GCT and GMT for a trigger decision. A table of selection criteria is encoded in Field-Programmable Gate Arrays (FPGA) which allows fast decision making and fast changes in the algorithms to adapt to changing run conditions. If the collision event is considered interesting by the GT, it sends a Level-1 Accept (L1A) message to the individual sub-detectors to begin the Data Acquisition (DAQ) read-out of the event. The total time between a collision and a L1A decision is required to be less than 3.2 μs.

2.3.2 High-Level Trigger

The CMS High-Level Trigger uses the full detector data to reconstruct the collision event and to make a decision CMS Collaboration (2002b). The event reconstruction software is similar to the full reconstruction suite used for offline analyses, with some simplifications to satisfy time constraints. For the DAQ builder units, CMS employs 720 off-the-shelf PCs, each with eight processing cores. In order to reduce the 100 kHz data event rate of L1As (at LHC maximum instantaneous luminosity) to the $\approx$ 100 Hz rate allowed by the storage hardware, the HLT algorithm has to be applied with a mean time of 50 ms per event. To do this, the HLT focuses only on those areas of the detector where the L1 algorithms identified interesting physics objects, such as individual particles, jets, energy deposits. The HLT is the first stage in which the central tracking data are used. Tracks are reconstructed using the silicon pixel and strip tracker to achieve higher momentum resolution for charged particles. The HLT is configured to trigger events according to a list of algorithms (trigger menu) that correspond to single or combined physics objects. Triggers are split into single object (i.e. single and double leptons, single and double photons, single, double and quadruple jets) and cross-triggers (i.e. mu plus electron or photon or jet). For studies of charmonium ($c\bar{c}$) and bottomomium ($b\bar{b}$) states, such as J/ψ(nS) and Υ(nS), and B hadrons decaying into a J/ψ (with subsequently J/$\psi \rightarrow \mu^+\mu^-$), a dedicated set of unbiased triggers with loose muon selection criteria was provided during the 2010 data taking period. For these triggers (named as `DoubleMu_X`), a total bandwidth of $\sim$ 40 Hz was assigned from the total $\sim$ 100 Hz available. The dominant fraction was allocated for fundamental perturbative QCD measurements involving the b and the c quarks (prompt and non-prompt J/ψ, Υ, and B mesons production cross sections). Once an event is flagged by one of the HLT algorithms, the reconstructed physics objects (formatted into C++ objects) are written along with the raw data to file in ROOT format Antcheva et al. (2009). These files are transferred to global data centers and the events are reconstructed offline in more detail and using newer calibration and alignment information.

2.4 CMS Analysis Software

To aid in processing the enormous amounts of data that the CMS detector produces, a framework of dedicated analysis software packages called CMSSoftware (CMSSW) was developed by the CMS community of physicists and software engineers CMS Collaboration (2005). It is designed around the abstract concept of the event, or a single triggered beam-crossing, and contains all detector digitized hit information (RAW) and reconstructed physics data (candidate kinematic variable) for the particles produced in that beam-crossing. CMSSW uses the ROOT analysis framework to store all the event data as object representations in C++ Antcheva et al. (2009). Software producer modules can build and insert virtually any software object into events that can be represented in a C++ class. Filter modules can analyze and remove those events that do not meet certain criteria from data files, similar to an offline trigger. Analysis modules allow a user to apply custom algorithms deriving more complex information such as angular or invariant mass distributions on the events and produce summary output in a format of the user's choosing. The analysis software also specifies ways to access distributed databases for detector conditions and configurations for every event.

2.4.1 Event Reconstruction

One of the most important functions of the analysis software is to reconstruct representations of candidate physics objects such as electrons, muons, photons, and jets from the raw digitized detector data. Once all the candidate objects in an event, such as momenta and energies, have been reconstructed (RECO objects) they can be distributed separately from the raw detector data to save physical storage space and network transfer times. Many different producer modules are used to generate the different RECO candidate objects, and sometimes multiple producers are used to reconstruct the same candidate objects in different ways. The following sections will focus only on those reconstruction routines that pertain to this analysis: charged tracks and muons.

Track Reconstruction

The track reconstruction can be divided into five logical steps:

- Hit reconstruction
- Seed generation
- Pattern recognition (trajectory building)

- Ambiguity resolution (trajectory cleaning)
- Final track fit (trajectory smoothing)

The digitized raw data from the sub-detectors, together with detector geometry and alignment information that it is retrieved from the conditions database, are used to build three-dimensional Reconstructed Hits (RecHits). At least three RecHits or two RecHits compatible with the beam spot are required to initiate a track search (seed generation). Seeding provides the initial description of the five parameters of the helical trajectory. The recognition of a track is based on the combinatorial Kalman filter method Fruhwirth (1987). A Kalman filter fits a parameterized functional form to data by iterating over the data points and taking advantage of known correlations between data points and measurement resolutions. From the position of the seed, a trajectory is built propagating each seed to the next detector layer taking into account multiple scattering and energy losses and a trajectory candidate is formed for each hit that falls within a certain χ-square range. Several combinations of hits in the vicinity of a projected trajectory are tested. The procedure is repeated for all trajectories that can be independently formed until the outermost layer is reached or until a stopping condition [†] applies. This creates a large number of tracks, many of which share the same hits. If the fraction of shared hits between two trajectories is too large, the ambiguity is resolved by keeping only the highest-quality trajectory. To avoid biases during trajectory building, all valid tracks are refitted with a Kalman filter. Furthermore, a second filter (smoother) is applied starting from the outermost layer toward the beam line searching for hit positions to improve the quality of the trajectory. In this dissertation, the charged tracks are selected with a minimum transverse momentum of $p_{\mathrm{T}} > 0.7$ GeV/c within the acceptance $|\eta| < 2.4$. They are required to have at least five hits in the tracking system (at least one hit in the pixel detector), and a normalized track fit probability χ^2 of less than five ($\chi^2/\mathrm{n}_{\mathrm{d.o.f.}} < 5$).

[†] e.g. to limit the CPU time in the HLT, where only a partial track reconstruction with less than $5-6$ hits is necessary to achieve the required accuracy.

Muon Reconstruction

In collision data, muons are tracks that are reconstructed using the track-building algorithms in both the central tracker and the muon detectors. Reconstruction starts with track segments from the muon chambers which result from local reconstruction. State vectors containing the track position, their momentum and direction are used to seed the muon trajectories for the track reconstruction with the Kalman filter technique. The muon trajectories are, then, extrapolated inward to the outer tracker surface. The track reconstruction in the silicon tracker is performed in a region close to the predicted track position. In a separate step, muon candidates are reconstructed in the silicon detector and then propagated from the innermost layers toward the potential muon system. Information from the ECAL is used to verify the compatibility of a track with the muon hypothesis (minimum ionizing particle). At the outer tracker surface, the two separately reconstructed tracks are matched and the full trajectory is refit with the the standard Kalman filter method. For the analysis presented here triggered muons had to fulfill the following criteria:

- $p_{\mathrm{T}}^{\mu} > 3.3$ and $|\eta_{\mu}| < 1.3$ or
- $p^{\mu} > 2.9$ and $1.3 < |\eta_{\mu}| < 2.2$ or
- $p_{\mathrm{T}}^{\mu} > 0.8$ and $2.2 < |\eta_{\mu}| < 2.4$

This acceptance requirements select muons well within the active volume of the detector. This region is well modeled by the Monte Carlo simulation of collision events.

Chapter 3

The CMS Pixel Detector

3.1 Introduction

The products of the collisions at the LHC are likely to contain several long-lived particles, such as b-hadrons, produced with other particles in jets. In order to allow an efficient identification of these jets, as well as of other objects (c quarks and τ lepton), the tracking must extend as closely as possible towards the primary collision point. Owing the extremely high particle flux at these small distances, pattern recognition requires that the innermost tracking layers are composed of pixel devices delivering true space point information with high resolution. Over the full acceptance of the CMS detector, the silicon pixel tracker provides two or more hits per charged particle track. Once a track has been successfully matched to the hits from the outer tracker layers, the two pixel hits will be crucial to extrapolate this track to the vertex with high precision. To fulfill these requirements a resolution on the position of the decay of a long-lived particle of about 100 μm or better is needed. This resolution depends on three design parameters of the pixel vertex detector:

- the single hit resolution,
- the distances of the layers from the interaction region,

- the material budget.

The position of the pixel layers is constrained by the size of the beam pipes and by the particle flux which results in a hit rate that decreases with the radius squared. The uncertainty of the particle decay position is due to multiple scattering in the beam pipe and detector. The multiple scattering angle depends directly on the distance traversed in the medium (in radiation lengths), while it is inversely proportional to the momentum and velocity of the incident particle Nakamura et al. (2010). This translates into a particle decay position uncertainty that depends on the thickness of the pixel sensors. To achieve the required position precision at the smallest possible radius, the width of the sensor is chosen to corresponds to 0.3% of the silicon radiation length. In this chapter, the principles of the pixel detector are described in Section 3.2. The pixel readout scheme is introduced in Section 3.3 and the online software architecture for data acquisition is introduced in Section 3.4, with emphasis on the Pixel Online Software and the DiagSystem package that monitors the status of the pixel detector and reports errors that occurred during the pixel data transfer to the central data acquisition system.

3.2 Pixel Sensors

When a charged particle passes through silicon it interacts with its constituents via the Coulomb force. The two most important processes taking place are the elastic scattering on nuclei, in which the particle is deflected from its incident direction, and the electromagnetic interaction, in which the particle loses its energy due to the inelastic collisions with the atomic electrons of the material. The excited electrons transit to the conduction band where they behave as free carriers, leaving holes, which are missing electrons, in the valence band. In a silicon sensor with a thickness of 285 μm, a (perpendicularly incident) Minimum Ionizing Particle (MIP) releases an ionization charge of approximately 23 ke^-. In semiconductors the charge transportation mainly occurs as diffusion and drifts. In the absence of electric field, electrons move randomly in all directions. Therefore, the total momentum is lost due to lattice collision in silicon. Typically a voltage of 100 V is applied to the sensor corresponding to a field strength of $E \lesssim 300$ kV/m. A signal is obtained by collecting all the charge carriers with an electrode on one side of the silicon bulk material. The typical mobility of electrons in silicon is $\mu_e = 0.14$ m^2/(Vs) which results in a drift-velocity of $v_D = \mu_e E = 2.1 \times 10^6$ m/s, that is attained very quickly and remains constant over the time of the drift. Hence, the collection time across the sensor thickness (d) is $t_D = d/v_D \approx 0.1$ ns. The total drift force (F) acting on a charged particle in the presence of constant electric (E) and magnetic (B) fields is given by the Lorentz force (see Figure 3.1)

$$\vec{F} = q \cdot \left(\vec{E} + \vec{v} \times \vec{B}\right)$$

where $\vec{v}$ is the velocity of the charge carriers. If the magnetic field is perpendicular to the electric field, the carriers drift at an angle, the so-called Lorentz angle θ_L, which is given as:

$$\tan\theta_L = \mu_e \cdot |\vec{B}|.$$

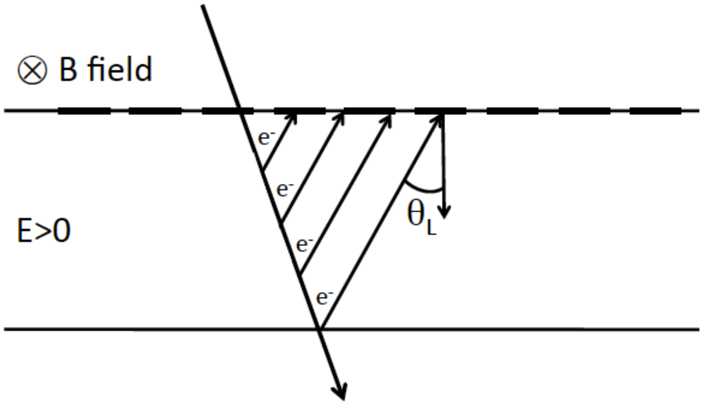

Figure 3.1: Graphic representation of the Lorentz angle (θ_L) for a charged particle traversing active material.

For a 4 Tesla magnetic field the Lorentz angle is $\theta_L \approx 30^\circ$ resulting in a smearing of the position of the electrons on the collection electrodes. The electron mobility is a factor higher than for holes, therefore, it leads to a larger Lorentz angle.

The sensor of the CMS silicon pixel detector is a semiconductor of p-type and n-type joined together ($p - n$ junction). P-type semiconductors are obtained by adding atoms (process of doping) that have a deficit in valence electrons (acceptor) to the silicon; n-type semiconductors are, instead, obtained by adding atoms that provide extra valence electrons (donor) to the host material. Once the contact is established between p- and n-type semiconductors, the excess electrons in the n-side diffuse into the p-side while the excess holes in the p-side diffuse into the n-side. Thus, an excess amount of positive charge is created in the n-side while negative charge in the p-side. While the holes (electrons) are diffusing, some of the negative (positive) acceptor (donor) ions ($N_{A(D)}$) near the p-side (n-side) are left uncompensated since the number of acceptors (donor) are fixed in the semiconductors. Therefore, an electric field is created. Due to this electric field a zone around the junction becomes free of mobile charges (depletion zone). The electric field counteracts the diffusion and prevents further movement of the charge carriers. Diffusion and drift currents are in opposite directions which means the net electron and hole currents will be zero on the borders of the depleted region (equilibrium condition). The width of an intrinsic depletion region is in the order of 10 μm corresponding to a $V_{bi} \approx 0.5$ V. A larger depletion zone is realized by applying a reverse bias voltage V_{bias} across the junction where the $-V_{bias}$ is applied on the p-side, while the $+V_{bias}$ on the n-side, as shown in Figure 3.2. With a field strength of less than 100 V the depletion zone is practically extended over the full detector. Any liberated charge is quickly collected in this strong external field. The width of the depletion zone is inversely proportional to the density of acceptor N_A and donor N_D. Hence, the depletion zone can be extended into one side of the semiconductor if the concentration of doping atoms of the other side of the junction is much larger.

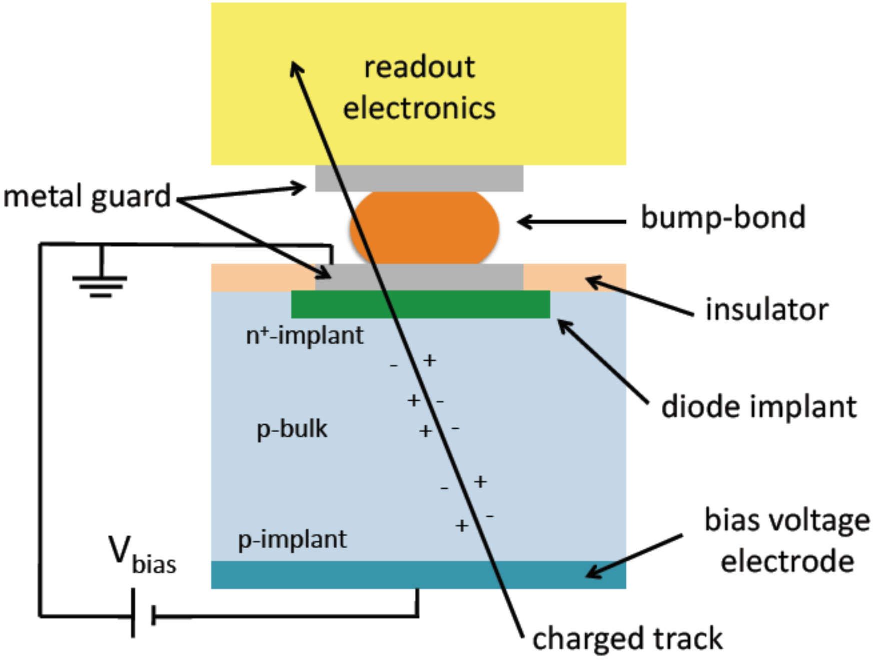

Figure 3.2: Scheme of a single silicon pixel. It is defined electrically by the readout electrode on top that is bump bonded to a readout channel on the readout chip (ROC). The backside is a continuous electrode.

The BPix layers and FPix disks are composed of modules; these consist of segmented rectangular regions (pixels) of size 100 μm × 150 μm with highly integrated readout chips (ROC) connected to them using the bump bonding technique (see Figure 3.2). The pixel of the detector is designed as a high concentration n-implant (n^+) emerged in a high resistive n-substrate that is the active volume. The $p - n$ junction is realized by a high concentration p-implant at the back in contact with the n-substrate, as shown in Figure 3.3. The bulk material inverts its type from n to p when irradiated at LHC, mostly by pions from collisions (beam-beam interactions). The necessary dose of order 10^{12} $n_{eq}\text{cm}^{-2}$ was delivered within days during the startup of LHC. Exposure to the high particle flux has the adverse effect that it

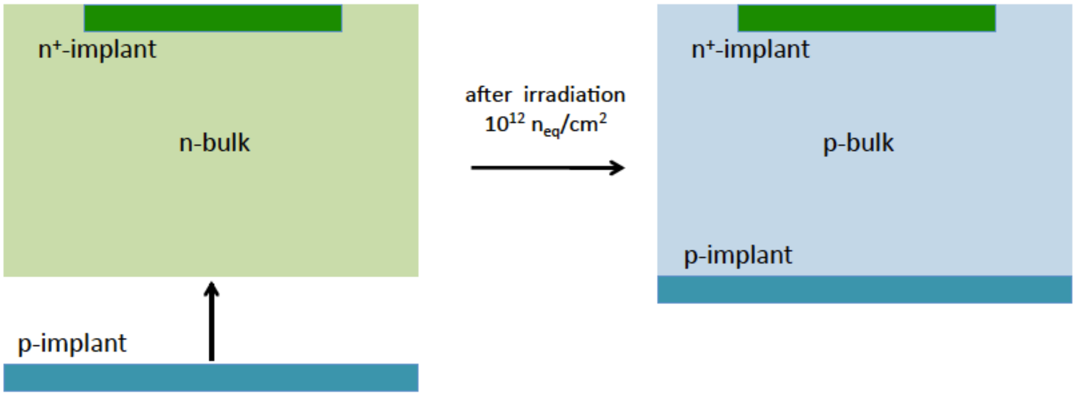

Figure 3.3: $P - n$ junction configuration before (left) and after (right) the irradiation which results in the type-inversion of the active volume.

- changes the effective carrier concentration requiring higher bias voltages to achieve depletion over the full detector depth,
- increases the leakage current,
- reduces the charge collection as free charge carriers get trapped hence near displaced atoms.

Furthermore, noise is introduced by the random release of trapped charges. Initially the pixel detector operates at a voltage of 150 V. After irradiation with a fluence of about 10^{15} $n_{eq}\text{cm}^{-2}$ higher bias voltages of up to 600 V will be needed to compensate for the irradiation damage in the sensor. Finally, after three years operating at the LHC design conditions the innermost layer of the detector needs to be replaced. The small gap between the collecting electrodes (i.e. the n-implant) ensures a homogeneous drift field. The rectifying $p - n$ junction is placed on the back of the sensor and is surrounded by a multi guard ring structure that allows all sensor edges to be kept to a ground potential (see Figure 3.2). To perform an on-wafer measurement of the current-voltage characteristics, each pixel is connected to a bias grid through a high resistance punch through connection (bias dot).

The pixel detector is arranged in three cylindrical (barrel) layers (BPix) of pixel detector modules at radii of 4.4, 7.3 and 10.2 cm, as illustrated in green in Figure 3.4 CMS Collaboration (2006a). The forward pixel (FPix) detector consists, instead, of two disks placed on each side at $z = \pm 34.5$ and $z = \pm 46.5$ cm. The disks have inner and outer radii of approximately 6 cm and 15 cm and are subdivided in 24 trapezoidal blades, as shown in orange in Figure 3.4.

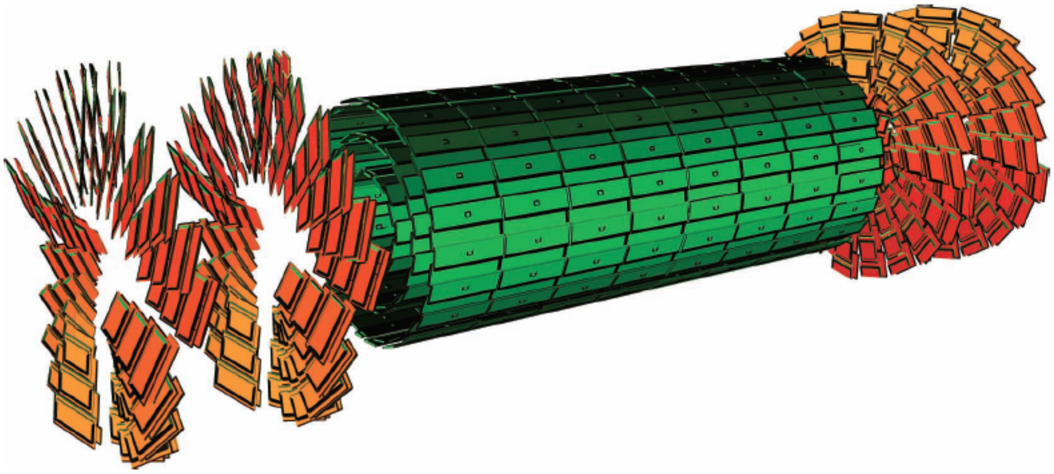

Figure 3.4: Sketch of the CMS forward and barrel pixel detectors. The barrel pixel detector consists of three central layers whereas the forward pixel detector consists of two disks on each side.

When a particle traverses one pixel (hit), the charges liberated below such a pixel are well contained and drifted toward the collection electrode. The amount of collected charge is proportional to the path length of the particle within the pixel.

The average hit position is estimated from the charge-weighted average of the pixel location

$$\bar{x} = \frac{\sum_i Q_i x_i}{Q} \tag{3.1}$$

where $Q = \sum_i Q_i$ is the total charge collected. Interpolating positions between pixels, based on the amount of the collected charge, requires pulse-height information. Without charge sharing the position cannot be resolved within the pixel boundaries to better than the pixel length/$\sqrt{12}$, which corresponds to a resolution of about 40 μm. With charge sharing, an intrinsic hit resolutions of $10 - 15$ μm can be obtained.

For the reconstruction of the hit position the shift due to the Lorentz-angle has to be corrected. Hence, it needs to be known to a high precision. The grazing angle method Henrich et al. (2002) is shown in Figure 3.5. It is based on well reconstructed tracks with shallow impact angle with respect to the direction parallel to the magnetic field. Ionizing particles, traversing the detector, generate signals which can be seen on a chain of successive pixels. Each pixel in the chain collects charge from a given segment of the traversing particles trajectory. The signal ends at the pixel row under which the particle leaves the detector. Due to the Lorentz force, the drifting charge carriers reach the surface with a displacement proportional to their drift-length. Therefore, it is expected that pixels near the end of the chain will loose some charge to the adjacent pixel rows. According to Figure 3.5, one can measure the Lorentz-angle as

$$\tan\theta_L = \frac{\tan\beta}{\tan\alpha} \tag{3.2}$$

where α is the grazing angle and β is the angle of the charge deflection measured at the surface.

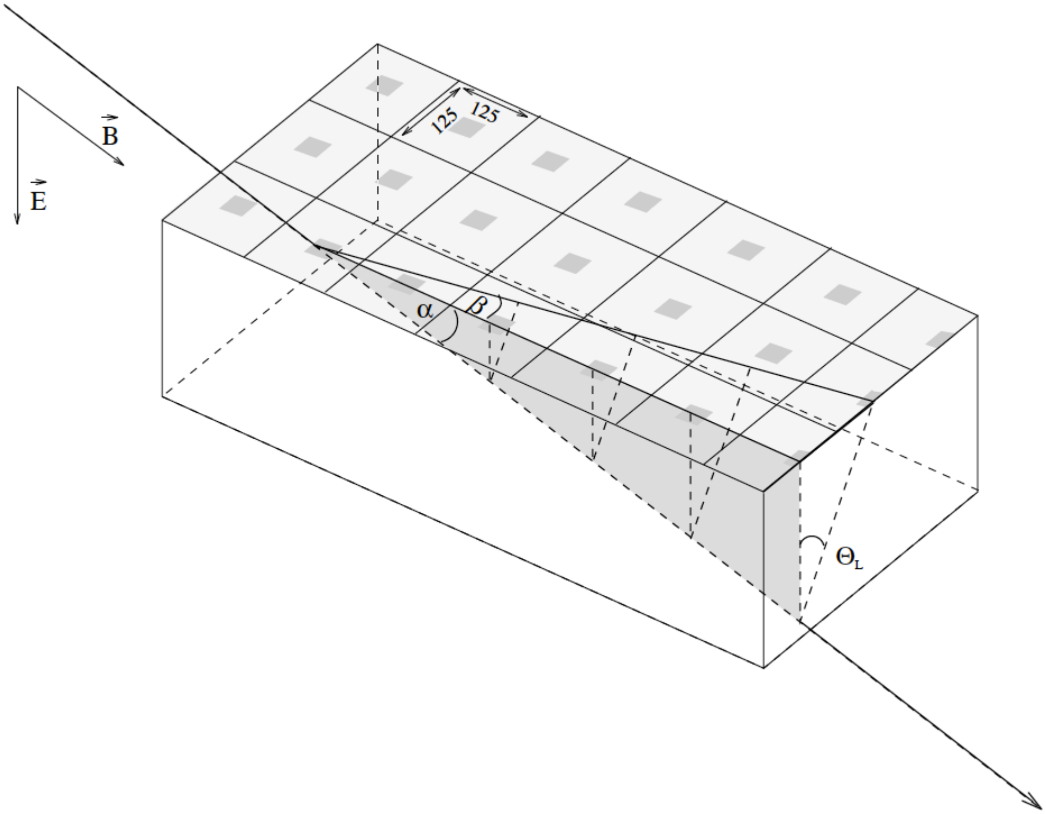

Figure 3.5: Measurement of the Lorentz angle θ_L with the grazing angle method.

For the characterization of the barrel pixel detector with the magnetic field of 3.8 T, the Lorentz angle has been measured in collision data (at the energy in the center-of-mass of 3.5 GeV) to be $21.72^\circ \pm 0.01^\circ$ Ivova (2011).

Other corrections to charge smearing effects can be evaluated with the so-called η distribution Belau et al. (1983). It is measured to find the spatial distribution of the electrons collected by the electrodes. If the charge Q is deposited in two adjacent pixel left (L) and right (R), the fraction of charge deposited in the right pixel is

$$\eta = \frac{Q(R)}{Q(R) + Q(L)}. \tag{3.3}$$

For a given passing particle the average impact point between the two pixels and its resolution can be obtained by integrating the η distribution up to the measured η. This method is limited by statistical fluctuations, mainly due to due to electronics noise and electrons from secondary ionization.

The pixel shape of the CMS pixel detector results in comparable resolution in both directions. In the direction parallel to the magnetic field (z-direction), there is no Lorentz drift but sufficiently inclined tracks are detected in more than one pixel, allowing interpolation in both directions. At high rapidity, where tracks hit the barrel detector at low angles, the small z-size is a disadvantage because increasing cluster size in the z-direction is only beneficial for the z-resolution until it exceeds two pixels. Higher multiplicities also overload the readout system. Therefore, the choice was made to complement the barrel detector with pixel disks in forward and backward directions. Sufficient charge sharing in the FPix is achieved with a tilt angle of 20° between the blades. The Lorentz angle measured in the forward pixel detector is smaller and found to be $4.40^\circ \pm 0.55^\circ$ Ivova (2011) in the 2010 cosmic rays data.

3.3 Pixel Readout System

The pixel barrel (BPix) layers and the forward/backward (FPix) disks are composed of modules (half-modules) that contain the readout electronics and the power supply. A module (half-module) consists of:

- 16 (8) ReadOut Chip (ROC): it performs the signal readout,
- Token Bit Manager (TBM): it controls the read-out of several ROCs,
- High Density Interconnect (HDI): it is a circuit board that distributes the control and power signals to the readout chips and the TBM,
- Base stripes: they are used for mechanical stability and as a contact between the module and the cooling structure,
- Kapton cable: it transfers the control and analog signals,
- Power cable: it supplies the analog, digital, and bias voltages.

Figure 3.6 illustrates the components of a module as they are assembled. The modules are attached to cooling frames, with the cooling tubes being an integral part of the mechanical structure. The analog charge signal is readout and digitized at a higher level with a Flash ADC. A schematic view of the pixel readout is shown in Figure 3.7. The ionization charge of a CMS pixel sensor is read out by a corresponding channelled Pixel Unit Cell (PUC). It is connected electrically via a bump bond. In a ROC, there are 26 double columns and 80 rows in the active area to read out 4160 pixels in total. The ROC chip periphery contains:

- a serial programming interface to configure the pixels,
- digital-to-analog converters (DAC) to adjust offsets, gains, thresholds, supply voltages, timings, etc.,
- control registers to set the trigger latency and readout speed,

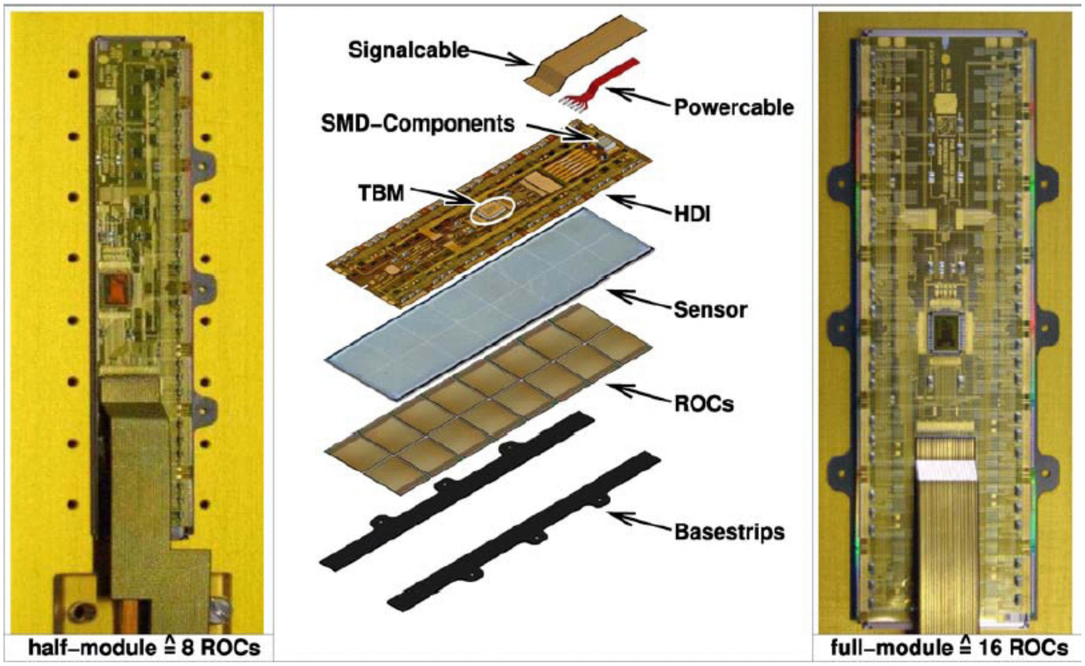

Figure 3.6: View of a half-module (left) and a full module (right) fully assembled. Middle: Exploded view of a barrel pixel module showing the two silicon nitride base strips, the 16 readout chips (ROCs), the pixel silicon sensors, the High Density Interconnect (HDI) with the Token Bit Manager (TBM) and the power and Kapton cables.

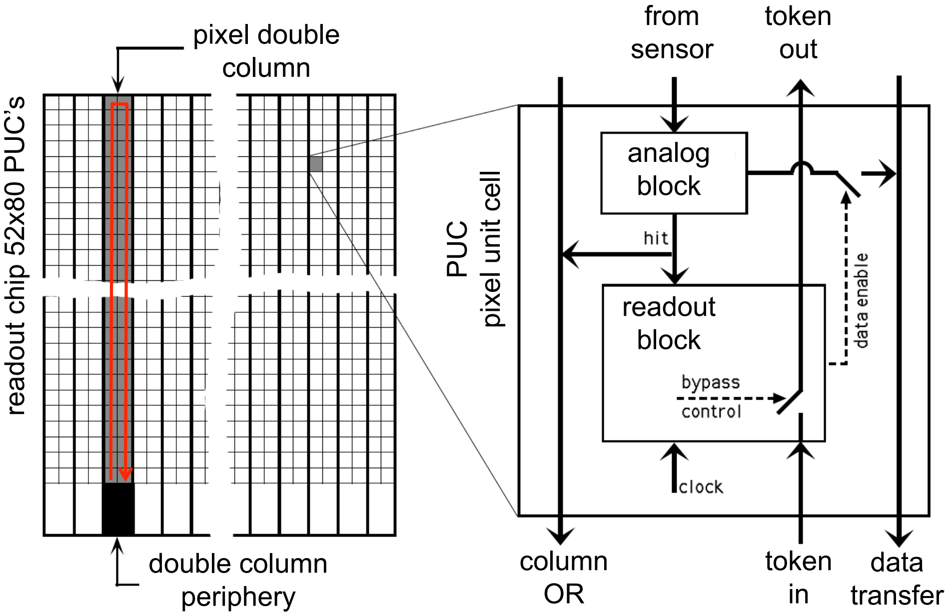

Figure 3.7: A schematic view of the readout chip.

- an analog event generator that collects the pixel hit information from the double columns and generates the output data stream,
- a fast double-column hit counter that can be used in principle by the CMS first level trigger or for self-triggering when no external trigger is available.

A sketch of the PUC is shown in Figure 3.7 on the right. It can be divided into an analog part and the digital logic. The charge produced by an ionizing particle traversing the silicon sensor is collected at the electrode formed by the n-implant and by a capacitor. The charge signal enters a two stage charge sensitive pre-amplifier/shaper system. Alternatively, calibration signals can be injected through an injection capacitor connected directly to the amplifier input node. This feature is used to study pixel efficiencies. A global threshold can be programmed for the whole chip using the DAC. Pixel cells within one double column are connected to its periphery with a set of local bus lines, one of them being the column-OR, which combines all pixel cells in a double column into a global OR. Only signals that are above the threshold are allowed to trigger the digital part of the circuit. Once the comparator is above threshold (zero suppression) the shaper output signal is stored in a memory buffer and the double column periphery is notified immediately through a fast hard-wired column OR. The pixel becomes insensitive and waits for a column readout token. Its dead-time ($\geq$ 50 ns) is short. The double column periphery controls the transfer of hit information from the pixels to the storage buffers (column drain mechanism) and performs trigger verification. The column drain cycle takes place within each double-column and runs at 40 MHz. The readout starts with the pixel closest to the periphery on the left side of a double-column and returns along the right side (see Figure 3.7). The time information is stored (within 25 ns) in the time-stamp buffer and the address and the analogue signal of each pixel hit is transferred to the column data buffer located in the column periphery. For the average of two pixel hits per double column, about six clock cycles (at 40 MHz) are required to complete the readout. This data has to be stored for 3.2 μs while waiting for the Level-1 (L1) trigger decision. For every clock the bunch crossing counter (BC) stored in the time stamp buffer is compared with the search counter (WBC). If both agree the time stamp is considered for trigger confirmation. The data confirmed by the L1 are saved for the second stage of the readout while the unconfirmed data are erased. In the second readout stage the triggered data are transmitted to the CMS data acquisition (DAQ). They are drained from each double-column and are sent via optical links to the readout electronics (Front End Driver modules - FEDs) in a room 100 m away from the detector. Groups of 8 or 16 ROCs are connected to one readout link. In order to synchronize the data transmission a token-bit manager chip (TBM) is used. The TBM controls the readout of the ROCs by initiating a token pass for each incoming L1 trigger. On each token pass, it writes a header and a trailer word to the data stream to facilitate event recognition. The header contains an 8-bit event number and the trailer contains 8-bits of error status. The token bit is passed on from ROC to ROC and finally back to the TBM where the trailer is generated and the TBM becomes ready to accept another trigger. A schematic view of the pixel readout and the token bit mechanism is shown in Figure 3.8.

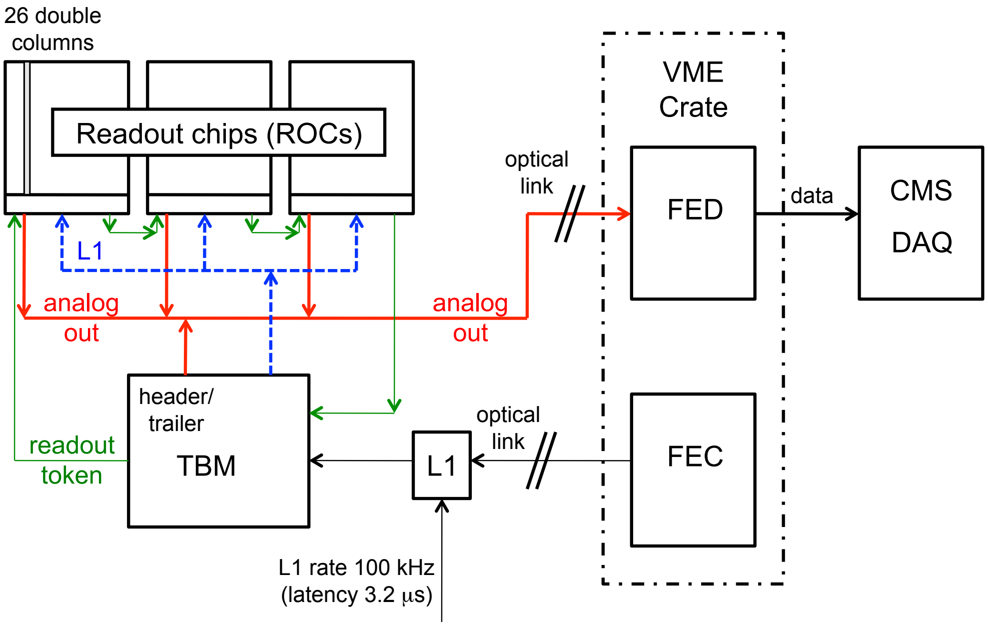

Figure 3.8: A schematic view of the pixel readout system.

The FED modules, located in the counting room, receive data packets, perform digitization, format events and send them to the CMS DAQ: a single FED can buffer up to 100 events. The Front-End Control modules (FECs), also located in the counting room, send the clock, trigger and all other control and reset signals to the detector. The ROC chip programming (e.g. setting of the pixel thresholds) is also performed with the FECs. The FED and FEC modules which service the same segment of the detector are located in the same VME crate. This way both can communicate with the same crate controller CPU allowing for efficient system monitoring and fast resets in case of error conditions. Each crate controller communicates with a monitoring workstation where more global data diagnostics is performed. Other standard components of the pixel readout system are:

- Trigger Timing and Control (TTC): sends the L1 accept signal to the FED and FEC, distributes the 40 MHz clock, and manages various synchronization and calibration commands,

- Local Trigger Control (LTC): is used in combination with the TTC manages the local trigger control,

- Tracker FEC (TKFEC): communicates with the Communication and Control Unit (CCU) which performs slow controls of the pixel readout chips, such as configuring them for data acquisition, calibration, or standby mode, setting thresholds etc.

The average amount of data from the pixel detector for one complete event during the 2010 run was 50 kB.

3.3.1 Detector Commissioning

Tests on modules are necessary to verify that all pixels function correctly, each ROC can be programmed properly, and all modules are calibrated satisfactorily. A list of configuration and calibrations have been performed before the 2010 data taking campaign:

- noise measurements: the noise of a pixel is determined by measuring the efficiency of the pixel as a function of the amplitude of the calibration signal. Noisy pixels may flood the ROC with a high rate of fake hits and cause significant dead time and data losses. Therefore, either the threshold of these pixels has to be increased or the pixels have to be removed from the data taking (masked),

- trimming: the aim of the trim calibration is to unify the thresholds of all pixels on a ROC to the lowest possible value. A common threshold (V_{pix}) for all pixels is set in the ROC. To account for the pixel to pixel variations, four-bits trim values (v_{trim}) are set in each PUC. The strength of the correction is determined by the trim voltage (V_{trim}) which is set per ROC. It is set with respect to the absolute threshold ($V_{threshold}$) at which the response has to be unified. The relation existing is approximately:

$$V_{pix} = V_{threshold} + v_{trim} * V_{trim},$$

- pulse height calibration: this calibration is performed by injecting signals with various amplitudes to each pixel via the PUC calibration capacitor and measuring the corresponding pulse heights. For each pixel, the height of the generated pulse is recorded and an extensive offline analysis performed,

- other calibrations: they involve the testing of the module response to the charge injected to the silicon sensor and the calibration of the internal signal of each ROC.

The turn-around time for calibrating all 66M pixels is about one month. The studies yield pixel response efficiencies of 98.8% and 96.4% (overall 98.2%) for BPix and FPix, respectively.

3.4 Online Data Acquisition Software (DAQ) Architecture

The online software CMS Collaboration (2002a) is a composition of all the software tools and services needed for the transportation and processing of data, as well as for the configuration, control, and monitoring of all devices in the data acquisition system. The design and implementation of the online software is unified for all subsystems. In accordance with this homogenous approach, all components participate in the data acquisition process through a uniform communication backbone with a common format of exchanged data. The main parts of the online software scheme, connected by a distributed processing environment, are shown in Figure 3.9 and described in more details in the following sections.

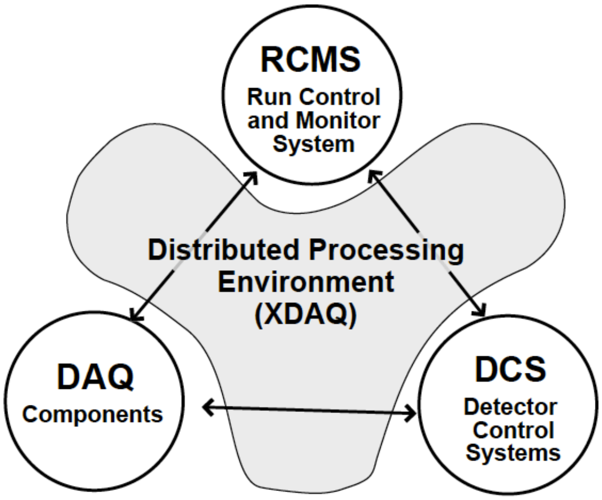

Figure 3.9: Overall online software architecture. Circles represent sub-systems that are connected via XDAQ.

3.4.1 Run Control and Monitor System

The Run Control and Monitor System (RCMS) is the collection of hardware and software components that centrally manages the CMS experiment during data taking. The three main functions of the RCMS are:

- control and monitoring, with the support of the Detector Control System (DCS), to ensure the correct and proper operation of the CMS experiment,
- control and monitoring of the Data Acquisition Components (DAC),
- provide user interfaces to access the system from anywhere in the world with the internet.

The RCMS communicates with the DCS, DAC, and the trigger subsystem, through the services provided by the distributed processing environment (Cross-Platform DAQ Framework - XDAQ). For configuration, user administration and logging, the RCMS makes use of a database management system. The RCMS views the experiment as a set of partitions when performing its main functions. A partition is the smallest grouping of DAQ components of sub-detectors that can be configured and operated independently. The RCMS can perform configuration, monitoring, error handling, logging, and synchronization with partitioned sub-systems.

3.4.2 Detector Control System

The Detector Control System (DCS) is responsible for maintaining and monitoring the operational state of the experiment. Its main goals are:

- to control, configure, readout, and monitor the hardware devices of the CMS experiment,
- to communicate with the experimental hall, as well as, with the accelerator,
- to monitor the external systems, such as the electrical and the cooling systems,

- to protect the experiment from any adverse events, such as the overheating, loss of pressure in the gas and fluid sub-systems.

During data-taking the DCS operates under the supervision of the RCMS. An user interface is provided to access all DCS functionality for autonomous detector control and maintenance. All information needed to sustain the environmental conditions and their history are stored persistently within a database. These data are provided on demand to the RCMS and to the DACs, and are available for investigations.

3.4.3 Data Acquisition Components

They are a collection of application with three functions:

- assembling event data fragments from different sub-detector readout computers and assemble complete physics events (EventBuilder),
- configuring, controlling, and monitoring the readout during global running,
- providing procedures that configure, calibrate, and synchronize the readout system.

These applications follow an hierarchy in the transmission of the information to the RCMS services, which centrally control the data acquisition. The University of Tennessee worked on the Pixel Online Software (POS) the online software architecture for managing the CMS pixel detector. I introduced a flexible error diagnostic system (see Section 3.5) that continuously monitors the integrity of the data sent to the following reconstruction stages and provides fast feedback in case of data corruption.

3.4.4 Cross-Platform Framework

XDAQ is a framework specifically designed for the development of distributed data acquisition systems CMS Collaboration (2002a). It provides the following basic system services:

- memory management,
- hardware access,
- peer-to-peer communication services,
- event logging,
- web browser-based interfaces,
- database access,
- configuration, control, and monitoring tools.

Applications for the sub-systems are built on these service libraries. The distributed programming environment follows a layered middleware approach, designed object-oriented, and implemented using the C++ programming language. The middleware services include:

- information dispatching to applications,
- data transmission,
- exception handling facilities,
- access to configuration parameters,
- synchronization in the communication, task execution, and memory management.

These are in common for the core and the application interfaces. This middleware configuration makes the distributed processing infrastructure scalable. In fact, applications can be partitioned in smaller functional units that can be distributed over multiple processing units. They communicate with each other through a peer-to-peer message passing model. The content of the messages comprises commands, status reports, and execution flags. Therefore, each application acts both as a client and a server. Messages are formatted and sent asynchronously. They trigger the activation of callback procedures when they arrive at the receiver side. The framework supports two data formats, one based on the `I2O` specification I_2O Special Interest Group (1999) and the other one based on `XML` Boyer (2001). `I2O` messages are primarily intended for the efficient exchange of binary information, e.g. data acquisition flow. They have a limited size and their content is platform-dependent. Despite its efficiency, the `I2O` scheme is not universal and lacks flexibility. A second type of communication, then, has been chosen for tasks that require higher flexibility such as configuration, control and monitoring. This message-passing protocol, called Simple Object Access Protocol (`SOAP`) relies on the standard Web protocol (`HTTP`) and encapsulates data using the eXtensible Markup Language (`XML`). The adoption of `SOAP` allows to use web services that standardize the way in which applications export their interfaces to clients. `XML`-formatted data have the following advantages:

- it is very portable,
- it uses grammar and named elements that allow detection of malformed messages,
- it avoids large quantities of data to be sent across the network at once,
- it can be read from disk or remote web sites.

3.5 Pixel Online Software

Amongst the online DAQ components, the Pixel Online Software (POS) Das (2009) provides the software interface for controlling and calibrating the pixel detector. This includes:

- a graphic user interface (`GUI`),
- suit to analyze calibration data in the online farm,

- monitor the status of the detector during data taking,
- communication with the DCS to control the systems of cooling and power supply.

The POS is based on the XDAQ toolkit and is built from a number of different applications called supervisors. A supervisor is the software complement to a front-end readout driver (FED) or controller (FEC). They communicate via the VME crate controllers, with electronic boards in crates in the counting room, which in turn program or receive readout from the front-end electronics on the pixel detector. One crate of electronic boards is controlled by one PC with one XDAQ application and they are named after the electronic component they supervise, i.e. PixelFECSupervisor for the FECs, PixelFEDSupervisor for the FEDs and so on. The supervisors are integrated in a prototype framework, HyperDAQ, that comprises a set of technologies that give users the access to distributed data acquisition systems CMS Collaboration (2002a) J. et al. (2003). HyperDAQ includes

- a HTTP protocol engine, implemented as a peer-transport for the XDAQ system,
- Uniform Resource Name (URN)- and Universal Resource Locator (URL)-based identification of applications,
- a dispatcher for incoming requests, invoked when the HTTP engine recognizes a request for information from an XDAQ application,
- an API to implement dynamically web pages,
- data serialization methods for binary and XML formats, i.e. `SOAP` messages,
- a peer-to-peer mechanism of acknowledgment that simplifies the interaction between applications.

Any XDAQ application component is accessible through the web protocol. All the supervisor applications are coordinated by the PixelSupervisor, that is executed on a central PC. The communication between supervisors occurs via `SOAP` messages. Figure 3.10 shows the implementation scheme for the POS. At the top of the hierarchy within the pixel detector, the PixelSupervisor is connected to the CMS Run Control (RCMS) and DCS systems via two specific applications. The communication between the central Run Control and the pixel detector is mediated by the Pixel Function Manager (FM) CMS Collaboration (2002a), a Java application that receives requests from the RCMS and transforms them into commands that are sent to the sub-system as `SOAP` messages. The Pixel FM incorporates a Finite State Machine (FSM) that can transition between the states start, stop, pause, and resume. It works as a standalone application (for local operations) or in synchronization with all the other sub-detectors Function Managers (for global operations). The status of the detector, i.e. high and low voltages, temperatures, pressure of the fluid in the cooling system, is provided to the DCS Supervisor by the PixelSupervisor via the `I2O` protocol. The DCS is a slave of the RCMS which is in charge of the overall control and monitoring of the data-taking

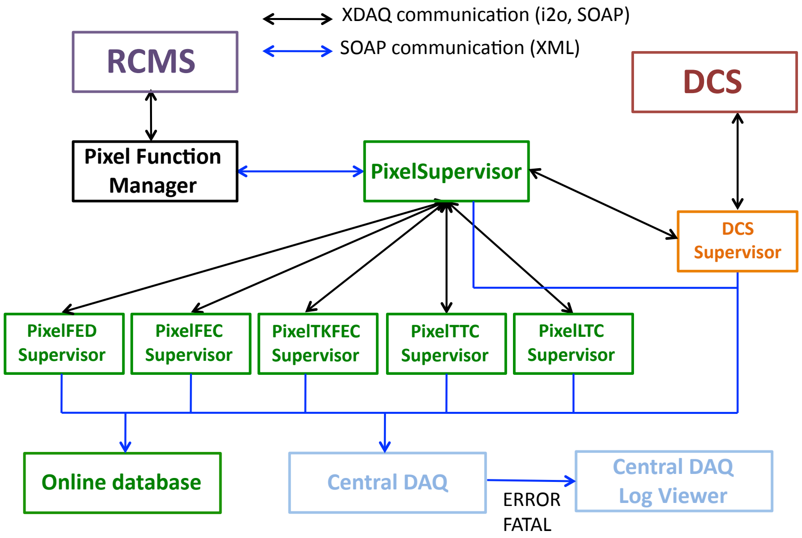

Figure 3.10: Scheme of the pixel online software architecture. The pixel XDAQ applications implemented are shown in green. The color-code arrows indicate the different communication protocols used among the different modules.

process. When the DCS operates outside data-taking periods it acts as the master of the individual detector electronics. The PixelSupervisor provides a graphic user interface to access the detector components for calibration, to retrieve and load the condition database, and to monitor the status parameters, such as the temperature of the components and cooling fluid pressure, in which the pixel detector operates. Requests of configuration or calibrations from the PixelSupervisor to the hardware components occurs in two steps. First, the PixelSupervisor sends a message via `SOAP` to the supervisor that control the part of detector; then, the supervisor acknowledges the request and transmits it to the hardware via `I2O` protocol.

The PixelSupervisor, by controlling a large number of resources both at the hardware and software level, can be affected by failures. These can be categorized in hardware-related, i.e. data format corruption, and software-related, i.e. wrong address saved in the decoding stage or an action request not received by the supervisor. Initialization and configuration have to tolerate these failures at different levels of severity, if they are related to non-critical components. The synchronization of state changes and transmission of state feedback to the RCMS also requires an efficient control mechanism to fulfill timing requirements (avoid time-outs or non-responsive communication between components). Faults can significantly change run conditions, and, therefore, their occurrence together with the state transitions and time stamp information must be recorded. However, a combination of non-critical faults can generate a critical system fault (error), that can interrupt permanently the data-taking and raise alarms. To monitor these failures, each supervisor requires a logging mechanism. Logging is the process of tracking changes in the execution of a program. This task facilitates the detection and recovery of errors and helps gathering information about the program progress. Information stored for logging purposes must allow the user to unambiguously identify the event content and its occurrence. The following information must be recorded to satisfy these requirements:

- Who: identifies the routine that sources the information,

- When: provides a time stamp about the creation of the event,
- What: tells the user what routines were executed.

The logging package `log4cplus`, as part of the XDAQ framework, provides those functions. Error conditions are algorithmically identified and implemented in the source code of the supervisors as C++ exceptions and reported to the central DAQ via `SOAP` protocol. The high flow of messages issued by many supervisors at once required the development of a diagnostic system that reflected the complex communication structure and provides immediate diagnostic information to the personnel that monitors detector operations (shift takers). The DiagSystem (DS) package, originally developed by Laurent Gross for the silicon tracker detector Gross (2007), provides a new supervisor intercommunication with specific tools for an intuitive and in real-time monitoring. The logging has been adopted and tuned for the full pixel detector in this dissertation. The implementation of the DiagSystem is shown in Figure 3.11. The DS has been developed within the XDAQ framework and it fully integrates with all components of the pixel DAQ software. The central component is the Global Error

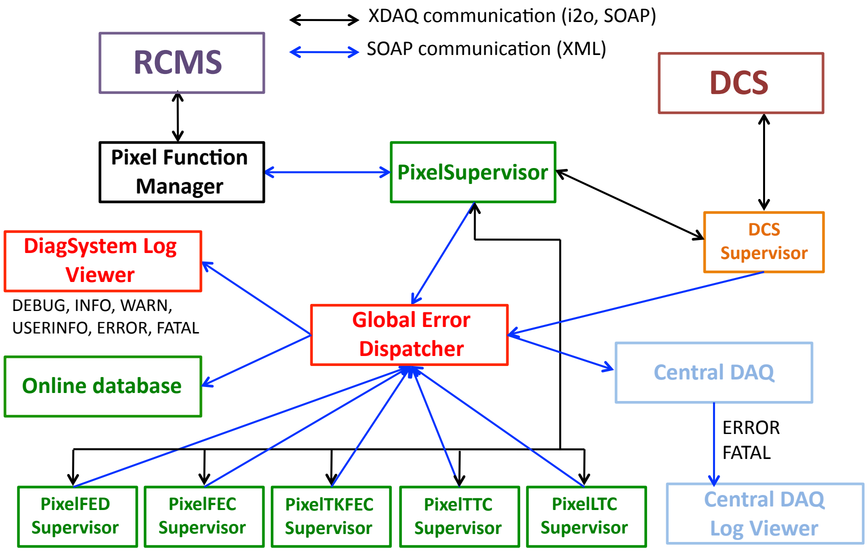

Figure 3.11: Implementation scheme of the DiagSystem package within the POS architecture.

Dispatcher (GED), which collects and processes messages from XDAQ applications. It is structured analogously to the supervisors, providing information accessible via web pages. The GED wraps the `log4cplus` logging calls and redirects the `SOAP` error messages. It retains the formatted messages into a local data buffer for an immediate web visualization and copies them in XML files. These log files are stored in a dedicated pixel errors database and sent to two specialized log viewers, overview screens that display error messages to the shift takers. The use of XML files increases the robustness of the system and reduces the risk of losing logging information. The HyperDAQ Log Reader provides a graphic user interface that displays a managed list of messages that were received by the GED. Each message is identified by a time stamp, a severity level, and a content (printout) message. The severity levels are:

- `TRACE`: the less critical level for a message between developers; this is mostly information about the execution flow of the program (hidden by default),
- `DEBUG`: it is for code debugging; information is introduced by developers to diagnose algorithms (hidden by default),
- `INFO`: it is used to report configuration and calibration status and parameter updates (hidden by default),
- `WARN`: it notifies that something is not behaving as expected during data taking and it could escalate in severity when encountered more often,
- `USERINFO`: it notifies the change of state of a component of the detector during configuration, calibration, and powering,
- `ERROR`: it reports a situation that leads to faulty or interrupted data taking; this level is, also, reported to the central DAQ,
- `FATAL`: it reports conditions that lead to a crash of the readout hardware components and unrecoverable data corruption.

The severity is indicated in the `GUI` by color code: white for `INFO`, yellow for `WARN`, green for `USERINFO`, and red for `ERROR`. The full description of the source (host URL, port, name of the process that emits the message), an user-supplied description of the issue, and the detector component that sent it, are also displayed. The Log Reader has been developed with Asynchronous JavaScript and XML (AJAX) J. (2005) methods and runs as applet in a standard web browser (such as Firefox Ross et al. (2004)). To minimize the dead time between receiving and displaying a message, the LogReader runs on the same machine as the GED. It also can be used to display in the same way previously saved log files for a post-mortem analysis of the pixel detector. Figure 3.12 shows a screenshot of an active Log Reader window as seen in the CMS control room during data taking in 2011. The applet page splits into two areas: on the left side is an expandable list of all the active XDAQ processes connected to the GED, and on the right side is the control panel. All running processes are identified and listed by machine, domain, and port. The control panel has an active and a passive area. The active area manages the applet interface, while the passive area displays the messages in a table. In the active area, the following parameters can be set

- Connection parameters: used to connect to the LogReader process that does not runs on the same HTTP server than the one hosting the applet,
- Update rate: poll delay between two checks for availability of new logs. The poll rate must be entered in milliseconds and by default it is set to 500 ms,
- Display log severity: it displays or hides the logs in the local buffer according to the severity level; the lowest level to be displayed is `WARN`,
- Set LogTable columns properties: it displays or hides columns in the log table,
- Number of lines to display: it sets the size in lines (one line = one log message) of the local log storage buffer. By default it is set to 250.

The configuration of all the DiagSystem tools is based on text files. The main configuration parameters are the host URL and the port of the destination of the

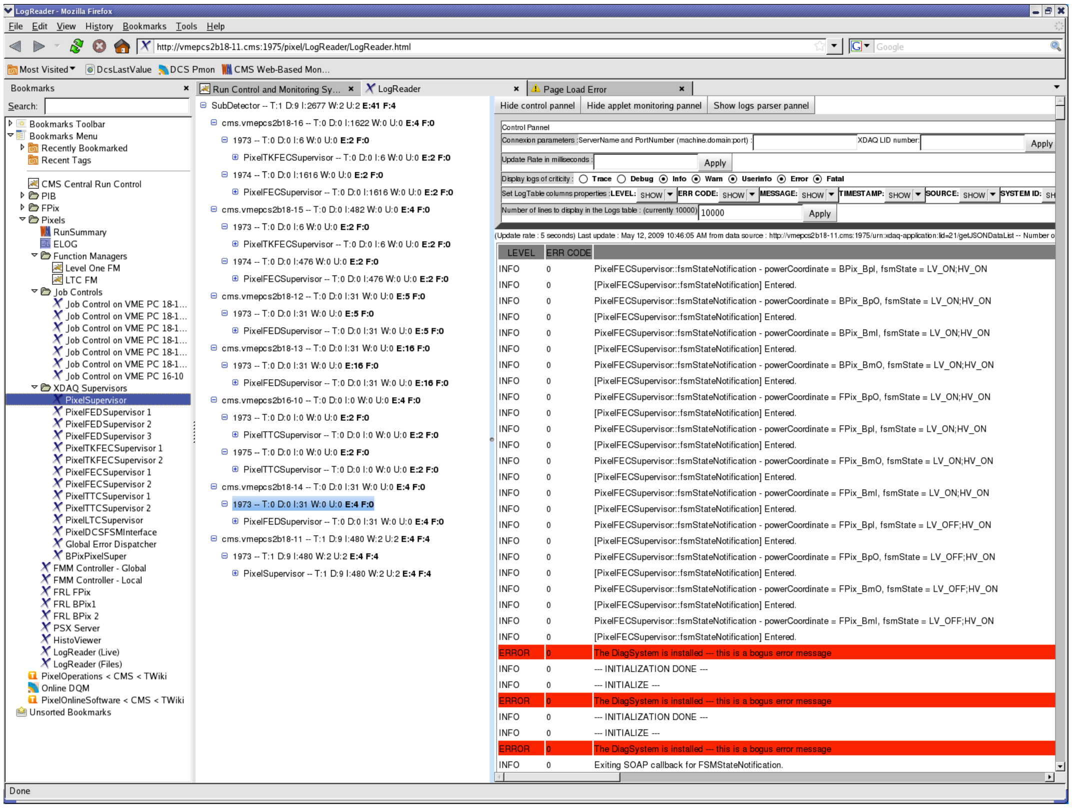

```
SubDetector -- T:1 D:9 I:2677 W:2 U:2 E:41 F:4
  cms.vmepcs2b18-16 -- T:0 D:0 I:1622 W:0 U:0 E:4 F:0
    1973 -- T:0 D:0 I:6 W:0 U:0 E:2 F:0
      PixelTKFECSupervisor -- T:0 D:0 I:6 W:0 U:0 E:2 F:0
    1974 -- T:0 D:0 I:1616 W:0 U:0 E:2 F:0
      PixelFECSupervisor -- T:0 D:0 I:1616 W:0 U:0 E:2 F:0
  cms.vmepcs2b18-15 -- T:0 D:0 I:482 W:0 U:0 E:4 F:0
    1973 -- T:0 D:0 I:6 W:0 U:0 E:2 F:0
      PixelTKFECSupervisor -- T:0 D:0 I:6 W:0 U:0 E:2 F:0
    1974 -- T:0 D:0 I:476 W:0 U:0 E:2 F:0
      PixelFECSupervisor -- T:0 D:0 I:476 W:0 U:0 E:2 F:0
  cms.vmepcs2b18-12 -- T:0 D:0 I:31 W:0 U:0 E:5 F:0
    1973 -- T:0 D:0 I:31 W:0 U:0 E:5 F:0
      PixelFEDSupervisor -- T:0 D:0 I:31 W:0 U:0 E:5 F:0
  cms.vmepcs2b18-13 -- T:0 D:0 I:31 W:0 U:0 E:16 F:0
    1973 -- T:0 D:0 I:31 W:0 U:0 E:16 F:0
      PixelFEDSupervisor -- T:0 D:0 I:31 W:0 U:0 E:16 F:0
  cms.vmepcs2b16-10 -- T:0 D:0 I:0 W:0 U:0 E:4 F:0
    1973 -- T:0 D:0 I:0 W:0 U:0 E:2 F:0
      PixelTTCSupervisor -- T:0 D:0 I:0 W:0 U:0 E:2 F:0
    1975 -- T:0 D:0 I:0 W:0 U:0 E:2 F:0
      PixelTTCSupervisor -- T:0 D:0 I:0 W:0 U:0 E:2 F:0
  cms.vmepcs2b18-14 -- T:0 D:0 I:31 W:0 U:0 E:4 F:0
    1973 -- T:0 D:0 I:31 W:0 U:0 E:4 F:0
      PixelFEDSupervisor -- T:0 D:0 I:31 W:0 U:0 E:4 F:0
  cms.vmepcs2b18-11 -- T:1 D:9 I:480 W:2 U:2 E:4 F:4
    1973 -- T:1 D:9 I:480 W:2 U:2 E:4 F:4
      PixelSupervisor -- T:1 D:9 I:480 W:2 U:2 E:4 F:4
```

Control Pannel

Connexion parameters :ServerName and PortNumber (machine.domain:port) : XDAQ LID number:

Update Rate in milliseconds :

Display logs of criticity : ○ Trace ○ Debug ● Info ● Warn ● Userinfo ● Error ● Fatal

Set LogTable columns properties :LEVEL: SHOW ERR CODE: SHOW MESSAGE: SHOW TIMESTAMP: SHOW SOURCE: SHOW SYSTEM ID: SH

Number of lines to display in the Logs table : (currently 10000) 10000

(Update rate : 5 seconds) Last update : May 12, 2009 10:46:05 AM from data source : http://vmepcs2b18-11.cms:1975/urn:xdaq-application:lid=21/getJSONDataList -- Number o

```
LEVEL   ERR CODE
INFO    0         PixelFECSupervisor::fsmStateNotification - powerCoordinate = BPix_BpI, fsmState = LV_ON;HV_ON
INFO    0         [PixelFECSupervisor::fsmStateNotification] Entered.
INFO    0         PixelFECSupervisor::fsmStateNotification - powerCoordinate = BPix_BpO, fsmState = LV_ON;HV_ON
INFO    0         [PixelFECSupervisor::fsmStateNotification] Entered.
INFO    0         PixelFECSupervisor::fsmStateNotification - powerCoordinate = BPix_BmI, fsmState = LV_ON;HV_ON
INFO    0         [PixelFECSupervisor::fsmStateNotification] Entered.
INFO    0         PixelFECSupervisor::fsmStateNotification - powerCoordinate = BPix_BmO, fsmState = LV_ON;HV_ON
INFO    0         [PixelFECSupervisor::fsmStateNotification] Entered.
INFO    0         PixelFECSupervisor::fsmStateNotification - powerCoordinate = FPix_BpO, fsmState = LV_ON;HV_ON
INFO    0         [PixelFECSupervisor::fsmStateNotification] Entered.
INFO    0         PixelFECSupervisor::fsmStateNotification - powerCoordinate = FPix_BpI, fsmState = LV_ON;HV_ON
INFO    0         [PixelFECSupervisor::fsmStateNotification] Entered.
INFO    0         PixelFECSupervisor::fsmStateNotification - powerCoordinate = FPix_BmO, fsmState = LV_ON;HV_ON
INFO    0         [PixelFECSupervisor::fsmStateNotification] Entered.
INFO    0         PixelFECSupervisor::fsmStateNotification - powerCoordinate = FPix_BmI, fsmState = LV_ON;HV_ON
INFO    0         [PixelFECSupervisor::fsmStateNotification] Entered.
INFO    0         PixelFECSupervisor::fsmStateNotification - powerCoordinate = FPix_BpI, fsmState = LV_OFF;HV_ON
INFO    0         [PixelFECSupervisor::fsmStateNotification] Entered.
INFO    0         PixelFECSupervisor::fsmStateNotification - powerCoordinate = FPix_BpO, fsmState = LV_OFF;HV_ON
INFO    0         [PixelFECSupervisor::fsmStateNotification] Entered.
INFO    0         PixelFECSupervisor::fsmStateNotification - powerCoordinate = FPix_BmO, fsmState = LV_OFF;HV_ON
INFO    0         [PixelFECSupervisor::fsmStateNotification] Entered.
INFO    0         PixelFECSupervisor::fsmStateNotification - powerCoordinate = FPix_BmI, fsmState = LV_OFF;HV_ON
INFO    0         [PixelFECSupervisor::fsmStateNotification] Entered.
ERROR   0         The DiagSystem is installed --- this is a bogus error message
INFO    0         --- INITIALIZATION DONE ---
INFO    0         --- INITIALIZE ---
ERROR   0         The DiagSystem is installed --- this is a bogus error message
INFO    0         --- INITIALIZATION DONE ---
INFO    0         --- INITIALIZE ---
ERROR   0         The DiagSystem is installed --- this is a bogus error message
INFO    0         Exiting SOAP callback for FSMStateNotification.
```

Figure 3.12: Screenshot of the DiagSystem log viewer running in the CMS control room. The window area on the right side is updated automatically each time a message arrived; new messages are added on the top while old messages scroll to the bottom. The three red lines indicate messages that have the severity of `ERROR`: they are not real and have been added for demonstration purposes.

`SOAP` message, i.e. for any supervisor the destination is the GED. Once the message is received by the GED, the destinations can be multiple and each of them needs to be uniquely defined, i.e. at least it needs to use different communication ports on the same machine. The pivoting role of the GED guarantees a great flexibility because it is the only application that has the double role of receiving and sending message.

The pixel DiagSystem has been extensively tested offline before deployment on a standalone system. Two features of the configuration displayed in Figure 3.11 were particularly tested: the stability of receiving and displaying messages without interruptions over long time intervals and with heavy loads of incoming messages (back-pressure). Early tests were based on a standalone supervisor with limited functionalities within the POS scheme. Tests extended over 24 hours with increasing amount of messages (up to a thousand messages were sent over few seconds) simulating a very extreme situation for the pixel detector. This provided feedback to the development and optimization of the package code. In the final version all the extreme situations could be handled. The communication supervisors-GED and GED-Log Reader did not stop and no single message was lost. Also, no signs of back-pressure were found: the messages kept being saved and streamed with negligible delays. The results obtained gave the confidence necessary to deploy the POS configuration for the official start of the CMS experiment in 2009. Since then, the DiagSystem package has been running non-stop throughout the period of constant increase of the instantaneous luminosity in 2010 and 2011. It has been demonstrated to be a useful and intuitive tool for the pixel shift takers. During the 2010 data taking campaign, a rate of 150 messages per minute were issued. The size of a message is 1 kB, so, at the end of an average eight hours running period, $\sim 70,000$ messages were daily saved for a corresponding storage occupation of ~ 70 MB. The majority of the them are `INFO` messages that are sent every second to monitor the status of the connection between the readout components and the GED. This system generates reports for the GED itself. If the GED experiences a network-related problem, such as a connection timeout, it directly notifies the shift taker with a `WARN` message in the Log Reader. All saved messages are sent to the Pixel Online database for book keeping. In the full year 2010, a total amount of 110 GB of space has been reserved for log-messages.

Chapter 4

Analysis of the Decay $\mathrm{B_s^0} \rightarrow \mathrm{J}/\psi\ \phi$

The aims of the analysis presented here are:

- the measurement of the differential and total cross sections, i.e. the number of produced $\mathrm{B_s^0}$ mesons that decay into the J/ψ and ϕ mesons per unit luminosity,
- an estimation of the $\mathrm{B_s^0} \rightarrow \mathrm{J}/\psi\ \phi$ branching fraction obtained from the combination of three CMS exclusive-B cross section measurements,
- the measurement of the average lifetime and lifetime difference for $\mathrm{B_s^0}$ mesons, and CP fractions of the $\mathrm{B_s^0} \rightarrow \mathrm{J}/\psi\ \phi$ decay.

The analysis is performed in different steps based on simulated Monte Carlo events and collision data. The strategy is to use a data-driven technique as much as possible. Monte Carlo simulations are either not reliable to a level of precision that can be achieved with statistics in data (from extrapolation from Tevatron) or not available at all. Sensible events are selected with a dedicated trigger and reconstructed. An optimized selection of the $\mathrm{B_s^0}$ candidate events leads to the extraction of the results with a Maximum Likelihood (ML) fit, performed on the 2010 CMS dataset, that corresponds to an integrated luminosity of about 40 pb^{-1}.

This Chapter is structured as follows: the simulation of the signal and background samples is discussed in Section 4.1. The event selection and reconstruction are presented in Section 4.2, while the sample composition and the background studies are reported in Section 4.3. The Maximum Likelihood fit procedure, its validation, and the fit results are described in Section 5.2. The efficiency extraction is studied in Section 5.7, followed by a discussion of the systematic uncertainties in Section 5.8. Results are presented in Section 5.9, Section 6, and Section 7.

4.1 Data and Simulation Samples

To setup the strategy and validate the analysis technique, sets of events that describe the signal $\mathrm{B_s^0} \to \mathrm{J}/\psi\ \phi$ and several B hadron decays have been generated with Monte Carlo (MC) technique. The main categories are:

- events with production and decay of b hadrons,
- events with prompt production of J/ψ mesons,
- events with production of a single or a non-resonant muon pair (called muon enriched).

The proton-proton collisions at the center-of-mass energy of 7 TeV and the consequent jet production are simulated with the PYTHIA6.422 Sjöstrand et al. (2006) generator. This software implements the different production QCD processes (see Section 1.3). The PYTHIA is interfaced to the EVTGEN Lange (2001) generator that simulates the decays of hadrons to the final state particles. This is necessary since in PYTHIA physical features of the decays, such as CP violation in the $\mathrm{B_s^0} \to \mathrm{J}/\psi\ \phi$, are not taken into account. The long-lived particles of a generated event are handed over to the stage that simulates the CMS detector response. The base package is the GEANT4 Agostinelli et al. (2003). It produces raw digitized detector responses. Finally, each event is reconstructed simultaneous to the data using the identical software.

4.1.1 Generation of b Hadrons

PYTHIA implements QCD high-p_T processes, such as $qq \to qq$ and $gg \to qq$. The total cross section of such events is $\sigma \approx 50$ mb. This choice includes amongst others, the three $\mathrm{b\bar{b}}$ production mechanism described in Section 1.3.1. Only events containing a $\mathrm{b\bar{b}}$ pair are selecting by a filter routine that reduces the sample size by a factor of ~ 100. With a effective cross section of $\sigma(\mathrm{pp} \to \mathrm{b\bar{b}}) = 429\ \mu\mathrm{b}$, the events are forced to hadronize into the different b-hadron flavors (B^+, B^0, B^0_s, and Λ_b) according to Table 1.3 and decay to $J/\psi\ X$, with X any number of particles. At the EVTGEN stage, any J/ψ meson is forced to decay into a pair of oppositely charged muons with requirements on their total momentum $p > 2.5$ GeV/c and pseudorapidity $|\eta| < 2.5$. Each decaying particle is characterized by the branching ratio, the list of final state particles, and a model for angular momentum dependencies between the decay particles. The events are reconstructed in the CMS software CMS Collaboration (2005), release `CMSSW_3_8_5` and tagged as `Fall10` by the CMS bookkeeping system.

Signal $B^0_s \to\ J/\psi\ \phi$

A large sample of events has been generated, forcing one of the b-quarks to hadronize as a B^0_s (or $\bar{B}^0_s$) meson and to decay via $B^0_s \to J/\psi\ X$, where X is any hadron known to recoil against J/ψ. A sample with choice $X = \phi \to K^+K^-$ only was generated at the University of Tennessee in the local computer cluster. The total sample contains $15,000$ exclusive signal events. The parameters for the simulation are taken from Tab 1.4.

The cross section for $B^0_s \to\ J/\psi\ \phi$ decay can be written as:

$$\begin{aligned}\sigma(B^0_s \to\ J/\psi\ \phi) &= \sigma(pp)\cdot\epsilon_{\text{filter}}\cdot\frac{BF^{PDG}(B^0_s \to\ J/\psi\ \phi)}{BF^{DEC}(B^0_s \to\ J/\psi\ \phi)}\cdot \\ &\cdot\ \mathcal{B}(J/\psi \to \mu^+\mu^-)\cdot\mathcal{B}(\phi \to K^+K^-). \end{aligned} \tag{4.1}$$

For pp collisions at $\sqrt{s} = 7$ TeV, PYTHIA uses the total reaction cross section $\sigma(pp) = 48.4$ mb, as extrapolated from measurements at the Tevatron Sjöstrand et al. (2006). The term ϵ_{filter} is the product of the probability for a $\bar{b}$ (or a b) quark, to be in the event that hadronizes in one B^0_s (or $\bar{B}^0_s$) meson, and to find two muons from the J/ψ decay that pass the kinematic requirements. These are determined from studies of the minimum threshold values for the transverse momenta of muons that are triggered at the L1 level. The term BF^{PDG} and $\mathcal{B}(A \to B)$ are the branching fraction values for the decay $B^0_s \to\ J/\psi\ \phi$ and for the subsequent decays, respectively, as published by the Particle Data Group (PDG) Nakamura et al. (2010). The BF^{DEC} term is the relative fraction of the decay $\mathrm{B}_\mathrm{s}^0 \to \mathrm{J}/\psi\ \phi$ with respect to the total B_s^0 decays as defined in the EVTGEN configuration file. This term is correlated to the definition of ϵ_{filter}, where only B_s^0 mesons have been selected. The following branching fractions Nakamura et al. (2010)

$$
\begin{aligned}
\mathrm{BF}^{PDG}(\mathrm{B}_\mathrm{s}^0 \to \mathrm{J}/\psi\ \phi) &= (1.4 \pm 0.4) \times 10^{-3} \\
\mathrm{BF}^{DEC}(\mathrm{B}_\mathrm{s}^0 \to \mathrm{J}/\psi\ \phi) &= (15.47 \pm 0.01) \times 10^{-2} \\
\mathcal{B}(\mathrm{J}/\psi \to \mu^+\mu^-) &= (5.93 \pm 0.06) \times 10^{-2} \\
\mathcal{B}(\phi \to \mathrm{K}^+\mathrm{K}^-) &= (48.9 \pm 0.5) \times 10^{-2}.
\end{aligned}
$$

and $\epsilon_{\text{filter}} = 0.0042 \pm 0.0001$ yield a predicted cross section for B_s^0 production and decay to the J/ψ and ϕ mesons of

$$
\sigma(\mathrm{B}_\mathrm{s}^0 \to \mathrm{J}/\psi\ \phi) = 53.3 \pm 16.3\ \text{nb}. \tag{4.2}
$$

The uncertainty is mostly due to uncertainty in the $\mathrm{B}_\mathrm{s}^0 \to \mathrm{J}/\psi\ \phi$ branching fraction ($\sim 30\%$). The error on this estimation does not consider that the total $\mathrm{b}\bar{\mathrm{b}}$ cross section at LHC energies is an extrapolation and the distribution of the transverse momentum distribution of b-quarks is scarcely known (up to 50% uncertainty Baines (2006)). The distributions of kinematic variables are correlated from data in a second step to improve those efficiencies that are determined from MC simulations. Since both the signal and the background are proportional to the same $\mathrm{b}\bar{\mathrm{b}}$ cross section, the study of the signal-to-background ratio is unaffected.

Other b Hadron Decays

All the decay channels involving a B-hadron decay that is not the $\mathrm{B}_\mathrm{s}^0 \to \mathrm{J}/\psi\ \phi$ decay are potential sources of background. These are misreconstructed events that decay into a J/ψ meson and hadrons and very likely have a well displaced reconstructed secondary vertex. Hadrons can fake a signal event by either acquiring (losing) a charged particle from (in) the background that matches the total number of charged particles in the final state or, in case the hadron decays to multiple particles, by misidentifying them. Four decays have been considered: $\mathrm{B}^+ \to \mathrm{J}/\psi\ X$, $\mathrm{B}^0 \to \mathrm{J}/\psi\ X$, $\mathrm{B}^0_\mathrm{s} \to \mathrm{J}/\psi\ X$, and $\Lambda_b \to \mathrm{J}/\psi\ X$. A detailed study of the main B background sources can be found in Section 4.3. The list of the fully simulated samples with total number of generated events N_ev, effective production cross section σ (including the branching fractions for the b hadron to decay into $\mathrm{J}/\psi \to \mu^+\mu^-$), filter efficiency ϵ_{filter} (defined as for the signal sample), and effective integrated luminosity $\mathcal{L}$ (calculated as $\mathcal{L} = N_\mathrm{ev}/\ \sigma\ \cdot\ \epsilon$) is reported in Table 4.1.

Table 4.1: Simulated B-background samples.

Process	$N_\mathrm{ev}(10^6)$	σ	ϵ	$\mathcal{L}\,(\mathrm{pb}^{-1})$
$\mathrm{B}^+ \to \mathrm{J}/\psi\ X$	2.0	29.8 μb	0.00119	62
$\mathrm{B}^0 \to \mathrm{J}/\psi\ X$	2.2	26.5 μb	0.00121	64
$\Lambda_b \to \mathrm{J}/\psi\ X$	0.5	8.1 μb	0.00026	255

4.1.2 Generation of Prompt J/ψ Production

The direct production of J/ψ mesons is an important background at the trigger level. It occurs as results of two processes: $\mathrm{c\bar{c}}$ bind states emerging from the parton interactions and radiative decay of high energy excitation states. In both case, these J/ψ mesons are also known as prompt due to their production and decay very close to the collision point. Measurements at the Tevatron Abe et al. (1997) have shown that the predictions implemented in the PYTHIA generator underestimate the production by two orders of magnitude. Perturbative QCD is used in this model to generate $\mathrm{c\bar{c}}$ pairs, which then hadronize to a charmonium state in a non-perturbative way. To overcome the discrepancy, a different approach Cano-Coloma and Sanchis-Lozano (1997) is implemented in the current version of PYTHIA6.422, and model parameters are tuned to describe data from the Tevatron. A $c\bar{c}$ pair is first formed taking into account all perturbative QCD diagrams, regardless of the final color state. The $c\bar{c}$ state is then transformed into a colorless meson by non-perturbative processes. This prompt J/ψ sample was subjected to the same kinematic criteria that apply to the signal and background simulations. The simulated cross section is $\sigma_{prompt} = 12.6\ \mu$b (considering the J/$\psi$ mesons decaying into two muons). About 9×10^6 events were generated with a filter efficiency $\epsilon_{filter} = 0.0433$ resulting in a sample that corresponds to an integrated luminosity of 13 pb^{-1}.

4.1.3 Simulation of Muon Enriched Background

In principle, any event containing one or two muon presents background. The inclusive production and decay type pp $\rightarrow \mu X$ and pp $\rightarrow \mu\mu X$ applying all know QCD processes has such large cross section that the amount of simulated events per pb^{-1} of luminosity (like the amount of unbiased collision data) exceeds practical limits in computing and storage. A luminosity equivalent of 0.5 pb^{-1} was available by the time of this work.

4.1.4 The 2010 CMS Data

The analysis presented in this dissertation uses data that were collected during the year 2010 by the CMS experiment. The data is organized as a collection of time intervals called runs, identified by a consecutive number. One run corresponds to a time interval during which the CMS experiment was running in safe conditions and was recording data. Each run contains all the events that are reconstructed by the detector. These are saved in ROOT files and stored in a distributed online database. Data were accumulated in two periods (`Run2010A` and `Run2010B`) with different running conditions at the LHC (Section 2.1.3). The measurement of the instantaneous luminosity is performed with the hadronic forward calorimeter. The method, called zero counting method, calculates the luminosity by estimating the mean number of interactions per bunch crossing (N_{avg}) according to:

$$\mathcal{L} = \frac{N_{avg} f}{\sigma} \tag{4.3}$$

where f is the bunch crossing frequency and σ is the effective interaction cross section. The distribution of the average number of interactions per bunch crossing is assumed to be a Poisson distribution centered at $N_{avg} = \mu$. The probability that a bunch crossing will yield N_{avg} events is given by

$$P(N_{avg}; \mu) = \frac{e^{-\mu} \mu^{N_{avg}}}{N_{avg}!}. \tag{4.4}$$

The number of bunch crossings that yield no events (m) is calculated as:

$$P(0; \mu) = m \rightarrow \mu = -\log(m). \tag{4.5}$$

The amount of bunch crossings that yield zero events must exceed 1% of the total bunch crossings to yield a reliable estimate. Therefore, the zero counting method is only appropriate if and only if

$$\mu \leq -\log(m) = -\log(\frac{1}{100}) \approx 4.6. \tag{4.6}$$

The running conditions of the LHC during the year 2010, $f = 50$ ns, $\sigma = 80$ mb, and $\mathcal{L} = 2 \times 10^{32}$ cm^{-2}s^{-1}, yield $N_{avg} \approx 1$, making the zero counting scheme work. The average number of interactions is given by the ratio of average fraction of the HF calorimeter towers that were not traversed by the collision products, i.e. no energy measurements performed, to the total number of interactions, as measured by the ZeroBias trigger. This selects only active beam bunch crossings to maximize the probability of obtaining events with valid collisions. The zero counting method is compared to two offline methods. The first method, called energy deposition method, uses the coincidence in time between the sum of the energy depositions of at least 1

GeV in the forward and backward HF arrays. The sum in each HF runs over all towers. Time intervals are restricted to eliminate non-collision backgrounds. The second method, called vertex method, makes use of tracking and vertex finding. It requires that at least one vertex with at least two tracks is found in the event. The z-position of the vertex has to be closer than 150 mm to the center of the interaction region. The offline methods have the drawback that typically 24 hours elapse before the offline information is available, but allow for better background rejection than the online methods. Most importantly, the offline techniques employ a largely independent data-handling path, and in the case of the vertex-counting method, involve a completely separate set of systematic uncertainties. The agreement between the online and the offline methods is within 5%. To set the absolute scale for the luminosities, the separation scan method, pioneered by S. Van Der Meer (VdM) Van der Meer (1968), is used. It measures the size and shape of the interaction region. During the VdM scan the two proton beams are scanned across each other and the relative interaction rate as a function of the transverse beam separations is recorded. The time for data acquisition and the measurement of beam intensities per bunch at each step is typically a few seconds. The luminosity obtained with the VdM scan deviate by about 0.7%. The uncertainty of this deviation due to limited statistics is ±0.003 and due to systematic uncertainties is ±0.040. The latter error is dominated by the measurement of the beam currents. Other sources are: beam-shape uncertainty, fit parameterization, and scale calibrations. The integrated luminosity,

$$\mathcal{L}_{int} = \int \mathcal{L} dt, \tag{4.7}$$

analyzed in this dissertation is $\mathcal{L}_{int} = 39.6 \pm 1.6$ pb^{-1}. The uncertainty is the systematic error of the luminosity measurement.

The data sample has been selected with the requirements that two muons have been reconstructed at the HLT trigger level and their invariant mass is between 2 GeV/c^2 and 4 GeV/c^2. The list of dataset used in the analysis can be found in Table 4.2. Some runs have been omitted (8% of the total recorded) since they did not fulfill certain quality criteria, such as the proper functioning of all the sub-systems during data taking.

Table 4.2: List of data samples used in this analysis.

Process	Dataset
Data Runs 135821–140042	/Mu/Run2010A-Nov4ReReco_v1/RECO
Data Runs 140042–144114	/MuOnia/Run2010A-Nov4ReReco_v1/RECO
Data Runs 146240–149442	/MuOnia/Run2010B-Nov4ReReco_v1/RECO

4.2 Event Reconstruction and Selection

The event reconstruction and selection occurs in three steps:

- HLT trigger selection,
- reconstruction and online pre-selection of the $\mathrm{B_s^0} \rightarrow \mathrm{J}/\psi\ \phi$ decays, and
- offline selection and optimization of the requirement criteria.

The statistical precision of the analysis is dominated by the available number of identified exclusive $\mathrm{B_s^0}$ decays in data and the amount of background events. Therefore, an optimization is required to maximize the number of signal to background.

4.2.1 Trigger Selection

The first level of selection is provided by the HLT trigger. The choice of the trigger is motivated by the ability to select the highest number of signal-like events. The dimuon triggers apply different criteria to the transverse momentum of the muons. The following dimuon triggers have been extensively studies:

- `HLT_L1DoubleMuOpen`, a double muon pass-through trigger, where no selection requirements beyond the Level-1 are applied,
- `HLT_DoubleMu0`, a double muon pass-through trigger, with at least two muons identified at the Level-3, without any p_T requirement and di-muon invariant mass interval between 2 and 4 GeV/c^2,
- `HLT_DoubleMu3`, a double muon pass-through trigger, with at least two Level-3 muons with a minimum threshold of $p_\mathrm{T} > 2.5\ \mathrm{GeV}/c$ and invariant mass interval between 2 and 4 GeV/c^2.

The trigger efficiency is dependent on the transverse momentum of the $\mathrm{B_s^0}$ candidate ($p_{\mathrm{T}}^{\mathrm{B}}$) and defined as:

$$\epsilon(p_{\mathrm{T}}^{\mathrm{B}}) = \frac{N_{trg}(p_{\mathrm{T}}^{\mathrm{B}})}{N_{gen}(p_{\mathrm{T}}^{\mathrm{B}})} \tag{4.8}$$

where N_{trg} is the number of events passing the trigger in the given $p_{\mathrm{T}}^{\mathrm{B}}$ bin, and N_{gen} is the number of events generated in the same bin. The trigger efficiencies for all three trigger scenarios as a function of transverse $\mathrm{B_s^0}$ momentum are displayed in Figure 4.1. For each of them, the total and the transverse momentum distribution of the exclusive decay channel $\mathrm{B_s^0} \rightarrow \mathrm{J}/\psi\ \phi$ is compared with the original generated distribution and shown in Figure 4.2. The choice of the trigger needs to satisfy the following requirements:

- provide the highest signal efficiency while running for the longest periods of time,
- provide the highest possible background suppression,
- avoid to introduce biases on variables.

The trigger path that satisfied all these criteria during the 2010 data acquisition campaign was the `HLT_DoubleMu0` (in two compatible versions, `HLT_DoubleMu0` and `HLT_DoubleMu0_Quarkonium_v1`). This choice implies a similar or higher minimum transverse momentum threshold for the $\mathrm{B_s^0}$ mesons at a later stage selection. The p_{T} criterion suppresses low-p_{T} background events from soft and semi-soft scattering processes, as shown in Figure 4.2-4.3. One of the sensitive variable is ct, which is defined as the distance between the primary and the $\mathrm{B_s^0}$ decay vertex boosted in the transverse plane. This is one of the two discriminating variables that are used in the analysis. Therefore, a test to verify if biases were introduced is performed. An insignificant distortion of the original distribution after application of the trigger requirement is observed in Figure 4.4. Figure 4.5 displays the ratio between the `HLT_DoubleMu0` and the generated events with the statistical error per bin for the chosen trigger.

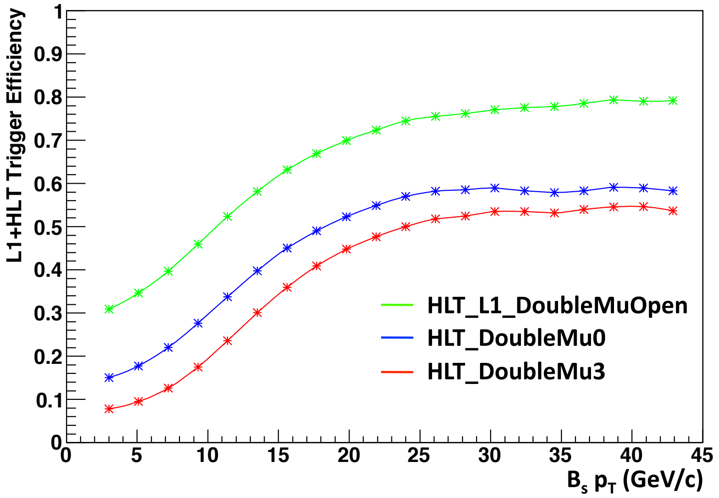

Figure 4.1: Trigger efficiencies for $B_s^0 \to J/\psi\ \phi$ MC events for the three trigger scenarios as a function of p_T^B.

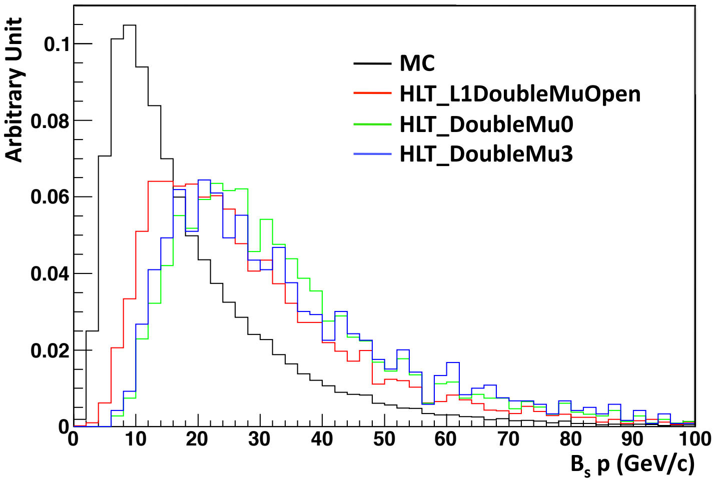

Figure 4.2: B_s^0 total momentum distribution for the generated events before and after application of the different trigger criteria. The distributions have been normalized to the total number of events in each selected sample.

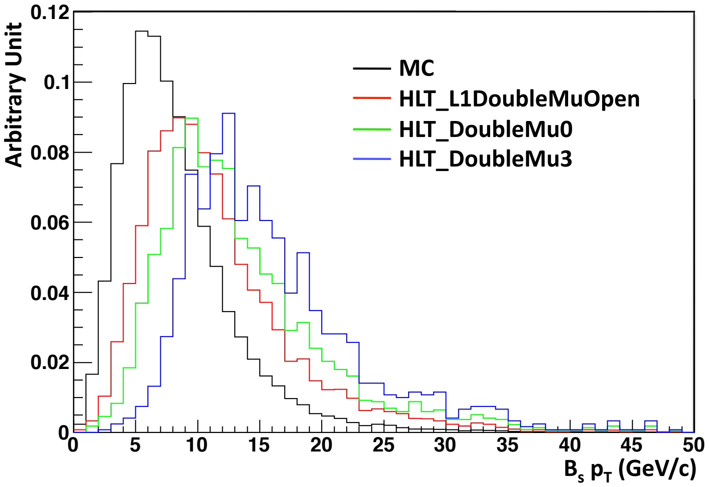

Figure 4.3: B_s^0 transverse momentum distribution for the generated events before and after application of the different trigger criteria. The distributions have been normalized to the total number of events in each selected sample.

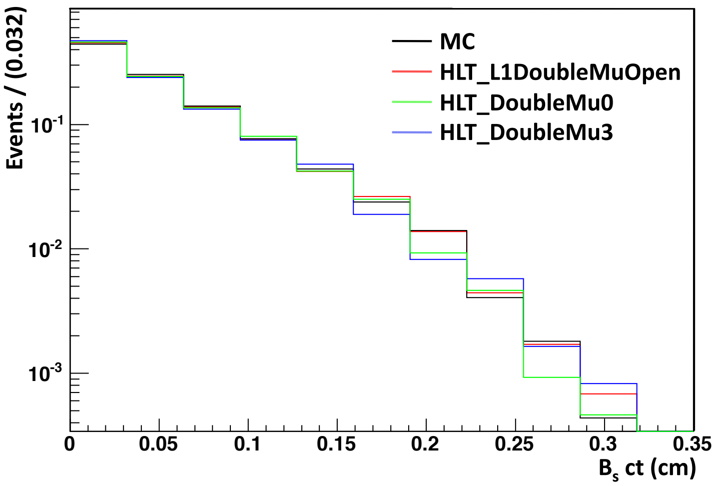

Figure 4.4: B_s^0 proper decay length distribution for generated events and after application of various trigger scenarios. The colors are explained in the legend.

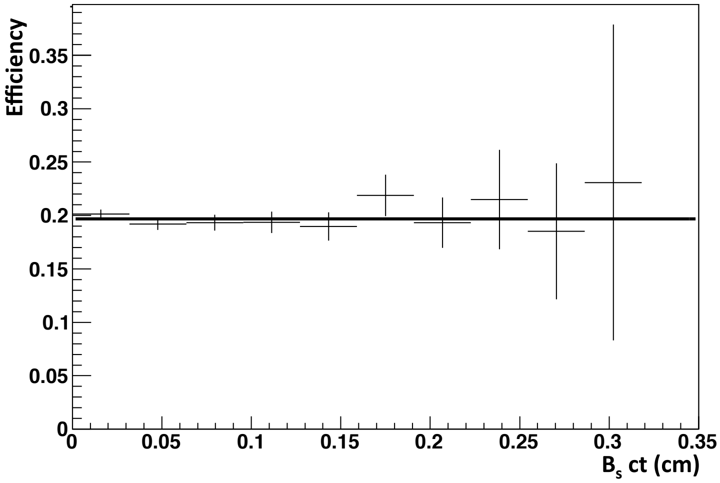

Figure 4.5: The ratio between signal events passing the `HLT_DoubleMu0` trigger requirements and generated events. This efficiency is $\epsilon = (19.7 \pm 0.3)\%$.

4.2.2 Pre-Selection of $B_s^0 \to J/\psi\ \phi$ Decays

Primary Vertex Reconstruction

The primary vertex is reconstructed with the standard primary vertex finder of CMS CMS Collaboration (2006a, 2010e), which uses all reconstructed tracks in the pixel and silicon strip detectors to measure the location and the uncertainty of an interaction vertex. The prompt tracks originating from the primary interaction region are selected based on the significance of the perpendicular distance between the trajectory of one collision product and the interaction vertex, number of strip and pixel hits, and the normalized track χ^2 probability. To ensure high reconstruction efficiency, there is no requirement on the track transverse momentum. The selected tracks are then clustered based on their z coordinates at the point of closest approach to the beam line. Vertex candidates are formed by intersecting the trajectories of the tracks that are separated in z by less than a distance at 1 cm from their nearest neighbor. Candidates containing at least two tracks are then fit with an adaptive vertex fit CMS Collaboration (2007) to compute the best estimate of vertex parameters i.e. position and its uncertainty. It returns indicators of the success of the fit, i.e. number of degrees freedom of the vertex and track weights of the tracks in the vertex. In the adaptive vertex fit, each track in the vertex is assigned a track weight between 0 and 1 based on its compatibility with the common vertex. For a track consistent with the common vertex, its weight is close to 1. Once the primary vertices are found, they are collected in a list and sorted according to the sum of the p_{T} squared of the tracks associated to each vertex, such that the vertex with largest sum, likely to be the signal vertex, appears first. If the primary vertex is not found for an event, the beam spot position is assumed to be the primary vertex. Although the instantaneous luminosity in the early collision data is far below the design luminosity of the LHC, the luminosity per bunch crossing was already high enough to produce multiple collisions in the events. For the luminosities concerning this analysis, the average number of primary vertices is one. The possibility of multiple primary interactions in the same bunch crossing is taken into account by a simple clustering step as described in the previous paragraph. Vertices separated by about 1 cm or less are not separated by this procedure and are merged into a single reconstructed vertex. Depending on the track content and separation of the vertices, the result of the subsequent adaptive vertex fit is often close to the vertex with higher multiplicity. Tracks separated by more than 1 cm from the true collision point are likely to be split off from the vertex by this procedure. For separations larger than the typical z-resolution this has little impact on the reconstructed vertex position because such tracks are either be down-weighted by the adaptive vertex fit or have very poor resolution. For very soft interactions with a small number of mostly low resolution tracks, splitting can lead to the complete loss of the real vertex. In case of multiple primary vertices, the one with highest χ^2 probability was chosen. This selection identifies the correct primary vertex in more than 95% of the times, as determined from simulated signal events.

Event Pre-Selection

The B_s^0 candidates are formed by combining a candidate J/ψ meson with a candidate ϕ meson. The J/ψ candidates are reconstructed from unique pairs of muon objects with opposite electric charge that originate from a common vertex. The vertex is estimated with a Kalman Filter Fruhwirth (1987). All the J/ψ candidates that have an invariant mass within 150 MeV/c^2 to the world average value ($M_{J/\psi} = 3096.916 \pm 0.011$ MeV/c^2) Nakamura et al. (2010) are retained, and a transverse momentum $p_T^{J/\psi} > 0.5$ GeV/c is required. Figure 4.6 shows the reconstructed $\mu^+\mu^-$ invariant mass for $B_s^0 \to J/\psi\ \phi$ signal MC events.

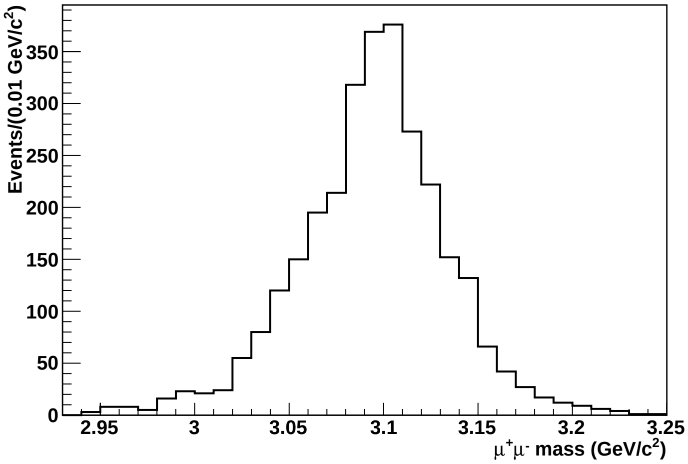

Figure 4.6: Distribution of the $\mu\mu$ invariant mass for $B_s^0 \to J/\psi\ \phi$ MC signal events after preliminary J/ψ selection.

To reconstruct the ϕ mesons, all tracks are reconstructed with standard track reconstruction. The CMS experiment does not possess a particle identification system that separates pions from kaons. Therefore, all measured tracks have to be considered as possible kaon candidates and the corresponding mass is assigned ($M_K = 493.677 \pm 0.016$ MeV/c^2) Nakamura et al. (2010). For each track pair the invariant mass is calculated: combinations with an invariant mass within 50 MeV/c^2 to the world average ($M_\phi = 1019.455 \pm 0.020$ MeV/c^2) Nakamura et al. (2010) are retained.

A J/ψ and a ϕ candidate are finally combined to form a B_s^0 candidate and the invariant mass is required to lie between 4.5 GeV/c^2 and 6 GeV/c^2.

4.2.3 Kinematic Vertex Fit

For a precise reconstruction of the B_s^0 decay vertex a kinematic vertex fit is used Prokofiev and Speer (2004); Prokofiev (2005). Kinematic fitting is the application of energy and momentum conservation to improve the estimation of the position coordinates and their uncertainties. The underlying mathematical approach in the kinematic fit is a χ^2 minimization with Lagrange multipliers. The χ^2 probability is associated with the distance between the tracks and the reconstructed vertex. In this analysis the following constraints are applied to the fit:

- The four final state tracks are required to originate from a common secondary decay vertex, since the decay time of the two intermediate states (J/ψ and ϕ) in the decay is negligible,

- The invariant mass of the two muons is constraint to the nominal J/ψ mass value since the experimental resolution on the J/ψ mass is much higher than its natural width of $\Gamma_{J/\psi} = 93.2 \pm 2.1$ keV/c^2 Nakamura et al. (2010). It is impossible to impose such a constraint on the kaon pair, since the width of the ϕ ($\Gamma_\phi = 4.26 \pm 0.04$ MeV/c^2 Nakamura et al. (2010)) is larger than the experimental resolution of 1.6 ± 0.5 MeV/c^2, as presented in this dissertation.

A detailed description of the kinematic fit applied to $B_s^0 \to J/\psi(\to \mu^+\mu^-)\phi(K^+K^-)$ events can be found in Prokofiev (2005).

The effects of the kinematic fit in terms of J/ψ ϕ invariant mass resolution are shown in Figure 4.7. It improves the resolution from $\sigma = 43$ MeV/c^2 to $\sigma = 17$ MeV/c^2.

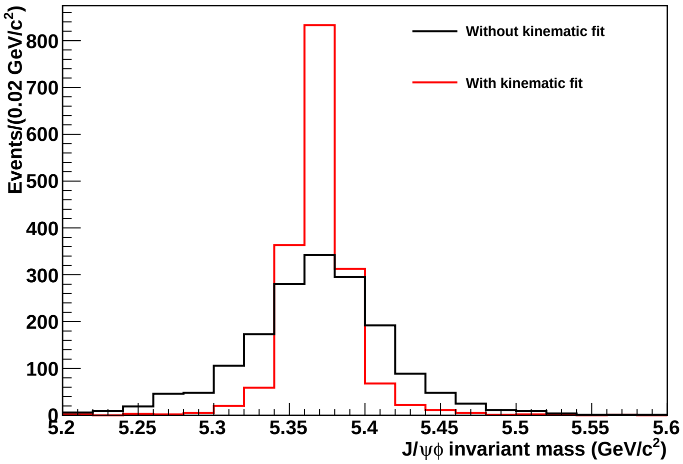

Figure 4.7: Distribution of the J/$\psi\phi$ invariant mass for $\mathrm{B_s^0} \rightarrow$ J/ψ ϕ MC signal events before and after the kinematic fit.

4.2.4 Optimized $\mathrm{B_s^0}$ Candidate Selection

The kinematic fit returns a χ^2-probability which can be used as selection criterion to determine how likely the reconstructed charged tracks originate from a common vertex. For signal events, the distribution of the χ^2-probability is expected to be shifted toward one, while, for background events peaks at zero. This trend quantifies the capability of the kinematic fit to find a common origin point for the charged tracks. For signal events, the decay position is likely to be found so high values of probability are returned. For background events, where random tracks can be added from the background, the energy-momentum conservation can fail or be not accurate. In this case, the fit returns a low probability value. In case of multiple $\mathrm{B_s^0}$ candidates, the selection is based on the highest vertex fit probability. This choice identifies the correct $\mathrm{B_s^0}$ candidate in 97% of all cases, as determined from MC signal events after matching the reconstructed candidates with the generated ones. Other selection criteria are then applied to the selected $\mathrm{B_s^0}$ candidates to suppress the background while retaining most of the signal. Their optimization is based on the figure-of-merit (FOM), a quantity used to characterize the performance of a selection requirement on a specific discriminating variable, relative to its alternatives. It is defined as

$$\kappa = \frac{S}{\sqrt{S+B}} \tag{4.9}$$

where S is the expected signal yield and B the number of estimated background events, which in good approximation estimates the statistical significance as function of an event variable. The MC signal and background samples are used for these studies. The variable κ is scanned as function of the event variables, as the example in Figure 4.8 which shows the figure-of-merit as function of the $\mathrm{B_s^0}$ vertex probability and the ϕ mass range (the final criteria are already applied to the other variables).

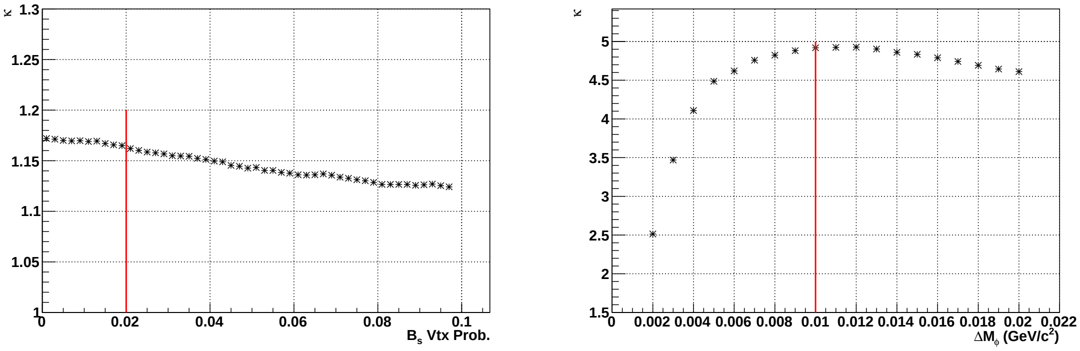

Figure 4.8: Figure-of-merit scans for $\mathrm{B_s^0}$ vertex probability (left), and for the ϕ mass window (right). The red line marks the value chosen for the final selection.

The following event variables and criteria for discrimination between signal and background have been chosen:

- the probability of the kinematic fit for the $\mathrm{B_s^0}$ candidates $> 2\%$,
- the transverse momentum of the kaon candidates $p_\mathrm{T} > 0.7$ GeV/c,
- invariant $\mathrm{K^+K^-}$ mass within 10 MeV/c^2 of the world average value,
- the transverse momentum of the $\mathrm{B_s^0}$ candidates $p_\mathrm{T} > 8$ GeV/c,
- invariant J/ψ ϕ mass in the interval $[5.20, 5.65]$ GeV/c^2,

- the proper decay length ct*, -0.05 cm $< ct <$ 0.35 cm.

The two-dimensional (2D) proper decay length (ct) of the selected $\mathrm{B_s^0}$ candidates is shown in Figure 4.9. It is determined from the measured distance (L_{xy}) between the primary and $\mathrm{B_s^0}$-decay vertices projected onto the transverse momentum p_T, and the transverse boost of the reconstructed $\mathrm{B_s^0}$ meson,

$$ct = c\frac{M_\mathrm{B}}{p_\mathrm{T}^\mathrm{B}}L_{xy} \tag{4.10}$$

where M_B and p_T^B are the mass and transverse momentum of the $\mathrm{B_s^0}$ candidate, respectively. The transverse flight length L_{xy} is the 2D projection of the vector $\vec{s}$

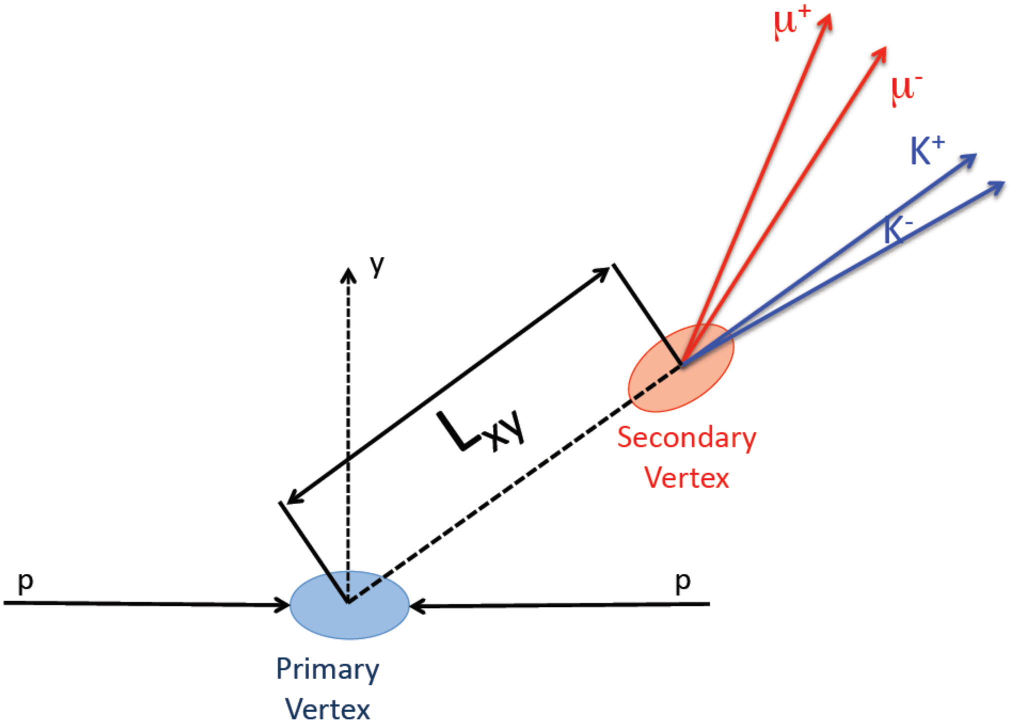

Figure 4.9: Definition of the flight length distance L_{xy}.

---

[*] Throughout this work ct (t) is used to denote the proper decay length (time).

pointing from the primary to the secondary vertex onto the transverse momentum,

$$L_{xy} = \frac{\vec{s} \cdot \vec{p}_{\mathrm{T}}^{\mathrm{B}}}{|\vec{p}_{\mathrm{T}}^{\mathrm{B}}|}. \tag{4.11}$$

The primary vertex is calculated according to the procedure described in Section 4.2.2. The difference of the decay length distribution values ($ct_{reco} - ct_{generated}$) is called residual and it is shown in Figure 4.10 for simulated signal events. The root-mean-square in the presented range is (47.6 ± 2.1) μm. It is also possible to define a three-dimensional (3D) proper decay length, where the distance between the primary and secondary vertex is measured for all three coordinates. The residual for the 3D decay length distribution has been calculated and shown in Figure 4.11. The root-mean-square in this case is (49.3 ± 2.1) μm. The results obtained from fits of the 2D and 3D residual distributions are in agreement within the error: eventually, the 2D definition has been chosen and used throughout the analysis because it was studied first. The 3D definition has been used only as cross-check.

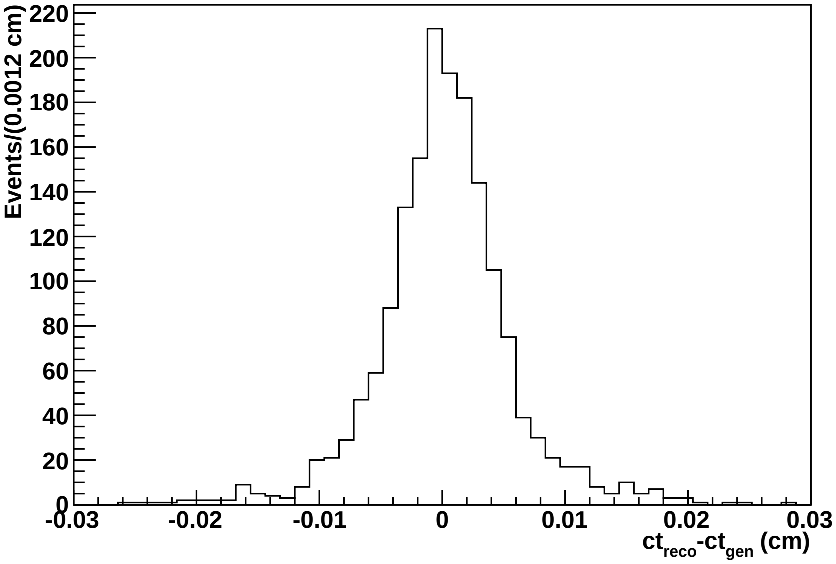

Figure 4.10: 2D Decay length (for definition see Eq. 4.10) residual from simulated signal events. The RMS is found to be 47.6 ± 2.1 μm.

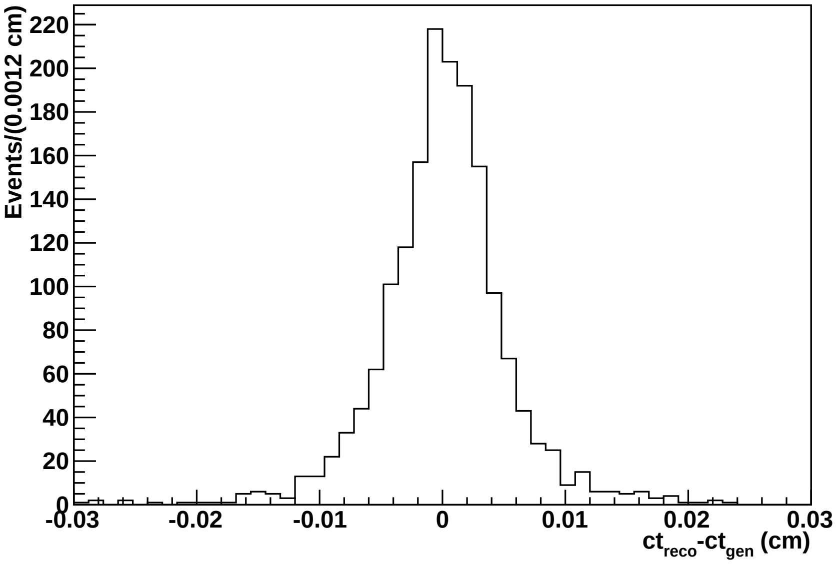

Figure 4.11: 3D Decay length residual from simulated signal events. The RMS is found to be 49.3 ± 2.1 μm.

The total signal reconstruction and selection efficiency from Monte Carlo is (32.9 ± 0.8) %. In data, we find 6,200 events after application of all requirements. Figure 4.12 shows the selected candidate events from data with the additional criterion $ct > 0.01$ cm to suppress the prompt background for demonstration purposes. The $\mathrm{B_s^0} \to \mathrm{J}/\psi\ \phi$ signal is significantly observed. For a detailed description of the fit, please see Section 5.2. Figure 4.13 shows the ϕ mesons from the $\mathrm{B_s^0} \to \mathrm{J}/\psi\ \phi$ decays in data. These events have been isolated and closely defined as signal: the ϕ peak resolution has been measured to be $\sigma_\phi = (1.6 \pm 0.5)$ MeV/c^2. The fit has been performed with a Voigtian function (Breit-Wigner function convoluted with a Gaussian function for the resolution) for the signal and a first order polynomial for the background. Figures 4.14-4.16 show a comparison data versus Monte Carlo for the $\mu^+\mu^-$ invariant mass, the vertex fit probability of the $\mathrm{B_s^0}$ candidates, and the $\mathrm{K^+K^-}$ invariant mass. For all these plots, the events have been fully reconstructed and selected for maximum purity after requirements on the observables to enhance the $B_s^0 \rightarrow J/\psi\ \phi$ signal: distributions in MC and data events show a good agreement.

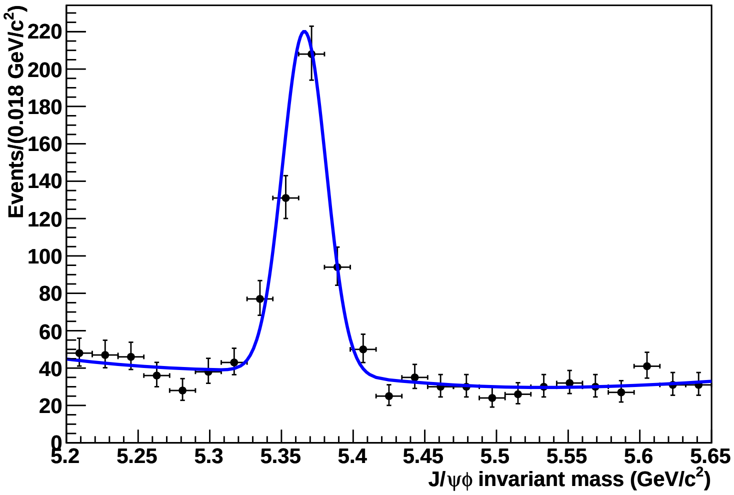

Figure 4.12: The invariant $J/\psi\ \phi$ mass distribution for selected candidate events with $ct > 0.01$ cm. The signal to background ratio is greater than 10 : 1.

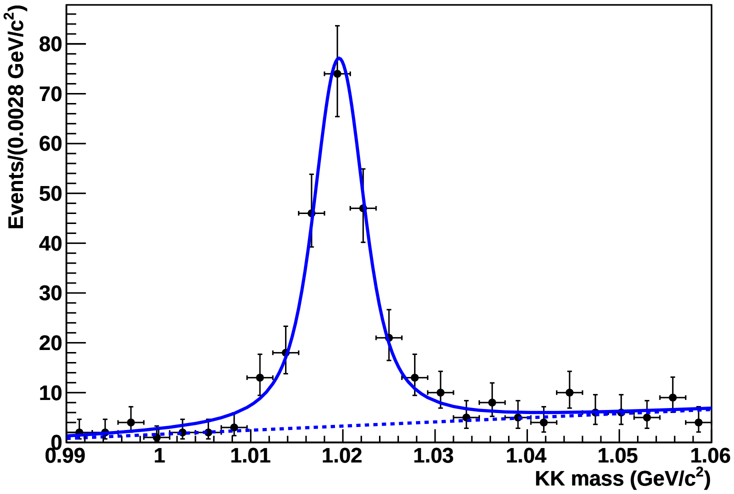

Figure 4.13: K^+K^- invariant mass for events selected in a $J/\psi\ \phi$ invariant mass range between 5.35 and 5.39 GeV/c^2 close to the expected B_s^0 signal. Also a minimal requirement on the proper decay length, $ct > 0.025$ cm, has been applied. A fit (solid blue line) with a Voigtian for the signal and a first order polynomial for the background (dashed blue line) is over-imposed to the data.

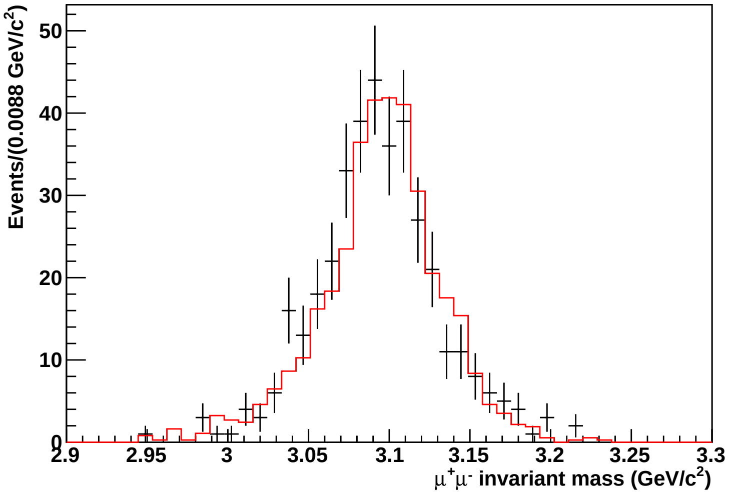

Figure 4.14: Comparison of the $\mu^+\mu^-$ invariant mass between (cross) and simulation (histograms) for events selected in a $J/\psi\ \phi$ invariant mass range between 5.35 and 5.39 GeV/c^2 and the proper decay length $ct > 0.01$ cm.

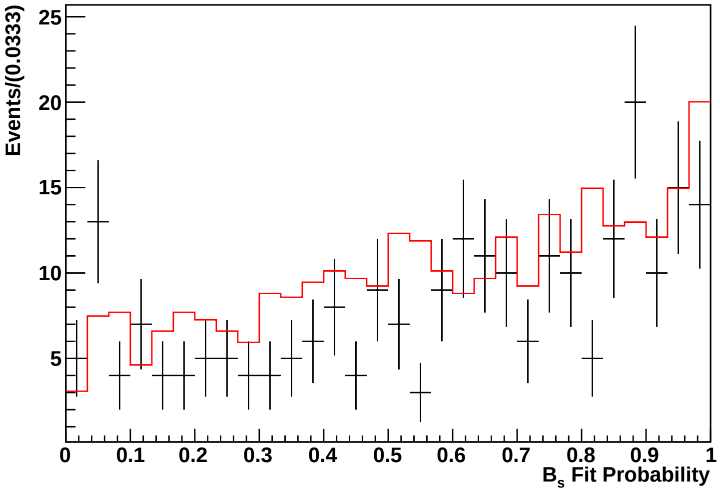

Figure 4.15: Comparison of the probability of the combined kinematic and vertex fit between data (cross) and simulated candidate (histograms) for events selected in a J/ψ ϕ invariant mass range between 5.35 and 5.39 GeV/c^2 close to the expected $\mathrm{B_s^0}$ signal and the proper decay length, $ct > 0.025$ cm.

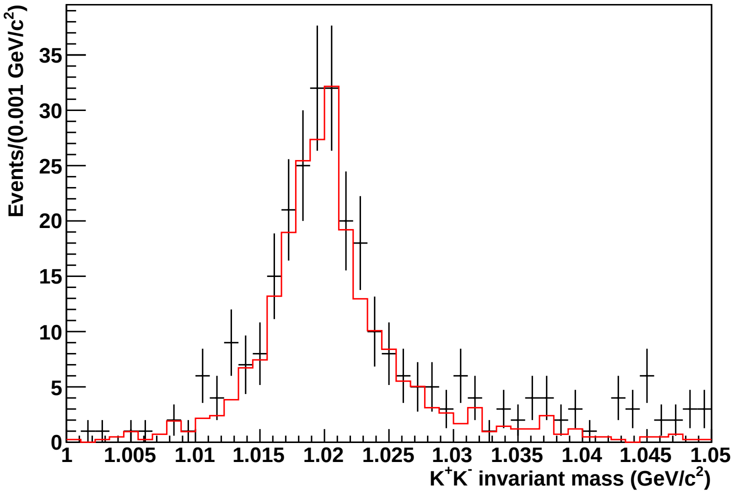

Figure 4.16: Comparison of the $\mathrm{K^+K^-}$ invariant mass between (cross) and simulation (histograms) for events selected in a J/ψ ϕ invariant mass range between 5.35 and 5.39 GeV/c^2 close to the expected $\mathrm{B_s^0}$ signal. Also a minimal requirement on the proper decay length, $ct > 0.025$ cm, has been applied.

4.3 Sample Composition

Three main background sources have been identified and studied in the MC samples, as described in Section 4.1. They are:

- b Hadron (non-prompt J/ψ)

  These are misreconstructed B $\rightarrow$ J/ψ X events that very likely have a well displaced reconstructed secondary vertex. The composition of the B background has been studied in details from the generator information of simulated events and all the non-negligible contributions for the expected integrated luminosity of ≈ 40 pb^{-1} are listed:

  - $\mathrm{B}^0 \rightarrow \mathrm{J}/\psi\ \mathrm{K}^{*0}(892)$: the signature of this channel is very similar to the signal $\mathrm{B}_s^0 \rightarrow \mathrm{J}/\psi\ \phi$ by replacing a kaon with a pion. This is the most important source of background and the selection optimizes the discrimination between this channel and the signal.
  - $\mathrm{B}^0 \rightarrow \mathrm{J}/\psi\ \mathrm{K}_1^0$: for this channel the K_1^0 meson primarily decays into ρ and a charged K. The misreconstruction occurs when one of the two charged pions from the ρ meson decay is identified as a charged K, and the second one is lost (feed-down channel).
  - $\mathrm{B}^0 \rightarrow \mathrm{J}/\psi\ \mathrm{K}_s^0$ (with $\mathrm{K}_s^0 \rightarrow \pi^+\pi^-$): the misreconstruction occurs where both charged pions are misidentified as charged kaons.
  - $\mathrm{B}^+ \rightarrow \mathrm{J}/\psi\ \mathrm{K}^{*+}/\mathrm{K}_2^+$: for this channels the higher-mass K-meson states primarily decay into $\mathrm{K}^{*0}(892)$ and a charged pion. The misreconstruction occurs when either the pion from the $\mathrm{K}^{*0}(892)$ meson decay or the other pion in the event is identified as a charged K, and the second one is lost (feed-down channel).
  - $\mathrm{B}^+ \rightarrow \mathrm{J}/\psi\ \mathrm{K}^+$: for this channel the charged K is matched to a flying K from the background to make a ϕ meson. Channels where a particle is acquired to fake a signal event are called feed-up channels.

  - $\Lambda_b \rightarrow J/\psi\ \Lambda$: for this channel the Λ barion decays in a proton and a charged pion. The misidentification of the pion and the acquisition of a charged kaon from the event could fake a signal event (feed-up channel).
  - Other B^0_s decays into J/ψ plus other daughter particles.
  - Other B^0 decays into J/ψ plus other daughter particles.
  - Other: all the remaining decays from the hadronization of $b\bar{b}$ quarks or produced by pp collisions.

- Prompt J/ψ

  The prompt J/ψ mesons are produced from pp collisions as result of $c\bar{c}$ bind states from soft and semi-hard parton interactions or from radiative decay of high energy excitation states. Their decay occurs very close to the production point because the lifetime is about 10^{-20} s. As consequence, they do not show a displaced decay vertex. This background is formed by events with a J/ψ directly produced from pp collisions combined with two charged tracks. It clusters in *ct* near zero and smoothly varies in the $J/\psi\ \phi$ invariant mass. This background is the least correlated with the signal. It is, therefore, easily separated and has little impact on the signal-yield uncertainty.

- Muon enriched background

  All other background channels that include at least one true muon at generator level. This includes $b\bar{b}$, $c\bar{c}$, and gluon/light-quark events with muons from decays in flight of π and K mesons. The corresponding Monte Carlo sample suggests that the expected amount of such events is negligible. But due to the small effective integrated luminosity of the available sample (0.5 pb^{-1}) and the large uncertainty in cross sections the precision of this estimate is limited. However, the regions of the dimuon mass distribution aways from the peak, as shown in Figure 4.14, are sparsely populated indicating a small amount of events of this kind in the data sample.

Tables 4.3-4.5 summarize the event reduction in sequential application of the selection criteria in the data and MC samples: all the values are given in percentage (%) except for data. The number of background events expected in 40 pb^{-1}, for each B decay channels, is summarized in Table 4.6. All these components are added together according to their known fraction (cocktail sample). The plot demonstrates that there are no signal-like structures (peaking) neither in the J/ψ ϕ or in the K^+K^- invariant mass distributions (Figure 4.17 and Figure 4.18, respectively). Furthermore, for selected B-background channels, the J/ψ ϕ invariant mass is plotted

Table 4.3: Event reduction in sequential application of the selection criteria for data, signal, and several B background channels, respectively.

	Data	$B_s^0 \to J/\psi\ \phi$	$B^0 \to J/\psi\ K^{*0}(892)$	$B^0 \to J/\psi\ K_1^0$
Trigg. events	7216401	15204	25386	34159
Pre Kinem. fit	815617	64.5%	36.5%	41.1%
After Kinem. fit	587638	56.7%	16.0%	15.8%
B_s^0 Vtx prob.> %	241796	51.3%	10.5%	9.7%
Kaon $p_T > 0.7$ GeV/c	74870	41.5%	4.3%	3.3%
$\Delta M_{K^+K^-} < 10$ MeV/c^2	23660	35.6%	1.2%	1.0%
$M_{J/\psi\phi} \in [5.2, 5.65]$ GeV/c^2, $-0.05 < ct(B_s^0) < 0.35$ cm	10933	35.6%	1.0%	0.8%
$p_T(B_s^0) > 8$ GeV/c	6200	32.9%	0.8%	0.6%

Table 4.4: Event reduction in sequential application of the selection criteria in Monte Carlo for several B background channels.

	$B^0 \to J/\psi\ K_s^0$	$B^+ \to J/\psi\ K^+$	$B^+ \to J/\psi\ K^{*+}/K_2^+$
Trigg. events	28118	31073	205406
Pre Kinem. fit	30.5%	29.0%	38.1%
After Kinem. fit	13.2%	12.0%	14.6%
B_s^0 Vtx prob.> %	7.8%	7.5%	9.0%
Kaon $p_T > 0.7$ GeV/c	2.2%	2.2%	2.8%
$\Delta M_{K^+K^-} < 10$ MeV/c^2	0.6%	0.6%	0.9%
$M_{J/\psi\phi} \in [5.2, 5.65]$ GeV/c^2, $-0.05 < ct(B_s^0) < 0.35$ cm	0.5%	0.5%	0.7%
$p_T(B_s^0) > 8$ GeV/c	0.4%	0.4%	0.5%

Table 4.5: Event reduction in sequential application of the selection criteria in Monte Carlo for several B background channels.

	$\Lambda_\mathrm{b} \to \mathrm{J}/\psi\ \Lambda$	Other B_s^0	Other B^0	Other
Trigg. events	50164	41965	132682	1080
Pre Kinem. fit	35.5%	40.4%	37.8%	34.6%
After Kinem. fit	13.5%	14.4%	14.4%	13.9%
B_s^0 Vtx prob.> %	8.4%	8.9%	8.9%	8.1%
Kaon $p_\mathrm{T} > 0.7$ GeV/c	2.5%	2.6%	2.7%	1.9%
$\Delta M_{\mathrm{K}^+\mathrm{K}^-} < 10$ MeV/c^2	0.8%	0.9%	0.8%	0.7%
$M_{\mathrm{J}/\psi\phi} \in [5.2, 5.65]$ GeV/c^2, $-0.05 < ct(\mathrm{B}_\mathrm{s}^0) < 0.35$ cm	0.6%	0.7%	0.7%	0.6%
$p_\mathrm{T}(\mathrm{B}_\mathrm{s}^0) > 8$ GeV/c	0.4%	0.5%	0.5%	0.6%

Table 4.6: Estimate of contributions from non-prompt ($\mathrm{B} \to \mathrm{J}/\psi X$) and prompt J/$\psi$ decay channels from Monte Carlo simulations.

Channel	Efficiency (%)	Lumi. in MC sample (pb^{-1})	Events in 40 pb^{-1}
$\mathrm{B}^0 \to \mathrm{J}/\psi\ \mathrm{K}^{*0}(892)$	0.8	64.3	122
$\mathrm{B}^0 \to \mathrm{J}/\psi\ \mathrm{K}_1^0$	0.6	64.3	120
$\mathrm{B}^0 \to \mathrm{J}/\psi\ \mathrm{K}_\mathrm{s}^0$	0.4	64.2	64
$\mathrm{B}^+ \to \mathrm{J}/\psi\ \mathrm{K}^+$	0.4	62.1	73
$\mathrm{B}^+ \to \mathrm{J}/\psi\ \mathrm{K}^{*+}/\mathrm{K}_2^+$	0.5	95.6	437
$\Lambda_\mathrm{b} \to \mathrm{J}/\psi\ \Lambda$	0.4	254.6	44
Other B^0	0.5	64.3	394
Other B_s^0	0.5	51.1	171
Other	0.6	62.1	4
Prompt J/ψ	0.4	13	4283

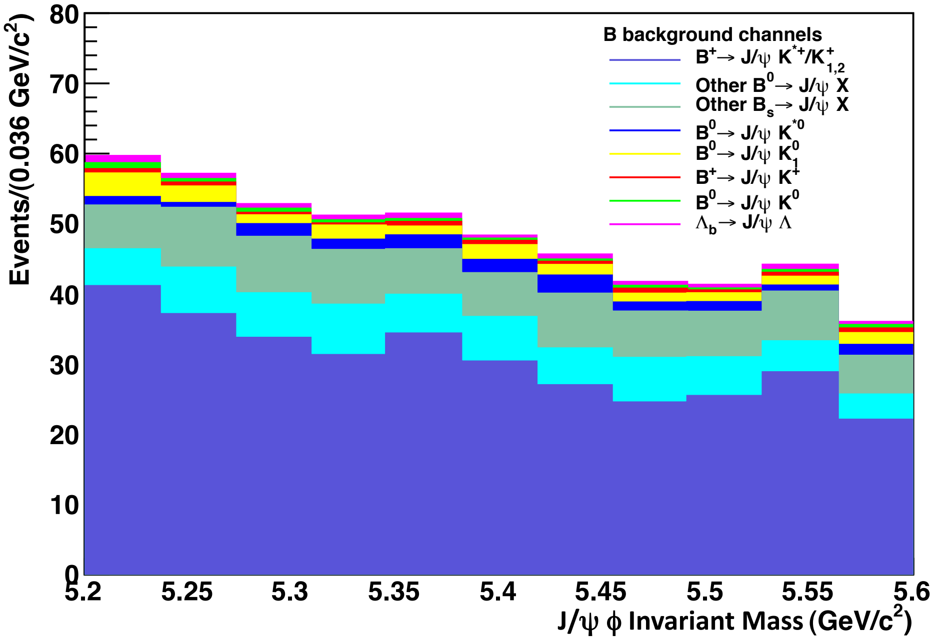

Figure 4.17: $J/\psi\ \phi$ invariant mass distribution plot for all the identified B background decay channels reconstructed and summed up in the correct expected ratio as foreseen in the MC. Contributions from each decay channel are color-coded and listed in the legend. The average shape does not exhibit a peaking structure around the B^0_s mass value.

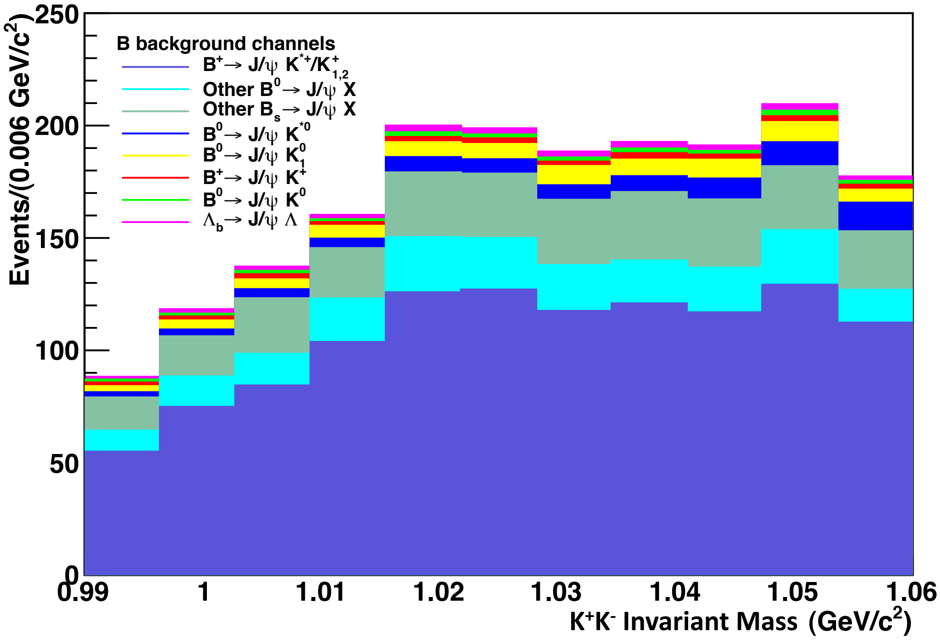

Figure 4.18: K^+K^- invariant mass distribution plot for all the identified B background decay channels reconstructed and summed up in the correct expected ratio as foreseen in the MC. Contributions from each decay channel are color-coded and listed in the legend. The average shape does not exhibit a peaking structure around the ϕ mass value.

versus the K^+K^- invariant mass: none exhibits an accumulation of events in the signal region, which is defined by $M_{J/\psi\phi}$ around 5.37 GeV/c^2 and $M_{K^+K^-}$ around 1.02 GeV/c^2 (see Figures 4.19-4.22). Since the extraction of the signal events depends on the shape as event variable distribution, for the background, the combination of all the background channels provides a starting point for their parameterization. An absolute determination of the number of background events from MC is not needed.

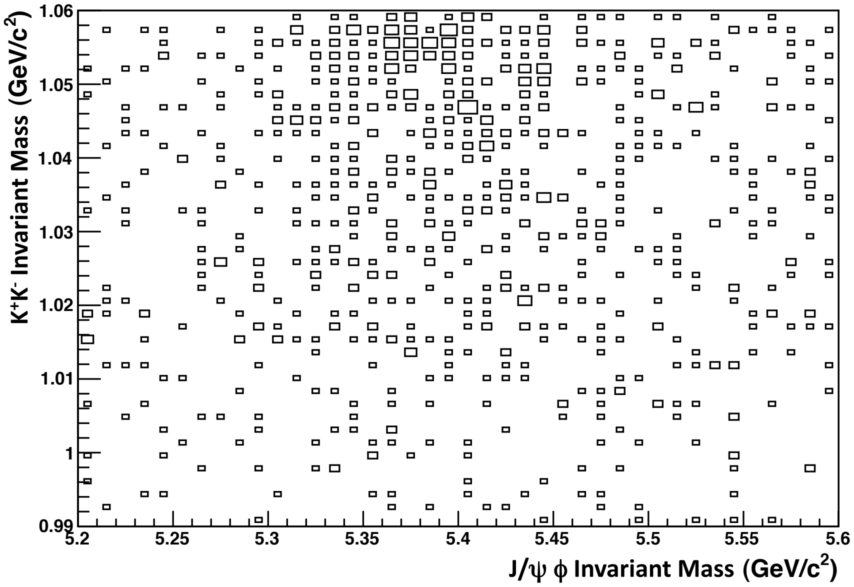

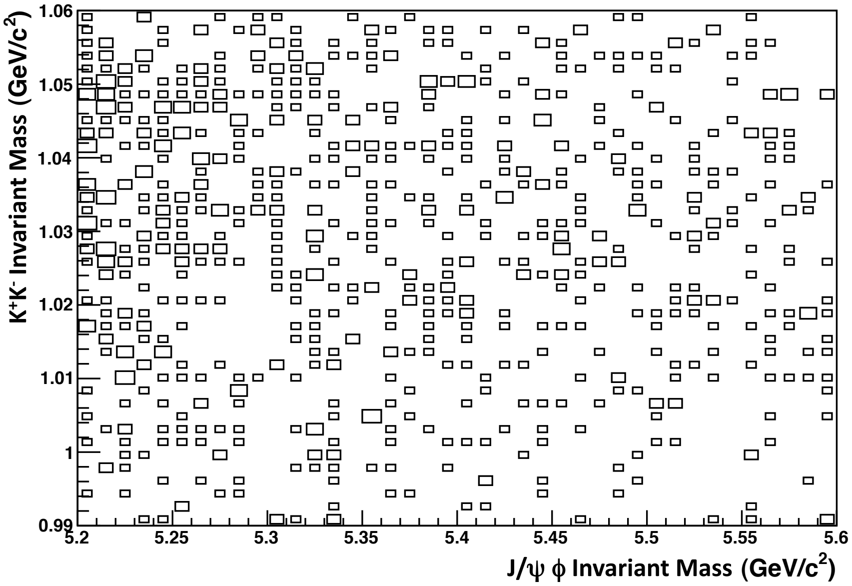

Figure 4.19: Reconstructed K^+K^- invariant mass versus $J/\psi\ \phi$ invariant mass for $B^0 \to J/\psi\ K^{*0}(892)$ (top) and $B^0 \to J/\psi\ K_1^0$ (bottom). All the plots are shown with the full available statistics and not scaled to the expected numbers as reported in Table 4.6.

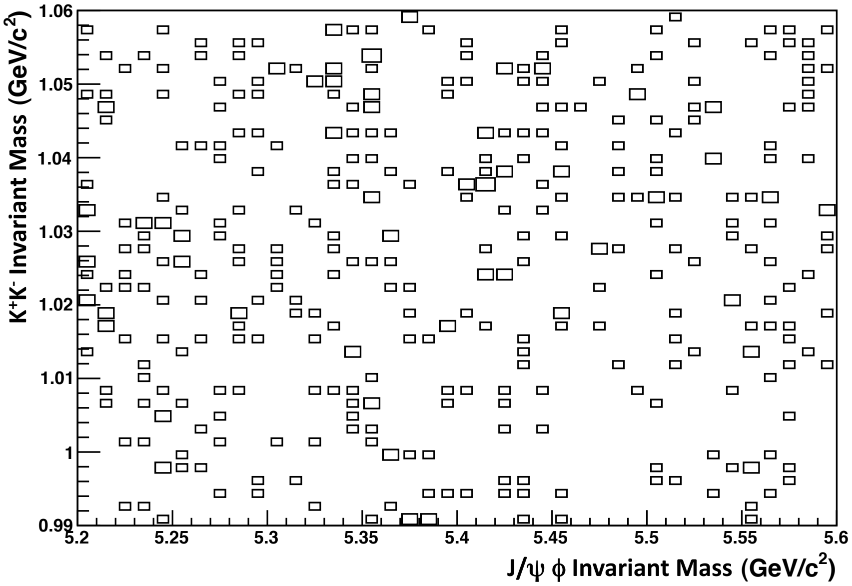

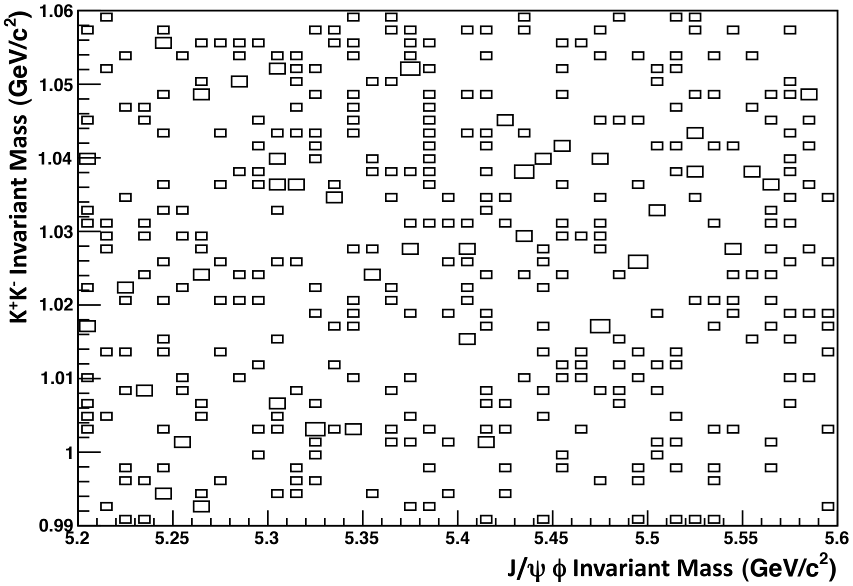

Figure 4.20: Reconstructed K^+K^- invariant mass versus $J/\psi\ \phi$ invariant mass for $B^0 \to J/\psi\ K^0_s$ (top) $B^+ \to J/\psi\ K^+$ (bottom). All the plots are shown with the full available statistics and not scaled to the expected numbers as reported in Table 4.6.

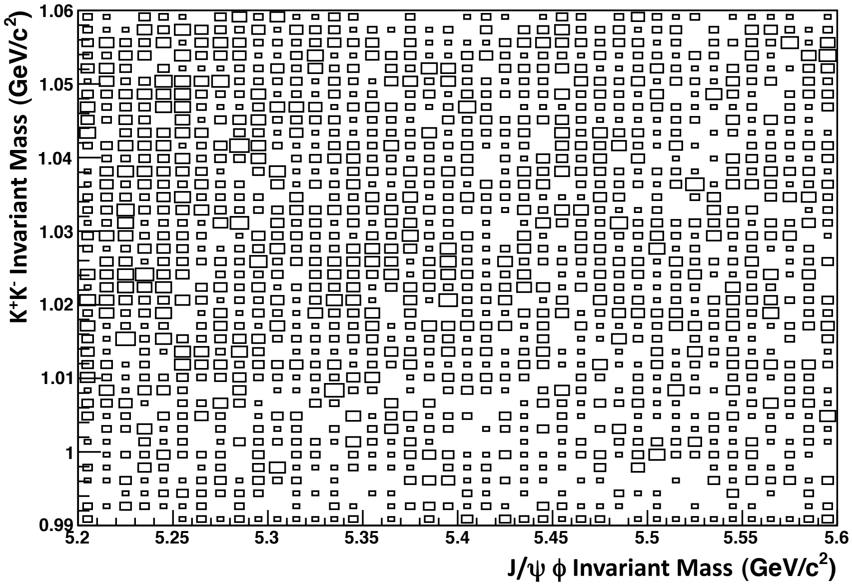

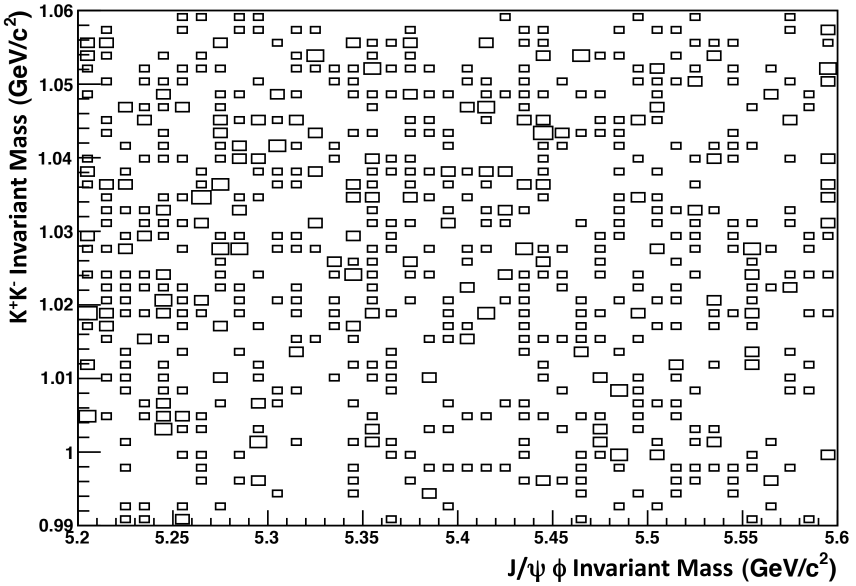

Figure 4.21: Reconstructed K^+K^- invariant mass versus $J/\psi\ \phi$ invariant mass for $B^+ \rightarrow J/\psi\ K^{*+}/K_2^+$ (left) and $\Lambda_b \rightarrow J/\psi\ \Lambda$ (right). All the plots are shown with the full available statistics and not scaled to the expected numbers as reported in Table 4.6.

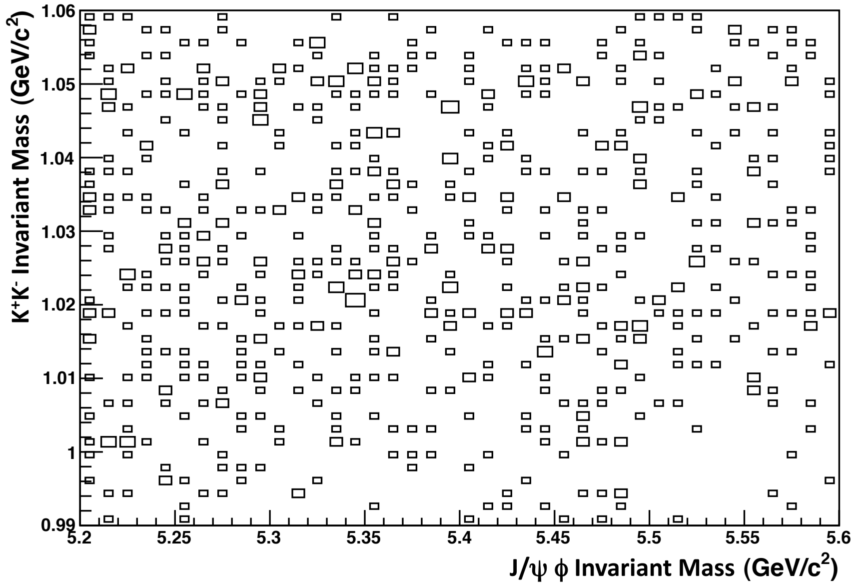

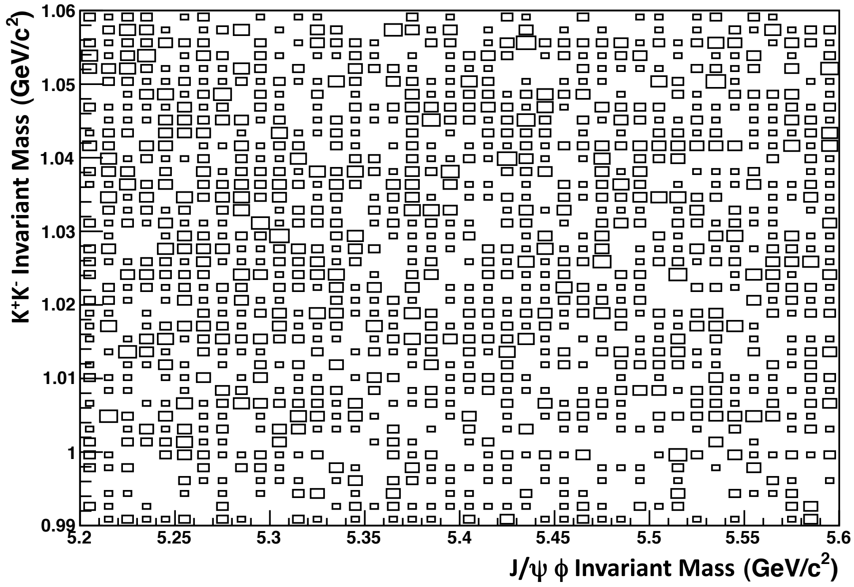

Figure 4.22: Reconstructed $\mathrm{K}^+\mathrm{K}^-$ invariant mass versus $\mathrm{J}/\psi\ \phi$ invariant mass for other $\mathrm{B}^0_\mathrm{s} \to \mathrm{J}/\psi X$ decays (left) and other $\mathrm{B}^0 \to \mathrm{J}/\psi X$ decays (right). All the plots are shown with the full available statistics and not scaled to the expected numbers as reported in Table 4.6.

Chapter 5

Production Cross Section Measurement

5.1 Strategy

The goal of this analysis is to measure the cross section for the production of $\mathrm{B_s^0}$ mesons that decay in J/ψ and ϕ with the available data recorded by the CMS detector in 2010. The differential production cross sections, $d\sigma/dp_{\mathrm{T}}^{\mathrm{B}}$ and $d\sigma/dy^{\mathrm{B}}$, are determined as functions of the transverse momentum $p_{\mathrm{T}}^{\mathrm{B}}$ and rapidity $|y^{\mathrm{B}}|$ of the reconstructed $\mathrm{B_s^0}$ candidate. The signal is extracted with an unbinned extended ML fit to the invariant J/ψ ϕ mass and proper decay length ct. The cross sections for $\mathrm{B_s^0} \rightarrow$ J/ψ ϕ, in bins of quantity x, is given as:

$$\frac{d\sigma(pp \rightarrow \mathrm{B_s^0} \rightarrow \ \mathrm{J}/\psi\ \phi)}{dx} = \frac{n_{\mathrm{sig}}}{2 \cdot \epsilon \cdot \mathcal{B} \cdot L \cdot \Delta x} \ , \tag{5.1}$$

where

- n_{sig} is the fitted number of signal events in the given bin. The number is corrected for a bin-to-bin migration factor (i.e. fraction of reconstructed and generated candidates in a given bin);

- $\epsilon = \epsilon_{acceptance} \cdot \epsilon_{2\mu} \cdot \epsilon_{reco}$ is the total efficiency, where the first term is the efficiency calculated as the fraction of true signal decays generated in a given bin that have two muons within the chosen acceptance, the second term is the efficiency calculated from the Tag-and-Probe method (see Section 5.7 for more details) in a given bin for reconstructing, identifying, and triggering on two muons in the acceptance, while the latter is efficiency calculated from the reconstructed and selected event in the signal Monte Carlo sample in a given bin given two reconstructed and triggered muons;
- $\mathcal{B} = \mathrm{BF}(\mathrm{J}/\psi \to \mu^+\mu^-) \cdot \mathrm{BF}(\phi \to \mathrm{K}^+\mathrm{K}^-)$ is the product of the two sub-decay branching fractions (see Table 4.2 for their values);
- $\mathcal{L}$ is the total integrated luminosity of the dataset;
- $\Delta x = \Delta p_{\mathrm{T}}^{\mathrm{B}}, \Delta|y^{\mathrm{B}}|$ is bin size for the quantity x.

The result is reported as a cross section for $\mathrm{B}_{\mathrm{s}}^0$ production alone, while both $\mathrm{B}_{\mathrm{s}}^0$ and $\bar{\mathrm{B}}_{\mathrm{s}}^0$ are included in the measured n_{sig}. Hence, Equation 5.1 is multiplied by a factor of two. Table 5.1 shows the bins in $p_{\mathrm{T}}^{\mathrm{B}}$ and $|y^{\mathrm{B}}|$. The relative interval choice is optimized from signal Monte Carlo events to achieve a statistical uncertainty on n_{sig} which is comparable in each of them (about 10%).

Table 5.1: Bin definitions for $p_{\mathrm{T}}^{\mathrm{B}}$, and $|y^{\mathrm{B}}|$.

Bin #	$p_{\mathrm{T}}^{\mathrm{B}}$ (GeV/c)	$\lvert y^{\mathrm{B}}\rvert$
1	$(8, 12)$	$(0.00, 0.80)$
2	$(12, 16)$	$(0.80, 1.40)$
3	$(16, 23)$	$(1.40, 1.70)$
4	$(23, 50)$	$(1.70, 2.40)$

5.2 Maximum Likelihood (ML) Procedure

Data samples are a collection of N independent events. An event is the measurement of a set of $\mathcal{O}$ *observables* $\hat{x} = (x^1, ..., x^{\mathcal{O}})$ (energies, masses, spatial and angular variables...) recorded in a brief span of time by the detectors. The events can be classified in $\mathcal{S}$ different *species*, which are generally classified with *signal*, for the events of interest for their physics phenomena, and *backgrounds*, all the remaining. Each observable x^j is distributed for the given species $\mathcal{S}$ with a probability distribution function (PDF) $\mathcal{P}^j_{\mathcal{S}}(x^j; \hat{\theta}^j_{\mathcal{S}})$, where $\hat{\theta}^j_{\mathcal{S}}$ are the parameters of the PDF. Several data analysis techniques can be used to discriminate signal and background events, using particular observables which have different PDF distributions for signal and background events. The Maximum Likelihood (ML) fitting procedure is a popular statistical technique used to estimate the number of events belonging to each species and the parameters $\hat{\theta}_{\mathcal{S}} = (\hat{\theta}^1_{\mathcal{S}}, \ldots, \hat{\theta}^{\mathcal{O}}_{\mathcal{S}})$ of the PDFs, that can be related to the prediction obtained from physics models Aldrich (1997). In the case in which the observables are uncorrelated to each other, the total PDF for the species $\mathcal{S}$ is expressed as

$$\mathcal{P}_{\mathcal{S}}(\hat{x}; \hat{\theta}_{\mathcal{S}}) = \prod_{j=1}^{\mathcal{O}} \mathcal{P}^j_{\mathcal{S}}(x^j; \hat{\theta}^j_{\mathcal{S}}) \tag{5.2}$$

The *extended likelihood function* is

$$\mathcal{L} = \frac{e^{-\sum\limits_{s=1}^{\mathcal{S}} n_s}}{N!} \prod_{i=1}^{N} \sum_{s=1}^{\mathcal{S}} n_s \mathcal{P}_{\mathcal{S}}(\hat{x}_i; \hat{\theta}_{\mathcal{S}}) \tag{5.3}$$

where n_s are the number of events belonging to each species. The ML technique allows to estimate the values of the parameters by maximizing this function with respect to the free parameters. Usually, it is used to minimize the equivalent function $-\ln(\mathcal{L})$, the negative log-likelihood (NLL). So the NLL to be minimized has the form [*]:

$$\mathrm{NLL} = \sum_{s=1}^{\mathcal{S}} n_s - \sum_{i=1}^{N} \left(\ln \sum_{s=1}^{\mathcal{S}} n_s \mathcal{P}_{\mathcal{S}}(\hat{x}_i; \hat{\theta}_{\mathcal{S}}) \right) . \tag{5.4}$$

The function is a sum of logarithms and the search for its minimum can be carried out numerically. The whole procedure of minimization requires several evaluations of the NLL, and in turn requires the calculation of the corresponding PDFs for each variable and each event of the data sample. The algorithm for the evaluation of the NLL is implemented in the ROOT/RooFit package Antcheva et al. (2009). It is based on the numerical minimization package MINUIT James et al. (1975).

The likelihood for event j is obtained by summing the product of the yield n_i and the PDF $\mathcal{P}_i$ and $\mathcal{Q}_i$ for each of the signal and background hypotheses i. Three main individual components have been identified and considered: signal, combinatorial B, and prompt J/ψ background. The extended likelihood function is then the product of likelihoods for each event j:

$$\mathcal{L} = \exp\left(- \sum_{i=1}^{3} n_i \right) \prod_j \left[\sum_{i=1}^{3} n_i \mathcal{P}_i(M_{\mathrm{B}};\, \vec{\alpha}_i) \mathcal{Q}_i(ct;\, \vec{\beta}_i) \right] . \tag{5.5}$$

The PDFs $\mathcal{P}_i$ and $\mathcal{Q}_i$ are parameterized separately for each fit component with shape parameters $\vec{\alpha}_i$ for M_{B} and $\vec{\beta}_i$ for ct. The yields n_i are then determined by minimizing the quantity $-\ln \mathcal{L}$ with respect to the signal yields and a subset of the PDF parameters Antcheva et al. (2009). The ansatz to express the probabilities for each component in terms of the product PDF of the event variables has been verified with simulated events. The linear correlation coefficients between the event variables in signal and prompt background are found to be 1.2% and 1.8%, respectively. The correlations in signal and any individual or combined B background components do not exceed 8%. Therefore, they are assumed to have a negligible impact on the fit,

---

[*] The $N!$ term in the expression is omitted because does not depend on the parameters.

and potential biases arising from this assumption are accounted for in the systematic uncertainty on the fitted signal yield, as described later.

5.3 Probability Density Functions

The PDFs are constructed from common functions (Gaussian, exponential, etc) and the parameters are initially determined from the MC samples. For the final fit, shape parameters are either obtained from data and fixed or let free to float. The guiding principle in designing the PDFs is to use the simplest function with the least number of parameters necessary to adequately describe the observed distribution of events in $M_{\mathrm{J}/\psi\phi}$ and ct for each component.

5.3.1 J/ψ ϕ Invariant Mass

For the signal the sum of two Gaussian functions is used to parameterize the J/ψ ϕ invariant mass shape (see Figure 5.1 on the left). This choice well describes the variable distribution and it has been verified in early data when the J/ψ ϕ invariant mass peak parameters have been measured and found to be consistent with the PDG value CMS Collaboration (2010b). Alternative parameterizations (single and triple Gaussian functions) have been use for cross-check and to establish systematic uncertainties. As shown in Figure 4.17, for the non-prompt B background a 2^{nd} order Chebychev polynomial function has been chosen (see also Figure 5.2 on the left). The prompt J/ψ background is well parametrized by a 1^{st} order Chebychev polynomial function (see Figure 5.3 on the left). Table 5.2 lists the functional forms used to define the PDFs for the J/ψ ϕ invariant mass.

5.3.2 Proper Decay Length ct

For the signal, the ct PDF is a single exponential parameterized in terms of the proper decay length ($c\tau$). It is convolved with a resolution function that is a combination of two Gaussian functions to account for a dominant core and small outlier distribution. The core fraction is varied in the fit and found to be consistently larger than 95%, as shown in Figure 5.1 on the right. The ct distribution for the non-prompt J/ψ background is described by a sum of two exponentials, with effective lifetimes that are allowed to be different (see Figure 5.2 on the right). The long-lifetime exponential corresponds to decays of b-hadrons to a J/ψ plus some charged particles that survive the ϕ selection, while the short-lifetime exponential accounts for events where the muons from the J/ψ decay are wrongly combined with hadron tracks originating from the pp collision point. The exponential functions are convolved with a resolution function with the same parameters as the signal. For the prompt J/ψ component the pure resolution function is used, as shown in Figure 5.3 on the right. Table 5.3 list the functional forms used to define the PDFs for the proper decay length.

Table 5.2: Summary of the functional forms for the $M_{\mathrm{J}/\psi\phi}$ distributions in the sample components. Only the signal shape has been fixed from Monte Carlo. $\{\mu,\sigma\}$ are the {mean, standard deviation} for a gaussian, a_i are constants.

Component	PDF $M_{\mathrm{J}/\psi\phi}$	Parameters
Signal	$f\ e^{-\frac{(x-\mu_1)^2}{2\sigma_1^2}}+(1-f)e^{-\frac{(x-\mu_2)^2}{2\sigma_2^2}}$	$\mu_1, \sigma_1, \mu_2, \sigma_2, f$
B background	$a_0 x + a_1 x^2$	a_0, a_1
Prompt J/ψ	$a_2 x$	a_2

Table 5.3: The ct PDFs used in the fit. The common ct resolution function $\mathcal{R}$ is defined as the sum of two Gaussians, one for the core and one for the tail. The core Gaussian is common for signal and background, the ratio between the two is floated independently. By definition $\lambda_i = c\tau$, where $i = B, 1, 2$.

Component	PDF ct	Parameters
Signal	$\mathcal{R} \otimes e^{-ct/\lambda_B}$	$\mu_1, \sigma_1, \mu_2, \sigma_2, f; \lambda_B$
B background	$\mathcal{R} \otimes (f_{12}e^{-ct/\lambda_1} + (1-f_{12})e^{-ct/\lambda_2})$	$\mu_1, \sigma_1, \mu_2, \sigma_2, f; f_{12}, \lambda_1, \lambda_2$
Prompt J/ψ	$\mathcal{R}$	$\mu_1, \sigma_1, \mu_2, \sigma_2, f$

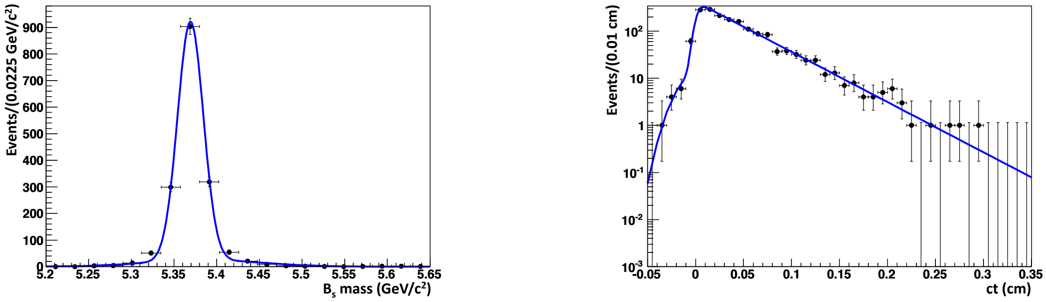

Figure 5.1: Fits to determine preliminary PDF parameters for $M_{\mathrm{J}/\psi\phi}$ (left) and ct (right) in signal Monte Carlo.

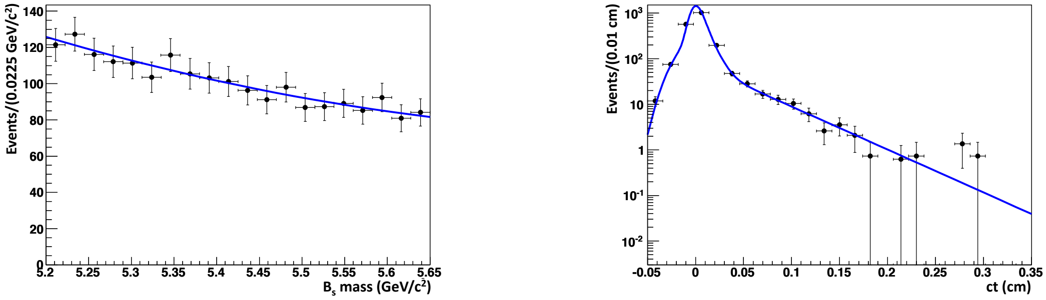

Figure 5.2: Fits to determine preliminary PDF parameters for $M_{\mathrm{J}/\psi\phi}$ (left) and ct (right) in a combined B background set where the events from different sources contribute according to an estimated expectation for 40 pb^{-1}.

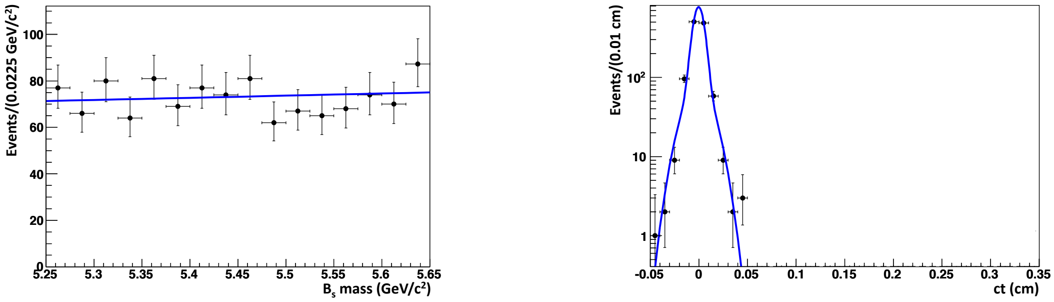

Figure 5.3: Fits to determine preliminary PDF parameters for $M_{\mathrm{J}/\psi\phi}$ (left) and ct (right) in J/ψ prompt background events.

5.4 Data-driven Procedure to Determine PDF Parameters

To minimize the dependency on the MC simulation most of the shapes are parameterize from data. To accomplish this goal, regions in $M_{\mathrm{J}/\psi\phi}$ that are separated by more than four times the width of the observed B_s^0 signal from the mean peak position ($M_{\mathrm{J}/\psi\phi}$ sidebands) are identified. The intervals, shown in Figure 5.4, are defined as follows: $5.20 < M_{\mathrm{J}/\psi\phi} < 5.29$ GeV/c^2 and $5.45 < M_{\mathrm{J}/\psi\phi} < 5.65$ GeV/c^2. This data-driven technique proceeds in several steps and relies on the assumption that in the $M_{\mathrm{J}/\psi\phi}$ sidebands there are only two contributions: prompt J/ψ and combinatorial B background. From the sidebands it is possible to extract the ct resolution function parameters and the lifetime parameters describing the non-prompt B background events simultaneously. The resolution function is common for the

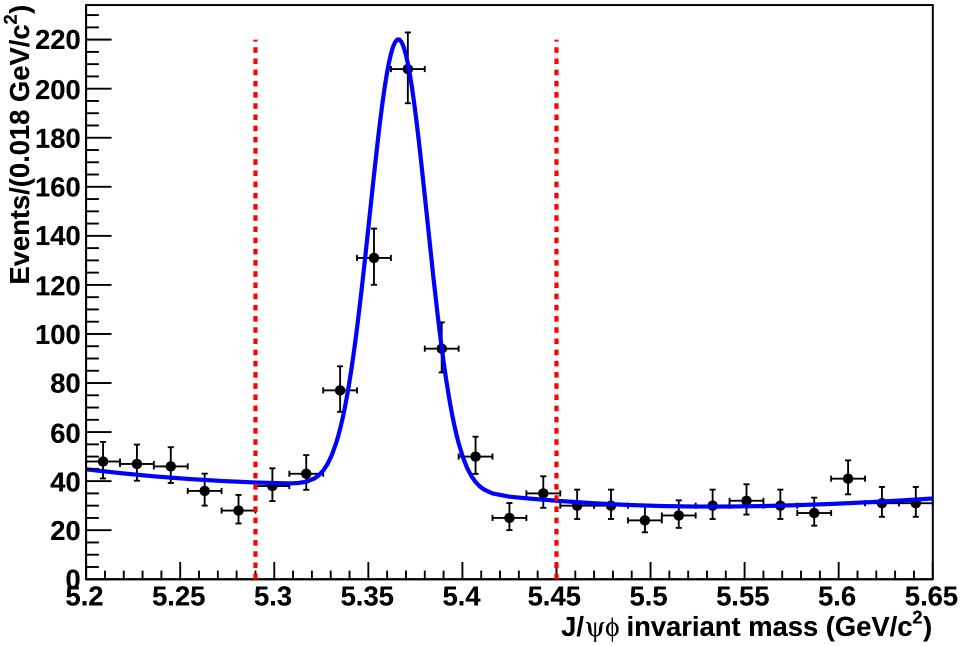

Figure 5.4: The invariant J/ψ ϕ mass distribution for selected candidate events with $ct > 0.01$ cm. The dashed lines indicate the limits for the sideband regions.

prompt and non-prompt J/ψ background components. The upper and lower sideband regions have been separately tested for the extraction of the resolution function parameters. Because of the agreement of the distributions, as shown in Figure 5.5, events from the two regions are combined. From simulations it is found that a double gaussian function adequately describes the resolution in all components. The parameters of the core Gaussian are common; the tail contribution is found negligible in the signal. The ratio f between the two Gaussian functions is left free to float for the signal resolution function and found to have value of $f = 0.0 \pm 0.6$. This suggests that a single Gaussian is the dominant contribution and a double Gaussian function is in agreement with the B background within the uncertainty. The overall width of the core Gaussian (in the interval $8 < p_{\mathrm{T}} < 50$ GeV/c and $|y^{\mathrm{B}}| < 2.4$) is (44.7 ± 3.1) μm in good agreement with the residual (see Figure 4.10 for a comparison).

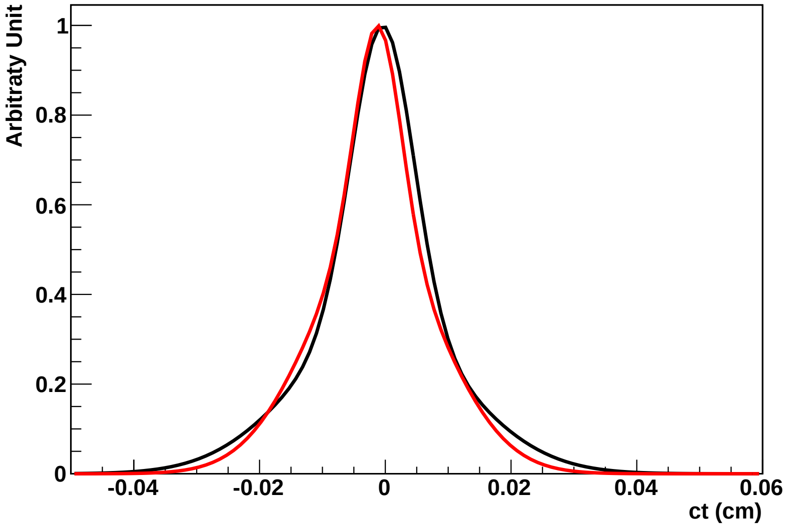

Figure 5.5: Overlaid PDFs for the proper decay length ct as obtained from the fit to the upper (black) and lower (red) mass sidebands, separately.

The fit for the extraction of the PDF parameters proceeds in three steps:

Step 1 – Fit the ct event distribution in the sideband regions for all candidates with $8 < p_{\mathrm{T}}^{\mathrm{B}} < 50$ GeV/c and $|y^{\mathrm{B}}| < 2.4$, assuming two components (prompt and non-prompt J/ψ) to obtain the parameters describing the lifetime of the combinatorial B background (two lifetime parameters). In this fit the parameters of the resolution function, which is the same for both components, are varied freely.

Step 2 – Fix the lifetime parameters obtained in `Step 1` and fit ct in the mass sideband separately in each bin of $p_{\mathrm{T}}^{\mathrm{B}}$ and $|y^{\mathrm{B}}|$ to obtain the p_{T}- and $|y^{\mathrm{B}}|$-dependent resolution function parameters.

Step 3 – Fix all the ct PDF parameters that were determined in `Step 1` and `Step 2`, and perform the fit to the full mass range, including the signal region, to obtain the signal yield in each bin of $p_{\mathrm{T}}^{\mathrm{B}}$ (or $|y^{\mathrm{B}}|$). The floating parameters in this fit are the yields for each individual component, the signal decay length, and the parameters that define the shapes of the $M_{\mathrm{J}/\psi\phi}$ distributions for the prompt and combinatorial backgrounds. The signal $M_{\mathrm{J}/\psi\phi}$ shape is determined from MC events in each $p_{\mathrm{T}}^{\mathrm{B}}$ and $|y^{\mathrm{B}}|$ bin while the signal lifetime is fixed to the value fitted from the full $p_{\mathrm{T}}^{\mathrm{B}}$ and $|y^{\mathrm{B}}|$ range for each bin.

Tables 5.4-5.5 summarize the parameters determined in each of the ct fits in the $M_{\mathrm{J}/\psi\phi}$ sideband regions, while Figures 5.6-5.8 show the results obtained from the fits.

Table 5.4: Summary of the background ct parameters determined by fitting the lower and the upper $M_{\mathrm{J}/\psi\phi}$ sideband in data for different bins in $p_{\mathrm{T}}^{\mathrm{B}}$. The parameters of the resolution function $\mathcal{R}$ for Bin 4 have been fixed to the ones found in Bin 3 for lack of statistics.

Parameter	$8 < p_{\mathrm{T}}^{\mathrm{B}} < 50$ GeV/c	Bin 1	Bin 2	Bin 3
f	0.381 ± 0.061	0.369 ± 0.061	0.491 ± 0.092	0.386 ± 0.227
$\mu_{\mathrm{tail}}\,(\mu\mathrm{m})$	-18.1 ± 16.4	-31.2 ± 19.4	-18.0 ± 23.2	-10.6 ± 42.6
$\mu_{\mathrm{core}}\,(\mu\mathrm{m})$	-5.7 ± 4.4	-11.1 ± 8.0	-2.9 ± 7.3	-6.6 ± 8.9
$\sigma_{\mathrm{tail}}\,(\mu\mathrm{m})$	126.4 ± 6.1	133.6 ± 8.2	103.4 ± 8.7	95.0 ± 14.8
$\sigma_{\mathrm{core}}\,(\mu\mathrm{m})$	44.7 ± 3.1	48.6 ± 4.4	34.2 ± 5.8	35.4 ± 7.7
$c\tau_1\,(\mu\mathrm{m})$	48.9 ± 2.1	fixed	fixed	fixed
$c\tau_2\,(\mu\mathrm{m})$	355 ± 44	fixed	fixed	fixed
σ_{RMS}	75.8 ± 13.7	80.0 ± 15.9	68.2 ± 18.2	58.4 ± 37.3

Table 5.5: Summary of the background ct parameters determined by fitting the lower and the upper $M_{\mathrm{J}/\psi\phi}$ sideband in data for different bins in $|y^{\mathrm{B}}|$.

Parameter	$0 < \lvert y^{\mathrm{B}} \rvert < 2.4$	Bin 1	Bin 2	Bin 3	Bin 4
f	0.381 ± 0.061	0.257 ± 0.131	0.455 ± 0.062	0.213 ± 0.104	0.613 ± 0.089
$\mu_{\mathrm{tail}}\,(\mu\mathrm{m})$	-18.1 ± 16.4	-28.6 ± 28.5	3.3 ± 7.1	-76.3 ± 62.3	-13.9 ± 26.5
$\mu_{\mathrm{core}}\,(\mu\mathrm{m})$	-5.7 ± 4.4	-16.5 ± 7.2	3.7 ± 2.8	-13.7 ± 18.2	-3.4 ± 10.2
$\sigma_{\mathrm{tail}}\,(\mu\mathrm{m})$	126.4 ± 6.1	94.8 ± 12.6	124.0 ± 8.5	143.5 ± 22.4	128.1 ± 8.2
$\sigma_{\mathrm{core}}\,(\mu\mathrm{m})$	44.7 ± 3.1	36.6 ± 5.2	43.5 ± 4.1	59.7 ± 8.4	35.8 ± 6.7
$c\tau_1\,(\mu\mathrm{m})$	48.9 ± 2.1	fixed	fixed	fixed	fixed
$c\tau_2\,(\mu\mathrm{m})$	355 ± 44	fixed	fixed	fixed	fixed
σ_{RMS}	75.8 ± 13.7	51.6 ± 28.1	80.1 ± 14.4	77.5 ± 41.2	92.4 ± 22.7

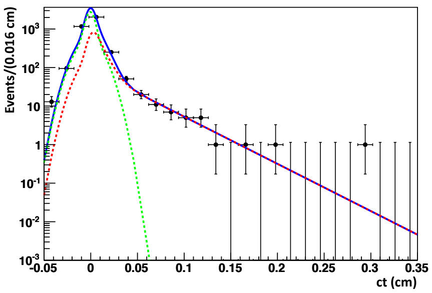

Figure 5.6: Results of fitting ct in the lower and upper sideband of $M_{\mathrm{J}/\psi\phi}$ for events with $8 < p_{\mathrm{T}} < 50$ GeV/c and $|y^{\mathrm{B}}| < 2.4$ in order to determine the parameters of $\mathcal{R}$ separately in each bin. Individual contributions from the various components are shown in different colors: B background (red), and J/ψ prompt background (dashed green).

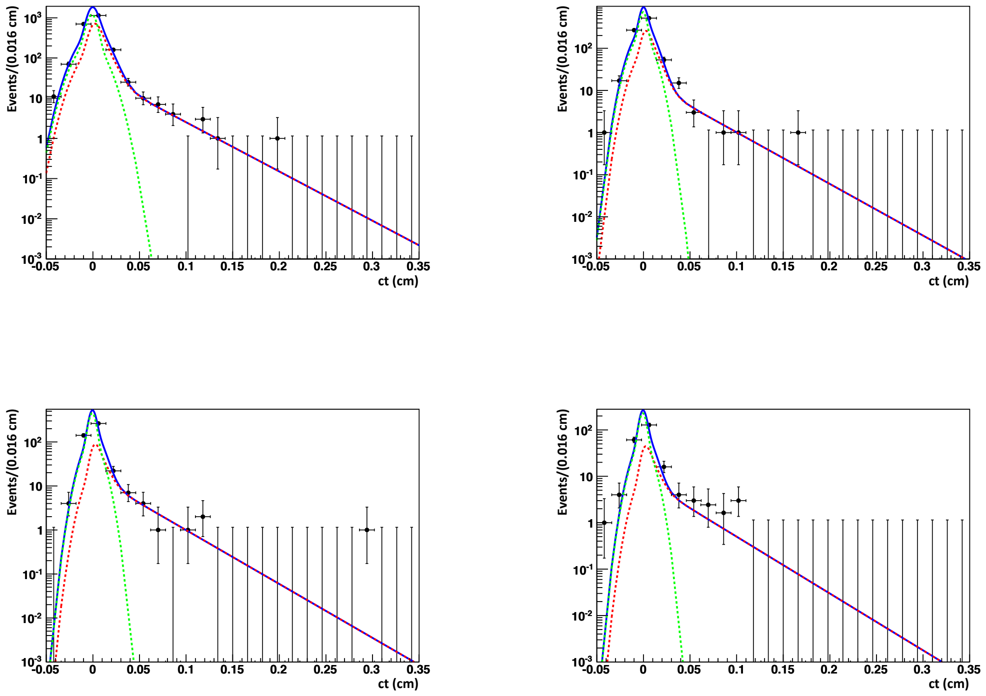

Figure 5.7: Results of fitting ct in the lower and upper sideband of $M_{\mathrm{J}/\psi\phi}$ for events in the four bins of $p_{\mathrm{T}}^{\mathrm{B}}$ in order to determine the parameters of $\mathcal{R}$ separately in each bin. The bins are: 8–12, 12–16, 16–23, and 23–50 (GeV/c). Individual contributions from the various components are shown in different colors: B background (red), and J/ψ prompt background (dashed green).

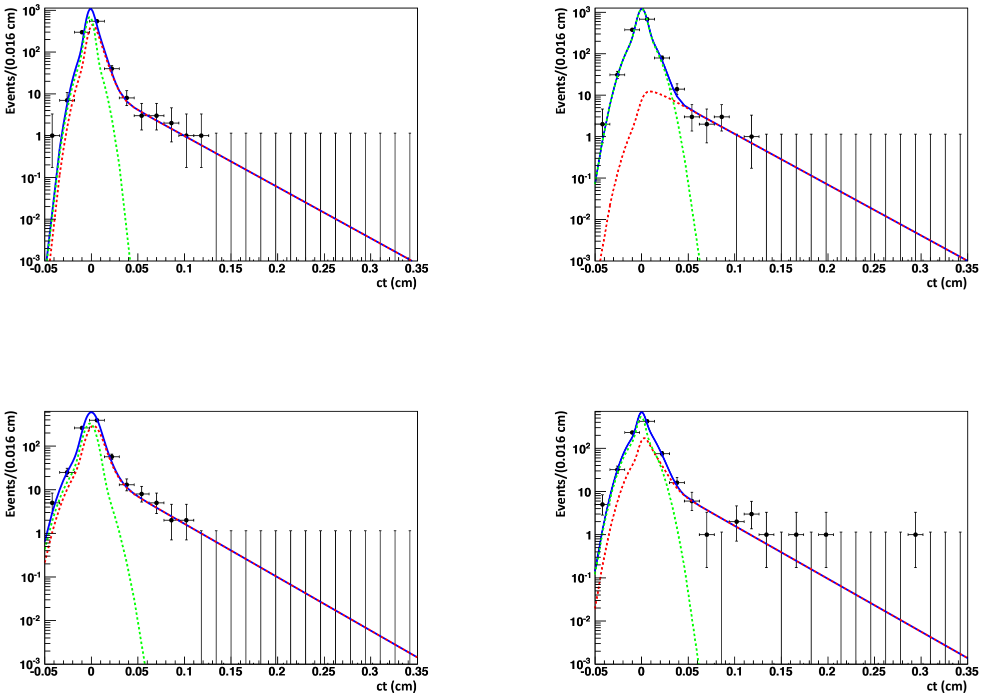

Figure 5.8: Results of fitting ct in the lower and upper sideband of $M_{\mathrm{J}/\psi\phi}$ for events in the four bins of $|y^{\mathrm{B}}|$ in order to determine the parameters of $\mathcal{R}$ separately in each bin. The bins are: 0.0–0.8, 0.8–1.4, 1.4–1.7, and 1.7–2.4. Individual contributions from the various components are shown in different colors: B background (red), and J/ψ prompt background (dashed green).

5.5 The Minimization

In this section, the fit results to the full data sample and to the $p_{\mathrm{T}}^{\mathrm{B}}$ and $|y^{\mathrm{B}}|$ bins are presented; Table 5.6 lists the numerical results. Figure 5.9 shows the projections of the fit components to the full data range in $p_{\mathrm{T}}^{\mathrm{B}}$ and $|y^{\mathrm{B}}|$. Figure 5.10 and Table 5.7 summarize the results for the fits in bins of $p_{\mathrm{T}}^{\mathrm{B}}$, while Figure 5.11 and Table 5.8 for the fits in bins of $|y^{\mathrm{B}}|$. In Appendix, the plots of the J/ψ ϕ invariant mass projections without requirement on ct in bins of $p_{\mathrm{T}}^{\mathrm{B}}$ (Figure A.1) and $|y^{\mathrm{B}}|$ (Figure A.2) are shown.

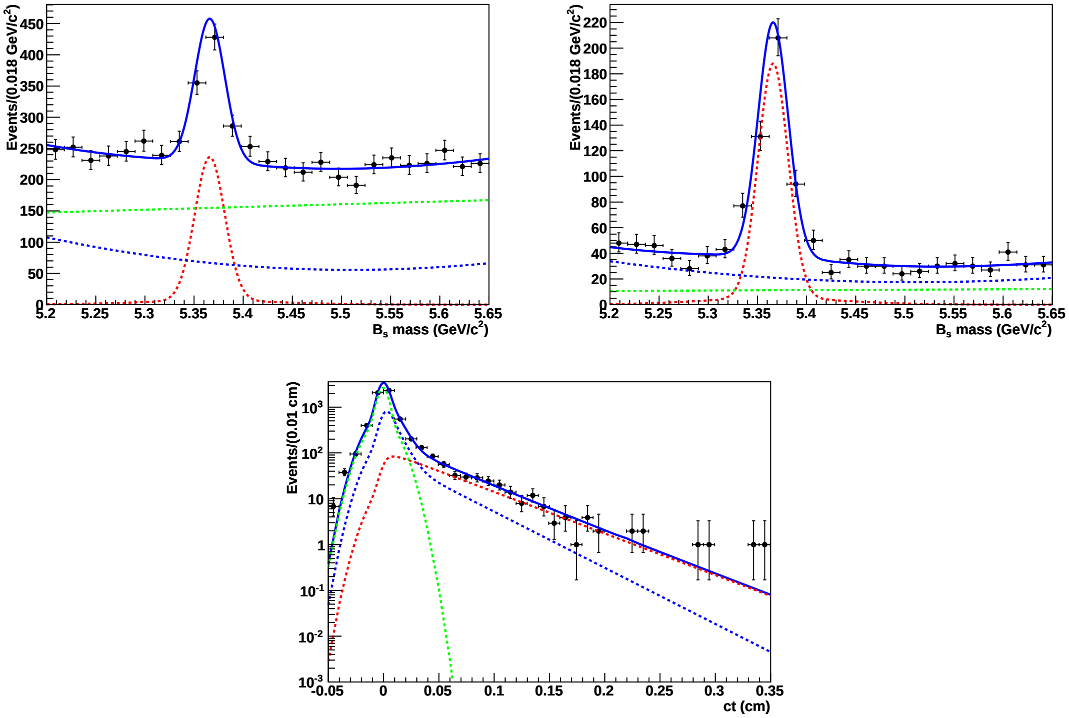

Figure 5.9: Projections of the fit results in $M_{\mathrm{J}/\psi\phi}$ (left), $M_{\mathrm{J}/\psi\phi}$ with the requirement $ct > 0.01$ cm (center) and scale the yields accordingly, and ct (right) for the full range of $8 < p_{\mathrm{T}}^{\mathrm{B}} < 50$ GeV/c and $|y^{\mathrm{B}}| < 2.4$. Individual contributions from the various components are shown in different colors: signal (red), B background (dashed blue), and J/ψ prompt background (dashed green).

Table 5.6: Summary of signal and background yields determined by fitting simultaneously $M_{\mathrm{J}/\psi\phi}$ and ct for all events satisfying $8 < p_{\mathrm{T}}^{\mathrm{B}} < 50$ GeV/c and $|y^{\mathrm{B}}| < 2.4$.

Parameter	$8 < p_{\mathrm{T}}^{\mathrm{B}} < 50$ GeV/c,$\lvert y^{\mathrm{B}}\rvert < 2.4$
N_{sig}	548.8 ± 32.0
N_{prompt}	3935 ± 109
$N_{\mathrm{Bbackground}}$	1716 ± 105
$\lambda = c\tau$	478.4 ± 25.5

Table 5.7: Summary of signal and background yields determined by fitting simultaneously $M_{\mathrm{J}/\psi\phi}$ and ct in bins of $p_{\mathrm{T}}^{\mathrm{B}}$.

Parameter	Bin 1	Bin 2	Bin 3	Bin 4
N_{sig}	137.6 ± 16.0	175.9 ± 16.6	162.3 ± 15.8	85.5 ± 11.4
N_{prompt}	1848 ± 92	890 ± 54	536 ± 33	184 ± 21
$N_{\mathrm{Bbackground}}$	1389 ± 92	459 ± 53	175 ± 30	160 ± 23

Table 5.8: Summary of signal and background yields determined by fitting simultaneously $M_{\mathrm{J}/\psi\phi}$ and ct in bins of $|y^{\mathrm{B}}|$.

Parameter	Bin 1	Bin 2	Bin 3	Bin 4
N_{sig}	150.6 ± 14.7	143.7 ± 15.4	129.3 ± 15.4	138.8 ± 16.5
N_{prompt}	654 ± 50	1759 ± 44	580 ± 54	811 ± 54
$N_{\mathrm{Bbackground}}$	745 ± 52	72 ± 16	641 ± 57	376 ± 54

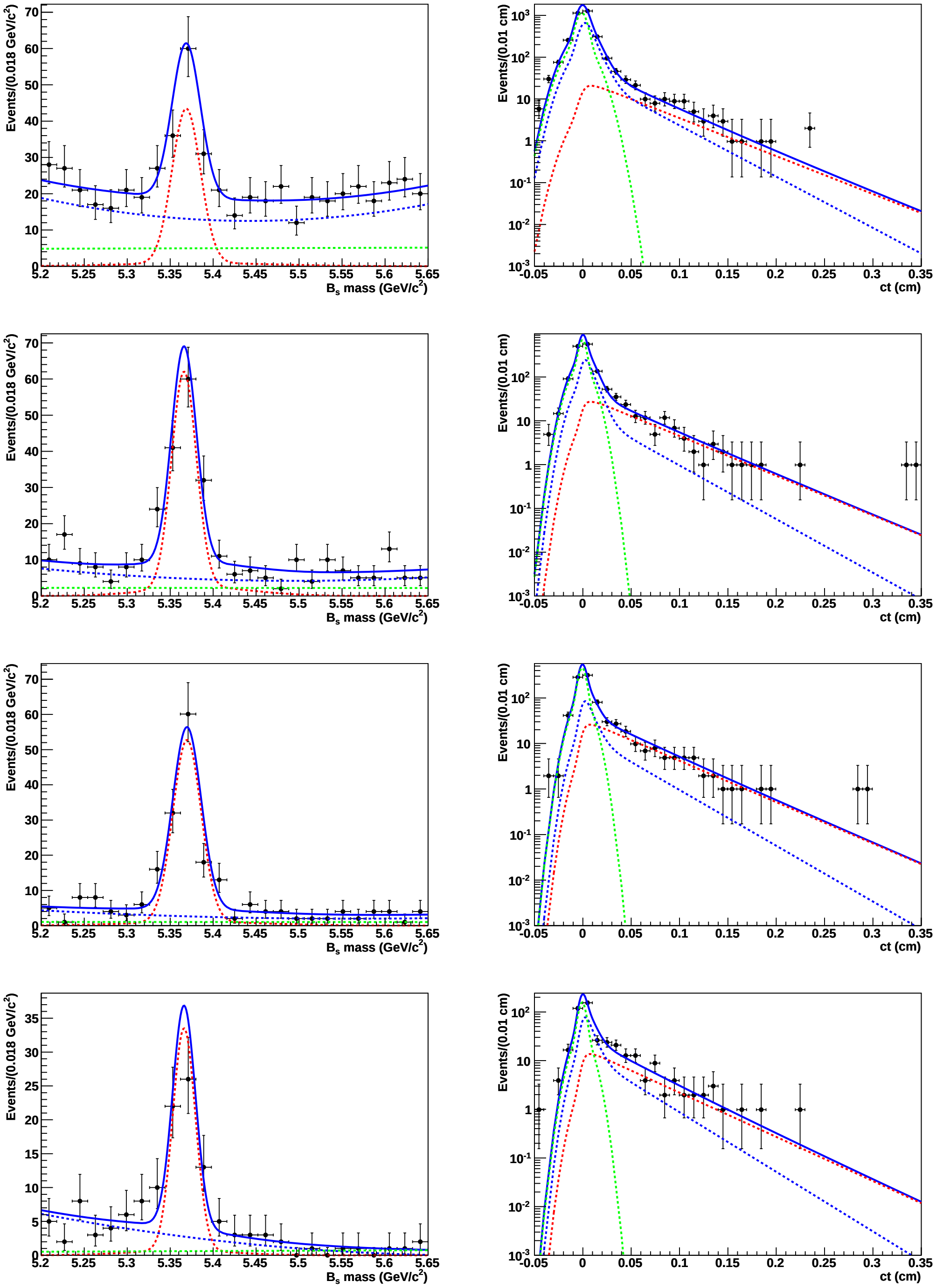

Figure 5.10: Projections of the fit results in $M_{\mathrm{J}/\psi\phi}$ (left) with the requirement $ct > 0.01$ cm and scale the yields accordingly, and ct (right) for the $\mathrm{B}_{\mathrm{s}}^{0}$ fits in four different p_{T} bins (from top to bottom): 8–12, 12–16, 16–23, and 23–50 (GeV/c). Individual contributions from the various components are shown in different colors: signal (red), B background (dashed blue), and J/ψ prompt background (dashed green).

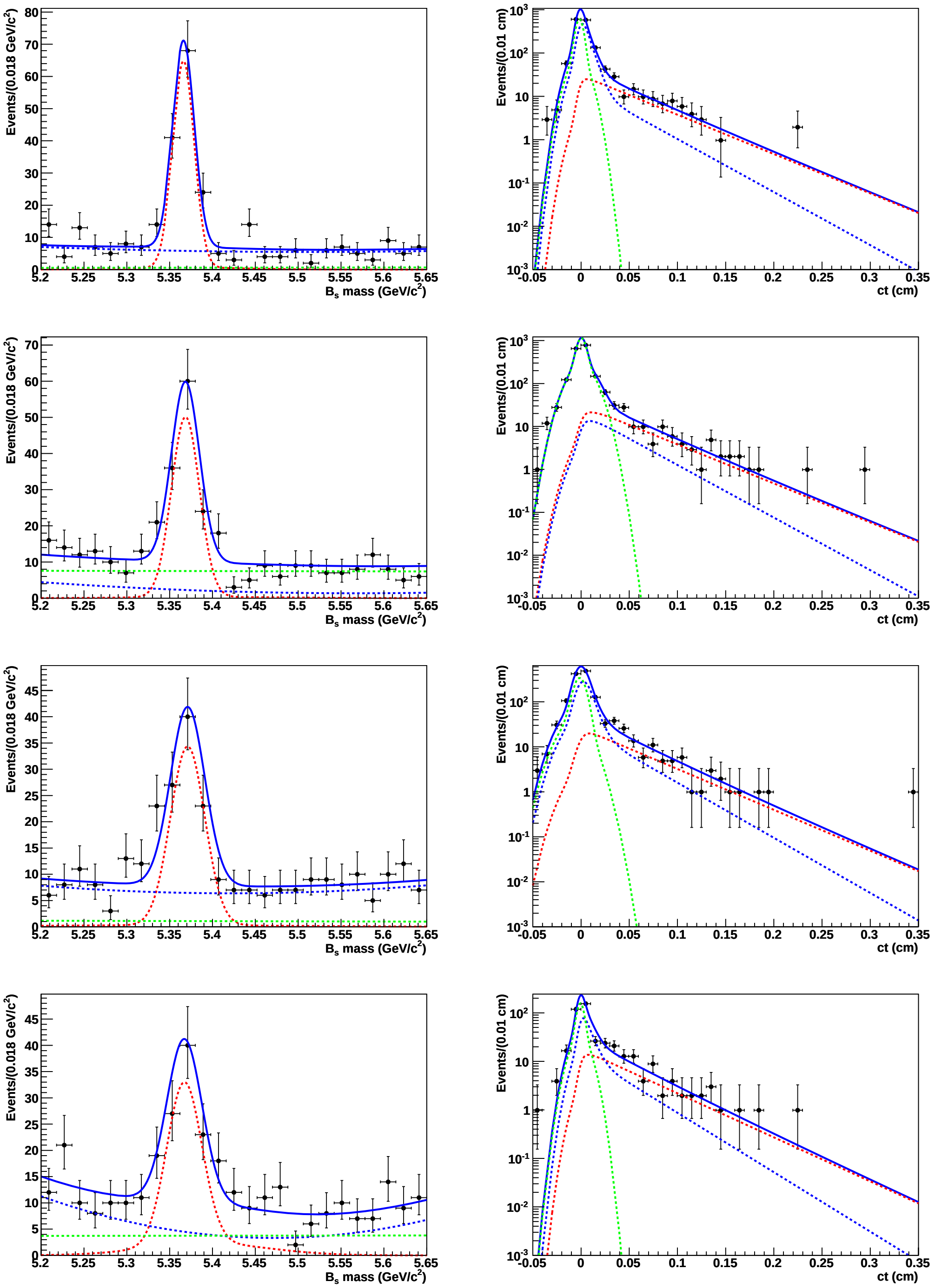

Figure 5.11: Projections of the fit results in $M_{\mathrm{J}/\psi\phi}$ (left) with the requirement $ct >$ 0.01 cm and scale the yields accordingly, and ct (right) for the B_s^0 fits in four different $|y^{\mathrm{B}}|$ bins (from top to bottom): 0–0.8, 0.8–1.4, 1.4–1.7, and 1.7–2.4. Individual contributions from the various components are shown in different colors: signal (red), B background (dashed blue), and J/ψ prompt background (dashed green).

5.6 Fit Validation and Tests of the Analysis Procedure

The following section describes several tests of the fit convergence and stability and several cross-checks of the PDF parameterization, the peaking B background, and the resolution function $\mathcal{R}$.

5.6.1 Fit Validation

Stability of the Fit

To test the stability of the fitting procedure, the fits for all samples have been repeated on events that have been generated from the PDFs (toy experiments). Four hundred of such fits have been performed and the distribution of the yields inspected. No significant bias was found: the yields and their uncertainties are in agreement with the central fits. The yield distributions of these experiments are listed in Figure 5.12 for the total fit, in Figure 5.13 for the $p_{\mathrm{T}}^{\mathrm{B}}$ bins, and in Figure 5.14 for the $|y^{\mathrm{B}}|$ bins. Tables 5.9 and 5.11 list the numerical results for these toy experiments.

Potential bias due to residual correlations between $M_{\mathrm{J}/\psi\phi}$ and ct in signal events has been tested by combining full-detector simulated signal and background events in the expected ratio (mock fit). Due to the finite size of the signal and background samples, some oversampling was accepted in this study. Since oversampling tends to amplify correlations, the results are considered a conservative upper limit. The fitted yields for the total spectrum and the four bins in $p_{\mathrm{T}}^{\mathrm{B}}$ and $|y^{\mathrm{B}}|$ are consistent with the input values as listed in Table 5.10-5.12.

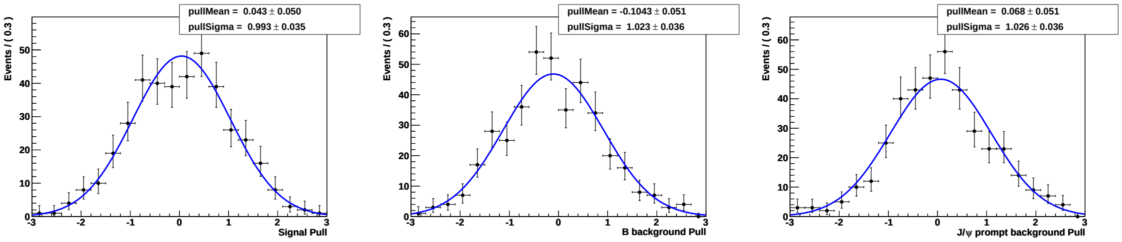

Figure 5.12: Pull distributions $(n_{\text{fit}} - \langle n \rangle)/\sigma_{\text{fit}}$ for 400 toy experiments simulating the final fit (the sideband fitting procedure in these studies has not been replicated). From left to right within a given row the pull distribution for signal, B background, and prompt J/ψ for $8 < p_{\mathrm{T}}^{\mathrm{B}} < 50$ GeV/c and $|y^{\mathrm{B}}| < 2.4$ are plotted.

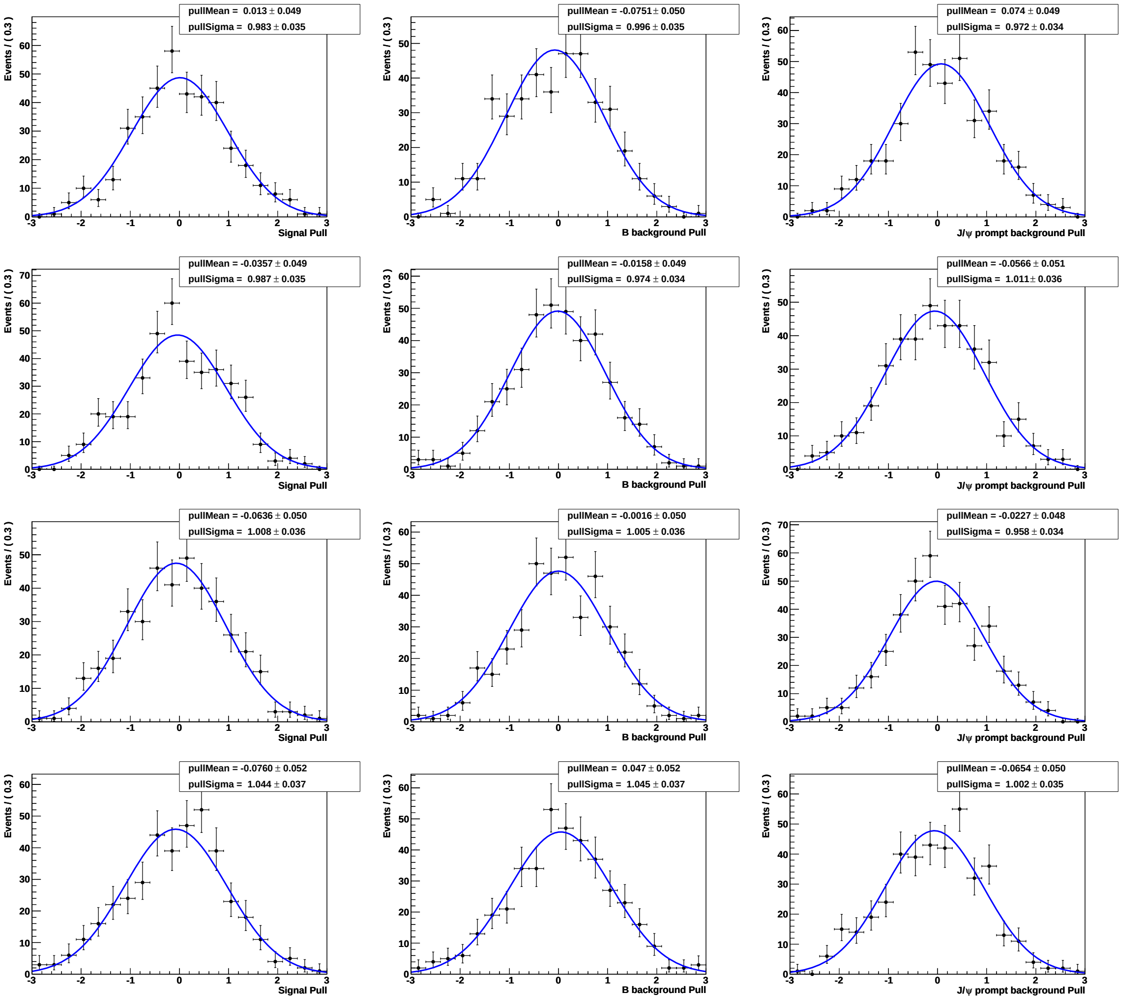

Figure 5.13: Pull distributions $(n_{\mathrm{fit}} - \langle n \rangle)/\sigma_{\mathrm{fit}}$ for 400 toy experiments simulating the final fit (the sideband fitting procedure in these studies has not been replicated). From the top to the bottom row the four $p_{\mathrm{T}}^{\mathrm{B}}$ bins (in GeV/c): 8–12, 12–16, 16–23, and 23–50. Also $|y^{\mathrm{B}}| < 2.4$ is required. From left to right within a given row the pull distributions for signal, B background, and prompt J/ψ are plotted.

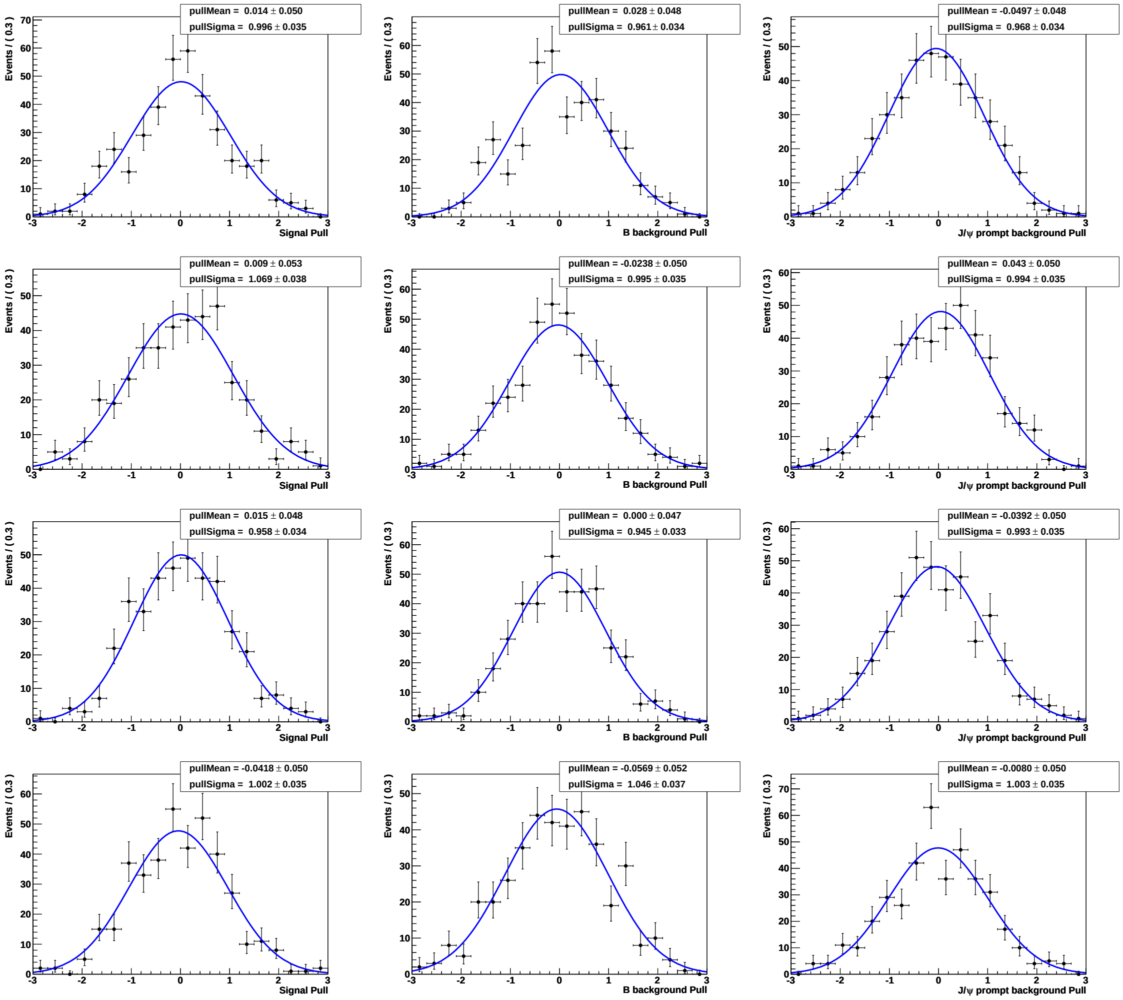

Figure 5.14: Pull distributions $(n_{\mathrm{fit}} - \langle n \rangle)/\sigma_{\mathrm{fit}}$ for 400 toy experiments simulating the final fit (the sideband fitting procedure in these studies has not been replicated). From the top to the bottom row the four $|y^{\mathrm{B}}|$ bins: 0.0–0.8, 0.8–1.4, 1.4–1.7, and 1.7–2.4. From left to right within a given row the pull distributions for signal, B background, and prompt J/ψ are plotted.

Table 5.9: Summary table of the pull distributions $(n_{\text{fit}} - \langle n \rangle)/\sigma_{\text{fit}}$ for 400 toy experiments simulating the final fit in the full range, and each of the p_{T}^{B} bins for the three components.

Parameter	$8 < p_{\text{T}}^{\text{B}} < 50$ GeV/c	Bin 1	Bin 2	Bin 3	Bin 4
N_{sig}	553 ± 30	138 ± 17	173 ± 16	161 ± 15	84 ± 11
μ_{pull}^{sig}	0.043 ± 0.050	0.013 ± 0.049	-0.036 ± 0.049	-0.064 ± 0.050	-0.076 ± 0.052
$\sigma_{\text{pull}}^{sig}$	0.993 ± 0.035	0.983 ± 0.035	0.987 ± 0.035	1.008 ± 0.036	1.044 ± 0.037
N_{Bbkg}	1703 ± 102	1845 ± 97	458 ± 52	175 ± 27	162 ± 19
μ_{pull}^{Bbkg}	-0.104 ± 0.051	-0.075 ± 0.050	0.016 ± 0.049	-0.002 ± 0.050	0.047 ± 0.052
$\sigma_{\text{pull}}^{Bbkg}$	1.023 ± 0.036	0.996 ± 0.035	0.974 ± 0.034	1.005 ± 0.036	1.045 ± 0.037
N_{prompt}	3943 ± 107	1397 ± 97	887 ± 54	535 ± 32	183 ± 18
$\mu_{\text{pull}}^{prompt}$	0.068 ± 0.051	0.074 ± 0.049	-0.057 ± 0.051	0.023 ± 0.048	-0.006 ± 0.050
$\sigma_{\text{pull}}^{prompt}$	1.026 ± 0.036	0.972 ± 0.034	1.011 ± 0.036	0.958 ± 0.034	1.002 ± 0.035

Table 5.10: Summary table for toy experiments (in bins of $p_{\mathrm{T}}^{\mathrm{B}}$) with signal and background events embedded from Monte Carlo datasets. In parentheses the number of embedded events in each category.

Parameter	Full spectrum	Bin 1	Bin 2	Bin 3	Bin 4
N_{sig}	549 ± 33 (550)	141 ± 17 (140)	179 ± 16 (175)	163 ± 15 (160)	97 ± 11 (90)
N_{Bbkg}	1370 ± 97 (1400)	1380 ± 90 (1340)	460 ± 53 (430)	143 ± 27 (145)	65 ± 12 (70)
N_{prompt}	4337 ± 106 (4400)	1914 ± 90 (1940)	887 ± 54 (900)	566 ± 32 (570)	267 ± 19 (270)

Table 5.11: Summary table of the pull distributions $(n_{\mathrm{fit}} - \langle n \rangle)/\sigma_{\mathrm{fit}}$ for 400 toy experiments simulating the final fit in each of the $|y^{\mathrm{B}}|$ bins for the three components.

Parameter	Bin 1	Bin 2	Bin 3	Bin 4
N_{sig}	151 ± 15	144 ± 15	129 ± 15	139 ± 16
$\mu^{sig}_{\mathrm{pull}}$	0.014 ± 0.050	0.020 ± 0.052	0.015 ± 0.048	-0.042 ± 0.050
$\sigma^{sig}_{\mathrm{pull}}$	0.996 ± 0.035	1.030 ± 0.036	0.958 ± 0.034	1.002 ± 0.035
N_{Bbkg}	746 ± 51	72 ± 16	642 ± 55	374 ± 45
$\mu^{Bbkg}_{\mathrm{pull}}$	0.028 ± 0.048	0.024 ± 0.050	0.000 ± 0.047	-0.057 ± 0.052
$\sigma^{Bbkg}_{\mathrm{pull}}$	0.961 ± 0.034	0.995 ± 0.035	0.945 ± 0.033	1.046 ± 0.037
N_{prompt}	651 ± 49	1762 ± 44	570 ± 53	810 ± 48
$\mu^{prompt}_{\mathrm{pull}}$	-0.049 ± 0.048	0.043 ± 0.050	-0.039 ± 0.050	-0.008 ± 0.050
$\sigma^{prompt}_{\mathrm{pull}}$	0.968 ± 0.034	0.994 ± 0.035	0.993 ± 0.035	1.003 ± 0.035

Table 5.12: Summary table for toy experiments (in bins of $|y^{\mathrm{B}}|$) with signal and background events embedded from Monte Carlo datasets. In parentheses the number of embedded events in each category.

Parameter	Bin 1	Bin 2	Bin 3	Bin 4
N_{sig}	153 ± 16 (150)	144 ± 16 (145)	131 ± 16 (130)	139 ± 17 (140)
N_{Bbkg}	648 ± 52 (650)	1763 ± 45 (1760)	578 ± 55 (580)	801 ± 55 (800)
N_{prompt}	758 ± 53 (760)	68 ± 16 (70)	639 ± 57 (640)	379 ± 55 (380)

Goodness of the Fit

From the fit to data, a negative log likelihood value of NLL=-71567 is extracted. Figure 5.15 shows the negative log likelihood value from a series of toy experiments performed with yields and floating parameters as in the fit to the full $p_{\mathrm{T}}^{\mathrm{B}}$ and $|y^{\mathrm{B}}|$ range. The likelihood value from the fit to data (red line in Figure 5.15) is close to the mean value of the distribution obtained from the toy experiments. The same comparison was conducted for each p_{T} and $|y^{\mathrm{B}}|$ bin. Results are shown in Table 5.13: $\mathcal{P}_{LH}$ is defined as the probability of having a likelihood value for the toy experiments higher than the value of the likelihood fitted on data. The statistical uncertainty in each bin is about 5%.

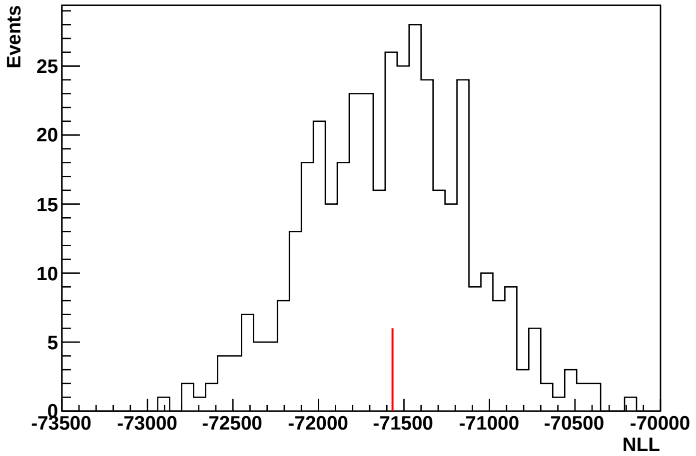

Figure 5.15: Negative log likelihood distributions from toy experiments performed with the yields and floating parameters as in the unbinned fit to data. The red line marks the value found in the fit to data.

Table 5.13: Summary of the comparison of the goodness of fit for data and toy experiments. $\mathcal{P}_{LH}$ is defined as the probability of having a likelihood value for the toy experiments higher than the value of the likelihood fitted on data.

	$\mathcal{P}_{LH}$
$p_{\mathrm{T}}^{\mathrm{B}}$ bin 1	52.5%
$p_{\mathrm{T}}^{\mathrm{B}}$ bin 2	53.8%
$p_{\mathrm{T}}^{\mathrm{B}}$ bin 3	48.0%
$p_{\mathrm{T}}^{\mathrm{B}}$ bin 4	50.8%
$\lvert y^{\mathrm{B}}\rvert$ bin 1	54.0%
$\lvert y^{\mathrm{B}}\rvert$ bin 2	52.1%
$\lvert y^{\mathrm{B}}\rvert$ bin 3	51.8%
$\lvert y^{\mathrm{B}}\rvert$ bin 4	48.5%

5.6.2 Fit Cross Checks

Maximum Likelihood Fit: 2D vs 1D

The 2D ML fit as described in Section 5.3 is compared with a ML fit based on the J/ψ ϕ invariant mass (1D fit) only. For the 1D ML fit to the J/ψ ϕ invariant mass, a double Gaussian function is used to describe the signal with parameters fixed from simulated events. The background is parameterized by a first order polynomial function without distinction for the prompt/non-prompt background components. The background components are not distinguished and parameterized by a common polynomial of order two. Figure 5.16 shows the likelihood as function of the signal yield, demonstrating that 1D fit extracts the yields with reduced statistical significance. The fit converges and the yields are in agreement between 1D and 2D fit. The statistical uncertainty of the signal yield is ±32 for the 2D fit and ±42 for the 1D fit. The relative systematic uncertainties associated with the *ct* variable parameterization in the 2D model of $(2-3\%)$ are small compared to the increase in the statistical error ($\sim 8\%$). For more details on the calculation of the systematic uncertainties see Section 5.8. Another 1D ML fit using only the *ct* variable was also performed. For the 1D ML fit on the *ct* variable, the parametrization used for the standard 2D ML fit has been adopted for all the components (signal, prompt J/ψ, and combinatorial B background). The choice of the 2D ML fit is superior in terms of signal/background discrimination and fit results uncertainty. The uncertainty in the signal yield is larger than in the two other fits. Table 5.14 lists the signal yields for the 1D ML fits, using only the J/ψ ϕ invariant mass or the *ct* variables, and the standard 2D ML.

Maximum Likelihood Fit Fixing the B Background Lifetime

The fit to the full dataset yields a signal $\mathrm{B_s^0}$ lifetime 1.4 standard deviations higher than the PDG value Nakamura et al. (2010). The fit is performed with all the parameters free to float: one of the parameters, the long B lifetime, could be source

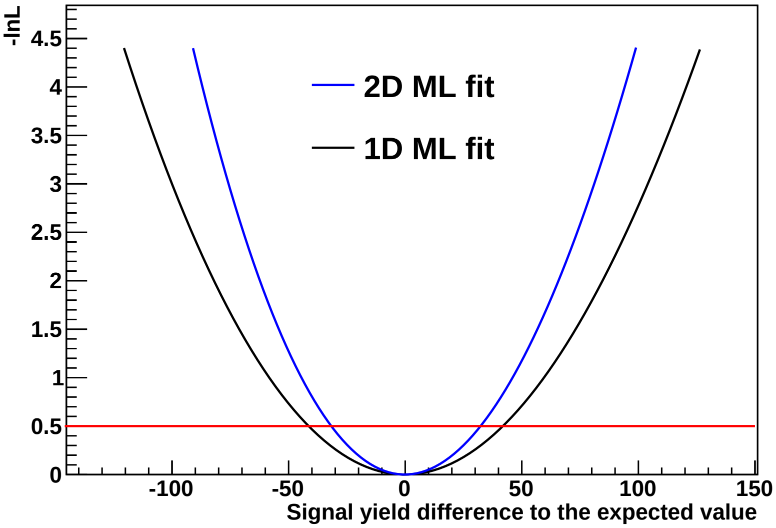

Figure 5.16: The -ln$\mathcal{L}$ ($= 0.5\chi^2$) as function of number of signal events, N_{sig}, for the 2D and the 1D ML fits.

Table 5.14: Summary table of the signal yields extracted with 1D and 2D ML fits on data in the full $p_{\mathrm{T}}^{\mathrm{B}}$-$|y^{\mathrm{B}}|$ range and in bins of $p_{\mathrm{T}}^{\mathrm{B}}$.

	Signal 1D (M_{B})	Signal 1D (ct)	Signal 2D (M_{B},ct)
Full $p_{\mathrm{T}}^{\mathrm{B}}$-$|y^{\mathrm{B}}|$ range	481 ± 42	559 ± 66	549 ± 32
$p_{\mathrm{T}}^{\mathrm{B}}$ bin 1	76 ± 28	160 ± 27	138 ± 16
$p_{\mathrm{T}}^{\mathrm{B}}$ bin 2	160 ± 20	181 ± 25	176 ± 17
$p_{\mathrm{T}}^{\mathrm{B}}$ bin 3	163 ± 19	144 ± 26	162 ± 16
$p_{\mathrm{T}}^{\mathrm{B}}$ bin 4	77 ± 12	48 ± 47	86 ± 11

of bias of the signal lifetime due to misreconstructed B background events with high values of the reconstructed proper decay length. To quantify this effect, the long B lifetime is fixed to the values of the B^0 and B^+ mesons, assuming that either of those dominates the B background. Table 5.15 shows the results obtained with the nominal fitting procedure when fixing the long B lifetime to $c\tau(B^+) = 492$ μm and $c\tau(B^0) = 450$ μm Nakamura et al. (2010). The newly measured B^0_s lifetime shows a non negligible reduction and is consistent, within the error, with the PDG value. The number of signal events is unchanged.

Table 5.15: Summary of signal and background yields determined by fitting simultaneously $M_{J/\psi\phi}$ and ct for all events satisfying $8 < p_T^B < 50$ GeV/c and $|y^B| < 2.4$ with the nominal procedure, fixing the long B lifetime to the nominal B^0 and B^+ PDG values.

Parameter	Nominal Fit	$c\tau(B^0) = 450$ μm	$c\tau(B^+) = 492$ μm
N_{sig}	549 ± 32	549 ± 32	547 ± 32
N_{prompt}	3935 ± 109	4412 ± 188	4637 ± 208
$N_{Bbackground}$	1716 ± 105	1239 ± 184	1015 ± 198
$\lambda = c\tau$	478 ± 26	465 ± 26	467 ± 26

Maximum Likelihood Fit Removing the Prompt J/ψ Background

Studies of the prompt J/ψ MC sample show that the criterion on the proper decay length ($ct > 0.01$ cm) suppresses the prompt background component significantly (about 95%). The ML fit is repeated for events selected by this criterion with only two components: signal and combinatorial B background. The $M_{J/\psi\phi}$ mass for the two components is parameterized identical to the nominal 2D ML fit. For ct, the signal is parameterized with a single exponential function (one parameter for the signal lifetime) while for the B background a double exponential function is used (with three parameters free to float, a short and a long B lifetime plus the relative fraction between the two contributions). Table 5.16 reports the numerical result for the ML fit leaving all the parameters free to float while fixing to long B lifetime to the nominal B^0 meson lifetime Nakamura et al. (2010). Figure 5.17 and Figure 5.18

show the projection plots for the J/ψ ϕ invariant mass (left) and the proper decay length *ct* (right). With this approach the signal lifetime measurement is not biased by the misreconstructed B background as in the nominal 2D fit procedure. The result is now measured within one standard deviation from the expected PDG value.

Table 5.16: Summary of signal and background yields determined by fitting simultaneously $M_{J/\psi\phi}$ and *ct* for all events satisfying $8 < p_T^B < 50$ GeV/c, $|y^B| < 2.4$, and $ct > 0.01$ cm with and without fixing the long B lifetime to the nominal B^0 value, as reported in PDG.

Parameter	Fit (all parameters free)	Fit (with $c\tau(B^0) = 450\ \mu$m)
$N_{\rm sig}$	448 ± 26	447 ± 26
$N_{\rm Bbackground}$	790 ± 32	791 ± 32
$\lambda = c\tau$	469 ± 27	460 ± 26

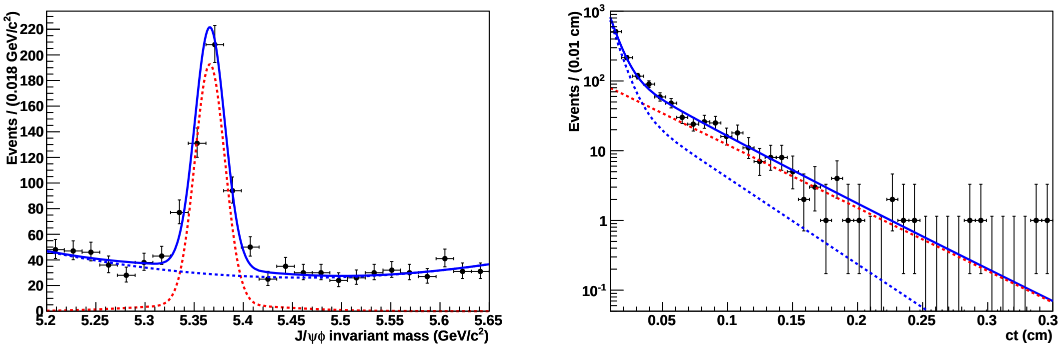

Figure 5.17: Projections of the fit results in $M_{J/\psi\phi}$ (left) and *ct* (right) for the full range of $8 < p_T^B < 50$ GeV/c and $|y^B| < 2.4$. The requirement $ct > 0.01$ cm has been applied to remove the J/ψ prompt background. All the parameters in the fit are free to float. Individual contributions from the various components are shown in different colors: signal (red), and B background (dashed blue).

Fit Projection Studies

After performing the nominal 2D ML fit, a requirement on the proper decay length is applied to visually enhance the signal over the background (for example, see Figure 5.9 in the center). To demonstrate that the number of signal and background events for any *ct* cut is correctly represented by the plots, yields are calculated in two steps:

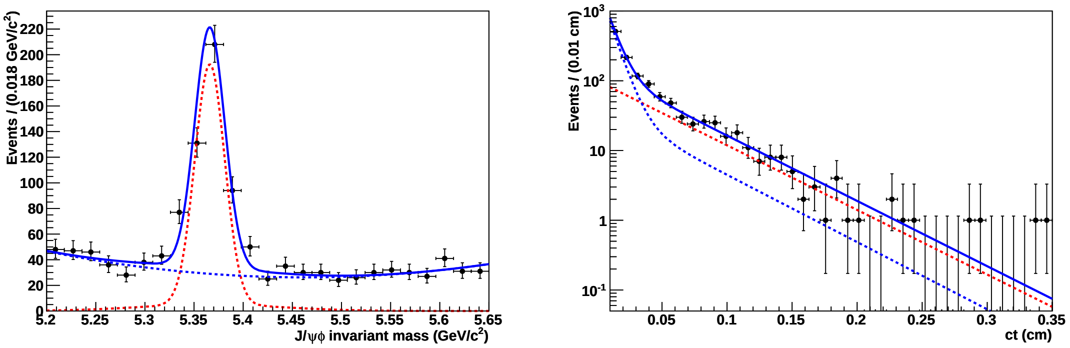

Figure 5.18: Projections of the fit results in $M_{J/\psi\phi}$ (left) and ct (right) for the full range of $8 < p_T^B < 50$ GeV/c and $|y^B| < 2.4$. The requirement $ct > 0.01$ cm has been applied to remove the J/ψ prompt background. The long B lifetime has been fixed to the B^0 meson lifetime Nakamura et al. (2010); all the others parameters are free to float. Individual contributions from the various components are shown in different colors: signal (red), and B background (dashed blue).

- The requirement $ct > 0.05$ cm (see Fig. 5.19 - right) is applied and the projection of the J/ψ ϕ invariant mass (Figure 5.19 - left) and ct (Figure 5.20 - left) are plotted. The yield of the prompt background is estimated to be zero leaving a sample of 258 events. The number of signal events as estimated from the two plots is 188, and hence, the number of background events is 70. This is in agreement with the previous counting.

- The J/ψ ϕ invariant mass projection plot with the requirement $ct < 0.05$ cm is plotted (Figure 5.20 - right) and the number of prompt J/ψ background events (dashed-green line) are counted. The integration of the dashed-green line results in 3937 prompt J/ψ events. This agrees with the fitted value of 3935. The total number of events in the region $-0.05 < ct < 0.05$ is 5942 and therefore the number of signal plus B background is 2005. If the full ct range is considered, the total number of signal and B background events is $2005 + 258 = 2263$ which is in good agreement with the fit result $(549 + 1716 = 2265)$.

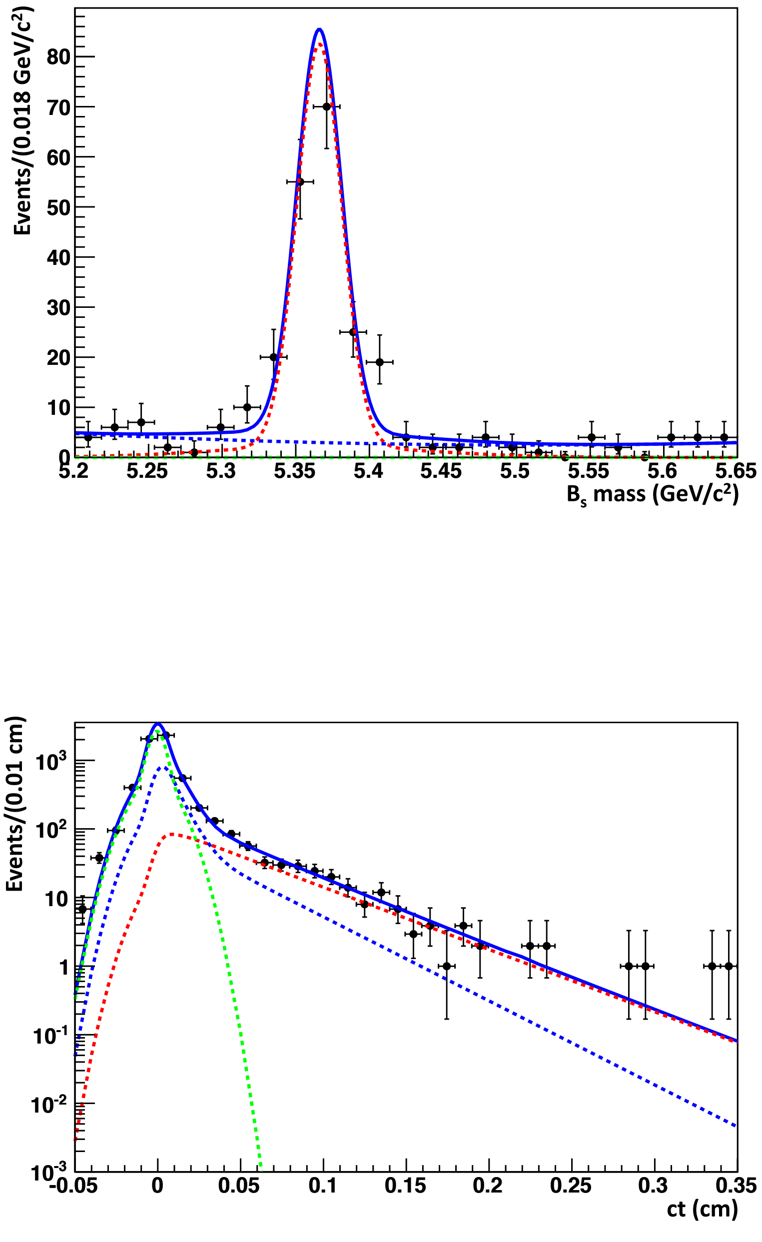

Figure 5.19: Plot of the J/ψ ϕ invariant mass projection with the additional requirement $ct > 0.05$ cm (top) and plot of the ct projection (bottom) as result of the fit.

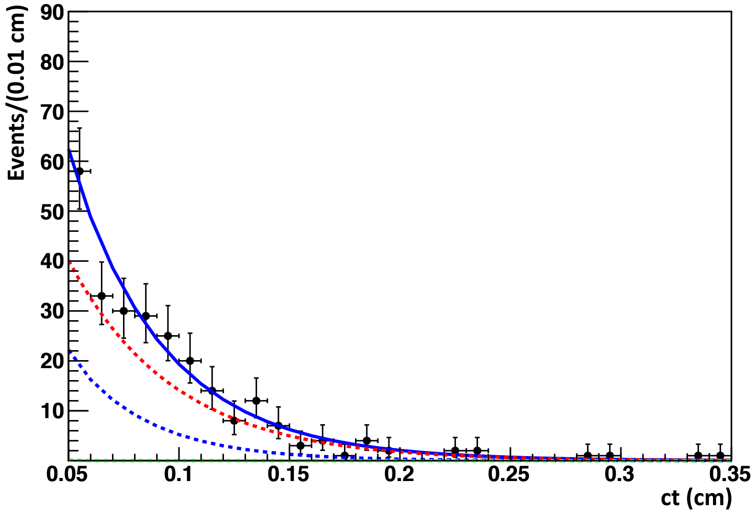

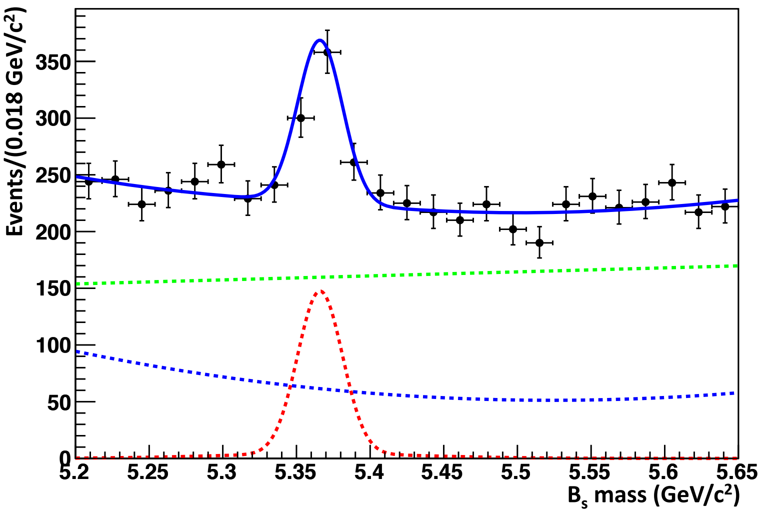

Figure 5.20: Plot of the ct projection with the additional requirement $ct > 0.05$ cm (top) and plot of the J/ψ ϕ invariant mass projection with the additional requirement $ct < 0.05$ cm (bottom).

Run2010A and Run2010B Comparison

To test the fit results as function of data taking periods, the 2010 dataset has beens split in the two samples corresponding to different running conditions `Run2010A` (≈ 8% of the events) and `Run2010B` (≈ 92% of the events). The yields are independently extracted from the two samples. For lack of statistics it is not possible to parameterize distribution shapes independently for the `Run201A` dataset. Therefore, the original PDFs are used. The results for the lifetimes agree within the statistical uncertainty as shown in Table 5.17 and the yields agree with the results presented in Table 5.6.

Table 5.17: Summary table for the extracted signal yields from data in the two data samples `Run2010A` and `Run2010B`.

Dataset Run2010A	$8 < p_T^B < 50, \lvert y^B \rvert < 2.4$
N_{sig}	42 ± 9
N_{prompt}	226 ± 26
N_{Bbkg}	88 ± 25
$\lambda = c\tau$	450 ± 85
Dataset Run2010B	$8 < p_T^B < 50, \lvert y^B \rvert < 2.4$
N_{sig}	508 ± 31
N_{prompt}	3703 ± 106
N_{Bbkg}	1634 ± 102
$\lambda = c\tau$	481 ± 27

Peaking B Background Component

Even though enhanced accumulations of events for the any of the non-prompt background sources are not found in the signal region, the separation of a B background component in the ML fit has been studied to further verify this assumption. From the B background cocktail sample (see Section 4.3) the decay channel $B^0 \rightarrow J/\psi\ K^{*0}(892)$ is removed because of the natural production rate (seven times higher) and the similar signature (two muons and two charged tracks, a pion and a kaon) to the signal. According to Table 4.6, the $J/\psi\ K^{*0}(892)$ channel contributes to the total B background sample with 8.5%. For this channel the misreconstructed J/ψ ϕ invariant mass has been parameterized with a double Gaussian (see Figure 5.21 on the left); the *ct* distribution is assumed to have the same shape as the average B background. The parameters for the J/ψ ϕ invariant mass in the B cocktail (2^{nd} order polynomial) are free to float on data. The relative contribution of the J/ψ $K^{*0}(892)$ channel is fixed to be 8.5%. The ML fit, then, contains signal, prompt background, B combinatorial background, and B peaking background (namely $B^0 \to J/\psi\ K^{*0}(892)$). The fit converged; the plot of the fitted J/ψ ϕ invariant mass projection is shown in Figure 5.21 (right). Table 5.18 lists the signal-yield results. Fits were repeated for different fractions of J/ψ $K^{*0}(892)$ in the B background. No dependence of the signal yield on the parametrized presence of this channel was observed even if exaggerated by a factor of two. Furthermore, this test has been performed in each p_T^B bin. The results are reported in Table 5.19. The signal yield in each bin is unaffected by this extra component. Indeed, the B background is just redistributed and the uncertainty of the average B background yield marginally increases.

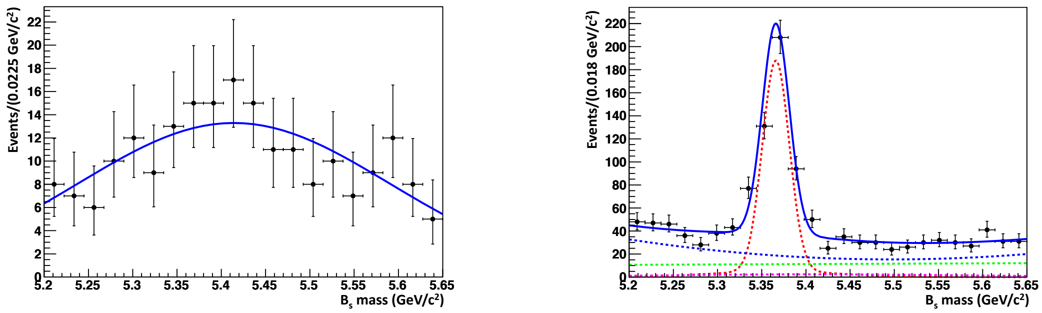

Figure 5.21: J/ψ ϕ invariant mass PDF for $B^0 \to J/\psi\ K^{*0}(892)$ decay channel from the MC sample (left) and projections of the fit results on data in $M_{J/\psi\phi}$ (right) for the full range of $8 < p_T^B < 50$ GeV/c and $|y^B| < 2.4$. Individual contributions from the various components are shown in different colors: signal (red), B background (dashed blue), B peaking (dashed magenta), and J/ψ prompt background (dashed green). When plotting $M_{J/\psi\phi}$ the requirement $ct > 0.01$ cm is requested and the yields scale accordingly.

Table 5.18: Summary table for the extracted signal yield from data in the full $p_{\mathrm{T}}^{\mathrm{B}}$ spectrum when a B peaking component is added to the ML fit.

Ratio J/ψ K^{*0}(892)/B background	N_{sig} (original fit)	N_{sig}
5%	549 ± 32	549 ± 32
7%	549 ± 32	549 ± 32
8.5%	549 ± 32	549 ± 32
10%	549 ± 32	548 ± 32
20%	549 ± 32	548 ± 32

Table 5.19: Summary table for the extracted signal yield from data in the four $p_{\mathrm{T}}^{\mathrm{B}}$ bins when a B peaking component is added to the ML fit. These results have been found fixing the relative fraction between J/ψ K^{*0}(892) and the B background to 8.5%.

f(J/ψ K^{*0}(892)/B$_{tot}$)= 8.5%	N_{sig} (original fit)	N_{sig}
Bin 1	138 ± 16	138 ± 16
Bin 2	176 ± 17	176 ± 17
Bin 3	162 ± 16	162 ± 16
Bin 4	86 ± 11	85 ± 11

J/ψ ϕ Mass Shape: MC vs Data

As presented in Section 5.3, the J/ψ ϕ invariant mass is parameterized with a double Gaussian function, where the parameters of the distribution are fixed from signal MC events. A comparison between the standard procedure and a fit to the data with the parameters of the core Gaussian function free to float is presented. Table 5.20 lists the results of the fit to MC simulated events and data in the full $p_{\mathrm{T}}^{\mathrm{B}}$-$|y^{\mathrm{B}}|$ range and in bins of $p_{\mathrm{T}}^{\mathrm{B}}$ and $|y^{\mathrm{B}}|$. The comparison between the parameters shows an agreement within the statistical error for both the mean and the resolution values.

Fit on Data with all Parameters Free to Float

In Section 5.4 the data-driven extraction of the resolution function parameters from the $M_{\mathrm{J}/\psi\phi}$ sideband regions is presented. The parameters in the fit for the extraction of the signal yield were fixed. To validate the procedure, data is fit with all the

Table 5.20: Summary of the $\mathrm{B_s^0}$ core Gaussian function parameters determined by fitting the signal MC and data.

J/ψ ϕ invariant mass PDF Parameter	MC	Data
$8 < p_\mathrm{T}^\mathrm{B} < 50$ GeV/c, $\lvert y^\mathrm{B}\rvert < 2.4$		
$\mathrm{mean_{core}}$	5.366 ± 0.001	5.367 ± 0.001
$\mathrm{width_{core}}$	0.016 ± 0.001	0.017 ± 0.001
p_T^B bin 1		
$\mathrm{mean_{core}}$	5.368 ± 0.001	5.369 ± 0.003
$\mathrm{width_{core}}$	0.018 ± 0.002	0.018 ± 0.002
p_T^B bin 2		
$\mathrm{mean_{core}}$	5.366 ± 0.001	5.365 ± 0.002
$\mathrm{width_{core}}$	0.015 ± 0.002	0.018 ± 0.002
p_T^B bin 3		
$\mathrm{mean_{core}}$	5.367 ± 0.001	5.367 ± 0.002
$\mathrm{width_{core}}$	0.015 ± 0.001	0.017 ± 0.001
p_T^B bin 4		
$\mathrm{mean_{core}}$	5.366 ± 0.001	5.365 ± 0.003
$\mathrm{width_{core}}$	0.015 ± 0.001	0.019 ± 0.003
$\lvert y^\mathrm{B}\rvert$ bin 1		
$\mathrm{mean_{core}}$	5.367 ± 0.001	5.367 ± 0.002
$\mathrm{width_{core}}$	0.011 ± 0.001	0.012 ± 0.001
$\lvert y^\mathrm{B}\rvert$ bin 2		
$\mathrm{mean_{core}}$	5.366 ± 0.001	5.367 ± 0.002
$\mathrm{width_{core}}$	0.016 ± 0.002	0.018 ± 0.002
$\lvert y^\mathrm{B}\rvert$ bin 3		
$\mathrm{mean_{core}}$	5.368 ± 0.001	5.366 ± 0.003
$\mathrm{width_{core}}$	0.020 ± 0.003	0.021 ± 0.003
$\lvert y^\mathrm{B}\rvert$ bin 4		
$\mathrm{mean_{core}}$	5.368 ± 0.001	5.367 ± 0.003
$\mathrm{width_{core}}$	0.024 ± 0.003	0.023 ± 0.003

parameters of the resolution function and the effective lifetimes of the non-prompt background free to float. Table 5.21 lists the results for the signal yields in the full spectrum and in bins of $p_{\mathrm{T}}^{\mathrm{B}}$ and $|y^{\mathrm{B}}|$. The number of signal events extracted is unchanged.

Table 5.21: Summary of the number of signal events extracted in two alternative approaches: $\mathcal{R}$ function extracted from the sideband regions and fixed in the final fit and $\mathcal{R}$ function left free to float in the final fit.

	Step-by-step	All free to float
Full $p_{\mathrm{T}}^{\mathrm{B}}$-$|y^{\mathrm{B}}|$ range	549 ± 32	550 ± 32
$p_{\mathrm{T}}^{\mathrm{B}}$ bin 1	137.6 ± 16.0	134.6 ± 16.2
$p_{\mathrm{T}}^{\mathrm{B}}$ bin 2	175.9 ± 16.6	175.7 ± 16.7
$p_{\mathrm{T}}^{\mathrm{B}}$ bin 3	162.3 ± 15.8	163.9 ± 16.1
$p_{\mathrm{T}}^{\mathrm{B}}$ bin 4	85.5 ± 11.4	94.7 ± 12.1
$|y^{\mathrm{B}}|$ bin 1	150.6 ± 14.7	154.9 ± 15.5
$|y^{\mathrm{B}}|$ bin 2	143.7 ± 15.4	145.3 ± 15.3
$|y^{\mathrm{B}}|$ bin 3	129.3 ± 15.4	124.8 ± 14.8
$|y^{\mathrm{B}}|$ bin 4	138.8 ± 16.5	140.8 ± 16.7

Studies of the Resolution Function

The *ct* variable has an important contribution in the signal/background discrimination, as shown in Section 5.6.2. On the other hand, this is not valid for the two background components, combinatorial B and prompt J/ψ, where the composition is somewhat less defined. Table 5.8 reports for the second $|y^{\mathrm{B}}|$ bin shows an unseen enhancement of J/ψ prompt events with respect to the B background, if compared to any of the other bins of $p_{\mathrm{T}}^{\mathrm{B}}$ and $|y^{\mathrm{B}}|$. This could be due to correlations between the background components and bias the number of signal events. To quantify these effects for the *ct* variable, the relative fraction between B and prompt J/ψ background components

$$\alpha = N_{Bbkg}/(N_{Bbkg} + N_{prompt}) \tag{5.6}$$

is fixed to different value between 0 and 1. The *ct* resolution function is still a double Gaussian function which is in common to the three fit components, as in the nominal 2D ML fit. The cross-check is performed in steps: first, the parameters of the *ct* resolution function are determined from the sidebands by forcing the relative ratio between prompt J/ψ and the combinatorial B background components to vary from zero to one. Then, these parameters are fixed and the signal yield is extracted. Table 5.22 lists the relative fraction between the two Gaussian function of the resolution, the mean and the width value (σ_{core} and σ_{tail}) of the resolution function, the likelihood of the fit for the resolution function, the signal and background yields determined from data, and the likelihood for the yield extraction for different values of α. Figure 5.22 plots the number of signal events as function of the parameter α. Table 5.23 lists the number signal yields and compares them with the value fit with the nominal procedure and reported in Table 5.8. It turns out that the signal yield deviates by at most 3.4%. Also, core-tail fraction of the resolution function varies only slightly but enough to compensate for the fixed value of α: this explains why the fit finds a solution at each α.

Table 5.22: Summary table of the relative fraction between the two Gaussians of the resolution function, the mean and the width value (σ_{core} and σ_{tail}) of the resolution function, the likelihood of the fit for the resolution function, the signal and background yields extracted from data, and the likelihood for the yield extraction for different values of α.

Fraction	f_{core}	σ_{core} (μm)	σ_{tail} (μm)	-lnL	N_{sig}	N_{Bbkg}	N_{prompt}	-lnL
$\alpha = 0.1$	0.46	43	123	-3897	146 ± 15	1660 ± 50	167 ± 34	-20700
$\alpha = 0.3$	0.42	40	117	-3895	148 ± 16	1300 ± 63	526 ± 59	-20698
$\alpha = 0.5$	0.41	37	112	-3894	149 ± 16	946 ± 64	526 ± 59	-20695
$\alpha = 0.7$	0.40	34	107	-3892	145 ± 16	571 ± 63	1259 ± 70	-20691
$\alpha = 0.9$	0.40	32	105	-3891	146 ± 16	203 ± 58	1624 ± 71	-20687

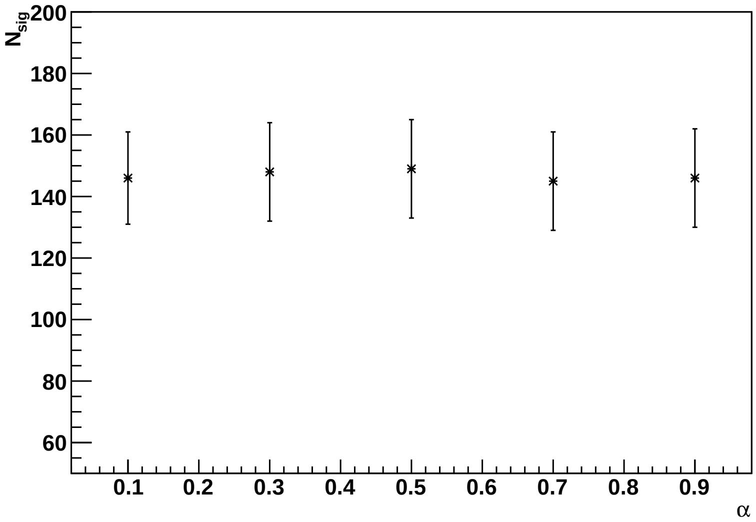

Figure 5.22: Plot of the number of signal events determined from data as function of the different α values. Numerical results are reported in Table 5.23.

Table 5.23: Summary table with the signal yield extracted for different α values and comparison with the signal yield determined with the nominal 2D ML fit, as reported in the second bin of $|y^{\mathrm{B}}|$ in Table 5.8.

α	N_{sig} (original fit)	N_{sig}	Difference (%)
0.1	144 ± 15	146 ± 15	1.4
0.3	144 ± 15	148 ± 16	2.8
0.5	144 ± 15	149 ± 16	3.4
0.7	144 ± 15	145 ± 16	0.7
0.9	144 ± 15	146 ± 16	1.4

To assign a systematic uncertainty on the parameterization of the resolution function, a fit to each of the $p_{\mathrm{T}}^{\mathrm{B}}$ and $|y^{\mathrm{B}}|$ bins is performed by fixing the resolution function to the one determined from the full $p_{\mathrm{T}}^{\mathrm{B}}$ and $|y^{\mathrm{B}}|$ spectrum. Table 5.24 lists the number of signal events. Differences up to 2% are found.

In time-dependent CP analyses published by the BaBar collaboration Aubert et al. (2002b), the resolution function is often corrected by the measured error. In this case, the resolution function is a double Gaussian function where the correction is applied

Table 5.24: Summary table of the results of the fit to data with the resolution function parameterized from the sidebands in each of the $p_{\mathrm{T}}^{\mathrm{B}}$and $|y^{\mathrm{B}}|$ bins and from the full spectrum. The percent difference is assigned as systematic uncertainty due to the parametrization choice.

$p_{\mathrm{T}}^{\mathrm{B}}$	$N_{sig}(bin-by-bin)$	$N_{sig}(average)$	Difference (%)
8-12	138 ± 16	136 ± 15	1.4
12-16	176 ± 17	173 ± 16	1.7
16-23	162 ± 16	164 ± 15	1.2
23-50	86 ± 11	87 ± 16	1.2
$\lvert y^{\mathrm{B}}\rvert$	$N_{sig}(bin-by-bin)$	$N_{sig}(average)$	Difference (%)
0.0-0.8	150 ± 15	148 ± 15	1.3
0.8-1.4	144 ± 15	146 ± 16	1.4
1.4-1.7	129 ± 15	126 ± 15	2.3
1.7-2.4	139 ± 17	142 ± 16	2.2

to the core Gaussian. It is analytically defined as:

$$\mathcal{R} = f * G'_{core} + (1-f) * G_{tail}. \tag{5.7}$$

where G' is the new definition corrected with the event-by-event error. The fit procedure is standard (as in the 2D ML fit) with all parameters left free to float. Table 5.25 lists the the number of signal events and the lifetime extracted from fit to data with the old and new definition of the resolution function. The two results agree within one standard deviation. It has been shown so far that the data-driven approach for the extraction of the parameters of the resolution function produces consistent results. Last cross-check involves a comparison between parameters obtained from

Table 5.25: Summary table with the signal yields and lifetimes determined with the original definition of the $\mathcal{R}$ function and with the $\mathcal{R}$ function corrected by the event-by-event error.

	Original	Error Event-by-Event
N_{sig}	549 ± 32	524 ± 30
$\lambda = c\tau$	478 ± 26	474 ± 28

the data sidebands and from MC simulated events. Table 5.26 shows results for the parameters obtained from a MC sample composed by combinatorial B and prompt J/ψ combined in the correct ratio. These can be compared with the first column of Table 5.4. The results agree within one standard deviation confirming the correctness of the adopted procedure. From these cross-checks, one can conclude that the non-perfect knowledge of the composition of the background does not bias the signal yield measurement.

Table 5.26: Summary of the *ct* parameters determined by fitting a combination of sample of prompt J/ψ and combinatorial B background events.

Parameter	$8 < p_{\mathrm{T}}^{\mathrm{B}} < 50$ GeV/c, $\lvert y^{\mathrm{B}}\rvert < 2.4$
f	0.351 ± 0.147
μ_{tail} (μm)	-42.6 ± 62.7
μ_{core} (μm)	-30.7 ± 20.3
σ_{tail} (μm)	147.2 ± 26.0
σ_{core} (μm)	51.3 ± 12.7
$c\tau_1$ (μm)	39.2 ± 30.0
$c\tau_2$ (μm)	310 ± 91

5.7 Efficiency Extraction

The efficiency for reconstructing signal events is computed from a combination of data-driven techniques (Tag-and-Probe) and MC simulation. The total efficiency (ϵ) can be divided into three components

$$\epsilon = \epsilon_{acceptance} \cdot \epsilon_{2\mu} \cdot \epsilon_{reco} \tag{5.8}$$

where $\epsilon_{acceptance}$ is the efficiency for having two muons within the geometrical acceptance, $\epsilon_{2\mu}$ is the efficiency for reconstructing, identifying and triggering on two muons, given that two muons are within the acceptance, and ϵ_{reco} is the efficiency for reconstructing a signal event if two reconstructed and triggered muons are present. The total efficiency is defined as the efficiency to reconstruct a single $\mathrm{B_s^0} \to \mathrm{J}/\psi(\to \mu^+\mu^-)\phi(\mathrm{K^+K^-})$ event.

5.7.1 The Tag-and-Probe Method

The Tag-and-Probe (T&P) method CMS Collaboration (2010d) used in this analysis, is a data driven method to measure the single muon tracking, identification and trigger efficiencies. It makes use of well-known dimuon resonances (such as J/ψ mesons) to supply tag and probe muon tracks. The choice of such resonance is due to the CMS experiment ability to reconstruct and identify muons with high efficiencies and to measure muon momenta with high precision. Events are selected with strict selection requirements on one muon (*tag*), and with a more relaxed selection criterion on the other track (*probe*) such that the selection of the probe track is the least biased. The probe tracks are separated into two categories depending on whether they pass or fail the more restrictive selection. The efficiency evaluation proceeds via the following steps: An event from a J/ψ event sample is kept if a tag muon together with a probe track is found, while satisfying the predefined selection criteria. In this case the invariant mass of the combination enters a muon-track mass histogram. The criteria for the choice of both, tag and probe, are optimized such that background is minimized and the J/ψ mass peak is clearly visible. If the track is subsequently identified as a muon the invariant mass of the tag and probe combination enters another muon-muon mass histogram. The latter should contain almost exclusively J/$\psi \rightarrow \mu^+\mu^-$ events. Figure 5.23 shows an example of the distributions for dimuon invariant masses for tag muons paired with passing (left) and failing (right) probes in collision data.

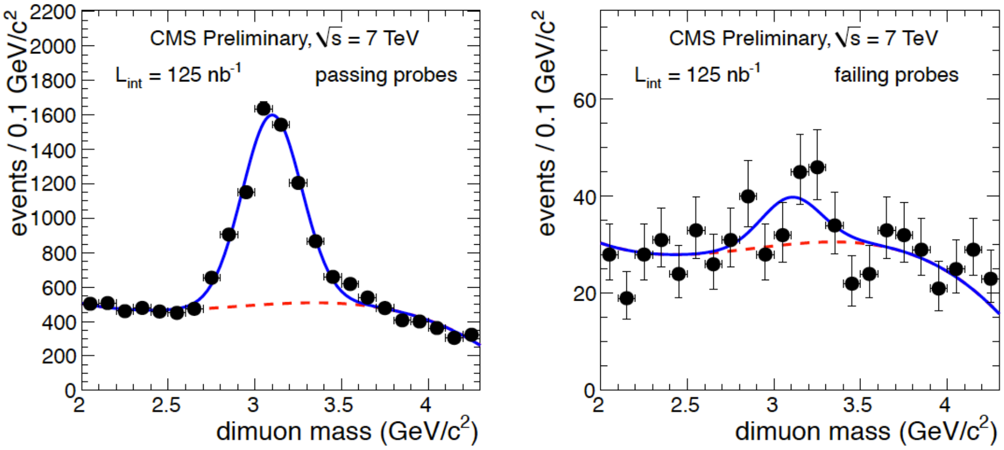

Figure 5.23: Distributions of dimuon invariant mass (data points) for tag muons paired with passing (left) and failing (right) probes in collision data. In this plots, the mass is calculated using only the muon detector information for all probe muons; the silicon track momentum for the passing probes is not used.

The efficiency can be determined in two ways. Both are expected to give consistent results and hence, their comparison provides a systematic test. They can be expressed as:

$$\epsilon(\mu) = \frac{N_{\mu\mu}}{N_{\mu\mu} + N_{\mu t}} = \frac{N_{\mu\mu}}{N_{\mu\mu} + N_{\mu\bar{\mu}}} \tag{5.9}$$

where $N_{\mu\mu}$ ($N_{\mu t}$) is the number of J/ψ mesons extracted from a fit to data with both, the tag and probe leptons (only the tag lepton), identified as muon. In the second approach, $N_{\mu\bar{\mu}}$ is the number of J/ψ mesons, again extracted from a fit to the data, but where the probe explicitly failed muon identification. In the above equations, all yields described by single Gaussian functions on top of a linear background. The procedure is applied in intervals of transverse momentum p_T and pseudorapidity η. The area under the Gaussian function is the signal yield. In principle the relation $N_{\mu t} = N_{\mu\mu} + N_{\mu\bar{\mu}}$ applies, but the practical determination of the numbers differs as they are extracted from fits to different histograms without constraints. The combined trigger and offline-reconstruction efficiency for a single muon is defined as

$$\epsilon_\mu = \epsilon_{track} \cdot \epsilon_{id|track} \cdot \epsilon_{trig|track+id} \tag{5.10}$$

where ϵ_{track} is the tracking efficiency, $\epsilon_{id|track}$ is the muon identification efficiency in the muon systems for a tracker-reconstructed muon, and finally $\epsilon_{trig|track+id}$ is the probability for an offline reconstructed muon to have also caused a trigger response. The tracking efficiency is constant in the momentum acceptance range, and it varies only slightly in the $\eta - \varphi$ plane. The muon identification and trigger efficiencies exhibit a p_T^μ and $|\eta|$ dependence, that requires a larger granularity in those variables.

5.7.2 Efficiency Extraction from Data

The efficiencies of muon reconstruction (ϵ_{track}), muon identification ($\epsilon_{id|track}$), and muons trigger ($\epsilon_{trig|track+id}$) are determined in bins of p_{T} and η of the muon using the standard Tag-and-Probe technique. The total efficiency $\epsilon_{2\mu}$ can be then summarized into three components for each of the two muons,

$$\epsilon_{2\mu} = \epsilon^{\mu_1}_{track} \cdot \epsilon^{\mu_1}_{id|track} \cdot \epsilon^{\mu_1}_{trig|track+id} \cdot \epsilon^{\mu_2}_{track} \cdot \epsilon^{\mu_2}_{id|track} \cdot \epsilon^{\mu_2}_{trig|track+id} \tag{5.11}$$

where μ_1 and μ_2 refer to the two muons from the J/ψ. Each component is evaluated individually. For $\epsilon_{id|track}$ and $\epsilon_{trig|track+id}$, the sample of tag muon is composed of global or arbitrated tracker muons within the acceptance that pass a `HLT_MuX` trigger (which requires a muon with any minimum transverse momentum value), or the muon leg of a `HLT_MuX_TrackY_Jpsi` trigger (which requires a muon and a track with any minimum transverse momentum values). The sample of probe muons for the trigger efficiency calculation consists of global or tracker muons within acceptance, without a requirement on the trigger. These probes are considered to be passing if they also pass the requirements for `HLT_DoubleMu0`. The probes for the muon ID efficiency are tracks required to lie within the muon acceptance. Passing probes are those which are successfully matched to a reconstruction muon.

The tag sample for the muon track efficiency calculation is again global or arbitrated tracker muons, but are required the pass `HLT_MuX` or `HLT_L1DoubleMuOpen` dimuon trigger (which requires two muons reconstructed at the L1 level without criteria on the transverse momenta). Standalone muons are used for probes, and those that match a reconstructed track are considered passing. Tables 5.27-5.30 summarizes the individual quantitative measurements and the bin definitions. Figure 5.24 shows the efficiency of a muon to be one leg of the `HLT_DoubleMu0` trigger as a function of p_{T}.

The Tag-and-Probe studies for muon ID and muon tracking efficiency have been performed on the full dataset. The muon trigger efficiency is known to have increased during the technical stop in July 2010 due to improvements in the L3 muon reconstruction algorithm. The tag and probe study is, then, performed for the HLT for the data before (`Run2010A` dataset) and after (`Run2010B` dataset) the technical stop, separately. The final trigger efficiency is computed as a weighted average in proportion to the luminosity from each run period. The total efficiency $\epsilon_{2\mu}$ is calculated in several steps. For each $\mathrm{B_s^0}$ reconstructed event, the p_T and η of the two muons are retrieved. For each couple of p_T-η values, the efficiencies reported in Tables 5.27-5.30, that correspond to the three terms extracted with the Tag-and-Probe techniques, are multiplied. The same procedure is applied to the second muon. The product of the total efficiency of the two muons results in $\epsilon_{2\mu}$. The $\mathrm{B_s^0}$ candidates are split in p_T and y bins and an average efficiency $\epsilon_{2\mu}$ per bin is calculated.

Table 5.27: Muon reconstruction and identification efficiencies measured in data using the Tag-and-Probe technique on a sample of inclusive J/ψ mesons.

	$\lvert\eta^\mu\rvert$			
p_T^μ(GeV/c)	0.0–0.8	0.8–1.2	1.2–1.6	1.6–2.4
0.0–1.5	0.0	0.0	0.679 ± 0.173	1.000 ± 0.033
1.5–3.0	0.0	0.0	0.733 ± 0.020	0.966 ± 0.032
3.0–4.5	0.901 ± 0.019	0.912 ± 0.021	1.000 ± 0.004	0.984 ± 0.014
4.5–6.0	1.000 ± 0.004	0.991 ± 0.017	0.997 ± 0.005	0.979 ± 0.025
6.0–9.0	0.996 ± 0.011	0.961 ± 0.018	1.000 ± 0.019	1.000 ± 0.006
9.0–20.0	0.994 ± 0.015	1.000 ± 0.020	0.999 ± 0.023	0.996 ± 0.016

Table 5.28: Muon tracking efficiencies measured in data using the Tag-and-Probe technique on a sample of inclusive J/ψ mesons.

	$\lvert\eta^\mu\rvert$			
p_T^μ (GeV/c)	0.0–0.8	0.8–1.2	1.2–1.6	1.6–2.4
0.0–1.5	0.0	0.0	0.790 ± 0.127	1.000 ± 0.055
1.5–3.0	0.0	0.0	0.997 ± 0.001	0.996 ± 0.009
3.0–4.5	0.999 ± 0.014	0.995 ± 0.006	0.999 ± 0.002	0.980 ± 0.005
4.5–6.0	0.999 ± 0.001	0.999 ± 0.002	1.000 ± 0.002	0.999 ± 0.011
6.0–9.0	1.000 ± 0.001	0.988 ± 0.014	0.981 ± 0.010	0.996 ± 0.002
9.0–20.0	0.999 ± 0.004	0.976 ± 0.029	0.969 ± 0.021	0.982 ± 0.062

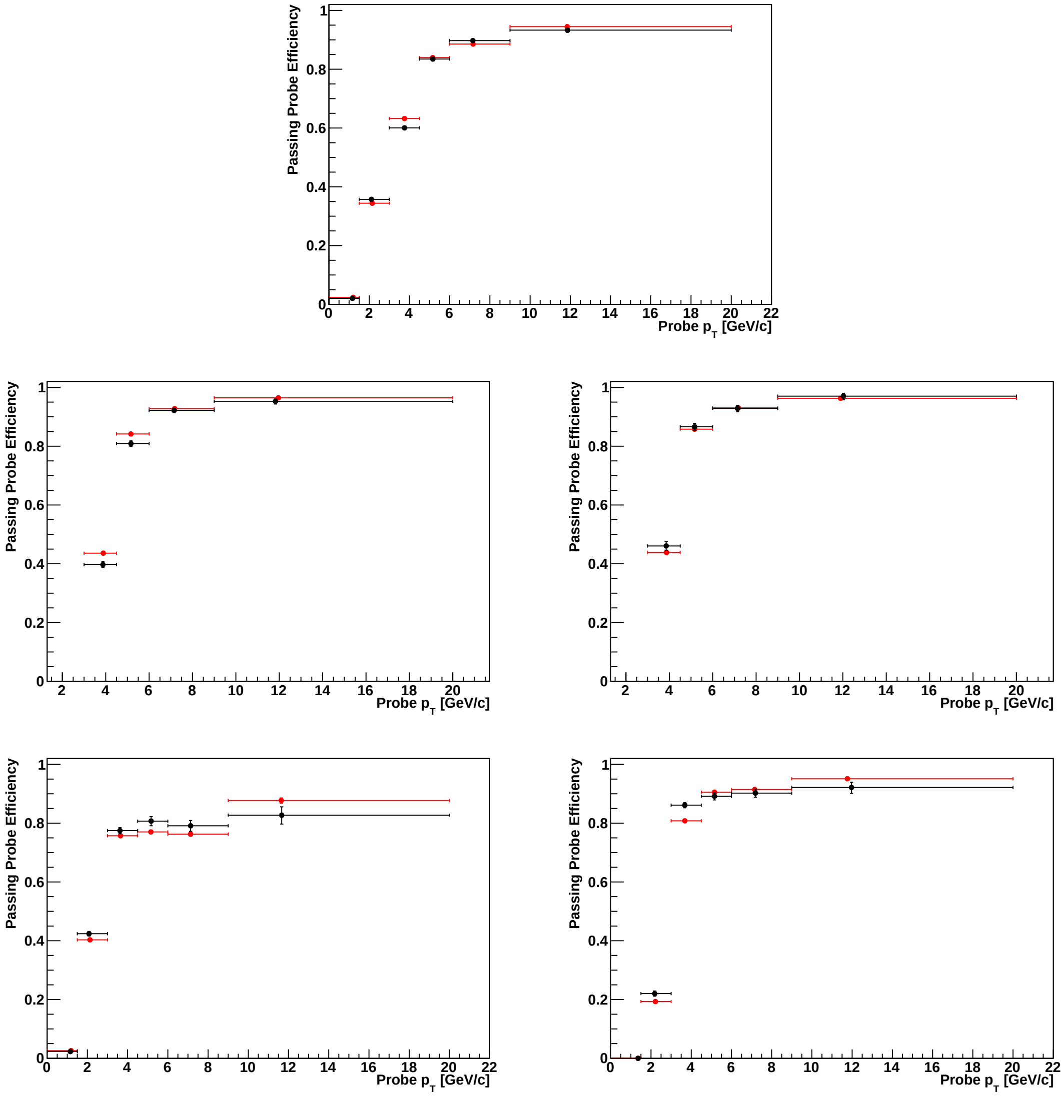

Figure 5.24: Efficiency of the `HLT_DoubleMu0` trigger as a function of p_{T} for $|\eta| < 2.4$ (top), and for several bins in pseudorapidity (clockwise from upper left in second row: $|\eta| < 0.8$, $0.8 < |\eta| < 1.2$, $1.2 < |\eta| < 1.6$, $1.6 < |\eta| < 2.4$), as measured with the Tag-and-Probe technique on an inclusive J/ψ sample in data. Data (black points and errors) are shown overlaid on simulation (red points and errors).

Table 5.29: Muon trigger efficiency for the `HLT_DoubleMu0` trigger measured in `Run2010A` data using the Tag-and-Probe technique on a sample of inclusive J/ψ mesons.

	$\lvert\eta^{\mu}\rvert$			
p_T^{μ},(GeV/c)	0.0–0.8	0.8–1.2	1.2–1.6	1.6–2.4
0.0–1.5	0.0	0.0	0.0	0.015 ± 0.001
1.5–3.0	0.0	0.0	0.176 ± 0.004	0.266 ± 0.003
3.0–4.5	0.384 ± 0.006	0.388 ± 0.008	0.751 ± 0.006	0.634 ± 0.006
4.5–6.0	0.764 ± 0.006	0.738 ± 0.009	0.821 ± 0.008	0.673 ± 0.009
6.0–9.0	0.870 ± 0.005	0.836 ± 0.009	0.817 ± 0.010	0.713 ± 0.012
9.0–20.0	0.952 ± 0.005	0.944 ± 0.009	0.886 ± 0.013	0.836 ± 0.018

Table 5.30: Muon trigger efficiency for the `HLT_DoubleMu0` trigger measured in `Run2010B` data using the Tag-and-Probe technique on a sample of inclusive J/ψ mesons.

	$\lvert\eta^{\mu}\rvert$			
p_T^{μ},(GeV/c)	0.0–0.8	0.8–1.2	1.2–1.6	1.6–2.4
0.0–1.5	0.0	0.0	0.0	0.023 ± 0.003
1.5–3.0	0.0	0.0	0.220 ± 0.009	0.424 ± 0.008
3.0–4.5	0.397 ± 0.009	0.461 ± 0.014	0.861 ± 0.009	0.774 ± 0.010
4.5–6.0	0.808 ± 0.010	0.866 ± 0.012	0.891 ± 0.012	0.807 ± 0.015
6.0–9.0	0.922 ± 0.007	0.929 ± 0.011	0.902 ± 0.013	0.791 ± 0.018
9.0–20.0	0.952 ± 0.009	0.970 ± 0.011	0.922 ± 0.019	0.827 ± 0.029

The T&P technique relies on the assumption that the dimuon efficiency is the product of the two single muon efficiencies. Any correlation between the two muons is, therefore, not accounted. The signal MC sample is used to measure the size of the effect due to correlation by performing a closure test, in which the Tag-and-Probe technique is applied to MC. The efficiency calculated directly from MC is compared to the efficiency obtained from the Tag-and-Probe method on MC and the discrepancy, attributed to the effect of correlations in the MC sample, is taken as systematic error for the method. Table 5.31 summarizes the results for the trigger efficiency from MC truth, calculated as ratio of generated events with two muons triggered within the acceptance over the number of generated events with two muons generated within the acceptance, and the Tag-and-Probe study performed on both MC and data: deviations at most as large as 3% are found. Table 5.32 summarizes the results for the total efficiency from MC truth, calculated as ratio of generated events with two muons reconstructed and triggered within the acceptance over the number of generated events with two muons generated within the acceptance, and the efficiency from the full Tag-and-Probe study as product of the three terms: in this case, deviations at most as large as 3% are found.

Table 5.31: Comparison table for the trigger efficiencies as extracted with Tag-and-Probe method on data and Monte Carlo with results from the closure test.

p_T^B	T&P$_{data}$ ϵ (%)	T&P$_{MC}$ ϵ (%)	MC ϵ (%)	Percent Difference (%)
8-12	0.376	0.371	0.362	+2.5
12-16	0.535	0.536	0.531	+0.9
16-23	0.634	0.646	0.655	−1.4
23-50	0.728	0.735	0.722	+1.8
$\lvert y^B \rvert$	T&P$_{data}$ ϵ (%)	T&P$_{MC}$ ϵ (%)	MC ϵ (%)	Percent Difference (%)
0.0-0.8	0.596	0.632	0.621	+1.8
0.8-1.4	0.584	0.585	0.571	+2.4
1.4-1.7	0.542	0.536	0.523	+2.5
1.7-2.4	0.441	0.423	0.415	+1.9

Table 5.32: Table for the total efficiency as product of the three components as extracted with the Tag-and-Probe procedure on Monte Carlo (T&P$_{MC}$) and results from the closure test (MC). The last column is assigned as systematic uncertainty that accounts for the correlation between the two muons.

$p_{\mathrm{T}}^{\mathrm{B}}$	T&P$_{MC}$ ϵ (%)	MC ϵ (%)	Percent Difference (%)
8-12	0.350	0.343	$+2.0$
12-16	0.502	0.512	-2.0
16-23	0.611	0.628	-2.8
23-50	0.712	0.702	$+1.4$
$\lvert y^{\mathrm{B}} \rvert$	T&P$_{MC}$ ϵ (%)	MC ϵ (%)	Percent Difference (%)
0.0-0.8	0.615	0.605	$+1.7$
0.8-1.4	0.545	0.553	-1.5
1.4-1.7	0.513	0.501	$+2.4$
1.7-2.4	0.397	0.411	-3.5

5.7.3 Efficiency Extraction from Monte Carlo Simulations

The efficiency terms $\epsilon_{acceptance}$ and ϵ_{reco} are determined from MC simulation. The efficiency is calculated from a sample of signal MC events generated without any kinematic requirements on the dimuons. It is evaluated in each bin as the ratio of the number of $\mathrm{B_s^0} \rightarrow \mathrm{J}/\psi\ \phi$ generated events with two muons with $p_\mathrm{T} > 2.5$ GeV/c and $|\eta| < 2.5$ to the total number of generated events. The reconstruction efficiency ϵ_{reco} is defined as the number of fully reconstructed and triggered signal events divided by the number of generated signal events with two reconstructed and triggered muons within the acceptance. This efficiency accounts for the bin to bin migration due to mismeasured $\mathrm{B_s^0}$ transverse momentum and rapidity, and it corrects the generated value for the corrected yield. Table 5.33 summarizes the average efficiencies in each p_T and $|y^\mathrm{B}|$ bin.

Table 5.33: Summary table for the efficiencies extracted from data ($\epsilon_{2\mu}$) and MC ($\epsilon_{acceptance}$ and ϵ_{reco}). Efficiencies are reported in each bin of p_T^B and $|y^\mathrm{B}|$.

p_T^B	$\epsilon_{acceptance}$ (%)	$\epsilon_{2\mu}$ (%)	$\epsilon_{\mathrm{B_s^0}}$ (%)	ϵ_{total} (%)
8-12	27.4 ± 0.3	34.3 ± 1.3	13.6 ± 0.2	1.28 ± 0.05
12-16	41.9 ± 0.6	51.0 ± 1.9	24.6 ± 0.4	5.26 ± 0.23
16-23	52.8 ± 0.9	61.2 ± 2.4	37.0 ± 0.7	11.9 ± 0.6
23-50	63.6 ± 1.4	69.5 ± 2.9	44.4 ± 1.1	19.6 ± 1.1
$\|y^\mathrm{B}\|$	$\epsilon_{acceptance}$ (%)	$\epsilon_{2\mu}$ (%)	$\epsilon_{\mathrm{B_s^0}}$ (%)	ϵ_{total} (%)
0.0-0.8	20.8 ± 0.3	56.2 ± 1.4	23.5 ± 0.4	2.75 ± 0.09
0.8-1.4	37.3 ± 0.5	55.5 ± 1.8	22.5 ± 0.4	4.65 ± 0.18
1.4-1.7	50.1 ± 0.9	51.5 ± 2.3	22.0 ± 0.5	5.68 ± 0.31
1.7-2.4	40.0 ± 0.6	42.3 ± 2.4	19.3 ± 0.4	3.26 ± 0.20

5.8 Systematic Uncertainties

Several sources of systematic uncertainty have been considered for the differential cross section measurement. These contributions are:

- **Branching Fractions** – These are the errors on the branching fractions for the J/ψ and ϕ decays, as reported in the PDG Nakamura et al. (2010).

- **PDF Shapes** – Different functional forms for the PDFs have been considered to account for imperfect knowledge of the PDFs. For the parameterization of the distribution of the J/ψ ϕ invariant mass alternatively the sum of three Gaussian functions has been considered to allow for outliers. The difference of the signal yields in the fits with the two signal shape parameterizations is taken as uncertainty. The parameters for the background polynomials, that resulted from the fit on data, have also been varied by one standard deviation. The systematic uncertainty of the resolution function is described in Section 5.6.2. The relative uncertainties are listed in Table 5.34 and Table 5.35. Residual correlations amongst the fit variables are estimated from the relative variation of the yields in toy experiments from the measured yields.

Table 5.34: Relative uncertainties (in percent) of the signal yield from the PDFs in the different bins of $p_{\mathrm{T}}^{\mathrm{B}}$.

Source	Bin 1 (%)	Bin 2 (%)	Bin 3 (%)	Bin 4 (%)
$M_{\mathrm{J}/\psi\phi}$ mass shape	2.3	2.7	2.6	2.5
Resolution function	1.4	1.7	1.2	1.2
Toy experiments	0.6	0.4	0.6	1.3
Total	2.8	3.2	2.9	3.1

- **Tag-and-Probe Statistical Uncertainties** – The muon ID, muon tracking, and trigger efficiencies have been measured in data with the Tag-and-Probe technique. A systematic uncertainty is associated with statistical effects due to the limited number of signal MC events used to obtain the distribution of muon

Table 5.35: Relative uncertainties (in percent) of the signal yield from the PDFs in the different bins of $|y^{\mathrm{B}}|$.

Source	Bin 1 (%)	Bin 2 (%)	Bin 3 (%)	Bin 4 (%)
M_{B} mass shape	1.8	2.9	3.2	3.5
Resolution function	1.3	1.4	2.3	2.2
Toy experiments	0.5	0.2	0.7	0.5
Total	2.3	3.2	4.0	4.1

kinematics. The uncertainty of the average efficiency calculation in each bin of the B^0_s transverse momentum $p_{\mathrm{T}}^{\mathrm{B}}$ and rapidity $|y^{\mathrm{B}}|$ is the sum in quadrature of the relative uncertainties for the two muons in that bin.

- **Tag-and-Probe Correlation Uncertainties** – Only half of the percent difference obtained from the closure test (see Table 5.32) is assigned as systematic uncertainty due to correlation effects between the muons. More detailed studies performed by the CMS Muon Physics Object Group (Muon POG) determined that the closure test provides results that overestimate the correlation effects. Therefore, they suggested to assume as systematic uncertainty only 50% of the discrepancy.

- **Hadron Tracking Efficiency** – The uncertainty of the reconstruction efficiency of a charged hadron track is 3.9%/track CMS Collaboration (2010c). The relative efficiency of reconstructing hadron tracks in data is determined by measuring the ratio of neutral charm-meson decays to final states of four ($\mathrm{D}^0 \to K^-\pi^+\pi^-\pi^+$) or two charged particles ($\mathrm{D}^0 \to K^-\pi^+$). In signal events two charged tracks from the ϕ decay are present. Under the assumption that the tracks are strongly correlated, the two uncertainties for the two hadron tracks are linearly added.

- **Reconstruction Efficiency** – This is dominantly the uncertainty of the reconstruction efficiency due to the finite Monte Carlo sample size. An additional uncertainty of 1% is added in quadrature. This corresponds to the relative change in the signal yield when varying the limits of the selection criteria for the events variables (vertex fit probability, transverse momentum of the kaons, $\mathrm{B_s^0}$ transverse momentum, and ϕ mass window) by up to 30% of the applied criterion requirement.

- **Misalignment** – To determine the uncertainty associated with the running conditions, such as the alignment of the CMS detector in different periods of data taking, two signal MC samples have been reconstructed and analyzed. They are characterized by different configuration parameters that simulate the status of the detector in Summer and Fall 2010. The two samples differ by the position of the simulated primary vertex and by the alignment of the pixel silicon detector with respect to the collision point. The full difference in the reconstruction efficiency in each p_T^B-$|y^\mathrm{B}|$ bin between the two samples is assigned as systematic uncertainty.

- **p_T^B-$|y^\mathrm{B}|$ Spectrum** – The efficiencies are extracted with a particular model (PYTHIA). The model dependency can be estimated by re-calculating the efficiencies for samples that are generated with different generators (MC@NLO). For the MC@NLO generated distributions, analogously, the efficiencies are calculated in each bin of p_T^B ($|y^\mathrm{B}|$) by integrating over $|y^\mathrm{B}|$ (p_T^B) in the kinematic region $8 < p_\mathrm{T}^\mathrm{B} < 50$ GeV/c and $|y^\mathrm{B}| < 2.4$. The bin-by-bin efficiency ratio ($\epsilon_\mathrm{MC@NLO}/\epsilon_\mathrm{PYTHIA}$) provides a correction factor that is applied to the efficiencies determined with the PYTHIA generator. The relative difference between the original and the recalculated efficiencies is adopted as systematic uncertainty.

- **Luminosity** – A relative uncertainty of 4% for the integrated luminosity is assigned (see Section 4.1.4).

The different contributions to the systematic uncertainty are summarized in Table 5.36 and Table 5.37 for each p_T-y bin. The total error is calculated as the sum in quadrature of the individual uncertainties, under the assumption that the error sources are uncorrelated.

Table 5.36: Summary of systematic uncertainties (%) in bins of $p_{\mathrm{T}}^{\mathrm{B}}$. The total uncertainty as been calculated as the sum in quadrature of the individual uncertainties.

Source	Bin 1 (%)	Bin 2 (%)	Bin 3 (%)	Bin 4 (%)
Uncorrelated systematic errors				
Probability Density Function	2.8	3.2	2.9	3.1
Tag and Probe Statistical	2.5	2.8	3.1	3.5
Tag and Probe Correlation	1.0	1.0	1.4	0.7
Hadron Tracking Efficiency	7.8	7.8	7.8	7.8
Reconstruction Efficiency	2.0	2.0	2.1	2.6
Misalignment	3.4	2.1	2.0	3.4
$\lvert y^{\mathrm{B}}\rvert$ Spectrum	1.2	1.1	1.4	2.7
Non-Luminosity	9.6	9.5	9.5	10.4
Correlated systematic errors				
Branching Fractions	1.4	1.4	1.4	1.4
Luminosity	4.0	4.0	4.0	4.0
Total	10.5	10.4	10.4	11.3

Table 5.37: Summary of systematic uncertainty (%) in bins of $|y^{\mathrm{B}}|$. The total uncertainty has been calculated as the sum in quadrature of the individual uncertainties.

Source	Bin 1 (%)	Bin 2 (%)	Bin 3 (%)	Bin 4 (%)
Uncorrelated systematic errors				
Probability Density Function	2.3	3.2	4.0	4.1
Tag and Probe Statistical	2.1	2.4	3.0	3.4
Tag and Probe Correlation	0.9	0.8	1.2	1.8
Hadron Tracking Efficiency	7.8	7.8	7.8	7.8
Reconstruction Efficiency	2.0	2.0	2.3	2.1
Misalignment	4.5	1.0	1.8	3.2
$p_{\mathrm{T}}^{\mathrm{B}}$ Spectrum	2.2	0.4	0.2	2.5
Non-Luminosity	10.0	9.1	9.8	10.6
Correlated systematic errors				
Branching Fractions	1.4	1.4	1.4	1.4
Luminosity	4.0	4.0	4.0	4.0
Total	10.9	10.0	10.7	11.4

5.9 Results for the Differential Cross Section Measurements

The differential cross section in bins of $p_{\mathrm{T}}^{\mathrm{B}}$ and $|y^{\mathrm{B}}|$ has been calculated, according to Equation 5.1, from the fitted number of signal events (n_{sig}) and from the total reconstruction efficiency (ϵ). Please see Table 5.7, 5.8, and 5.33 for numerical values. The differential cross section results are summarized in Table 5.38-5.39 and plotted in Figure 5.25.

Table 5.38: Summary of differential cross section $d\sigma/dp_{\mathrm{T}}^{\mathrm{B}}$ (nb/GeV/c) in bins of $p_{\mathrm{T}}^{\mathrm{B}}$. For the data measurements, the uncertainties are in order statistical, luminosity-independent and luminosity-dependent systematic.

Bin	$d\sigma/dp_{\mathrm{T}}^{\mathrm{B}}$ (nb/GeV/c)	MC@NLO	PYTHIA
1	$1.172 \pm 0.136 \pm 0.113 \pm 0.047$	0.719	1.513
2	$0.364 \pm 0.035 \pm 0.034 \pm 0.015$	0.240	0.515
3	$0.085 \pm 0.008 \pm 0.008 \pm 0.003$	0.074	0.144
4	$0.007 \pm 0.001 \pm 0.001 \pm 0.001$	0.008	0.010

Table 5.39: Summary of differential cross section $d\sigma/d|y^{\mathrm{B}}|$ (nb) in bins of $|y^{\mathrm{B}}|$. For the data measurements, the uncertainties are statistical, luminosity-independent and luminosity-dependent systematic.

Bin	$d\sigma/|y^{\mathrm{B}}|$ (nb)	MC@NLO	PYTHIA
1	$1.484 \pm 0.147 \pm 0.148 \pm 0.059$	1.040	2.281
2	$1.123 \pm 0.117 \pm 0.102 \pm 0.045$	1.023	2.051
3	$1.634 \pm 0.190 \pm 0.160 \pm 0.065$	0.929	1.833
4	$1.316 \pm 0.161 \pm 0.139 \pm 0.053$	0.801	1.559

The total cross section, integrating over the full $p_{\mathrm{T}}^{\mathrm{B}}$ range, is:

$$\sigma(\mathrm{pp} \to \mathrm{B_s^0}) \times \mathrm{BF}(\mathrm{B_s^0} \to \mathrm{J}/\psi\ \phi) = (6.9 \pm 0.6 \pm 0.6)\ \mathrm{nb} \tag{5.12}$$

with the first error statistical, and the second systematic. The statistical and systematic uncertainties are derived from the bin-by-bin uncertainties and are

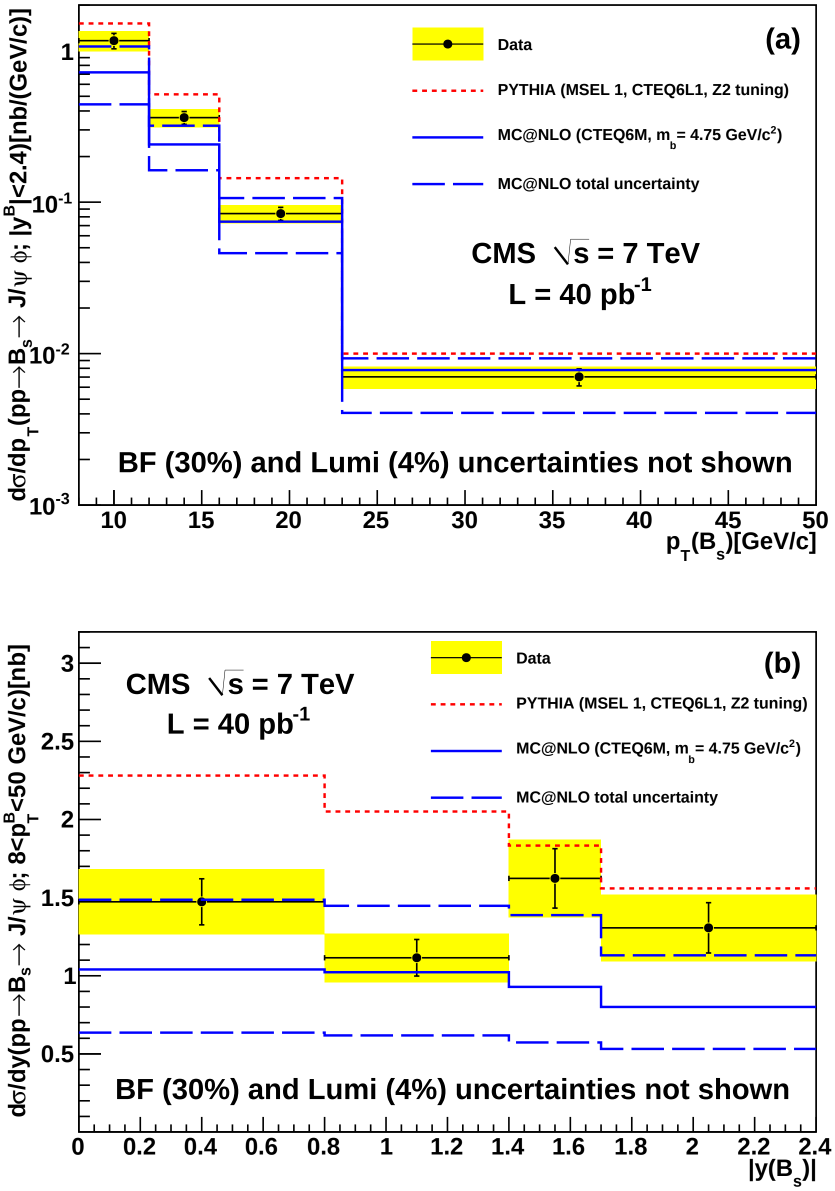

Figure 5.25: Measured differential cross sections $d\sigma/dp_{\mathrm{T}}^{\mathrm{B}}$ (a) and $d\sigma/dy^{\mathrm{B}}$ (b) together with theoretical predictions. The (yellow) band represents the sum in quadrature of statistical and systematic uncertainties. The dotted (red) line is the PYTHIA prediction; the solid and dashed (blue) lines are the MC@NLO prediction and its uncertainty, respectively. The common uncertainties of 4% on the data points, due to the integrated luminosity, and of 30% on the theory curves, due to the $\mathrm{B}_s^0 \to \mathrm{J}/\psi\ \phi$ branching fraction, are not shown.

propagated in the sum. When integrating over the full $|y^{\rm B}|$ range, the total cross section is:

$$\sigma({\rm pp} \to {\rm B_s^0}) \times {\rm BF}({\rm B_s^0} \to \ {\rm J}/\psi\ \phi) = (6.6 \pm 0.6 \pm 0.6)\ {\rm nb} \tag{5.13}$$

where, also, the first error is statistical, and the second is systematic. The results are in agreement within the error. The measured values are compared and lie between the the theoretical predictions of MC@NLO ($4.6^{+1.9}_{-1.7} \pm 1.4$ nb) and PYTHIA (9.4 ± 2.8 nb), where the last uncertainty is from the $\rm B_s^0 \to \ J/\psi\ \phi$ branching fraction Nakamura et al. (2010). The predictions of MC@NLO use the renormalization and factorization scales $\mu = \sqrt{m_{\rm b}^2 c^4 + p_{\rm T}^2 c^2}$, where $p_{\rm T}$ is the transverse momentum of the b-quark, a b-quark mass of $m_{\rm b} = 4.75\ {\rm GeV}/c^2$, and the CTEQ6M parton distribution functions Pumplin et al. (2002). The uncertainty on the MC@NLO cross section is obtained by simultaneously varying the renormalization and factorization scales by factors of two, varying $m_{\rm b}$ by $\pm 0.25\ {\rm GeV}/c^2$, and using the CTEQ6.6 parton distribution function set instead of CTEQ6M. The prediction of PYTHIA uses the CTEQ6L1 parton distribution functions Pumplin et al. (2002), a b-quark mass of $4.8\ {\rm GeV}/c^2$, and the Z2 tune Field (2010) to simulate the underlying event.

The measurement of the cross section of the $\rm B_s^0 \to \ J/\psi\ \phi$ decay completes the B-meson production studies with the CMS detector at the LHC for collisions at a center-of-mass energy of 7 TeV. The summary plot of the $\rm B^+$ Khachatryan et al. (2011), $\rm B^0$ Chatrchyan et al. (2011a), and $\rm B_s^0$ production cross sections is shown in Figure 5.26. The results indicate consistency amongst the three B-mesons cross sections with the NLO theoretical prediction.

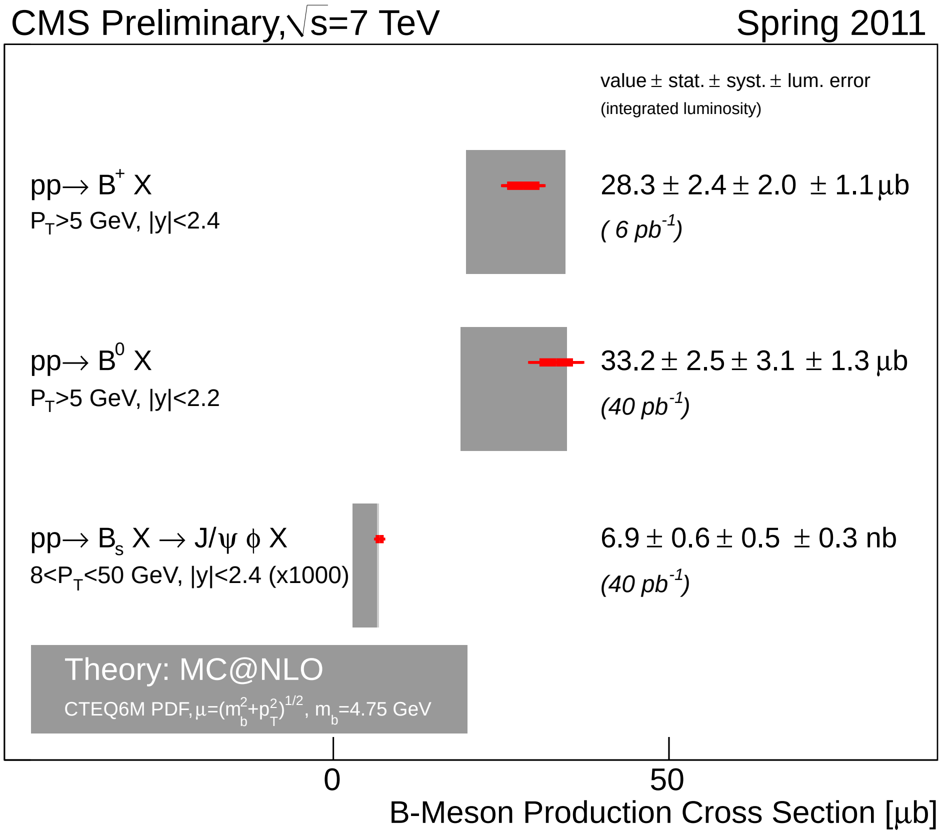

Figure 5.26: Summary of B-meson cross section measurements performed by CMS with 7 TeV center-of-mass energy pp collisions at LHC. The inner error bars of the data points correspond to the statistical uncertainty, while the outer thinner error bars correspond to the quadratic sum of statistical and systematic uncertainties. The outermost brackets in addiction include the luminosity uncertainty. Theory predictions at NLO are obtained using MC@NLO Frixione et al. (2003).

Chapter 6

Branching Fraction for $B_s^0 \rightarrow J/\psi\ \phi$

The branching fraction of the decay $B_s^0 \rightarrow J/\psi\ \phi$ is only known to about 30% uncertainty Nakamura et al. (2010). The present world average has been measured by CDF from their early collision data Abe et al. (1996) and since then the value has been changed from the original paper a different estimate of the hadronization fraction ratios by PDG Nakamura et al. (2010):

$$\mathrm{BF}(B_s^0 \rightarrow J/\psi\ \phi) = (1.4 \pm 0.4 \pm 0.2) \times 10^{-3} \qquad , \tag{6.1}$$

where the first error is the experimental uncertainty while the second error is obtained by averaging the uncertainties of the hadronization fractions found at the LEP and the Tevatron experiments Nakamura et al. (2010) . In this section, the previous measurements of the B^+ Khachatryan et al. (2011) and B^0 Chatrchyan et al. (2011a) production cross sections with the CMS experiment are used to reduce the experimental uncertainty of this branching fraction.

6.1 Strategy

The branching fraction $\mathrm{BF}(\mathrm{B_s^0} \rightarrow\ \mathrm{J}/\psi\ \phi)$ can be calculated independently with respect to either the inclusive $\mathrm{B^+}$ or $\mathrm{B^0}$ production cross sections. The observed cross section for the decay mode $\mathrm{B_s^0} \rightarrow\ \mathrm{J}/\psi\ \phi$ can be written as:

$$\sigma(\mathrm{pp} \rightarrow \mathrm{B_s^0} \rightarrow\ \mathrm{J}/\psi\ \phi) = \sigma(pp \rightarrow \bar{b}) \cdot f_s \cdot \mathrm{BF}(\mathrm{B_s^0} \rightarrow\ \mathrm{J}/\psi\ \phi) \cdot f_{kin}^{\mathrm{B_s^0}} \tag{6.2}$$

and similarly, for the $\mathrm{B^+}X$ and $\mathrm{B^0}X$ mode:

$$\sigma(\mathrm{pp} \rightarrow \mathrm{B^+}X) = \sigma(pp \rightarrow \bar{b}) \cdot f_u \cdot f_{kin}^{\mathrm{B^+}}, \tag{6.3}$$

$$\sigma(\mathrm{pp} \rightarrow \mathrm{B^0}X) = \sigma(pp \rightarrow \bar{b}) \cdot f_d \cdot f_{kin}^{\mathrm{B^0}}. \tag{6.4}$$

Here, the f_u, f_d, and f_s terms are the probabilities that the $\bar{\mathrm{b}}$ quark hadronizes and forms a $\mathrm{B^+}$, $\mathrm{B^0}$, and $\mathrm{B_s^0}$ meson, respectively. The f_{kin}^{B} term corrects for the limited range in rapidity and transverse momentum in the different analyses. The $\mathrm{B_s^0} \rightarrow\ \mathrm{J}/\psi\ \phi$ branching fraction can be derived from either Equation 6.3 or Equation 6.4 as:

$$\mathrm{BF}(\mathrm{B_s^0} \rightarrow\ \mathrm{J}/\psi\ \phi) = \frac{\sigma(\mathrm{pp} \rightarrow \mathrm{B_s^0} \rightarrow\ \mathrm{J}/\psi\ \phi)}{\sigma(\mathrm{pp} \rightarrow \mathrm{B^+}X)} \cdot \frac{f_u}{f_s} \cdot \frac{f_{kin}^{\mathrm{B^+}}}{f_{kin}^{\mathrm{B_s^0}}} \tag{6.5}$$

or

$$\mathrm{BF}(\mathrm{B_s^0} \rightarrow\ \mathrm{J}/\psi\ \phi) = \frac{\sigma(\mathrm{pp} \rightarrow \mathrm{B_s^0} \rightarrow\ \mathrm{J}/\psi\ \phi)}{\sigma(\mathrm{pp} \rightarrow \mathrm{B^0}X)} \cdot \frac{f_d}{f_s} \cdot \frac{f_{kin}^{\mathrm{B^0}}}{f_{kin}^{\mathrm{B_s^0}}} \tag{6.6}$$

where the only unpublished parameters are the ratios of the fraction of the kinematic ranges. Evaluating the $\mathrm{B_s^0} \rightarrow\ \mathrm{J}/\psi\ \phi$ branching fraction as ratio between the cross section measurements removes the systematic uncertainties that are in common, such as the luminosity.

6.2 Calculation

The values for the fragmentation fractions are introduced in Section 1.3.3. The values are:

- $\Gamma(\bar{b} \to \mathrm{B}^0_\mathrm{s}) = (11.0 \pm 1.2)\%$,
- $\Gamma(\bar{b} \to \mathrm{B}^+) = (40.3 \pm 1.1)\%$,
- $\Gamma(\bar{b} \to \mathrm{B}^0) = (40.3 \pm 1.1)\%$.

The ratio of the hadronization fractions is given by:

$$\frac{f_s}{f_{u,d}} = \frac{\Gamma(\mathrm{B}^0_\mathrm{s})}{\Gamma(\mathrm{B}^{+,0})} = (27.2 \pm 3.1)\ \%. \tag{6.7}$$

The cross section measurements in the different B decay modes Khachatryan et al. (2011); Chatrchyan et al. (2011a,b) are:

- $\sigma(\mathrm{pp} \to \mathrm{B}^0_\mathrm{s} \to \mathrm{J}/\psi\ \phi) = (6.9 \pm 0.6 \pm 0.5) \times 10^{-3}\ \mu\mathrm{b}\ (8 < p_\mathrm{T}^\mathrm{B} < 50\ \mathrm{GeV}/c$, $|y^\mathrm{B}| < 2.4)$,
- $\sigma(\mathrm{pp} \to \mathrm{B}^+ X) = (28.3 \pm 2.4 \pm 2.0)\ \mu\mathrm{b}\ (p_\mathrm{T}^\mathrm{B} > 5\ \mathrm{GeV}/c$, $|y^\mathrm{B}| < 2.4)$,
- $\sigma(\mathrm{pp} \to \mathrm{B}^0 X) = (33.2 \pm 2.5 \pm 3.1)\ \mu\mathrm{b}\ (p_\mathrm{T}^\mathrm{B} > 5\ \mathrm{GeV}/c$, $|y^\mathrm{B}| < 2.2)$.

The f^B_{kin} term quantifies explicitly the different kinematic ranges. The branching fraction in Equation 6.5-6.6 depends on the ratio of kinematic factors. The extrapolations to the full kinematic range are theory dependent. The NLO theory predictions for the expected differential cross section values are in good agreement with the measured ones in each of the three decay channels, as reported at the end of Section 5.9. Therefore, it is possible to identify the best central model (CTEQ6M, $Q_R = Q_F = 1$, and b-quark mass=4.75 GeV/c^2) to predict the full kinematic range in p_T^B and $|y^\mathrm{B}|$. The spectra are obtained from NLO generated event samples large enough to keep the relative statistical error of the predicted ratio at 0.1%. The parameters of the model are varied in the same way as for the evaluation of the theoretical uncertainty on the production cross section measurement (see Section 5.9). The ratios of the different kinematic ranges for the different model parameters are listed in Table 6.1. They vary slowly over a wide range of parameters. The plots of the B meson transverse momentum for the central model and for the theoretical corrections considered are shown in Figure 6.1. The branching fraction

Table 6.1: Table of the theoretical NLO predictions Frixione et al. (2003) for the ratio of kinematic range corrections. The first row corresponds to the central model parameter choice.

Model Parameters	$f_{kin}^{\mathrm{B_s^0}}/f_{kin}^{\mathrm{B^+}}$	$f_{kin}^{\mathrm{B_s^0}}/f_{kin}^{\mathrm{B^0}}$
$Q_r = 1.0, Q_f = 1.0, b = 4.75$	0.440	0.470
$Q_r = 0.5, Q_f = 1.0, b = 4.75$	0.425	0.466
$Q_r = 1.0, Q_f = 0.5, b = 4.75$	0.453	0.487
$Q_r = 1.0, Q_f = 2.0, b = 4.75$	0.420	0.456
$Q_r = 2.0, Q_f = 1.0, b = 4.75$	0.422	0.463
$Q_r = 1.0, Q_f = 1.0, b = 4.50$	0.421	0.461
$Q_r = 1.0, Q_f = 1.0, b = 5.00$	0.439	0.490

$\mathrm{BF}(\mathrm{B_s^0} \to \mathrm{J}/\psi\ \phi)$ is derived from the $\mathrm{B^+}$ meson production (Equation 6.5):

$$\mathrm{BF}(\mathrm{B_s^0} \to \mathrm{J}/\psi\ \phi) = (2.03 \pm 0.34) \times 10^{-3} \tag{6.8}$$

and Equation 6.6 from the $\mathrm{B^0}$ meson production :

$$\mathrm{BF}(\mathrm{B_s^0} \to \mathrm{J}/\psi\ \phi) = (1.63 \pm 0.28) \times 10^{-3}. \tag{6.9}$$

In both cases the errors are the combined experimental and PDG uncertainties, respectively. The sources of uncertainties are listed in Table 6.2. The experimental error is the sum in quadrature of the statistical and systematic uncertainties Khachatryan et al. (2011); Chatrchyan et al. (2011a,b). It contains the uncertainty of the yield as extracted from maximum likelihood fits, the uncertainty on the reconstruction and hadron-tracking efficiencies, misalignment, and the variation with different models

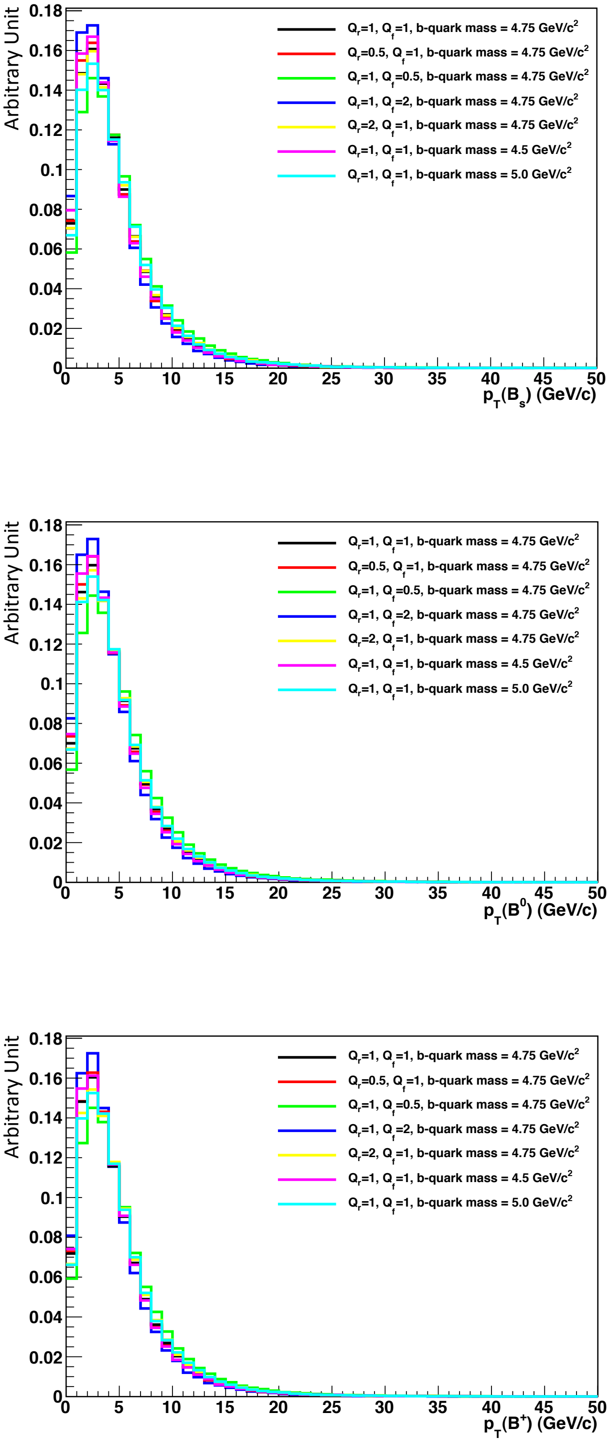

Figure 6.1: Plots of the different theoretical NLO predictions for the transverse momentum spectrum for the three B mesons considered: B_s^0 (top), B^0 (center), B^+ (bottom).

to correct for the limited kinematic ranges. The uncertainty of the ratios of the kinematic ranges is evaluated as the largest relative deviation from our central model independent of the sign. The PDG uncertainty is the sum in quadrature of the errors of the branching fractions and fragmentation fractions Nakamura et al. (2010).

Table 6.2: Relative uncertainties for the branching fraction calculated with respect to the B^+- and B^0-inclusive cross section measurements.

Source	$BF^{B_s^0 \to J/\psi\ \phi}_{B^+ \to J/\psi\ K^+}$	$BF^{B_s^0 \to J/\psi\ \phi}_{B^0 \to J/\psi\ K_s^0}$
	Experimental Uncertainties	
Signal yields	15.8%	16.5%
NLO spectrum	4.6%	4.3%
	PDG Uncertainties	
Branching fractions	3.5%	3.8%
Fragmentation fraction	11.2%	11.2%

6.3 Results

The two measurements of the branching fraction $BF(B_s^0 \to J/\psi\ \phi)$ overlap within one standard deviation. Their error weighted average is

$$BF(B_s^0 \to J/\psi\ \phi) = (1.8 \pm 0.2 \pm 0.2) \times 10^{-3}. \tag{6.10}$$

The result agrees within one standard deviation with the world average value $BF(B_s^0 \to J/\psi\ \phi) = (1.4 \pm 0.4 \pm 0.2) \times 10^{-3}$ Nakamura et al. (2010). The experimental uncertainty is reduced by a factor of two.

Chapter 7

B_s^0 Decay Property Measurements

The following Chapter describes the measurement of the average lifetime, the lifetime difference, and the CP content with the decay channel $B_s^0 \to J/\psi\ \phi$. The strategy and the results of a ML fit on the CMS 2010 dataset to extract the B_s^0 average lifetime $\bar{\Gamma}$, the lifetime difference $\Delta\Gamma$, and the CP fractions are presented. The Minimal Model (presented in Section 1.4.4) is applied.

7.1 Fitting Procedure

The ML fit reuses the yield measurement and extends it for measuring more details of the B_s^0 decay. The guiding principle in choosing the PDFs is to use the simplest function with the least number of parameters necessary to adequately describe the observed distribution of events in the three reconstructed variables: the $J/\psi\ \phi$ invariant mass $M_{J/\psi\phi}$, the proper decay time t, and $\cos\theta$ as defined in the transversity basis. Three sample contributions are considered: signal, B combinatorial (non-prompt), and prompt J/ψ background. A common resolution function $\mathcal{R}$, parameterized as single Gaussian function, is adopted for all three components. For the signal, the Minimal Model describes the time- and angular-dependency simultaneously. Equation 1.50 shows how this model can be factorized. Figure 7.1 shows the Minimal Model integrated over the two event variables $\cos\theta$

and t, respectively. The angular variable $\cos\theta$ for non-prompt and prompt J/ψ

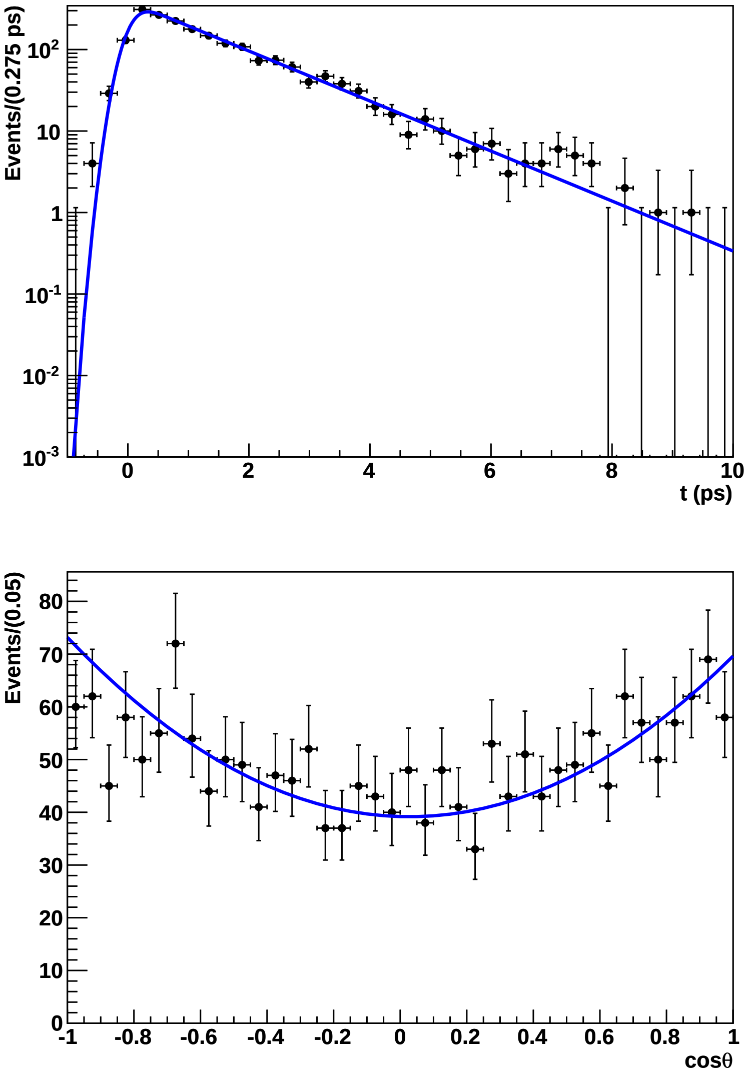

Figure 7.1: Projection of the Minimal Model onto the proper decay time t (top) and $\cos\theta$ (bottom) variables from signal $B_s^0 \rightarrow$ J/ψ ϕ events.

backgrounds has been parametrized from the MC simulated background events described in Section 4.3. For both contributions, a 2^{nd} order polynomial function proofed sufficient. Figure 7.2 shows the $\cos\theta$ distributions for B background and prompt J/ψ events. The J/ψ ϕ invariant mass sideband regions (as defined in Section 5.3.2) are assumed to contain only B and prompt J/ψ background events.

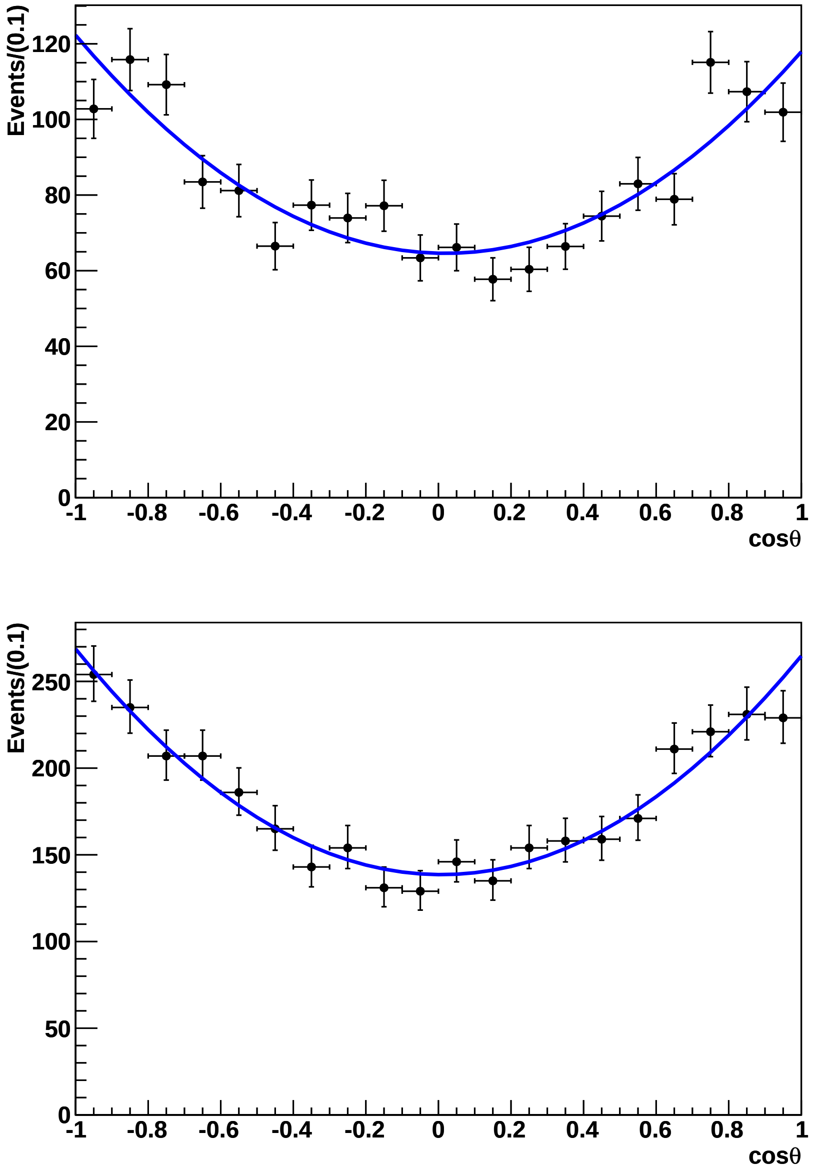

Figure 7.2: The $\cos\theta$ distribution for the B background cocktail (top) and for the prompt J/ψ (bottom) events in MC samples.

Table 7.1: Parameters used for the Monte Carlo simulation $\mathrm{B_s^0} \to$ J/ψ ϕ decay and results from the fit of the Minimal Model to signal events. The constraint $|A_{||}(0)|^2 = 1 - |A_0(0)|^2 - |A_\perp(0)|^2$ is applied.

Parameter	Embedded Value	Fitted Value
$\tau = 1/\bar{\Gamma}$	1.472 ps	1.452 ± 0.036 ps
$\Delta\Gamma/\Gamma$	0.1	0.112 ± 0.054
Δm	20 ps	20 ps (fixed)
$\|A_0(0)\|^2$	0.57	0.580 ± 0.072
$\|A_{\|\|}(0)\|^2$	0.25	constrained
$\|A_\perp(0)\|^2$	0.18	0.202 ± 0.051
δ_1	2.50	2.50 (fixed)
δ_2	-0.17	-0.17 (fixed)
ϕ_s	-0.04	0 (fixed)

Therefore, it is possible to take advantage of the distribution of the prompt J/ψ background, fully described within $t < 0.3$ ps, to select only B background events from the sideband regions. The solid line in the data is obtained from the fit to the Monte Carlo simulated B background sample (see Figure 7.3 on the left). It demonstrates that the distribution shape is correctly described by the MC B background sample. For the prompt J/ψ background the situation is more complicated. This component is irreducible in the sample extracted from the sideband region. However, it is the main source of background in the central kinematic region. The shape of the prompt J/ψ background is then obtained from data removing the requirement $t < 0.3$ ps and it is compared with the MC sample. Figure 7.3 (on the right) shows the $\cos\theta$ distribution for B and prompt J/ψ background events in data. Table 7.2 lists the parameters of the two background components for the PDF of $\cos\theta$ in data and MC. The values differ by less than one standard deviation.

The likelihood is parameterized as described in Section 5.2. Three individual components are considered: signal, combinatorial B, and prompt J/ψ backgrounds.

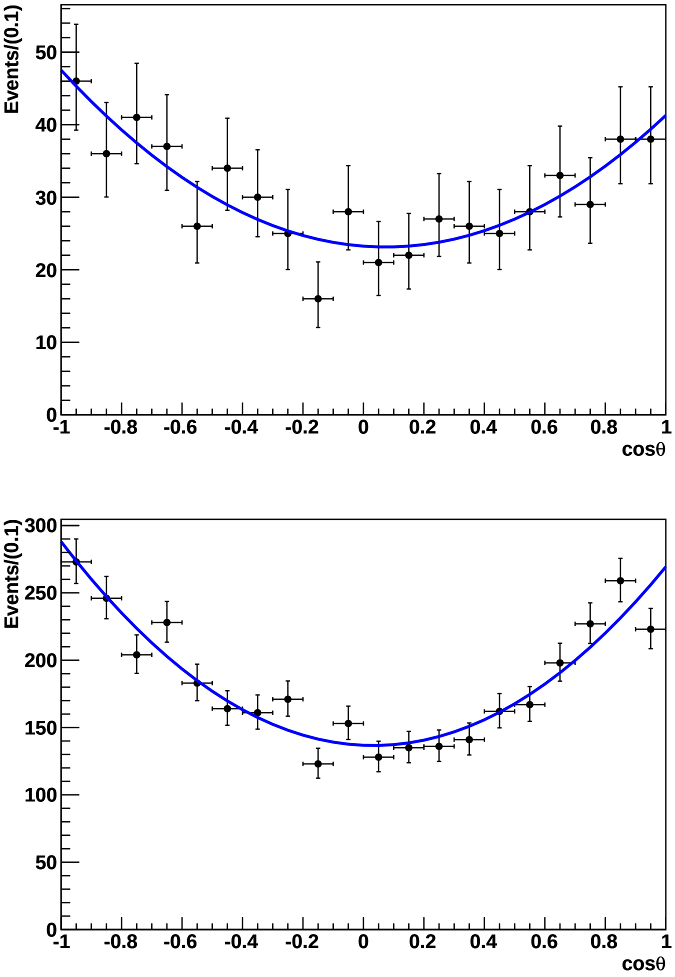

Figure 7.3: The $\cos\theta$ distribution for B background (left) and prompt J/ψ (right) events in data events from the J/$\psi\phi$ invariant mass excluding the B_s^0-signal region ($5.20 < M_{J/\psi\phi} < 5.29$ GeV/c^2 and $5.45 < M_{J/\psi\phi} < 5.65$ GeV/c^2).

Table 7.2: Summary table for the fit results of the $\cos\theta$ parameterization for the B and prompt J/ψ components in MC and data.

	B background	
	MC	Data
a_0	$-3.53 \cdot 10^{-02} \pm 5.34 \cdot 10^{-02}$	$-9.23 \cdot 10^{-02} \pm 6.75 \cdot 10^{-02}$
a_1	$2.97 \cdot 10^{-01} \pm 4.54 \cdot 10^{-02}$	$3.12 \cdot 10^{-01} \pm 5.68 \cdot 10^{-02}$
	Prompt J/ψ	
	MC	Data
a_0	$-7.50 \cdot 10^{-02} \pm 2.75 \cdot 10^{-02}$	$-4.50 \cdot 10^{-02} \pm 2.73 \cdot 10^{-02}$
a_1	$3.13 \cdot 10^{-01} \pm 2.32 \cdot 10^{-02}$	$3.41 \cdot 10^{-01} \pm 2.25 \cdot 10^{-02}$

The extended likelihood function is the product of likelihoods for each event j:

$$\mathcal{L} = \exp\left(-\sum_{i=1}^{3} n_i\right) \prod_j \left[\sum_{i=1}^{3} n_i \mathcal{P}_i(M_{\mathrm{B}};\, \vec{\alpha}_i) \mathcal{Q}_i(t, \cos\theta;\, \vec{\beta}_i)\right]. \tag{7.1}$$

The PDFs $\mathcal{P}_i$ and $\mathcal{Q}_i$ are parameterized separately for each fit component with shape parameters $\vec{\alpha}_i$ for $M_{\mathrm{J/\psi\phi}}$ and $\vec{\beta}_i$ for the two-dimensional function of the variables t and $\cos\theta$. For signal this latter one is given by the Minimal Model, while, for the background is the simple product of the t and $\cos\theta$ PDFs. The ansatz to express the probabilities for each component in terms of the product PDF of the event variables has been verified with simulated events. The linear correlation coefficients between the event variables amongst the three components are found to be at most 8%. Therefore, they are assumed to have a negligible impact on the fit.

7.2 Acceptance Function

The event reconstruction and selection can modify the proper decay time t and $\cos\theta$ distribution biasing the measurement of the physical parameter. This distortion is corrected with a two-dimensional function that can be factorized as follows:

$$\epsilon(t, \cos\theta) = \epsilon(t) \cdot \epsilon(\cos\theta). \tag{7.2}$$

where the first term models the effects of the reconstruction and selection on the decay time, while the second term the angular distribution. The correlation between the two event variables is about 3% percent.

The proper decay time distribution can be biased by the trigger or by the event selection. To quantify these effects, the ratio $\epsilon(t) = N_{reco}/N_{gen}$ is shown in Figure 7.4, where N_{reco} is the number of triggered, reconstructed, and selected signal events while N_{gen} is the number of signal events generated by PYTHIA. The efficiency function exhibits a flat and stable plateau. A deficit of events is observed at high proper decay

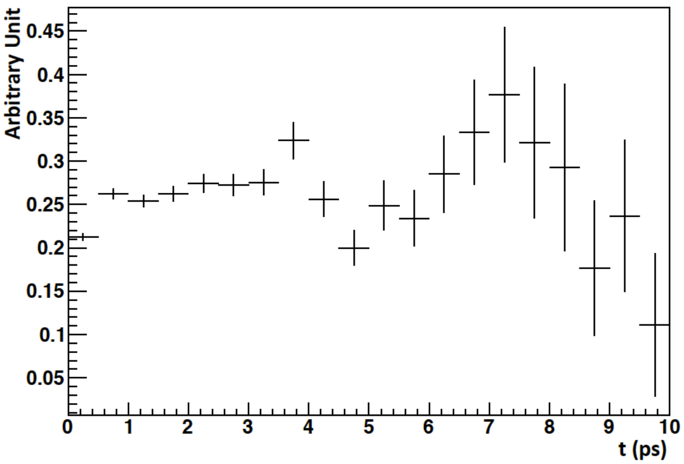

Figure 7.4: Distribution of the observed time-dependent efficiency $\epsilon(t)$ as a function of the proper time.

time values. This decrease in efficiency is attributed to the negative exponential term of the lifetime that drops rapidly as function of the variable t. This effect is mitigated by the large statistical uncertainty due to the limited-size of the signal sample with negligible effects on the fit results.

In principle, the angular efficiency $\epsilon(\cos\theta)$ is a three-dimensional efficiency which cannot be easily factorized due to the strong correlation between $\cos\theta$, $\cos\psi$, and φ in the angular distribution definitions (see Section 1.41). The three angular functions are, therefore, considered simultaneously and a three dimensional histogram is filled by calculating the ratio of the number of reconstructed and selected Monte Carlo events and the number of events expected from the generation only. The plots of the three variables when integrating over the other two are shown in Figure 7.5. Because the Minimal Model depends only on one of the three angular functions ($\cos\theta$), the corresponding acceptance function is taken. The two acceptance correction functions are multiplied to likelihood term for the signal component. Similar studies have been performed for the B background. The results demonstrate that an acceptance function for the B background has negligible effects (less that 1%) on the signal yield.

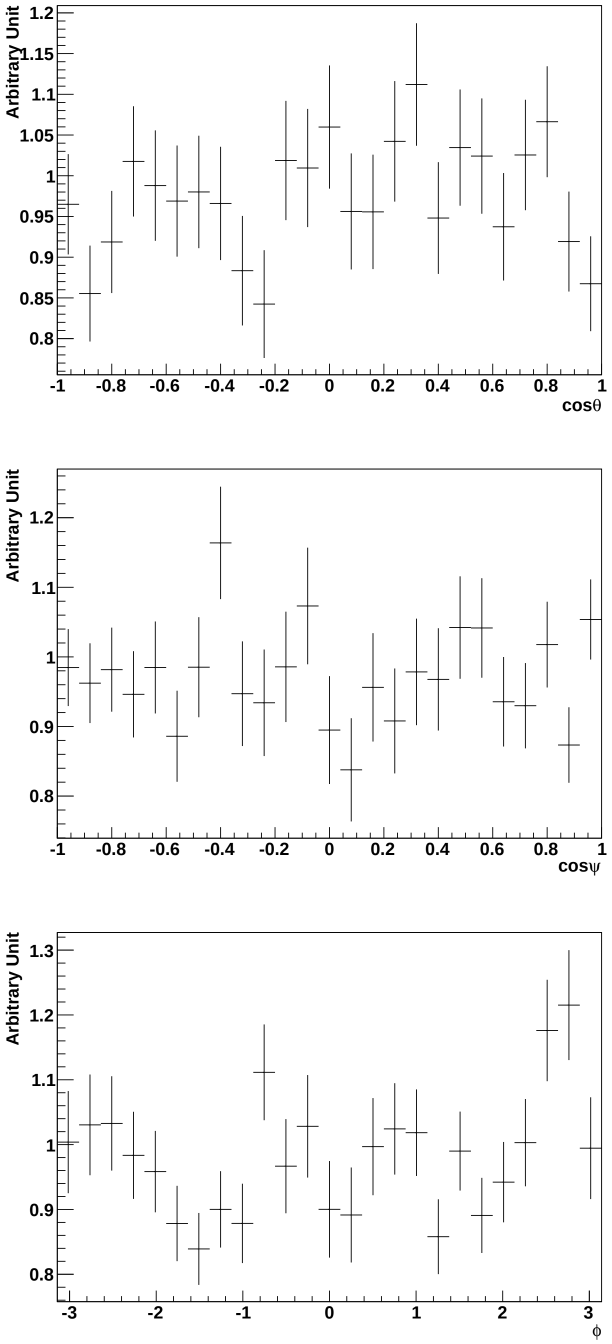

Figure 7.5: Projections onto the three transversity basis variables of the three dimensional acceptance function $\epsilon(\Theta)$: $\epsilon(\cos\theta)$ (top), $\epsilon(\cos\psi)$ (center), and $\epsilon(\phi)$ (bottom).

7.3 Fit Validation

To test the stability of the fit and to understand how well the Minimal Model predicts the physical parameters of interest 400 toy experiments are generated from the PDFs. For each toy sample, the expected signal and background yields correspond to those found in the ML fit for the cross section measurement. The list of the embedded and fitted parameter values is summarized in Table 7.3. The results determined from the toy experiments agree within the statistical uncertainty with the generated values. The statistical errors for the B_s^0 lifetime difference and the CP fraction in the decay are found to be of the order of 140% and 70%, respectively. The large uncertainties have two contributions: First, the low statistics sample of data does not allow a very precise distinction of the two B_s^0 states Γ_H and Γ_L; Second, the integration over the two-angular variable φ and $\cos\psi$ reduces the signal/background discrimination of the decay rate function. The statistical error was scanned when performing 400 fits for samples on events generated from the PDFs for a corresponding sample of integrated luminosity 400 pb^{-1} (ten times the available statistics) and 4 fb^{-1} (the total amount of data collected since the startup by the CMS detector). The results and the reduction of the uncertainty due to the increase of the statistics are summarized in Table 7.4-7.5. The statistical uncertainty for the yields scales correctly with the increase of statistics. For the physical parameters this does not happen. It is observed that the statistical uncertainty, for example, of $\Delta\Gamma$ decreases by 30% and 50% only. This indicates that the Minimal Model is not an optimal model for precise measurements

Table 7.3: Fit parameters for the 400 toy experiment samples each corresponding to an integrated luminosity of about 40 pb^{-1}.

	Embedded value	Fitted value
N_{sig}	550	553 ± 33
N_{prompt}	3935	3984 ± 234
$N_{\mathrm{Bbackground}}$	1715	1670 ± 232
Γ (ps^{-1})	0.690	0.684 ± 0.058
$\Delta\Gamma$ (ps^{-1})	0.145	0.156 ± 0.217
$f_{odd} = \vert A_\perp\vert^2$	0.18	0.202 ± 0.148

of B_s^0 decay properties. A new measurement applying the complete definition of time-dependent decay rate model, which involves also the study of CP-violation effects, will be performed by CMS in the future with the complete statistics. In this case, the precision of the measurement is limited by the increase of the instantaneous luminosity that requires adjustments of the trigger definitions. These new triggers will implement more strict requirements on the two muons, such a minimum value for the significance of the dimuon decay vertex, that could bias the B_s^0 decay properties. Therefore, the results will be sensitive to the systematic uncertainties assigned to the trigger requirement criteria.

Table 7.4: Fit parameters for the 400 toy experiment samples each corresponding to an integrated luminosity of about 400 pb^{-1}. The last columns represent the reduction of the statistical error when increasing the statistics by a factor of ten.

	Embedded value	Fitted value	Error reduction (1x → 10x)
N_{sig}	5500	5508 ± 133	–
N_{prompt}	39350	39208 ± 629	–
$N_{\mathrm{Bbackground}}$	17150	17284 ± 616	–
Γ (ps^{-1})	0.655	0.657 ± 0.047	8.5% → 7.2%
$\Delta\Gamma$ (ps^{-1})	0.112	0.105 ± 0.108	139% → 103%
$f_{odd} = \|A_\perp\|^2$	0.259	0.253 ± 0.101	73.3% → 39.9%

Table 7.5: Fit parameters for the 400 toy experiment samples each corresponding to an integrated luminosity of about 4 fb^{-1}. The last columns represent the reduction of the statistical error when increasing the statistics by a factor of one hundred.

	Embedded value	Fitted value	Error reduction (1x → 100x)
N_{sig}	55000	54837 ± 361	–
N_{prompt}	393500	393014 ± 2123	–
$N_{\mathrm{Bbackground}}$	171500	172149 ± 1997	–
Γ (ps^{-1})	0.655	0.654 ± 0.029	8.5% → 4.4%
$\Delta\Gamma$ (ps^{-1})	0.112	0.109 ± 0.081	139% → 74%
$f_{odd} = \|A_\perp\|^2$	0.259	0.261 ± 0.034	73.3% → 13.4%

7.4 Fit Results

The results of the fit to the full data sample is presented in Table 7.6. They are compared to the results obtained by the LHCb LHCb Collaboration (2011) and the CDF CDF Collaboration (2011) experiments. All the parameters, except the weak phase ϕ_s (fixed to the SM expected value) and the long lifetime for the B background (fixed to the B^0 lifetime), have been left free to float. In Figure 7.6 the fit projections on J/ψ ϕ invariant mass, proper decay time t, and $\cos\theta$ are shown. The results demonstrate the capabilities of the CMS pixel detector to reconstruct charged particle trajectories close to the interaction point for the determination of momentum and secondary vertices of long-lived objects.

Table 7.6: Summary table for the fit result to the 2010 CMS data, corresponding to 40 pb^{-1}, and comparison with the results from the LHCb and CDF experiments.

	CMS (40 pb^{-1})	LHCb (337 pb^{-1})	CDF (5.2 fb^{-1})
N_{sig}	567 ± 32	n.a.	n.a.
N_{prompt}	3818 ± 185	n.a.	n.a.
$N_{\text{Bbackground}}$	1824 ± 184	n.a.	n.a.
Γ (ps^{-1})	0.655 ± 0.050	$0.656 \pm 0.009 \pm 0.008$	$0.653 \pm 0.011 \pm 0.005$
$\Delta\Gamma$ (ps^{-1})	0.112 ± 0.345	$0.123 \pm 0.029 \pm 0.008$	$0.075 \pm 0.025 \pm 0.010$
$f_{odd} = \|A_\perp\|^2$	0.259 ± 0.234	$0.238 \pm 0.015 \pm 0.011$	$0.245 \pm 0.014 \pm 0.015$

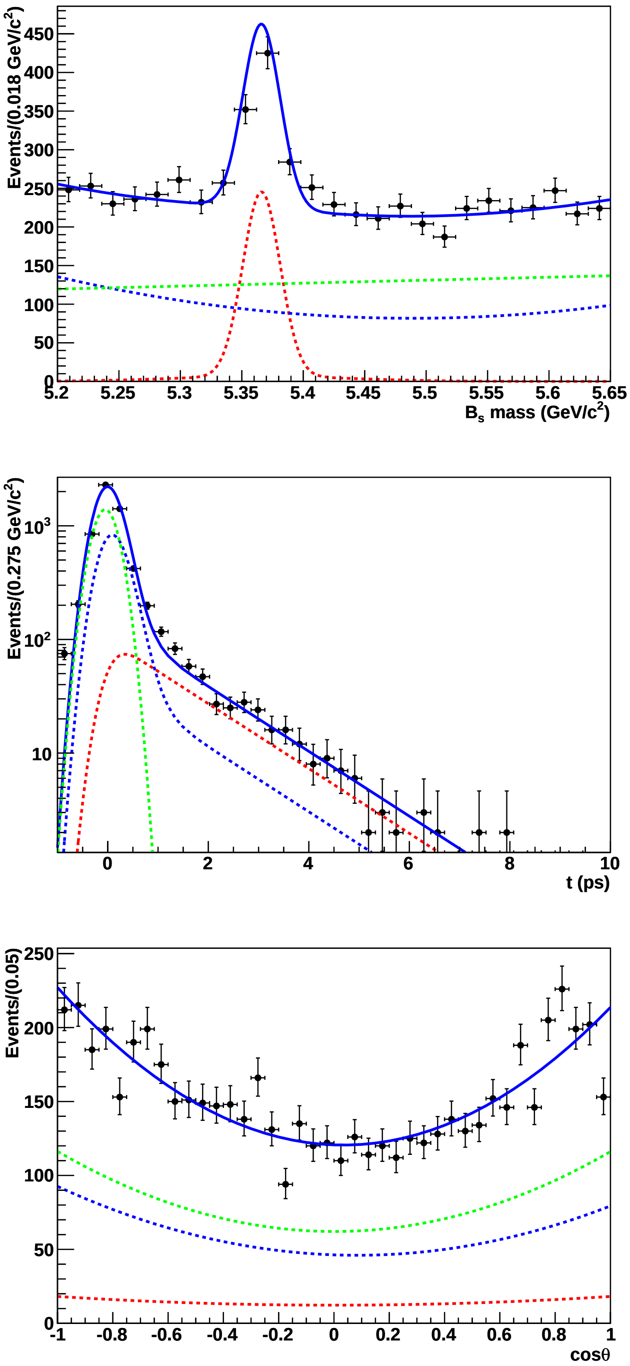

Figure 7.6: Projections of the fit results in the J/$\psi\phi$ invariant mass with the requirement $ct > 0.01$ cm (left) and with the yields scaled accordingly, proper decay time t (right), and $\cos\theta$ (center) for the full range of $8 < p_{\mathrm{T}}^{\mathrm{B}} < 50$ GeV/c and $|y^{\mathrm{B}}| < 2.4$. Individual contributions from the various components are shown in different colors: signal (red), B background (dashed blue), and J/ψ prompt background (dashed green).

7.5 Conclusion

The production of hadrons containing b-quarks has been measured in pp collisions at the new center-of-mass energy $\sqrt{s} = 7$ TeV with the CMS detector at the LHC. The $\mathrm{B_s^0}$ differential cross sections $d\sigma/dp_\mathrm{T}^\mathrm{B}$ and $d\sigma/dy^\mathrm{B}$ in the exclusive decay channel $\mathrm{B_s^0} \rightarrow \mathrm{J}/\psi\ \phi$ are presented in four bins in the kinematic range $|y^\mathrm{B}| < 2.4$ and $8 < p_\mathrm{T}^\mathrm{B} < 50$ GeV$/c$. They are calculate from the number of signal events, extracted with a ML fit to a dataset where selection requirements are applied to maximize the ratio signal over background, and from the reconstruction efficiencies using both Monte Carlo and data-driven methods. The total $\mathrm{B_s^0} \rightarrow \mathrm{J}/\psi\ \phi$ production cross-section is measured to be

$$\sigma(\mathrm{pp} \rightarrow \mathrm{B_s^0}) \times \mathrm{BF}(\mathrm{B_s^0} \rightarrow \mathrm{J}/\psi\ \phi) = (6.9 \pm 0.6 \pm 0.6)\ \mathrm{nb}. \tag{7.3}$$

It is compared to simulations to Next-to-Leading order (QCD) bin-by-bin and integrated over the full p_T- and η-range. Bin-by-bin, the distribution of the measured points lay between the values predicted by the PYTHIA and MC@NLO generators, reproducing the expected shape. While PYTHIA overestimates, MC@NLO shows cross section values in each bin that are somewhat lower. When integrating over the full kinematic range, the predicted total cross section at the NLO is $\sigma(\mathrm{pp} \rightarrow \mathrm{B_s^0}) \times \mathrm{BF}(\mathrm{B_s^0} \rightarrow \mathrm{J}/\psi\ \phi) = (4.6^{+1.9}_{-1.7} \pm 1.4)$ nb. An overall normalization factor and upward corrections bin-by-bin are required to improve the description of the b-hadron production cross section and match the measurement. In comparison with measurements of B^+ Khachatryan et al. (2011) and B^0 Chatrchyan et al. (2011a) production cross section, the same trend is observed. The measured cross section for the three B-meson species are used to retune the NLO generators for the Higgs search in early 2012.

The uncertainty of the $\mathrm{B_s^0} \rightarrow \mathrm{J}/\psi\ \phi$ branching fraction remains the largest source of uncorrelated systematic uncertainties. An estimation of the $\mathrm{B_s^0} \rightarrow \mathrm{J}/\psi\ \phi$ branching fraction has been calculated in combination with the other two CMS measurements of B^+ and B^0 production cross section. The value of the branching fraction for the $B_s^0 \rightarrow J/\psi\ \phi$ decay, assuming the fragmentation fraction values as extracted from measurements at the LEP and Tevatron, is $(1.8 \pm 0.2 \pm 0.2) \times 10^{-3}$ that agrees within one standard deviation with the value published from the Tevatron Nakamura et al. (2010).

The $B_s^0 \rightarrow J/\psi\ \phi$ decay is of particular interest since it allows to study the properties of the B_s^0 system such as the average lifetime, lifetime difference of the two weak states of the B_s^0 mesons, CP-content in the decay, as well as, CP-violating effects. A reduced version of the time-dependent decay rate model has been used. This model has been implemented in a ML fit and the analysis has been finalized on the 2010 CMS dataset that corresponds to an integrated luminosity of 40 pb^{-1}. The proper decay time, lifetime difference, and CP-fractions are measured and compared with the latest results from the LHCb LHCb Collaboration (2011) and the CDF CDF Collaboration (2011) experiments. The analysis presented here prototypes higher statistics measurement in 2012, where the full time-dependent decay rate model is implemented to, eventually, measure CP violation.

The results on the differential and partially integrated cross section and B_s^0 lifetime have been published in the journal Physical Review D Chatrchyan et al. (2011b) in 2011. Branching fraction and proper decay time dependent measurements have been presented in national and international meetings CMS Collaboration (2011a) CMS Collaboration (2011b).

Bibliography

Bibliography

Abachi, S. et al. (1995). Inclusive μ and b-quark Production Cross Sections in p$\bar{\text{p}}$ Collisions at $\sqrt{s} = 1.8$ TeV. *Phys. Rev. Lett.*, 74:3548. 21

Abbott, B. et al. (2000a). Cross section for b jet production in p$\bar{\text{p}}$ collisions at $\sqrt{s} = 1.8$ TeV. *Phys. Rev. Lett.*, 85:5068. 21

Abbott, B. et al. (2000b). Small angle muon and bottom quark production in p$\bar{\text{p}}$ collisions at $\sqrt{s} = 1.8$ TeV. *Phys. Rev. Lett.*, 84:5478. 21

Abe, F. et al. (1992a). Inclusive J/ψ, ψ(2S), and b-quark production in p$\bar{\text{p}}$ collisions at $\sqrt{s} = 1.8$ TeV. *Phys. Rev. Lett.*, 69:3704. 25

Abe, F. et al. (1992b). Measurement of the B-meson and b-quark cross sections at $\sqrt{s} = 1.8$ TeV using the exclusive decay $\mathrm{B}^{\pm} \rightarrow \mathrm{J}/\psi K^{\pm}$. *Phys. Rev. Lett.*, 68:3403. 25

Abe, F. et al. (1993). Measurement of the bottom quark production cross-section using semileptonic decay electrons in p$\bar{\text{p}}$ collisions at $\sqrt{s} = 1.8$ TeV. *Phys. Rev. Lett.*, 71:500. 21, 25

Abe, F. et al. (1995). Measurement of the B meson differential cross-section, $d\sigma/dp_{\mathrm{T}}$, in p$\bar{\text{p}}$ collisions at $\sqrt{s} = 1.8$ TeV. *Phys. Rev. Lett.*, 75:1451. 21

Abe, F. et al. (1996). Ratios of bottom meson branching fractions involving J/ψ mesons and determination of b quark fragmentation fractions. *Phys. Rev. D*, 54:6596. 217

Abe, F. et al. (1997). Production of J/ψ Mesons from χ_c Meson Decays in p$\bar{\text{p}}$ Collisions at $\sqrt{s} = 7$ TeV. *Phys. Rev. Lett.*, 79:578. 124

Abe, F. et al. (1998). Observation of the B_c Meson in p$\bar{\text{p}}$ Collisions at $\sqrt{s} = 1.8$ TeV. *Phys. Rev. Lett.*, 81:2432. 26

Abe, K. et al. (2002). Improved Measurement of Mixing-induced CP Violation in the Neutral B Meson System. *Phys. Rev. D*, 66:071102. 11, 25, 36

Abulencia, A. et al. (2007). Measurement of the B^+ production cross section in p$\bar{\text{p}}$ collisions at $\sqrt{s} = 1960$ GeV. *Phys. Rev. D*, 75:012010. 21

Acosta, D. E. et al. (2002). Measurement of the B^+ total cross section and B^+ differential cross section $d\sigma/dp_T$ in p$\bar{\text{p}}$ collisions at $\sqrt{s} = 1.8$ TeV. *Phys. Rev. D*, 65:052005. 21

Acosta, D. E. et al. (2005). Measurement of the J/ψ meson and b-hadron production cross sections in p$\bar{\text{p}}$ collisions at $\sqrt{s} = 1960$ GeV. *Phys. Rev. D*, 71:032001. 21

Agostinelli, S. et al. (2003). GEANT4: A simulation toolkit. *Nucl. Instrum. Meth. A*, 506:250. 121

Albajar, C. et al. (1988). Measurement of the bottom quark production cross section in proton-antiproton collisions at $\sqrt{s} = 0.63$ TeV. *Phys. Lett.*, B213:405. 21

Albrecht, H. et al. (1991). Reconstruction of semileptonic b → u decays. *Phys. Lett. B*, 255:297. 25

Aldrich, J. (1997). R.A. Fisher and the making of maximum likelihood 1912-1922. *Statist Sci.*, 2:162. 158

ALEPH Collaboration (1997). Improved measurement of the B(d)0 - anti-B(d)0 oscillation frequency. *Z Phys.*, C 75:397. 34

Andreev, V. (2007). B production at the LHC / QCD aspects. In *Proceedings of the IVIIth Rencontres de Moriond*, La Thuile, Italy. 21

Antcheva, I. et al. (2009). ROOT – A C++ framework for petabyte data storage, statistical analysis and visualization. *Comput. Phys. Commun.*, 180:2499. 85, 86, 159

Aubert, B. et al. (2002a). Measurement of $\mathrm{B}^0 - \overline{\mathrm{B}^0}$ Flavor Oscillations in Hadronic B^0 Decays. *Phys. Rev. Lett.*, 88:221802. 34

Aubert, B. et al. (2002b). Study of time-dependent CP-violating asymmetries and flavor oscillations in neutral B decays at the Υ(4S). *Phys. Rev. D*, 66:032003. 11, 25, 36, 195

Aubert, B. et al. (2005a). Measurement of CP asymmetries in $\mathrm{B}^0 \rightarrow \phi K^0$ and $\mathrm{B}^0 \rightarrow K^+K^-K_s^0$ decays. *Phys. Rev. D*, 71:091102. 16

Aubert, B. et al. (2005b). Measurements of Branching Fractions and Time-Dependent CP-Violating Asymmetries in B to η' K Decays. *Phys. Rev. Lett.*, 94:191802. 16

Baines, J. (2006). Heavy Quarks: Summary Report. In *HERA-LHC Workshop Proceedings: Summary report of Working Group 3*, page 98. 123

Belau, E. et al. (1983). Charge collection in silicon strip detectors. *Nuclear Instruments and Methods in Physics Research*, 214:253. 98

Bell, J. (1954). *CPT Violation and the Standard Model*. PhD in Physics, Birmingham University. 35

Bona, M. et al. (2005). The 2004 UTfit collaboration report on the status of the unitarity triangle in the standard model. *Journal of High Energy Physics*, 2005(07):28. 14

Boyer, J. (2001). Canonical XML Version 1.0, W3C Recommendation 15 March 2001. `http://www.w3.org/TR/xml-c14n`. 109

Branco, G., Lavoura, L., and Silva, J. (1999). *CP Violation.* Oxford Science Press. 31

Bruning, O. S. et al. (2004). *LHC Design Report.* CERN, Geneva. 45

Cabibbo, N. (1963). Unitary Symmetry and Leptonic Decays. *Phys. Rev. Lett.*, 10:531. 9

Cacciari, M. et al. (1998). The p_{T} spectrum in heavy-flavour hadroproduction. *JHEP*, 05:007. 22

Cacciari, M. et al. (2004). QCD analysis of first b cross-section data at 1.96 TeV. *JHEP*, 07:033. 22

Cacciari, M. and Greco, M. (1994). Large p_{T} hadroproduction of heavy quarks. *Nucl. Phys.*, B421:530. 22

Cano-Coloma, B. and Sanchis-Lozano, M. (1997). Charmonia production in hadron colliders and the extraction of colour-octet matrix elements. *Nuclear Physics B*, 508(3):753. 124

Catani, S. et al. (1991). High-energy factorization and small x heavy flavor production. *Nucl. Phys.*, B366:135. 21

CDF Collaboration (1998). Measurement of $\mathrm{B_d^0} - \bar{\mathrm{B}}_\mathrm{d}^0$ Oscillation Frequency Using $\pi - B$ Meson Charge-Flavor Correlations in $p\bar{p}$ at $\sqrt{s}1.8$ TeV. *Phys. Rev. Lett.*, 80:2057. 34

CDF Collaboration (2008). First Flavor-Tagged Determination of Bounds on Mixing-Induced CP Violation in $\mathrm{B_s^0} \rightarrow \mathrm{J}/\psi\ \phi$ Decays. *Phys. Rev. Lett.*, 100:7. 36

CDF Collaboration (2011). CP Violation with $\mathrm{B_s^0} \rightarrow \mathrm{J}/\psi\ \phi$ at the Tevatron. 233, 236

Charles, J. et al. (2005). CP violation and the CKM matrix: assessing the impact of the asymmetric B factories. *Eur. Phys. J. C*, 41:1. 14

Chatrchyan, S. et al. (2011a). Measurement of the B^0 production cross section in pp collisions at $\sqrt{s} = 7$ TeV. *Phys. Rev. Lett.*, 106:252001. 215, 217, 219, 220, 235

Chatrchyan, S. et al. (2011b). Measurement of the B_s^0 Production Cross Section with $\mathrm{B}_\mathrm{s}^0 \to \mathrm{J}/\psi\ \phi$ Decays in pp Collisions at $\sqrt{s} = 7$ TeV. *Phys. Rev. D*, 84:052008. 219, 220, 236

Christenson, J. (1964). Evidence for the 2π Decay of the K_2^0 Meson. *Phys. Rev. Lett.*, 13:138. 11, 35

CLEO Collaboration (2006). Observation of B_s^0 Production at the $\Upsilon(5\mathrm{S})$ Resonance. *Phys.Rev.Lett.*, 96:022002. 25

CMS Collaboration (1997a). *The CMS hadron calorimeter project: Technical Design Report*. Technical Design Report CMS. CERN, Geneva. 73

CMS Collaboration (1997b). *The CMS muon project: Technical Design Report*. Technical Design Report CMS. CERN, Geneva. 78

CMS Collaboration (2002a). *CMS TriDAS project: Technical Design Report; 1, the trigger systems*. Technical Design Report CMS. CERN, Geneva. 105, 107, 110, 111

CMS Collaboration (2002b). *CMS trigger and data-acquisition project: Technical Design Report*. Technical Design Report CMS. CERN, Geneva. 82, 84

CMS Collaboration (2005). *CMS computing: Technical Design Report*. Technical Design Report CMS. CERN, Geneva. 85, 122

CMS Collaboration (2006a). *CMS Physics Technical Design Report Volume I: Detector Performance and Software*. Technical Design Report CMS. CERN, Geneva. 46, 55, 95, 133

CMS Collaboration (2006b). *CMS physics Technical Design Report, Volume II: Physics Performance*, volume 34. CERN. xxiii, 81

CMS Collaboration (2006c). *CMS TriDAS project: Technical Design Report I; the trigger systems*. Technical Design Report CMS. CERN, Geneva. 82

CMS Collaboration (2007). Adaptive Vertex Fitting. *CMS Analysis Note*, CMS-AN-07-008. 134

CMS Collaboration (2008). The CMS experiment at the CERN LHC. *Journal of Instrumentation*, 3(08):S08004. 46, 55, 78

CMS Collaboration (2010a). $\mathrm{B_s^0} \to$ J/ψ ϕ event display from 7 TeV collision data. *CMS Detector Performance Summaries*, CMS-DP-2010-024. 61, 65

CMS Collaboration (2010b). $\mathrm{B_s^0} \to$ J/ψ ϕ invariant mass distribution. *CMS Detector Performance Summaries*, CMS-DP-2010-040. 160

CMS Collaboration (2010c). Measurement of Tracking Efficiency. *CMS Physics Analysis Summary*, CMS-PAS-TRK-10-002. 209

CMS Collaboration (2010d). Performance of muon identification in pp collisions at $\sqrt{s} = 7$ TeV. *CMS Physics Analysis Summary*, CMS-PAS-MUO-10-002. 198

CMS Collaboration (2010e). Tracking and Primary Vertex Results in First 7 TeV Collisions. *CMS Physics Analysis Summary*, CMS-PAS-TRK-10-005. 133

CMS Collaboration (2011a). Measurement of the Bs to Jpsi phi Production Cross Section in pp Collisions at sqrt(s)=7 TeV with the CMS Detector at LHC. In *Talk at the American Physical Society, Anaheim, CA, USA*. 236

CMS Collaboration (2011b). Study of the Bs to Jpsi phi decay with the CMS Detector at LHC. In *Talk at the Division of Particles and Fields of American Physical Society, Providence, RI, USA*. 236

Collins, J. C. and Ellis, R. K. (1991). Heavy quark production in very high-energy hadron collisions. *Nucl. Phys.*, B360:3. 21

Corcella, G. et al. (2001). HERWIG 6.5: an event generator for Hadron Emission Reactions With Interfering Gluons (including supersymmetric processes). *Journal of High Energy Physics*, 101(010):112. 25

D0 Collaboration (2006). Measurement of B_d mixing using opposite-side flavor tagging. *Phys. Rev. D*, 74:112002. 34

D0 Collaboration (2008). Measurement of $\mathrm{B_s^0}$ mixing parameters from the flavor-tagged decay. *Phys. Rev. Lett.*, 101:7. 36

Das, S. (2009). Status and Performance of the Compact Muon Solenoid Pixel Detector. In *Proceedings of the Technology and Instrumentation in Particle Physics*, Tsukuba, Japan. 109

DELPHI Collaboration (1997). Measurement of B(d)0 - anti-B(d)0 oscillations. *Z Phys.*, C 76:579. 34

Dighe, A., Dunietz, I., and Fleischer, R. (1999). Extracting CKM phases and mixing parameters from angular distributions of non-leptonic decays. *Eur. Phys. J. C*, 6:647. 38

Dighe, A. S., Dunietz, I., Lipkin, H. J., and Rosner, J. L. (1996). Angular distributions and lifetime differences in $\mathrm{B_s^0} \to \mathrm{J}/\psi\ \phi$ decays decays. *Phys. Lett. B*, 369:144. 38

Drutskoy, A. et al. (2007). Measurements of exclusive $\mathrm{B_s^0}$ decays at the Υ(5S). *Phys. Rev. D*, 76:012002. 25

Dunietz, I. et al. (2001). In Pursuit of New Physics with $\mathrm{B_s^0}$ Decays. *Phys. Rev. D*, 63:114015. 32, 37, 38, 43

Field, R. (2010). Early LHC Underlying Event Data–Findings and Surprises. In *Proceedings of the Hadron Collider Physics Symposium*. 215

Flügge, G (1994). Future Research in High Energy Physics. *In N. Ellis and M. B. Gavela, editors, 1993 European School of High Energy Physics, Yellow reports.* xxi, 27

Frixione, S. et al. (2003). Matching NLO QCD and parton showers in heavy flavour production. *JHEP*, 08:007. xviii, xxxi, 25, 216, 220

Fruhwirth, R. (1987). Application of Kalman filtering to track and vertex fitting. *Nucl. Instrum. Methods Phys. Res., A*, 262(HEPHY-PUB-503):444. 87, 135

Fulton, R. et al. (1990). Observation of B-meson semileptonic decays to noncharmed final states. *Phys. Rev. Lett.*, 64:16. 25

Glashow, S. (1961). Partial Symmetries of Weak Interactions. *Nucl. Phys.*, 22:579. 10

Gluckstern, R. L. (1963). Uncertainties in track momentum and direction due to multiple scattering and measurement errors. *Nucl. Instrum. Meth.*, 24:352. 61

Greenberg, O. W. (1964). Spin and Unitary Spin Independence in a Paraquark Model of Baryons and Mesons. *Phys.Rev.Lett.*, 13:598. 8

Gross, L. (2007). The DiagnosticSystem Package. `https://twiki.cern.ch/twiki/bin/view/CMS/DiagnosticSystem`. 113

Hastings, N. C. et al. (2003). Studies of $B^0 - B^0$ mixing properties with inclusive dilepton events. *Phys. Rev. D*, 67:052004. 34

Henrich, B. et al. (2002). Lorentz-angle in irradiated silicon. *Nucl. Instrum. Meth.*, A477:304. 96

Higgs, P. (1964). Broken Symmetries and the Masses of Gauge Bosons. *Phys. Rev. Lett.*, 13:508. 11

I_2O Special Interest Group (1999). Intelligent I/O (*I_2O*) Architecture Specification v2.0. `http://www.intelligent-io.com`. 109

Ivova, M. (2011). Lorenz angle in the CMS pixel detector. In *Talk at Tracker DPG, CERN, Switzerland*. 98

J., B. F., Branco, G. C., and Nebot, M. (2007). CP violation and limits on New Physics including recent measurements. *Nucl. Phys. B*, 768:1. 37

J., G., Murray, S., and Orsini, L. (2003). Towards a homogeneous architecture for high-energy physics data acquisition systems. *Computer Physics Communications*, 153(2):155. 110

J., G. J. (2005). Ajax: A New Approach to Web Applications. `http://www.AdaptivePath.com`. 115

James, F. et al. (1975). Minuit: a system for function minimization and analysis of the parameter errors and corrections. *Comput. Phys. Commun.*, 10(CERN-DD-75-20):343. 159

Jost, R. (1957). Eine Bemerkung zum CTP Theorem. *Helvetica Physica Acta*, 30:409. 35

Khachatryan, V. et al. (2011). Measurement of the B^+ production cross section in pp collisions at $\sqrt{s} = 7$ TeV. *Phys. Rev. Lett.*, 106:112001. 215, 217, 219, 220, 235

Kniehl, B. A. et al. (2008). Finite-mass effects on inclusive B-meson hadroproduction. *Phys. Rev. D*, 77:014011. 22

Kobayashi, M. and Maskawa, T. (1973). CP-Violation in the Renormalizable Theory of Weak Interaction. *Prog. Theor. Phys.*, 49:652. 9

Kovalskyi, D. et al. (2010). Fireworks: A physics event display for CMS. *Journal of Physics: Conference Series*, 219(3):032014. 61

Krocker, G. (2011). CP Violation in $\mathrm{B_s^0}$ Mixing at LHCb. In *Poster for Physics in Collision 2011*, Vancouver, Canada. 34

L., E. and Bryant, P. (2008). LHC Machine. *Journal of Instrumentation*, 3(08):S08001. 45

L3 Collaboration (1998). Measurement of the B0(d)-antiB0(d) oscillation frequency. *Eur. Phys. J.*, C 5:195. 34

Lange, D. J. (2001). The EvtGen particle decay simulation package. *Nucl. Instrum. Meth. A*, 462:152. 121

Leonardo, N. (2010). Measurement of J/ψ, Υ and b-hadron production in proton-proton collisions at $\sqrt{s} = 7$ TeV with the CMS experiment. In *Proceedings of the 35th International Conference of High Energy Physics*, Paris, France. 65

Lesiak, T. (2001). b-quark physics at LEP. *Acta Phys. Pol. B*, 32(6):1711. 25

LHCb Collaboration (2011). Combination of ϕ_s measurements from $\mathrm{B_s^0} \to$ J/ψ ϕ and $\mathrm{B_s^0} \to$ J/$\psi f_0(980)$. *LHC Note*, LHCb-CONF-2011-056. 233, 236

Luders, G. (1954). On the equivalence of invariance under time reversal and under particle-antiparticle conjugation for relativistic field theories. *Math.-Phys. Medd.*, 28:1. 35

Nakamura, K. et al. (2010). Review of particle physics. *J. Phys.*, G37:075021. xiii, xxx, 12, 13, 14, 18, 25, 26, 33, 34, 37, 52, 62, 63, 90, 123, 135, 136, 181, 183, 185, 208, 215, 217, 222, 236

Nason, P. et al. (1988). The Total Cross-Section for the Production of Heavy Quarks in Hadronic Collisions. *Nucl. Phys. B*, 303:607. 20, 21

Noether, E. (1918). Invariante Variationsprobleme. *Math.-Phys. Kl.*, 186207:235. 35

Norrbin, E. et al. (2000). Production and hadronization of heavy quarks. *Eur. Phys. J. C*, 17:137. xxi, 22, 25

OPAL Collaboration (1996). Measurement of B(d)0 - anti-B(d)0 oscillations. *Z. Phys.*, C 72:377. 34

Pauli, W., Rosenfeld, L., and Weisskopf, V. (1955). *Niels Bohr and the development of physics*. McGraw-Hill. 35

Prokofiev, K. (2005). *Study of the* $\mathrm{B}_\mathrm{s}^0 \rightarrow \mathrm{J}/\psi/\psi\phi \rightarrow \mu^+\mu^-K^+K^-$ *Decay with the CMS Detector at LHC*. PhD in Physics, Universität Zurich. 136

Prokofiev, K. and Speer, T. (2004). A kinematic and a decay chain reconstruction library. In *Proceedings of Computing in High Energy Physics and Nuclear Physics*, page 411, Interlaken, Switzerland. 136

Pumplin, J. et al. (2002). New generation of parton distributions with uncertainties from global QCD analysis. *JHEP*, 07:012. 25, 215

Raven, G. (2011). B Physics Results from LHC. In *Talk at Lepton-Photon, Mumbai, India*. 16

Ross, B. et al. (2004). Mozilla Firefox Web Browser. `http://www.mozilla.org/en-US/firefox/new/`. 115

S., F., Nason, P., and Webber, B. R. (2003). Matching NLO QCD and parton showers in heavy flavour production. *Journal of High Energy Physics*, 2003(08):007. 25

Salam, A. et al. (1964). Electromagnetic and weak interactions. *Phys. Lett.*, 13:168. 10

Sjöstrand, T. et al. (2006). PYTHIA 6.4 physics and manual. *JHEP*, 05:026. 25, 52, 121, 122 t'Hooft, G. (1971a). Renormalizable Lagrangians for massive Yang-Mills fields. *Nucl. Phys. B*, 35:167. 10

t'Hooft, G. (1971b). Renormalization of massless Yang-Mills fields. *Nucl. Phys. B*, 33:173. 10

Turner, M. (1999). Cosmology solved? Quite possibly! *Publ. Astron. Soc. Pac.*, 111:264. 6, 11

Van der Meer, S. (1968). Calibration of the effective beam height in the ISR. Technical Report CERN-ISR-PO-68-31. ISR-PO-68-31, CERN, Geneva. 127

Webber, B. (1994). Hadronization. In *Lectures at Summer School on Hadronic Aspects of Collider Physics*, Zuoz, Switzerland. 23

Weimberg, S. (1967). A Model of Leptons. *Phys. Rev. Lett.*, 19:1264. 10

Wolfenstein, L. (1964). Violation of CP Invariance and the Possibility of Very Weak Interactions. *Phys. Rev. Lett.*, 13:562. 11, 35

Wolfenstein, L. (1983). Parametrization of the Kobayashi-Maskawa Matrix. *Phys. Rev. Lett.*, 51:1945. 12

Wu, C. (1957). Experimental Test of Parity Conservation in Beta Decay. *Phys. Rev. Lett.*, 105:1413. 35

Appendix

Appendix A

Extra Results on the ML Fit

A.1 B_s^0 Mass PDFs Without Requirement on ct

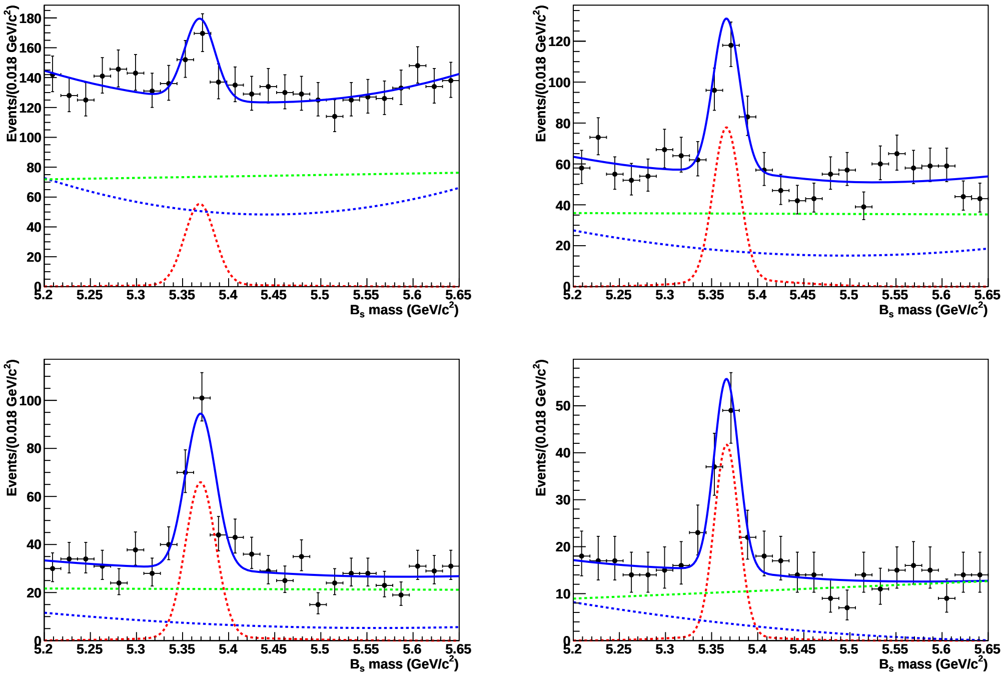

Figure A.1: Projections of the fit results in M_B for the four p_T^B bins: 8–12 (top left), 12–16 (top right), 16–23 (bottom left), and 23–50 (GeV/c) (bottom right). Individual contributions from the various components are shown in different colors: signal (red), B background (dashed blue), and J/ψ prompt background (dashed green).

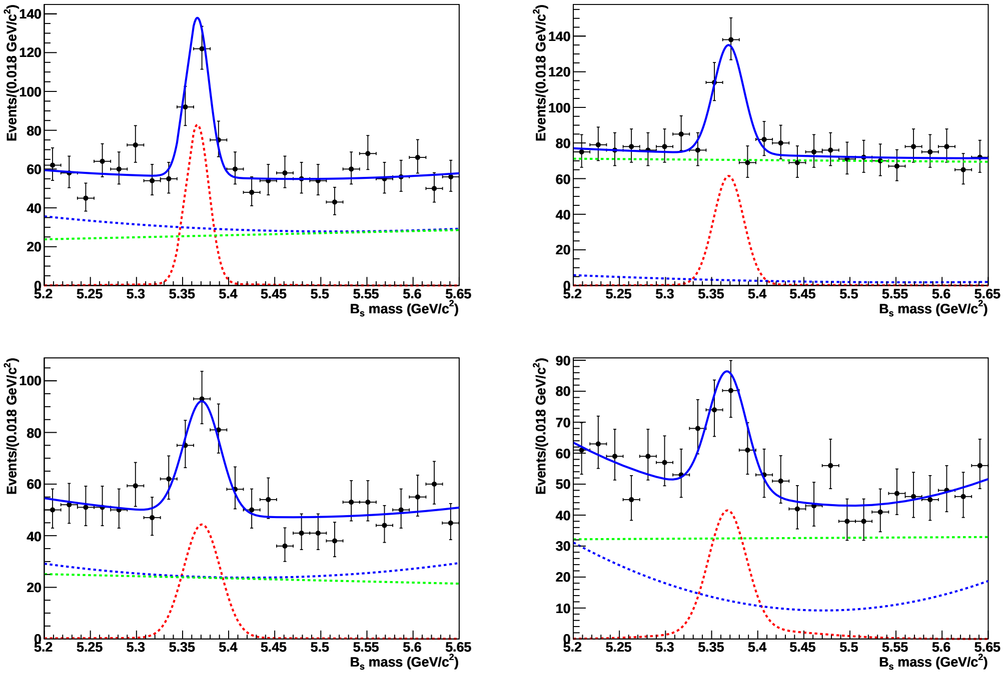

Figure A.2: Projections of the fit results in M_{B} for the four $|y|$ bins: 0.0–0.8 (top left), 0.8–1.4 (top right), 1.4–1.7 (bottom left), and 1.7–2.4 (GeV/c) (bottom right). Individual contributions from the various components are shown in different colors: signal (red), B background (dashed blue), and J/ψ prompt background (dashed green).

A.2 ML Fit Results

Table A.1: Summary table of the 2D ML fit results for $8 < p_{\mathrm{T}}^{\mathrm{B}} < 50$ GeV/c and $|y^{\mathrm{B}}| < 2.4$.

Parameter	$8 < p_{\mathrm{T}}^{\mathrm{B}} < 50$ GeV/c, $\lvert y^{\mathrm{B}}\rvert < 2.4$
N_{sig}	548.8 ± 32.0
N_{prompt}	3935 ± 109
$N_{\mathrm{Bbackground}}$	1716 ± 105
$\lambda = c\tau$	478.4 ± 25.5
p_0^{Bbkg}	$-2.82117 \cdot 10^{-01} \pm 9.15798 \cdot 10^{-02}$
p_1^{Bbkg}	$1.87481 \cdot 10^{-01} \pm 6.22441 \cdot 10^{-02}$
p_0^{prompt}	$6.27733 \cdot 10^{-02} \pm 4.70790 \cdot 10^{-02}$

Table A.2: Summary table of the 2D ML fit results for $8 < p_{\mathrm{T}}^{\mathrm{B}} < 12$ GeV/c and $|y^{\mathrm{B}}| < 2.4$.

Parameter	$8 < p_{\mathrm{T}}^{\mathrm{B}} < 50$ GeV/c, $\lvert y^{\mathrm{B}}\rvert < 2.4$
N_{sig}	137.6 ± 16.0
N_{prompt}	1848 ± 92
$N_{\mathrm{Bbackground}}$	1389 ± 92
p_0^{Bbkg}	$-5.52172 \cdot 10^{-02} \pm 1.04793 \cdot 10^{-01}$
p_1^{Bbkg}	$1.74631 \cdot 10^{-01} \pm 6.10288 \cdot 10^{-02}$
p_0^{prompt}	$2.79887 \cdot 10^{-02} \pm 8.55381 \cdot 10^{-02}$

Table A.3: Summary table of the 2D ML fit results for $12 < p_{\mathrm{T}}^{\mathrm{B}} < 16$ GeV/c and $|y^{\mathrm{B}}| < 2.4$.

Parameter	$8 < p_{\mathrm{T}}^{\mathrm{B}} < 50$ GeV/c, $\lvert y^{\mathrm{B}}\rvert < 2.4$
N_{sig}	175.9 ± 16.6
N_{prompt}	890 ± 54
$N_{\mathrm{Bbackground}}$	459 ± 53
p_0^{Bbkg}	$-2.23295 \cdot 10^{-01} \pm 1.67228 \cdot 10^{-01}$
p_1^{Bbkg}	$1.95002 \cdot 10^{-01} \pm 1.18806 \cdot 10^{-01}$
p_0^{prompt}	$-6.47847 \cdot 10^{-03} \pm 1.00247 \cdot 10^{-01}$

Table A.4: Summary table of the 2D ML fit results for $16 < p_{\mathrm{T}}^{\mathrm{B}} < 23$ GeV/c and $|y^{\mathrm{B}}| < 2.4$.

Parameter	$8 < p_{\mathrm{T}}^{\mathrm{B}} < 50$ GeV/c, $\lvert y^{\mathrm{B}}\rvert < 2.4$
N_{sig}	162.3 ± 15.8
N_{prompt}	536 ± 33
$N_{\mathrm{Bbackground}}$	175 ± 30
p_0^{Bbkg}	$-4.03296 \cdot 10^{-01} \pm 2.17191 \cdot 10^{-01}$
p_1^{Bbkg}	$1.66195 \cdot 10^{-01} \pm 1.94735 \cdot 10^{-01}$
p_0^{prompt}	$-1.21205 \cdot 10^{-02} \pm 1.02472 \cdot 10^{-01}$

Table A.5: Summary table of the 2D ML fit results for $23 < p_{\mathrm{T}}^{\mathrm{B}} < 50$ GeV/c and $|y^{\mathrm{B}}| < 2.4$.

Parameter	$8 < p_{\mathrm{T}}^{\mathrm{B}} < 50$ GeV/c, $\lvert y^{\mathrm{B}}\rvert < 2.4$
N_{sig}	85.5 ± 11.4
N_{prompt}	184 ± 21
$N_{\mathrm{Bbackground}}$	160 ± 23
p_0^{Bbkg}	$-1.02191 \cdot 10^{+00} \pm 1.66532 \cdot 10^{-01}$
p_1^{Bbkg}	$1.99470 \cdot 10^{-01} \pm 1.43738 \cdot 10^{-01}$
p_0^{prompt}	$6.56387 \cdot 10^{-01} \pm 2.11605 \cdot 10^{-01}$

Table A.6: Summary table of the 2D ML fit results for $8 < p_{\mathrm{T}}^{\mathrm{B}} < 50$ GeV/c and $|y^{\mathrm{B}}| < 0.8$.

Parameter	$8 < p_{\mathrm{T}}^{\mathrm{B}} < 50$ GeV/c, $\lvert y^{\mathrm{B}}\rvert < 2.4$
N_{sig}	150.6 ± 14.7
N_{prompt}	654 ± 50
$N_{\mathrm{Bbackground}}$	745 ± 52
p_0^{Bbkg}	$-1.04787 \cdot 10^{-01} \pm 1.14665 \cdot 10^{-02}$
p_1^{Bbkg}	$6.49022 \cdot 10^{-02} \pm 7.82779 \cdot 10^{-02}$
p_0^{prompt}	$9.14819 \cdot 10^{-02} \pm 1.26385 \cdot 10^{-01}$

Table A.7: Summary table of the 2D ML fit results for $8 < p_{\mathrm{T}}^{\mathrm{B}} < 50$ GeV/c and $0.8 < |y^{\mathrm{B}}| < 1.4$.

Parameter	$8 < p_{\mathrm{T}}^{\mathrm{B}} < 50$ GeV/c, $\lvert y^{\mathrm{B}}\rvert < 2.4$
N_{sig}	143.7 ± 15.4
N_{prompt}	1759 ± 44
$N_{\mathrm{Bbackground}}$	72 ± 16
p_0^{Bbkg}	$-6.10032 \cdot 10^{-01} \pm 2.76896 \cdot 10^{-01}$
p_1^{Bbkg}	$2.41693 \cdot 10^{-01} \pm 2.89976 \cdot 10^{-02}$
p_0^{prompt}	$-1.04921 \cdot 10^{-02} \pm 4.25024 \cdot 10^{-01}$

Table A.8: Summary table of the 2D ML fit results for $8 < p_{\mathrm{T}}^{\mathrm{B}} < 50$ GeV/c and $1.4 < |y^{\mathrm{B}}| < 1.7$.

Parameter	$8 < p_{\mathrm{T}}^{\mathrm{B}} < 50$ GeV/c, $\lvert y^{\mathrm{B}}\rvert < 2.4$
N_{sig}	129.3 ± 15.4
N_{prompt}	580 ± 54
$N_{\mathrm{Bbackground}}$	641 ± 57
p_0^{Bbkg}	$7.14063 \cdot 10^{-03} \pm 1.40316 \cdot 10^{-01}$
p_1^{Bbkg}	$1.02350 \cdot 10^{-01} \pm 8.94559 \cdot 10^{-02}$
p_0^{prompt}	$-8.75847 \cdot 10^{-02} \pm 1.54610 \cdot 10^{-01}$

Table A.9: Summary table of the 2D ML fit results for $8 < p_{\mathrm{T}}^{\mathrm{B}} < 50$ GeV/c and $1.7 < |y^{\mathrm{B}}| < 2.4$.

Parameter	$8 < p_{\mathrm{T}}^{\mathrm{B}} < 50$ GeV/c, $\lvert y^{\mathrm{B}}\rvert < 2.4$
N_{sig}	138.8 ± 16.5
N_{prompt}	811 ± 54
$N_{\mathrm{Bbackground}}$	376 ± 54
p_0^{Bbkg}	$-3.66732 \cdot 10^{-01} \pm 1.95899 \cdot 10^{-01}$
p_1^{Bbkg}	$4.25356 \cdot 10^{-01} \pm 1.25417 \cdot 10^{-02}$
p_0^{prompt}	$1.66231 \cdot 10^{-02} \pm 1.12399 \cdot 10^{-01}$

Vita

Giordano Cerizza was born on July 31st 1980. After completing high school at Liceo Scientifico G. Casiraghi, Cinisello Balsamo, Milano (Italy) in 1999, he attended Universita degli Studi di Milano from 1999-2005. He graduated with a B.S. and M.S. degree in Physics. In 2006, while teaching programming classes to college freshmen, he was accepted at the University of Tennessee for the Ph.D. program. He taught for two years before starting his research assistant position. He received his Ph.D. in February 2012.